Electronic Structure
and
Exchange Integrals
of
Low-Dimensional Cuprates

eingereicht von

Helge Rosner

geb. am 11. 01. 1967 in Eisenhüttenstadt

Contents

List of Figures

List of Tables

List of abbreviations

1(2,3)D	one(two,three)-dimensional
AFM	antiferromagnetism, antiferromagnetic
AHM	anisotropic HEISENBERG model
AO	atomic-like orbitals
ARPES	angle-resolved photoemission spectroscopy
ASA	atomic sphere approximation
BE	binding energy
BZ	BRILLOUIN zone
CQSCA	coupled quantum spin chain approach
DFT	density functional theory
dHvA	DE HAAS VAN ALPHEN
DOS	density of states
EELS	electron energy-loss spectroscopy
EHM	extended HUBBARD model
FLAPW	full-potential linear augmented plane wave
FM	ferromagnetism, ferromagnetic
FPLO	full-potential local-orbital minimum-basis
FWHM	full width at half maximum
FS	FERMI surface
FY	fluorescence yield
INS	inelastic neutron scattering
LAPW	linear augmented plane wave
LCAO	linear combination of atomic orbitals
L(S)DA	local (spin) density approximation
LHB	lower HUBBARD band
LMTO	linear muffin-tin orbitals
LSDA	local spin density approximation
PDOS	partial density of states
RPA	random phase approximation
SWA	spin wave approximation
TEY	total electron yield
TB	tight binding
UHB	upper HUBBARD band
VB	valence band
xc	exchange and correlation
XAS	x-ray absorption spectroscopy
XPS	x-ray photospectroscopy
ZRS(T)	ZHANG-RICE-singlet(triplet)

Chapter 1

Introduction

The knowledge of the electronic structure of solids is a fundamental ingredient to the understanding of their properties. In the last decades there was a tremendous progress in the investigation of electronic structures, but our knowledge is still far from being complete. The exact solution of the complete many-body problem of a solid is impossible due to the huge number of degrees of freedom. To approximate the solution, the standard way is a mapping onto an effective independent particle picture with every particle considered to move in the same potential created by all other particles. This procedure is very successful for many metals and intermetallic compounds, but it fails for example for some transition metal oxides such as CrO_2, NiO or CuO. For these compounds, the single electron picture yields metallic behavior instead of the experimentally observed insulating behavior. This fact is due to the strong COULOMB correlations present in the poorly screened d-states. Compounds where the effective mean field approximation[1] fails due to strong electron-electron interaction are commonly denoted as strongly correlated systems.

Initiated by the discovery of the high temperature superconductivity (HTSC) [1], the development of methods for a better description of such strongly correlated systems was, in particular during the last ten years, one of the most interesting directions in solid state physics. The knowledge of the mechanism of HTSC would be important for technical applications, but in spite of many efforts this mechanism is still unclear. A further detailed study of different aspects of strongly correlated systems might also provide a key for the solution of this fascinating HTSC problem.

The fundamental structural building block in all high temperature superconductors is a copper-oxygen plane built from CuO_2-plaquettes (see Figs. 3.1, 3.21).

---

[1]In this context, the expression *mean field approximation* should be understood more generally for approaches which neglect at least a part of dynamic interactions due to an approximate mapping onto an effective single particle picture.

Starting from isolated plaquettes of this type which can be written as $[\mathrm{CuO_4}]^{-6}$, a rich variety of topologically different copper-oxygen networks can be described. All members of this big family are kept together by Cu $3d$-O $2p$ molecular states. An important quantity for the electronic properties is the total number of d-holes in the plaquette. In the isolated plaquette mentioned above, one d-hole is already present on the copper site. Additional holes or electrons can be introduced either by substitution of different cations, or by an excess or a lack of oxygen. In the present work, only undoped compounds with one exception are investigated. For this class of compounds, the antibonding Cu $3d$-O $2p$ band is half-filled and splits into an upper and a lower band due to the strong electron-electron interaction on the copper site. A correlation gap opens, the groundstate is insulating and in most cases antiferromagnetic.

The essential difference between all these cuprates composed of copper-oxygen plaquettes is the varying connection between the plaquettes. Corresponding to the connection, these compounds can be classified as zero-, one-, two- and three-dimensional systems with respect to the electronic structure (see Chapter 3). A detailed analysis of the electronic properties especially for the low-dimensional compounds, which can be regarded in some sense as parent-compounds of the more complex high temperature superconductors, is the aim of the present work.

The understanding of low-dimensional cuprates might be not only the key for the problem of HTSC: The main issue addressed in this work are the unusually magnetic properties of these systems (see Chapter 4) that attracted large theoretical interest in recent years. In the class of quasi one-dimensional compounds, one finds for example nearly ideal realizations of the one-dimensional spin-1/2 HEISENBERG model [2]. Spin-charge separation [3] or phase transitions to antiferromagnetism [4] and to a spin PEIERLS state [5], respectively, are observed at low temperatures. These phase transitions are affected by large quantum fluctuations. In some cases the corresponding transition temperature is extremely low with respect to the dominating exchange interaction, furthermore unusual small magnetic moments are found. All these properties make the low-dimensional cuprates to be ideal model systems for checking, improving and developing theoretical approaches to physics in low-dimensions.

In this work, a typical strategy to investigate strongly correlated systems like cuprates is pursued: The relevant orbitals are found from band structure calculations. Using these orbitals and the related transfer matrix elements, models which take into account the strong correlations explicitly are constructed and lead to a more suitable description of such strongly correlated systems.

The thesis is organized as follows: The theoretical background of the band structure calculations performed on the basis of the density functional theory is presented in Chapter 2. In Chapter 3, a systematic overview of cuprate com-

pounds belonging to the typical network geometries is given, including band structure calculations and the discussion of the relevant orbitals for each presented compound. The extraction of model parameters from the above mentioned band structure calculations and a more appropriate treatment of the strong COULOMB correlations is presented in Chapter 4 with focus on typical examples. The interpretation of spectroscopic measurements starting from band structure calculations and subsequent model calculations is the topic of Chapter 5. Finally, a short summary and an outlook is given in Chapter 6.

Chapter 2

Electronic structure of solids

2.1 Density functional theory

A complete description of a solid could be achieved by solving the SCHRÖDINGER equation for the many-particle-problem. Due to the huge number of degrees of freedom in the order of magnitude of the AVOGADRO-constant, however, the many-particle wave function is much too complex for such a strategy. Moreover, the many-particle wave function contains much more information than necessary for a calculation of relevant physical properties. Density matrices are appropriate quantities to extract the relevant information out of such unhandy constructs as N-particle wave functions are. The use of reduced density matrices and some approximations yield a formulation of the many-particle theory in terms of effective single-particle equations. These can be treated numerically and are suited to describe many experimental situations with high accuracy.

The accuracy of bandstructure calculations performed using the density functional theory (DFT) within usual approximations[1] is especially good for reasonably closed packed structures where correlations play a minor role. For the strongly correlated systems which are presented in this work this approach fails. One has to deal with the correlations in a more explicit way within models on top of the DFT in its computable approximations. Such models will be discussed in later parts of the chapter.

In the following, the main ideas of the density functional theory developed by HOHENBERG and KOHN [7] and others are shortly presented, together with a calculational scheme based on this concept.

---

[1] The DFT is an exact theory, problems arise only due to the approximations for the unknown functional of the exchange correlation energy which are assumed for practical calculations [6], see also (2.1.2).

2.1.1   KOHN-SHAM-*Equations*

We start with the SCHRÖDINGER-equation for the many-body wave function Ψ in the SCHRÖDINGER-representation:

$$\hat{\mathcal{H}}(x_1 \ldots x_N, X_1 \ldots X_{N'})\Psi(x_1 \ldots x_N, X_1 \ldots X_{N'}) = E\Psi(x_1 \ldots x_N, X_1 \ldots X_{N'}) \, . \tag{2.1}$$

In this notation $x = (\sigma \mathbf{r})$ and $X = (\tau \mathbf{R})$ contain both the variables for space and spin. For an isolated system of N' Z-fold positively charged, pointlike nuclei and N negatively charged electrons, the Hamiltonian is given as:

$$\hat{\mathcal{H}}(x_1 \ldots x_N, X_1 \ldots X_{N'}) = -\sum_i^N \frac{\Delta_i}{2} + \frac{1}{2}\sum_{i \neq i'}^N \frac{1}{|\mathbf{r}_i - \mathbf{r}_{i'}|} - \sum_{i,n}^{N,N'} \frac{Z_n}{|\mathbf{r}_i - \mathbf{R}_n|} +$$
$$+ \frac{1}{2}\sum_{n \neq n'}^{N'} \frac{Z_n Z_{n'}}{|\mathbf{R}_n - \mathbf{R}_{n'}|} - \sum_n^{N'} \frac{\Delta_n}{2M_n} \, . \tag{2.2}$$

Here, $\mathbf{r}$ with the indices i, i' denote the position of the electrons, $\mathbf{R}$ and n, n' correspond to the position of nuclei. Atomic units are used, i.e., $m_e = \hbar = |e| = 1$. This Hamiltonian contains pure electronic contributions, pure nuclear contributions and coupling terms between them. Due to the fact that the ratio of mass $m_e/m_{proton} \approx 1/2000 \ll 1$, the movement of the nuclei is much slower than that of the electrons. Thus, we can consider the electronic system at any time in equilibrium with the corresponding configuration of the nuclei. This is the so-called adiabatic approximation [8] which is reasonable for most low energy excitations[2]. The kinetic energy of the nuclei in the last term of Eq. (2.2) is neglected in this approximation. We will focus now and in the remaining parts of this thesis on the electronic system considered in the external potential V_{ext} generated by the fixed nuclei and rewrite the Hamiltonian for the decoupled problem:

$$\hat{H} = \hat{T} + \hat{V}_{ext} + \hat{U} = \sum_i^N \left(\frac{\Delta_i}{2} + v_{ext}(\mathbf{r}_i) + \frac{1}{2}\sum_{i' \neq i}^N \frac{1}{|\mathbf{r}_i - \mathbf{r}_i'|} \right) \, , \tag{2.3}$$

$$\hat{T} = \sum_i^N \frac{\Delta_i}{2} \, , \tag{2.4}$$

---

[2]The adiabatic approximation is good as long as the kinetic energy of the nuclei is small compared with the electronic transfer integrals. For the case of strong electron-phonon coupling and high phonon energies (see Sec. 5.4.2), this approximation becomes inappropriate.

$$\hat{V}_{\text{ext}} = \sum_{i}^{N} v^{\text{ext}}(\mathbf{r}_i) = -\sum_{i,n}^{N,N'} \frac{Z_n}{|\mathbf{r}_i - \mathbf{R}_n|} , \tag{2.5}$$

$$\hat{U} = \frac{1}{2} \sum_{i' \neq i}^{N} \frac{1}{|\mathbf{r}_i - \mathbf{r}'_i|} . \tag{2.6}$$

Now we can define the ground state wave function Ψ_{G} of the electronic system, the ground state energy

$$E_{\text{G}} = \langle \Psi_{\text{G}} | \hat{H} | \Psi_{\text{G}} \rangle \tag{2.7}$$

and the ground state density

$$n_{\text{G}}(\mathbf{r}) = \sum_{\sigma} \int \Psi_{\text{G}}^{*}(\sigma\mathbf{r}, x_2 \dots x_n) \Psi_{\text{G}}(\sigma\mathbf{r}, x_2 \dots x_n) \, dx_2 \dots dx_n . \tag{2.8}$$

It is noteworthy, that HOHENBERG and KOHN [7] proved, that the groundstate density $n_{\text{G}}(\mathbf{r})$ alone already determines the external potential V_{ext} and hence Ψ_{G} and all ground state properties uniquely. A variational principle for E_{G}, formulated in the work of HOHENBERG and KOHN and generalized later by LEVY [9] and LIEB [10] gives the possibility to construct an explicit scheme to calculate E_{G} and $n_{\text{G}}(\mathbf{r})$ for a constant number of particles:

$$E_G[v^{\text{ext}}] = \min_{\Psi_n} \left\{ \langle \Psi_n | \hat{H} | \Psi_n \rangle \, \bigg| \, \int n(\mathbf{r}) \, d\mathbf{r} = N \right\} \tag{2.9}$$

$$= \min_{n} \left\{ F[n] + \int n(\mathbf{r}) \, v^{\text{ext}}(\mathbf{r}) \, d\mathbf{r} \, \bigg| \, \int n(\mathbf{r}) \, d\mathbf{r} = N \right\} , \tag{2.10}$$

where Ψ_n is the class of all normalized fermionic wave functions with the density n. The unknown HOHENBERG-KOHN functional $F[n] = \min_{\Psi \to n} \langle \Psi_n | \hat{T} + \hat{U} | \Psi_n \rangle$ is a functional of the density only and can be redefined as follows:

$$F[n] = T_0[n] + E_{\text{H}}[n] + E_{\text{xc}}[n] . \tag{2.11}$$

The HARTREE part of the electron-electron interaction energy is given by

$$E_{\text{H}}[n] = \frac{1}{2} \int \frac{n(\mathbf{r})n(\mathbf{r}')}{|\mathbf{r} - \mathbf{r}'|} \, d\mathbf{r} \, d\mathbf{r}' , \tag{2.12}$$

with self-interaction included. Otherwise, it could not be expressed by the total density only. $T_0[n]$ is the ground state kinetic energy of a non-interacting electron gas with the density n:

$$T_0[n] = \sum_{i}^{N} \langle \Phi_i | - \frac{\Delta_i}{2} | \Phi_i \rangle , \tag{2.13}$$

$$n = \sum_{i}^{N} \Phi_i \Phi_i^{*} , \tag{2.14}$$

$$\langle \Phi_i | \Phi_j \rangle = \delta_{ij} . \tag{2.15}$$

The functions Φ_i are the N lowest single particle eigenstates in an appropriate external potential. The only unknown part[3] of $F[n]$ is the exchange-correlation energy $E_{xc}[n] \stackrel{\text{def}}{=} F[n] - (T_0[n] + E_H[n])$, containing the whole information beyond mean field about kinematic (exchange) and dynamic (correlation) electron-electron interactions in the ground state. The functional derivative of the ground state energy with respect to the density under the constraint of Equation (2.10) has to be zero in the minimum:

$$
\frac{\delta}{\delta n}\left(F[n] + \int n(\mathbf{r})\, v^{\text{ext}}(\mathbf{r})\, d\mathbf{r} - \mu \int n(\mathbf{r})\, d\mathbf{r} \right) =
$$
$$
= \frac{\delta}{\delta n} T_0[n] + v_H(\mathbf{r}) + v_{xc}(\mathbf{r}) + v^{\text{ext}}(\mathbf{r}) - \mu = 0 \;. \tag{2.16}
$$

Herein, μ is the the chemical potential. The combination of (2.16) with the functional derivative of $T_0[n]$ with respect to the single particle function Φ_i^* leads to the KOHN-SHAM-equations:

$$
\left(-\frac{1}{2}\Delta + v_{\text{eff}}(\mathbf{r}) \right) \Phi_i = \varepsilon_i \Phi_i \;, \tag{2.17}
$$

which is a single particle equation in an effective potential:

$$
v_{\text{eff}}(\mathbf{r}) = \int \frac{n(\mathbf{r}')}{|\mathbf{r} - \mathbf{r}'|}\, d\mathbf{r}' + v_{xc}(\mathbf{r}) + v^{\text{ext}}(\mathbf{r}) \tag{2.18}
$$

where

$$
v_{xc}(\mathbf{r}) \stackrel{\text{def}}{=} \frac{\delta}{\delta n(\mathbf{r})} E_{xc}[n(\mathbf{r})] \;. \tag{2.19}
$$

The KOHN-SHAM-energies ε_i have been introduced as LAGRANGE-multipliers in the variation to ensure the normalization of the orbitals in the kinetic energy expression (2.13). The equations (2.17–19) together with the density expression (2.14) define a non-linear system of integro-differential equations for the determination of the ground state density. This system of equations has to be solved self-consistently. It should be noted that self-consistency means just that a stationary value of the energy is found, which is not necessarily the global minimum. Formally, the KOHN-SHAM-equations are correct, but the exchange-correlation potential (2.19) is unknown for most systems. For a practical solution, approximations of $E_{xc}[n]$ are needed. Such an approximation, the local density approximation (LDA), will be presented in the next section.

In many cases, experimental band structures and other measured quantities can be described with the solutions of Equation (2.17). This is understandable because of the similarity of the KOHN-SHAM-potential v_{xc} and a local approximation of the self-energy operator near the KOHN-SHAM FERMI level in most

---

[3]remark that T_0 is not explicitly known

metals [11]. Therefore, the band energies near the FERMI level can be interpreted as quasiparticle excitations.

2.1.2 The local spin density approximation

A weak point of the scheme shown in the last section was the absence of a practicable expression for the exchange-correlation potential v_{xc}. An exception is the homogeneous electron liquid, a model system with constant external potential and constant ground state density n_{G}. For this model system, which contains essential exchange and correlation effects, $v_{\mathrm{xc}}^{\mathrm{hom}}$ and the xc-energy per particle $\varepsilon_{\mathrm{xc}}^{\mathrm{hom}}$ can be determined with good accuracy by means of Monte Carlo calculations [12, 13]. Roughly, $\varepsilon_{\mathrm{xc}}^{\mathrm{hom}} \propto n^{1/3}$ and $v_{\mathrm{xc}}^{\mathrm{hom}} \propto n^{1/3}$.

As approximation for inhomogeneous systems, KOHN and SHAM [14] replaced the xc-energy density at the position $\mathbf{r}$ by the xc-energy density of an homogeneous electron liquid with the density $n(\mathbf{r})$:

$$E_{\mathrm{xc}}^{\mathrm{LDA}}[n(\mathbf{r})] = \int \varepsilon_{\mathrm{xc}}^{\mathrm{hom}}(n(\mathbf{r}))\, n(\mathbf{r})\, d\mathbf{r} \ . \tag{2.20}$$

This is called the local density approximation and seems reasonable for slowly varying densities, for instance in simple metals. There is no simple reason why this approach describes well such inhomogeneous systems like atoms, ions or molecules, where the electrons built up shells and directed bonds, respectively. Nevertheless, the LDA leads to remarkably good results for transition metals, molecules and, to a certain extend, even for atoms and ions. The cause for this success is that the xc energy originates only from the spherical part of the xc hole around an electron [15], due to the isotropy of the COULOMB interaction. This part of the xc hole is well described in LDA [16].

The KOHN-SHAM variational principle is valid independently of the nature of the groundstate, if it is itinerant or localized, non-magnetic or spin-polarized. However, within the above presented spin-degenerated theory it is not possible to distinguish the latter two situations. Even with the knowledge of the exact E_{xc} we could not calculate spin densities and related properties. It was shown by VON BARTH and HEDIN [17] that this theory can be generalized by replacing the density n by the spin density matrix $n_{\sigma\sigma'} = \mathbf{n}$, the potential v^{ext} by the spin-dependent potential[4] $v_{\sigma\sigma'}^{\mathrm{ext}}$ and the states (ε^i, Φ^i) by the corresponding spinor states $(\varepsilon_\sigma^i, \Phi_\sigma^i)$. Without repeating the previous considerations, we rewrite the

---

[4]The spin dependency of the potential is introduced for sake of flexibility, for instance it is needed for an initial spin-splitting for spin-polarized calculations.

KOHN-SHAM equations as follows:

$$\sum_{\sigma'}((-\frac{\Delta}{2} + v_{\mathrm{H}}(\mathbf{r}, [n]))\delta_{\sigma\sigma'} + v_{\sigma\sigma'}^{\mathrm{ext}}(\mathbf{r}) + v_{\mathrm{xc},\sigma\sigma'}(\mathbf{r}, [n]))\Phi_{\sigma'}^{i} = \varepsilon_{\sigma}^{i}\Phi_{\sigma}^{i} , \qquad (2.21)$$

$$n_{\sigma\sigma'} = \sum_{i}^{N} \Phi_{i}^{\sigma}\Phi_{i}^{\sigma'*} , \qquad (2.22)$$

$$v_{\mathrm{xc},\sigma\sigma'}(\mathbf{r}, [n]) = \frac{\delta E_{\mathrm{xc}}[\mathbf{n}]}{\delta n_{\sigma'\sigma}} , \qquad (2.23)$$

$$E_{\mathrm{xc}}^{\mathrm{LSDA}}[n^{+}, n^{-}] = \int \varepsilon_{\mathrm{xc}}^{\mathrm{hom}}(n^{+}(\mathbf{r}), n^{-}(\mathbf{r}))\, n(\mathbf{r})\, d\mathbf{r} , \qquad (2.24)$$

with the particle density

$$n = \sum_{\sigma} n_{\sigma\sigma} = n^{+} + n^{-} . \qquad (2.25)$$

Here, n^{+} and n^{-} are the spin up and spin down densities, respectively, with respect to a preferred axis. The HARTREE part of the potential is unchanged. Now we can calculate the spin momentum density

$$\mathbf{\Sigma} = tr(\sigma\mathbf{n}) \qquad (2.26)$$

and the related spin magnetic moment μ_{s} in a given volume $\mathcal{V}$

$$\mu_{s} = -\mu_{\mathrm{B}} \int_{\mathcal{V}} d\mathbf{r}\mathbf{\Sigma}(\mathbf{r}) . \qquad (2.27)$$

Herein, $\sigma = (\sigma_{x}, \sigma_{y}$ and $\sigma_{z})$ are the PAULI spin matrices, μ_{B} is the BOHR magneton.

   This spin-dependent theory is called local spin density approximation (LSDA) and allows the calculation of all kinds of magnetic systems. Corresponding to the LDA, the local approximation is done with respect to the xc energy per particle $\varepsilon_{\mathrm{xc}}^{\mathrm{hom}}$ of the spin-polarized homogeneous electron gas. For practical calculations, analytical expressions for $\varepsilon_{\mathrm{xc}}^{\mathrm{hom}}$ with free parameters fitted to the numerical results are usually used [17]. To find spin-polarized solutions, a spontaneous symmetry breaking has to be simulated by initially spin-splitting the external potential, because the non-magnetic state is always a local extremum in the energy functional due to the symmetry between both spin polarizations in a spin-independent external potential.

2.1.3   Quasiparticle excitations and L(S)DA+U

In Section 2.1.1, the KOHN-SHAM orbitals Φ_{i} with the related single particle energies ε_{i} have been introduced formally as auxiliary quantities needed to construct

the density n. For the case of a non-interacting system, the KOHN-SHAM states above the FERMI energy coincide with the excitations of the system. For certain excitations of the interacting system, this property is approximately kept. This allows an easy and straightforward interpretation of experimental spectra using KOHN-SHAM band structures.

We consider the DYSON equation originating from a rigorous many-body treatment of the interacting system [18]:

$$[-\frac{\Delta}{2} + v^{\text{ext}}(\mathbf{r}) + v_{\text{H}}(\mathbf{r})]\Psi_i(\mathbf{r}) + \int d\mathbf{r}' M(\mathbf{r}', \mathbf{r}, E_i)\Psi_i(\mathbf{r}') = E_i\Psi_i(\mathbf{r}) \qquad (2.28)$$

This equation describes weakly damped single-electron or single-hole excitations near the FERMI energy, the so-called quasiparticle excitations. In Eq. (2.28), all interactions beyond the mean field level are collected to an energy-dependent integral operator. Therein, $M(\mathbf{r}', \mathbf{r}, E_i)$ is the non-local complex self-energy, unknown like v_{xc} in the KOHN-SHAM equations. Being a ground state property, it is, according to the HOHENBERG-KOHN theorem, a functional of the ground state density. Formal equivalence of Eq. (2.28) with the KOHN-SHAM equations could be achieved by replacing

$$M(\mathbf{r}', \mathbf{r}, E_i) \longrightarrow \delta(\mathbf{r} - \mathbf{r}')v_{\text{xc}}(\mathbf{r}) \qquad (2.29)$$

In fact, the imaginary part of M vanishes at the FERMI level. If we consider the homogeneous electron gas, M should be translationally invariant and should depend only on $|\mathbf{r} - \mathbf{r}'|$:

$$M(\mathbf{r}', \mathbf{r}, E_{\text{F}}) \longrightarrow M^{\text{hom}}(|\mathbf{r}' - \mathbf{r}|, E_{\text{F}}, n), \qquad (2.30)$$

with the dependence on the density made explicit. It was argued by SHAM and KOHN [19] that the self-energy has a short range behavior, such that

$$M(\mathbf{r}', \mathbf{r}, E) \approx \delta(\mathbf{r} - \mathbf{r}')\tilde{v}_M(\mathbf{r}, E) \qquad (2.31)$$

is a good approximation for slowly varying densities. The Eqs. (2.30) and (2.31) can be merged into

$$M^{\text{hom}}(|\mathbf{r}' - \mathbf{r}|, E_{\text{F}}, n) \approx \delta(\mathbf{r} - \mathbf{r}')v_M(n) \qquad (2.32)$$

and applied to the inhomogeneous situation in the usual local density manner, replacing $v_{\text{xc}}^{\text{LDA}}(n(\mathbf{r}))$ by $v_M(n(\mathbf{r}))$ in the KOHN-SHAM equations.

This consideration establishes the formal equivalence between KOHN-SHAM eigenvalues and quasiparticle excitation energies at the FERMI level. Figure 2.1 shows the approximate numerical equivalence of $v_M(n)$ [20] with two approximate
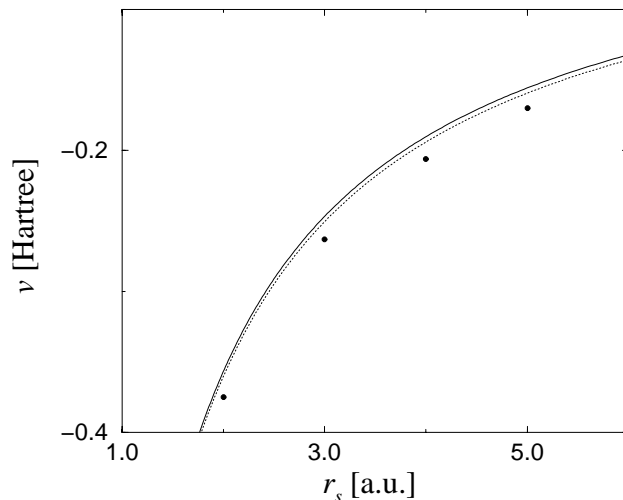
Figure 2.1: Comparison of two different approximate exchange poten-
tials for the homogeneous electron gas (full line: PERDEW-ZUNGER
[21], dotted line: HEDIN-LUNDQVIST [20]) with values of $v_M(n)$ given
by HEDIN and LUNDQVIST [20]. Note, that the distance between v_M
and the xc-potentials is almost independent on the density parameter,
$r_s = (3/4\pi n)^{1/3}$. This corresponds to an almost constant shift of the
potential in a large share of the volume (after RICHTER [22]).

LDA-xc potentials [20, 21]. It is clearly seen that $v_M(n)$ is almost constantly
shifted from the range of the different approximations for v_{xc}. Away from the
FERMI level, v_M becomes energy dependent, but this dependence is still in the
same range for $E_i - E_\mathrm{F}$ not larger than a few eV.

The discussed approximation is closely related to quasiparticle properties of
the homogeneous electron gas. Hence, it works best for nearly free electron states
forming broad bands. In this case, the KOHN-SHAM orbital densities well approx-
imate quasiparticle densities, including relaxation. If the bands become narrower,
deviations between L(S)DA band energies and spectra occur. The hopping rate
is lower, and hence a stronger COULOMB interaction is felt by other electrons
because of the reduced screening. Strong on-site correlations result in a jump of
M, as a function of energy, at E_F by an amount U_{eff}. This quantity is related to
the (screened) on-site COULOMB matrix element U. The simplest available ap-
proximation is called L(S)DA+U, where the energy dependence of M is reduced
to the jump at E_F and otherwise the L(S)DA approximation is used. Due to the
different screening, U_{eff} has to be calculated for each individual compound and

is not just an atomic property like U is. The value of the model parameter U_{eff} can be obtained by means of constrained DFT calculations [23].

In the Chapters 4 and 5 it is shown exemplarly how the strong on-site COULOMB correlations can be taken into account to improve L(S)DA results.

2.2 The optimized LCAO method

In this section, a calculational scheme to solve the KOHN-SHAM equations in LSDA (see 2.1.2) in the case of an ideal solid will be discussed. For most calculations of this work, an LCAO-method (linear combination of atomic-like orbitals) was used. For a detailed description see Ref. [24] which is the basis for the presentation given in this section.

2.2.1 The local basis set

An ideal solid consists of a geometrical arrangement of atoms on sites $\mathbf{R} + \mathbf{S}$ where $\mathbf{R}$ defines an infinite BRAVAIS lattice and $\mathbf{S}$ the atomic positions inside the unit cell. This periodic arrangement generates a periodic external potential caused by the positively charged nuclei. The KOHN-SHAM eigenfunctions can be represented as BLOCH wave functions $\langle \mathbf{r} | \mathbf{k} \rangle$ due to this periodicity. The translational invariance along the lattice vectors of the BRAVAIS lattice defines the conservation of the quasi-momentum $\mathbf{k}$. Each site of the unit cell can contribute more than one electron to the system, hence for each $\mathbf{k}$ point several states with the eigenenergies $\varepsilon_\nu^{\mathbf{k}}$ are occupied. So the BLOCH wave function $\langle \mathbf{r} | \mathbf{k} \rangle$ can be denoted with the band index[5] ν.

The wave function $\langle \mathbf{r} | \mathbf{k} \nu \rangle$ in our LCAO method is composed of overlapping, local, atomic-like wave functions $|\mathbf{R}\mathbf{S})$. These functions are solutions of an atomic SCHRÖDINGER equation[6]. We classify the basis functions as core states $|\mathbf{R}\mathbf{S}c)$ and valence states $|\mathbf{R}\mathbf{S}\mu)$. In general, the valence functions are extended beyond the nearest neighbor distance: they are overlapping and non-orthogonal. The core states $|\mathbf{R}_i\mathbf{S}_jc)$ centered at the site $\mathbf{R}_i + \mathbf{S}_j$ should not overlap with those of neighboring sites: $(\mathbf{R}_i\mathbf{S}_jc|\mathbf{R}_k\mathbf{S}_lc) = 0$ for $i \neq k$ or $j \neq l$. This condition is nearly fulfilled for completely filled shells. Orbitals which violate this condition have to be treated as valence states. Core states on the same site are orthogonal. The given subdivision reduces considerably the matrix rank of the band problem: The core states are already eigenstates in the effective crystal potential (in good

---

[5]The spin index σ is suppressed for sake of simplicity, the equations are the same for both spin directions.

[6]In the relativistic case the DIRAC equation is used for the calculation of the corresponding spinor states [25].

approximation). Since the BLOCH states should be eigenfunctions of the same crystal Hamiltonian, we choose a new set of valence functions $|\mathbf{RS}\mu\rangle$ which are orthogonal to all core states[7] of all atoms:

$$|\mathbf{RS}\mu\rangle = |\mathbf{RS}\mu) - \sum_{\mathbf{R}'\mathbf{S}'c} |\mathbf{R}'\mathbf{S}'c)(\mathbf{R}'\mathbf{S}'c|\mathbf{RS}\mu) \ . \tag{2.33}$$

Now, the HAMILTON matrix is strongly reduced in dimension by the projection on the HILBERT space of the valence states. If only one valence basis function per electron is chosen, the corresponding minimal basis set is complete enough to describe the occupied eigenstates and the low lying empty states.

The eigenfunctions $|\mathbf{k}\nu\rangle$ of the crystal Hamiltonian are, corresponding to the BLOCH theorem, invariant under translation by lattice vectors. Thus, we combine the basis functions $|\mathbf{RS}\mu\rangle$ in a BLOCH-sum ansatz with coefficients still be to determined:

$$|\mathbf{k}\nu\rangle = \frac{1}{\sqrt{N'}} \sum_{\mathbf{RS}\mu} |\mathbf{RS}\mu\rangle c^{\mathbf{k}}_{\mathbf{S}\mu,\nu} e^{i\mathbf{k}(\mathbf{R}+\mathbf{S})} \ . \tag{2.34}$$

We determine the coefficients inserting the ansatz (2.34) in the KOHN-SHAM equation (2.17) for the crystal:

$$\hat{H}|\mathbf{k}\nu\rangle = \varepsilon^{\mathbf{k}}_{\nu}|\mathbf{k}\nu\rangle \ . \tag{2.35}$$

Multiplying the expression (2.35) from the left side with $e^{-i\mathbf{k}\mathbf{S}'}\langle 0\mathbf{S}'\mu'|$ and inserting Eq. (2.34) we find the LCAO secular equation:

$$\sum_{\mathbf{RS}\mu} e^{i\mathbf{k}(\mathbf{R}+\mathbf{S}-\mathbf{S}')} \langle 0\mathbf{S}'\mu'| \hat{H} - \varepsilon^{\mathbf{k}}_{\nu} \mathrm{I} |\mathbf{RS}\mu\rangle c^{\mathbf{k}}_{\mathbf{S}\mu,\nu} = 0 \ . \tag{2.36}$$

Equation (2.36) can be written shortly in matrix form:

$$\sum_{\mathbf{S}\mu} \left(H^{\mathbf{k}}_{\mathbf{S}'\mu'\mathbf{S}\mu} - \varepsilon^{\mathbf{k}}_{\nu} S^{\mathbf{k}}_{\mathbf{S}'\mu'\mathbf{S}\mu} \right) c^{\mathbf{k}}_{\mathbf{S}\mu,\nu} = 0 \tag{2.37}$$

where $H^{\mathbf{k}}_{\mathbf{S}'\mu'\mathbf{S}\mu}$ and $S^{\mathbf{k}}_{\mathbf{S}'\mu'\mathbf{S}\mu}$ are the HAMILTON matrix and the overlap matrix, respectively, defined for each $\mathbf{k}$ vector:

$$H^{\mathbf{k}}_{\mathbf{S}'\mu'\mathbf{S}\mu} = \sum_{\mathbf{R}} e^{i\mathbf{k}(\mathbf{R}+\mathbf{S}-\mathbf{S}')} \langle 0\mathbf{S}'\mu'|\hat{H}|\mathbf{RS}\mu\rangle \ , \tag{2.38}$$

$$S^{\mathbf{k}}_{\mathbf{S}'\mu'\mathbf{S}\mu} = \sum_{\mathbf{R}} e^{i\mathbf{k}(\mathbf{R}+\mathbf{S}-\mathbf{S}')} \langle 0\mathbf{S}'\mu'|\mathbf{RS}\mu\rangle \ . \tag{2.39}$$

Now, the band energies $\varepsilon^{\mathbf{k}}_{\nu}$ and the coefficients $c^{\mathbf{k}}_{\mathbf{S}\mu,\nu}$ can be determined by solving the generalized eigenvalue problem for each $\mathbf{k}$. Occupying the lowest N eigenvalues for each $\mathbf{k}$ point, where N is the number of electrons in the unit cell, the

---

[7]In practice, the orthogonalization is done only with respect to the state with the highest main quantum number n for each angular momentum l.

FERMI energy of the metallic system can be determined as the highest occupied KOHN-SHAM eigenstate.

Using the above calculated BLOCH eigenfunctions $|\mathbf{k}\nu\rangle$ we compute the valence part of the particle density:

$$n(\mathbf{r}) = \sum_{\text{occ. }\mathbf{k}\nu} \langle \mathbf{r}|\mathbf{k}\nu\rangle\langle \mathbf{k}\nu|\mathbf{r}\rangle \tag{2.40}$$

$$= \sum_{\text{occ. }\mathbf{k}\nu} \frac{1}{N'} \sum_{\substack{\mathbf{R}\,\mathbf{S}\,\mu \\ \mathbf{R}'\mathbf{S}'\mu'}} \langle \mathbf{r}|\mathbf{R}\mathbf{S}\mu\rangle c_{\mathbf{S}\mu,\nu}^{\mathbf{k}} e^{i\mathbf{k}(\mathbf{R}+\mathbf{S}-\mathbf{R}'-\mathbf{S}')} c_{\mathbf{S}'\mu',\nu}^{\mathbf{k}*}\langle \mathbf{R}'\mathbf{S}'\mu'|\mathbf{r}\rangle \ . \tag{2.41}$$

The expression for the valence density (2.40) can be decomposed into a sum of local contributions consisting of a net part $n_{\mathbf{S}}^{\text{net}}(\mathbf{r})$[8] and an overlap part $n_{\mathbf{S}}^{\text{ovl}}(\mathbf{r})$ for each atom:

$$n_{\mathbf{S}}^{\text{net}}(\mathbf{r}) = \sum_{\mu\mu'}\langle \mathbf{r}|0\mathbf{S}\mu\rangle\frac{1}{N'}\sum_{\text{occ. }\mathbf{k}\nu} c_{\mathbf{S}\mu,\nu}^{\mathbf{k}} c_{\mathbf{S}\mu',\nu}^{\mathbf{k}*}\langle 0\mathbf{S}\mu'|\mathbf{r}\rangle \ , \tag{2.42}$$

$$n_{\mathbf{S}}^{\text{ovl}}(\mathbf{r}) = \sum_{\substack{\mu\mu' \\ \mathbf{R}'+\mathbf{S}'\neq\mathbf{S}}} \langle \mathbf{r}|0\mathbf{S}\mu\rangle\frac{1}{N'}\sum_{\text{occ. }\mathbf{k}\nu} c_{\mathbf{S}\mu,\nu}^{\mathbf{k}} e^{i\mathbf{k}(\mathbf{S}-\mathbf{R}'-\mathbf{S}')} c_{\mathbf{S}'\mu',\nu}^{\mathbf{k}*}\langle \mathbf{R}'\mathbf{S}'\mu'|\mathbf{r}\rangle \ . \tag{2.43}$$

The contribution of the core states to the charge density of an atom at the site $\mathbf{S}$ can be written as

$$n_{\mathbf{S}}^{\text{core}}(\mathbf{r}) = \sum_{core}\langle \mathbf{r}|\mathbf{S}c\rangle\langle \mathbf{S}c|\mathbf{r}\rangle \tag{2.44}$$

because the core states of one site do not overlap with those of the neighboring sites.

Starting from the particle density, the crystal potential has to be computed. It consists of the HARTREE part which is calculated solving the POISSON equation and the xc part which is treated in the parameterization of VON BARTH and HEDIN [17] or PERDEW and ZUNGER [21], respectively.

In compounds with crystallographically inequivalent sites, ionicities generated by the local density contributions result in a MADELUNG-problem. Its solution can be found by application of an EWALD technique [26].

After the computation of the potential, we can recalculate the basis set and close the cycle of self-consistency. This procedure has to be repeated until the potential and the density, respectively, are converged. It usually requires the application of advanced iteration techniques.

2.2.2   The calculation of the potential

In the previous section the general features of the LCAO scheme were illustrated. The following part describes some details and additional approximations, which

---

[8]The net part contains small orthogonalization corrections from Eq. (2.33).

optimize this scheme and allow to treat large crystals with a reasonable amount
of computational power and time.

The HARTREE-part of the crystal potential is constructed as a sum of overlap-
ping extended spherical site potentials. This is possible because of the linearity
of the POISSON-equation. Hence, a part of non-spherical effects which is de-
termined by crystal symmetry is taken into account self-consistently. On the
other hand, the intra-atomic asphericity is suppressed by azimuthal averaging
over the site-charge density during the iteration. This is a good approximation
for most close packed structures. For open structures, the results can be im-
proved by introduction of empty spheres[9] at interstitial sites. This construction
of the potential, together with the definition of the valence states as described
in Eq. (2.33) and below was quite successful in many applications and yields an
accuracy between so-called muffin-tin methods and full-potential schemes. Re-
cently, a generalization to a full-potential local-orbital minimum-basis scheme
(FPLO) has been implemented [27]. This scheme[10] allows higher accuracy with
only slightly enhanced requirements on computational time and storage.

At the beginning of each self-consistent iteration, atomic-like potentials $V_{\mathbf{RS}}$
are used to calculate the site-dependent valence orbitals. For the later steps $V_{\mathbf{RS}}$
is calculated from the local density of the previous step. The basis functions
$(\mathbf{r}|\mathbf{RS}\mu)$ are represented as a product of a radial and an angular-dependent part:

$$(\mathbf{r}|\mathbf{RS}\mu) = \phi_{nl\sigma}(|\mathbf{r} - \mathbf{R} - \mathbf{S}|)Y_{lm}(\mathbf{r} - \mathbf{R} - \mathbf{S}) . \qquad (2.45)$$

The multiindex $\mu = (nlm\sigma)$ denotes the main quantum number n, the angular
momentum quantum number l, the magnetic quantum number m and the spin
σ. The Y_{lm} are real spherical harmonics.

While the core states can be calculated directly from the local potential
$V_{\mathbf{RS}}$, for the calculation of the valence states a contraction potential $(r/r_0(l))^{n_0}$,
$(n_0 \geq 0)$ is added [28, 29, 24]. This artificial attractive potential is introduced to
compress the valence functions $|\mathbf{RS}\mu)$. Thus, the overlap of the $|\mathbf{RS}\mu)$ is strongly
reduced in comparison with uncompressed atomic wave functions while only small
changes occur in the inner atomic region. Hence, the number of multi-center in-
tegrals in the calculation of the HAMILTON-matrix and of the overlap-matrix is
reduced correspondingly. The main point of this procedure is, however, to obtain
a sufficiently complete basis for energies above the potential zero.

The variational parameters n_0 and $r_0(l)$ are found with numerical tests: $n_0 = 4$
(fixed) and $r_0(l) = x_0(l)R_{\mathrm{WS}}^{3/2}$, where R_{WS} is the WIGNER-SEITZ radius. The

---

[9]Empty spheres do not contribute to the external potential, but the valence functions cen-
tered on these sites improve the completeness of the basis set and the representation of the
potential.

[10]Herein, the calculation of the basis set is slightly modified: Instead of the spherical local
potential the spherically averaged crystal potential is used.

quantity $x_0(l)$ is an angular-momentum dependent variational parameter, which can be determined for each lattice type by minimization of band energies on symmetry points in empty lattice tests. Typically, $0.8 \leq x_0 \leq 1.2$. For open structures, especially if the atomic radii of various components are strongly different, the use of the basis set optimized in this way can cause difficulties.

The exchange-correlation part of the potential, used in the parameterization of VON BARTH and HEDIN [17], depends in a non-linear way on the density. Hence, a representation as sum of overlapping site potentials is difficult. On the other hand, the xc potential varies only slightly in the interstitial due to its approximate proportionality to $n^{1/3}(r)$. Therefore, the xc potential is calculated in atomic-sphere approximation (ASA)[11]. Spherically symmetric xc potentials are computed from the spherically averaged densities inside atomic spheres. The radii of these spheres are determined under the condition, that the densities on their surfaces are the same and the sum of their volumes is equal to the volume of the unit cell. For complex or open structures with strongly different types of atoms, these requirements can be only approximately fulfilled. For such cases, the introduction of empty spheres can improve the construction of the xc potential.

2.2.3 Advantages and disadvantages of the method

The presented LCAO-scheme has some advantages over other band structure methods. First, and extensively exploited in this thesis, the atomiclike character of the basis orbitals gives a natural possibility to extract the relevant orbitals for the construction of model Hamiltonians (see 4.3.1).

Second, the construction of the potential as a sum of overlapping local potentials provides a good description also for the interstitial region, at least for close packed structures. The so-constructed potential is more accurate than the muffin-tin approximation of LMTO schemes, for example. At variance with so-called tight binding models, the LCAO method fully takes into account the overlap-matrix when solving the eigenvalue problem. The calculation of the HAMILTON-matrix and of the overlap-matrix is time-consuming, but has to be considered with respect to the accuracy of the band structures, which is comparable with full-potential calculations like FLAPW [30]. So, the accuracy of LCAO for band structure calculations is comparable to the most sophisticated methods, while its performance is still comparable with fast methods like LMTO.

For historical reasons, in the implemented computer code, which has been used for the most calculations in the presented work, the basis orbitals are represented by SLATER-functions. This is the main source of the insufficient accuracy

---

[11]In the FPLO scheme, no shape approximation for the xc potential is done [27].

for the calculation of total energies[12]. Except saving computational time, there is
no reason for this representation. Improvements can be achieved by numerically
represented basis orbitals. Together with an improvement of the MADELUNG-
procedure, this problem is solved in the recently developed FPLO-code [27]. Here,
the determination of the variational parameters $x_0(l)$ for the optimization poten-
tial is less problematic due to a variational approach with respect to the total
energy. In its first applications, this minimum-basis scheme has provided as ac-
curate results as the best available augmented basis methods like WIEN97 [31].

2.3   Model calculations on top of DFT

In the previous sections it was discussed, that the L(S)DA fails for systems with
strong on-site COULOMB correlations. In Section 2.1.3, L(S)DA+U was men-
tioned as one possibility to improve L(S)DA while retaining an effective single-
particle scheme.

Another way to take into account the correlations that are poorly described
by LDA is sketched in the following. For the low energy physics, in most systems,
only a small number of orbitals is relevant. These orbitals can be extracted from
an LDA calculation. Subsequently, the energy bands corresponding to the orbitals
found in this way can be parameterized by fitting a tight-binding (TB) model. A
general TB Hamiltonian can be written in the form

$$\hat{H}_{\mathrm{TB}} = \sum_{i,\sigma} \varepsilon_i \big(c_{i,\sigma}^\dagger c_{i,\sigma}\big) + \sum_{<ij>\sigma} t_{ij} \big(c_{i,\sigma}^\dagger c_{j,\sigma} + \mathrm{H.c.}\big)\,, \qquad (2.46)$$

where $c_{i,\sigma}^\dagger$ and $c_{j,\sigma}$ are the usual creation or annihilation operators for an particle
at site i or j, respectively, for sakes of simplicity, additional orbital indices are
suppressed. The symbol $< ij >$ stands for the summation over bonds connecting
sites i and j, and ε_i is the so-called on-site energy of the orbital i.

Now, the Hamiltonian of the correlated system can be constructed by adding
terms guessed on the basis of physical intuition and adapted to the considered
compound and problem. For the simplest case of only one band[13] the famous
HUBBARD Hamiltonian [32] is given as an example

$$\hat{H}_{\mathrm{HM}} = \sum_{<ij>\sigma} t_{ij} \big(c_{i,\sigma}^\dagger c_{j,\sigma} + \mathrm{H.c.}\big) + U \sum_{i} \hat{n}_{i,\uparrow}\hat{n}_{i,\downarrow}\,, \qquad \hat{n}_{i,\sigma} = c_{i,\sigma}^\dagger c_{i,\sigma} \qquad (2.47)$$

where the variable U describes the COULOMB repulsion of two particles at the
same site i in addition to the mean field repulsion contained in the TB approach.

---

[12]An accurate representation of the potential near the nucleus with a finite number of
SLATER-functions results in small unphysical oscillations on neighboring sites.

[13]The sum over the on-site energies ε_i is a constant for the one-band case of Eq. (2.46).

If more than one band is required for a proper description of the system, the above mentioned Hamiltonian can be expanded easily [33]:

$$
\begin{aligned}
\hat{H}_{\mathrm{EHM}} &= \sum_{i,\sigma} \varepsilon_i(c_{i,\sigma}^\dagger c_{i,\sigma}) + \sum_{<ij>\sigma} t_{ij}(c_{i,\sigma}^\dagger c_{j,\sigma} + \mathrm{H.c.}) \\
&+ \sum_i U_i \hat{n}_{i,\uparrow}\hat{n}_{i,\downarrow} + \sum_{<ij>} V_{ij}\hat{n}_i\hat{n}_j .
\end{aligned}
\tag{2.48}
$$

In Eq. (2.48), the on-site COULOMB repulsion U_i is generalized to be orbital dependent and an intersite COULOMB interaction V_{ij} is added.

In general, also in such reduced models, the calculation of physical properties like the magnetic susceptibility or phase diagrams is extremely complicated for a wide region of parameters. Therefore, for some limiting cases, it is desirable to map these models onto more simple ones. For the case $U/t \to \infty$, the one band HUBBARD model of Eq. (2.47) turns into the so-called t-J model [34]

$$
\hat{H} = \sum_{ij\sigma} t_{ij}c_{i,\sigma}^\dagger (1 - \hat{n}_{i,\bar{\sigma}})\, c_{j,\sigma}(1 - \hat{n}_{j,\bar{\sigma}}) + \sum_{<ij>}(J_{ij}\hat{\mathbf{S}}_i\hat{\mathbf{S}}_j - \frac{1}{4}\hat{n}_i\hat{n}_j)\,,
\tag{2.49}
$$

where $\mathbf{S}_i$ are the usual spin operators and J_{ij} the exchange integrals between spins at site i and j. The parameters of the t-J model and the one band HUBBARD model are connected via

$$
J_{ij} = 4t_{ij}^2/U .
\tag{2.50}
$$

It is not the aim of this work to investigate the general behavior of the above mentioned models. Each of them can be applied to various situations to describe strongly correlated systems. For instance, within the t-J model, the low energy spin excitations of cuprates can be successfully described. It shall be demonstrated in this thesis, how this mapping procedure works and how some physical properties like magnetic moments or NÉEL temperatures can be estimated for a given compound using model calculations (see Chapter 4). A direct comparison of the measured quasiparticle dispersion with model calculations is given in Chapter 5.

Chapter 3

Cuprates – low-dimensional systems

Oxo-metallates with planar coordination-polyhedra are a challenging class of compounds in solid state chemistry [35]. These compounds show interesting principles of one-, two- or three-dimensional network formation from these planar structural units. The physical properties, especially the electronic properties, are strongly connected with the dimensionality of this network. A large subgroup of the Oxo-metallates are the cuprates. Nearly all of the rich variety of topologically different networks are found inside this subgroup. In this chapter, a systematic overview over the topologically different low-dimensional networks of various cuprates will be presented. Based on LDA-LCAO bandstructure calculations, a first insight in the electronic structure will be given for each presented compound. For the sake of simplicity and comparability, all band structure calculations presented in this chapter are carried out for the non-spin-polarized case, even if magnetic solutions exist. Derived from an analysis of the relevant orbitals, which should not depend on the magnetic or nonmagnetic character of the solution, the nature of the typical bonding in the considered compounds will be discussed.

3.1 The isolated CuO_4-plaquette

The basic element of all cuprate compounds is the planar CuO_4-plaquette. It is shown in Fig. 3.1 together with the relevant covalent σ-orbitals. The shell occupation of the Cu^{+2}-ion[1] is $3d^9 4s^0$, and that of the O^{-2}-ion is $2p^6$. The nominal anionic redox number of this complex is -6: $[CuO_4]^{-6}$. The highest occupied atomic orbitals are copper $3d$-orbitals and oxygen $2p$-orbitals. Most of those orbitals are non-bonding. There is one σ-orbital at each ion with the angular dependencies of the wavefunction given by $(x^2 - y^2)/r^2$ for the Cu $3d$-

---

[1] In order to simplify ionicity notations for the doped case in the sequel, we use the notation Cu^{+2} instead of the commonly used notation Cu^{2+}.

orbital and by x/r and y/r, respectively, for the O $2p$-orbitals. (The plane of the plaquette was taken to be the x-y-plane of a Cartesian coordinate system.)
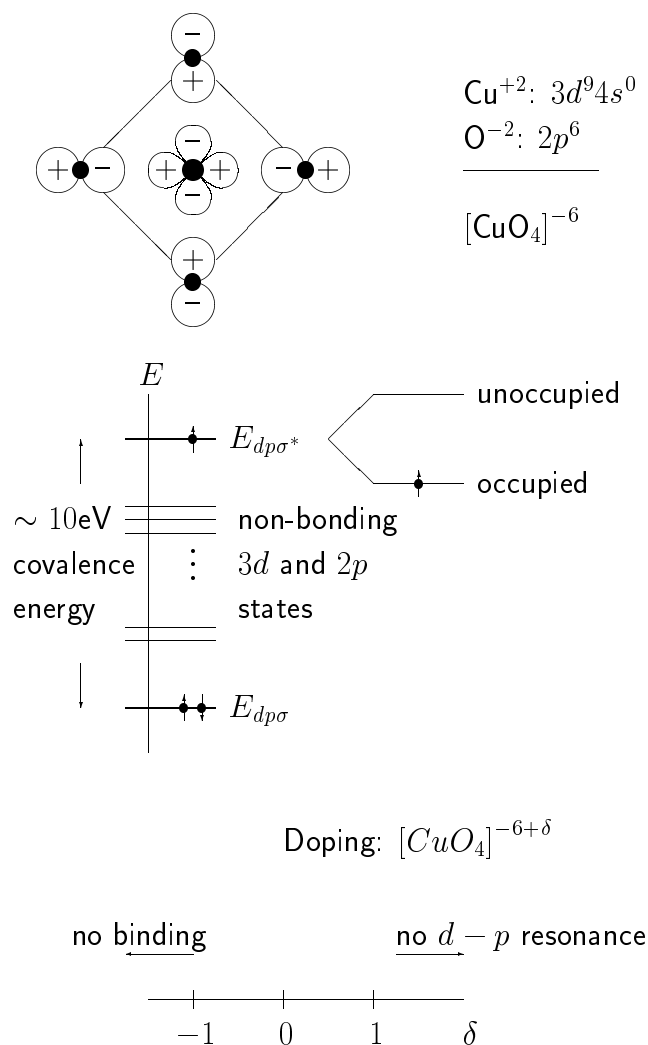
Figure 3.1: The covalent CuO$_4$-plaquette, most relevant ingredient for the cuprates. The copper ion resides in the center of the plaquette, and the four oxygen ions occupy the corners. The anti-bonding molecular orbital is shown with sign changes of the wavefunction on all four Cu-O-bonds. Further details see the text.

The relevant molecular orbital energy level scheme is sketched in Fig. 3.1. The strong covalent $dp\sigma$ bond leads to an energy splitting between the bonding and anti-bonding levels as large as 10 eV. The fully occupied non-bonding Cu-$3d$ and O-$2p$ levels are in between. Since due to the ionic $3d^9$ and $2p^6$ occupations one electron is missing compared to full $3d$ and $2p$ shells, the anti-bonding

$dp\sigma^*$-level must be half-filled. Hence, the prerequisites for covalent bonding are fulfilled. (The energy distance between the Cu $3d$-level and the oxygen $2p$-level in the molecular field is roughly 3 eV and hence small compared to the covalency splitting, and the covalent band complex is partially occupied.) Due to a strong intra-atomic correlation present in the Cu $3d$-orbitals, the molecular field approximation is, however, not sufficient to describe the electronic properties, and the half-filled anti-bonding level splits due to these correlations into a lower and an upper 'HUBBARD' level, each accessible to one electron only. The lower HUBBARD level is occupied.

For many cuprate compounds, especially for the HTSC, doping of the CuO$_4$-plaquette is an important issue. The doping charge is named δ in Fig. 3.1. If the plaquette is doped with electrons ($\delta < 0$), then the anti-bonding level becomes filled and the covalency is correspondingly reduced. At $\delta = -1$, the anti-bonding band is full, and there cannot be any covalent $dp\sigma$-binding any more. Doping the plaquette with holes ($\delta > 0$) increases the covalency. However, at large doping rates the oxygen potential is moved down against the copper potential (while copper remains essentially $3d^9$), and the level resonance is reduced, which reduces covalency again. Hence, the CuO$_4$-plaquette is strongly covalently bound around half-filling of the anti-bonding $dp\sigma^*$-orbital.

The architecture of quasi-planar cuprate structures by linking CuO$_4$-plaquettes which share in one or two oxygen ions was considered first by MÜLLER-BUSCH-BAUM [35] on empirical grounds. He made a systematic study of the cuprate structures long before the high-T_c superconductors were discovered. Composing the basic CuO$_4$ blocks like bricks from a toy box leads to more and more complex networks. Starting with the most simple structure, the main features due to different linking of these blocks will be discussed in the following sections. More detailed investigations of the electronic structure and the related magnetic properties are presented in the Chapters 4 and 5.

3.2 Stacks of isolated plaquettes – Bi$_2$CuO$_4$

The isolated CuO$_4$-plaquette has the very high reduction state -6, and the only structure known where it appears is Bi$_2$CuO$_4$ [35, 36]. The unit cell of this crystal structure is shown in Fig. 3.2. Bi$_2$CuO$_4$ occurs in the tetragonal space group P4/nnc with the lattice constants $a = 8.499$ Å and $c = 5.7973$ Å . The unit cell contains four formula units, but only three crystallographically different sites. The Cu-O distance within a CuO$_4$ unit is about 1.93 Å and corresponds to a typical covalent bond length. The plaquettes are arranged in turn stacks, forming chains of copper ions parallel to the tetragonal axis.
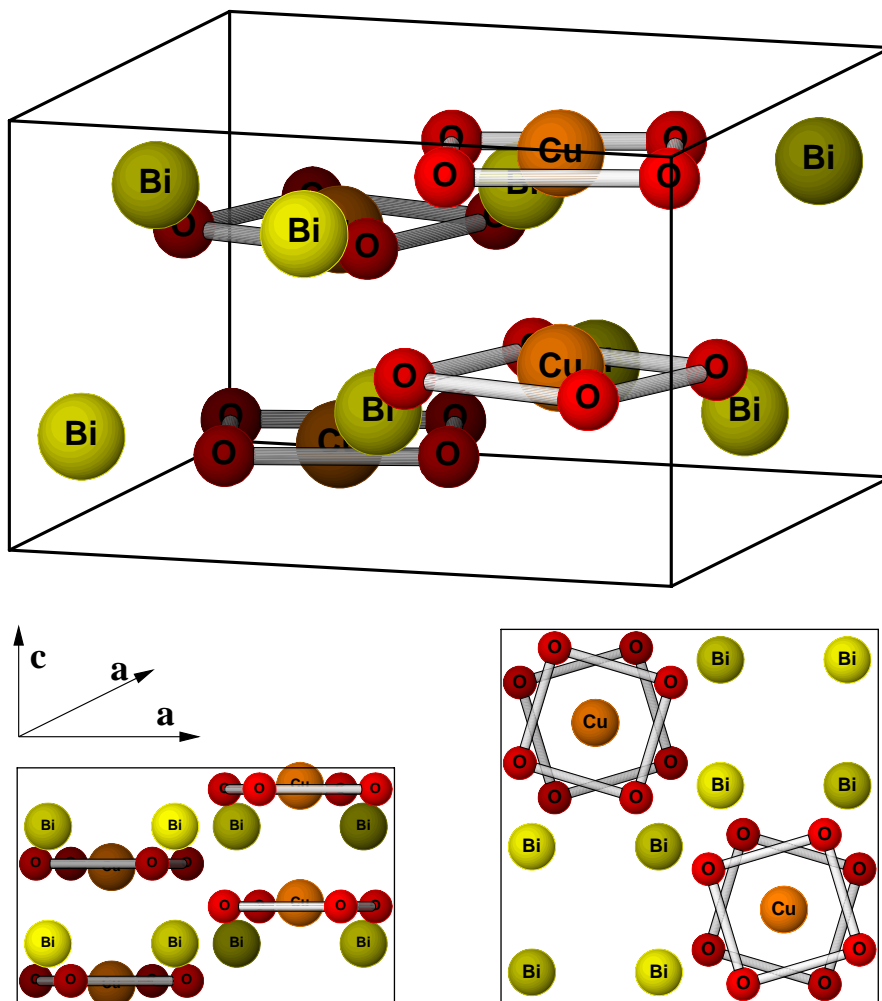
Figure 3.2: Unit cell of the Bi_2CuO_4-crystal, perspective view (top), front view (down left) and lateral view (down right). Here and in the sequel the rods between O-atoms are used only to highlight the planar CuO_4-plaquettes. The strong covalent σ-bonds that are present between the central copper and the four surrounding oxygens are not emphasized.

$BiCuO_4$ is an insulator with an antiferromagnetic phase transition below 50 K [36]. The exact magnetic moment of the copper atoms determined by neutron powder diffraction is still unclear. It was measured 0.93(6) μ_B at T = 1.5 K [36] and 0.56 ± 0.04 at T = 13 K [37], respectively. To resolve this discrepancy and to determine the three-dimensional (3D) magnetic structure, experiments on single crystals are required. Independent of the exact value of the magnetic moment, quantum fluctuations seem to play a minor role in the system because these moments are in the order of the saturation moment of Cu in the $3d^9$ configuration.

density of states of Bi_2CuO_4
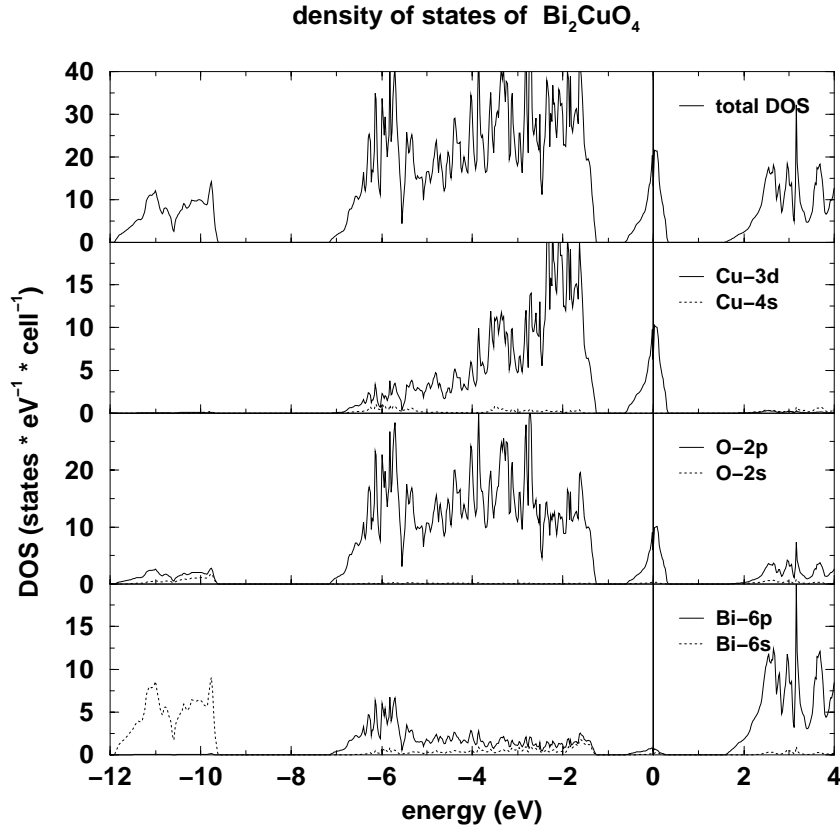
Figure 3.3: Total and partial DOS of Bi_2CuO_4. The FERMI level is at zero energy. The contribution of other states is less than 0.1% in the region shown.

The band-structure calculation for this compound was done scalar relativistically in the FPLO-scheme [27] and a basis set consisting of Cu ($4s$, $4p$, $3d$), O ($2s$, $2p$, $3d$) and Bi ($5s$, $5p$, $5d$, $6s$, $6p$) was chosen. All lower lying states were treated as core states. Due to the large extension of the Bi ($5s$, $5p$) wave functions it was necessary to treat them as valence states since they have a considerable overlap to the core states at neighboring sites (see 2.2.1). For the exchange and correlation potential the parameterization of PERDEW and ZUNGER was chosen.

As expected from the previous considerations, we find as result a $O-2p$-$Cu-3d$ band complex with a width of about 8 eV. The total and the partial densities of states (DOS) are shown in Fig. 3.3. It is to note that only the $Bi-6p$ states give a small further contribution to this complex, the admixture of all other states is negligible. The well-separated narrow peak at FERMI level originates from four narrow bands crossing the FERMI level, in accord with the four formula units per unit cell. Of course, the antibonding bands are correlation-split in reality.

band structure of Bi$_2$CuO$_4$
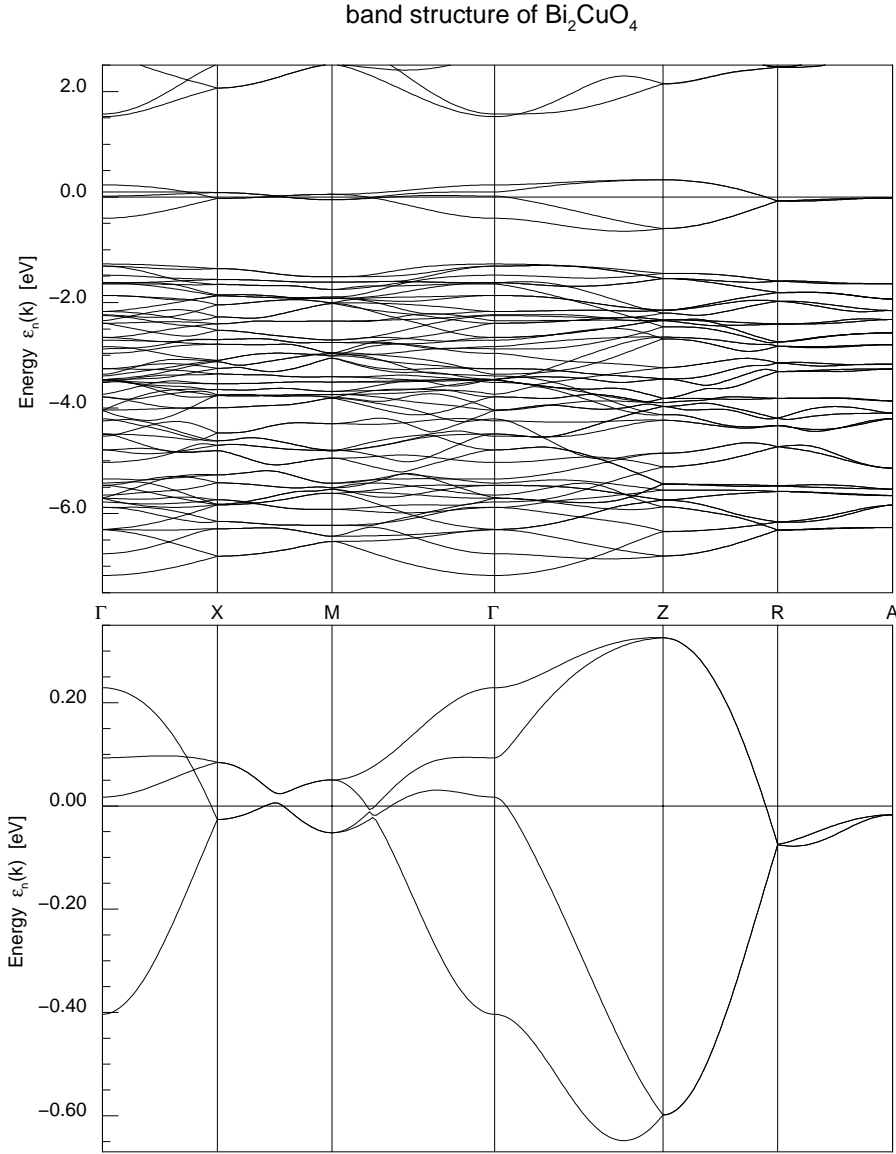
Figure 3.4: Band structure of Bi$_2$CuO$_4$. The FERMI level is at zero energy. In the upper panel the whole $p - d$ complex is shown, the band complex at the FERMI level is zoomed in the lower panel. The notation of symmetry points is as follows: Γ=(000), X=(100), M=(110), Z=(001), R=(011) and A=(111) in units of $(\pi/a, \pi/a, \pi/c)$.

The KOHN-SHAM band structure is shown in Fig. 3.4. Calculating the weight of the different orbitals (see Appendix A), we find that the bands at FERMI level have nearly pure in-plane character. This means that these bands are built from Cu-$3d_{xy}, 3d_{x^2-y^2}$ and O-$2p_x, 2p_y$ orbitals. The contribution of two different

Cu$-3d$ orbitals is due to the twisting of the plaquettes against each other (see Fig. 3.2). A local rotation of the quantization axis shows that for the description of a single plaquette only one copper orbital is necessary.

The half-filled band complex at the FERMI level shows sizable dispersion in all main directions of the BRILLOUIN-zone, of the order of half an electron volt (see Fig. 3.4). Thus, the coupling between the CuO_4 units is relatively isotropic. In a one-band tight-binding model, a first estimate for the effective transfer integrals t_1 to the nearest neighbors gives a value of $t_1 \lesssim 0.1$ eV. With respect to the small absolute value for the transfer integrals, the discussion of Bi_2CuO_4 as "zero-dimensional compound" [38] is understandable, especially for the interpretation of spectroscopic experiments which yield typical linewidths of half an eV. However, on the energy scale of magnetic excitations, this compound has to be considered as clearly three-dimensional due to the relatively isotropic dispersion. From the site-dependent orbital character of the antibonding bands it can be concluded, that the main contribution to the 3D coupling comes from a direct $O-2p_{x/y}$—$O-2p_{x/y}$ overlap between neighboring plaquettes in different stacks leading to an antiferromagnetic exchange, $J_{AFM} > 0$. $O-2p_{x/y}$ denotes a linear combination of the in plane $O-2p_x$ and $O-2p_y$ orbitals. A smaller contribution to the coupling discussed above comes from a covalent O–Bi–O bond. For the exchange coupling between the copper spins this should play a minor role due to the higher order of the process. In addition to these couplings which cause antiferromagnetic exchange, ferromagnetic exchange $J_{FM} < 0$ interactions in z direction within a stack originate from a small direct overlap between the copper in-plane orbitals on neighboring sites. The corresponding exchange integrals calculated from susceptibility data in mean-field spin-wave approximation [36] are $J_{AFM} = 11.5$ K and $J_{FM} = -5$ K, respectively. Because of the quite isotropic coupling, an RPA spin-wave approach should give reliable results. Due to the small absolute values of the exchange integrals, the direct ferromagnetic exchange between parallel plaquettes is experimentally accessible for this compound and can be used for a rough estimate of the corresponding interaction in the compounds discussed later, were the experimental situation is less favorable.

3.3   Chain cuprate structures

Resulting in the same covalency situation as in the isolated plaquette, but with a lower reduction state, CuO_4-plaquettes may share oxygen ions. Three of the possible arrangements are sketched in Fig. 3.5.

Depending on the number of shared oxygen ions, we can built corner-shared chains (see Fig. 3.5(b) and section (3.3.1)), edge-shared chains (Fig. 3.5(c) and
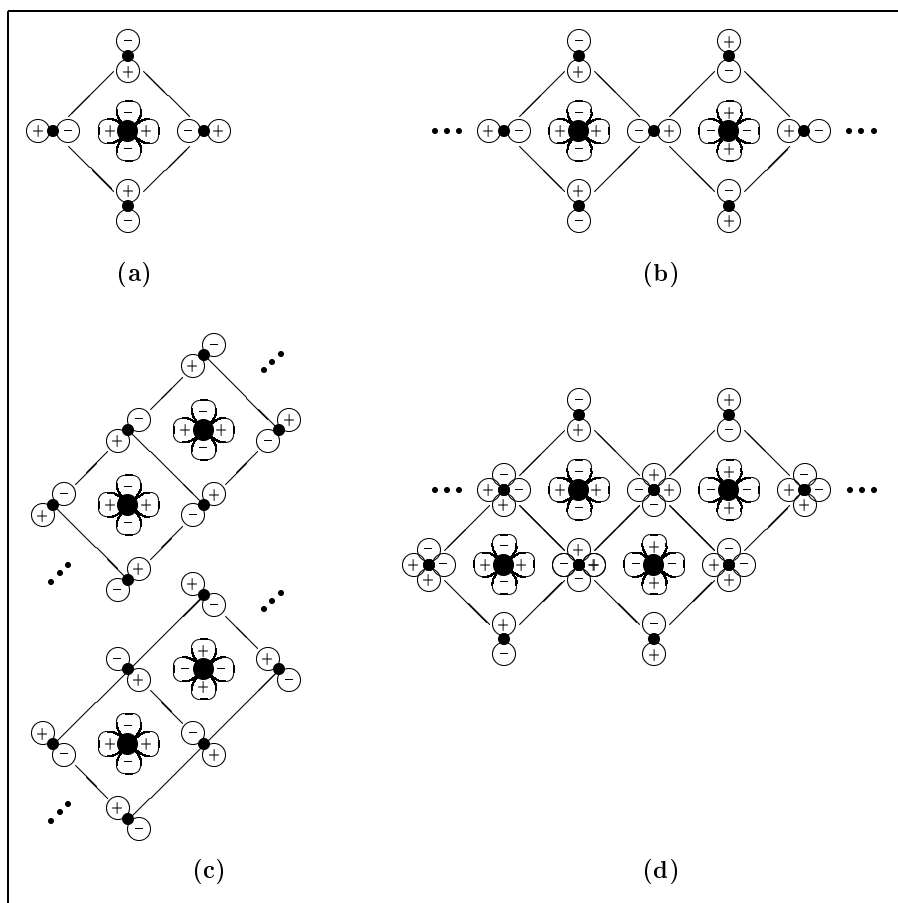
Figure 3.5: Cuprate chains formed from the plaquette (a) as the building block. A corner-sharing chain (b), an edge-sharing chain (c), and a double-chain (d) are shown. The phase factors of the orbitals correspond to the antibonding state. For details see the text.

section (3.3.2)) or double-chains (Fig. 3.5(d) and section (3.3.3)), which is in some sense a combination of the latter two. Composing the chains constructed in this way, a rich variety of two-, three- or multi-leg ladders can be build [39]. Thus, a quasi continuous transition is possible from one-dimensional to two-dimensional compounds, which are presented in Sec. 3.4.

3.3.1 Corner-shared cuprate chains

If a row of plaquettes is formed where adjacent plaquettes share a corner, a one-dimensional periodic anionic $[CuO_3]^{-4}$-complex results as shown in Fig. 3.5(b). As seen from this figure, subsequent orbitals along the chain have a relative phase

factor -1 in the totally anti-bonding state. That means that the one-dimensional energy band of this chain in molecular field approximation has its maximum at the BRILLOUIN-zone boundary. If the subsequent orbitals are forced to have the same phase to obtain a zero wave vector of the BLOCH state, then the state cannot be fully anti-bonding any more: the band has its minimum at the center (Γ-point) of the BRILLOUIN-zone. Thus, without any calculation we find a cosine-like anti-bonding band with the minimum at the zone center and the maximum at the zone boundary. Close to half-filling this band is again correlation-split into a lower and an upper HUBBARD sub-band, and the material is an insulator instead of a one-dimensional metal. Examples of this case are Sr_2CuO_3 and Ca_2CuO_3 [40].
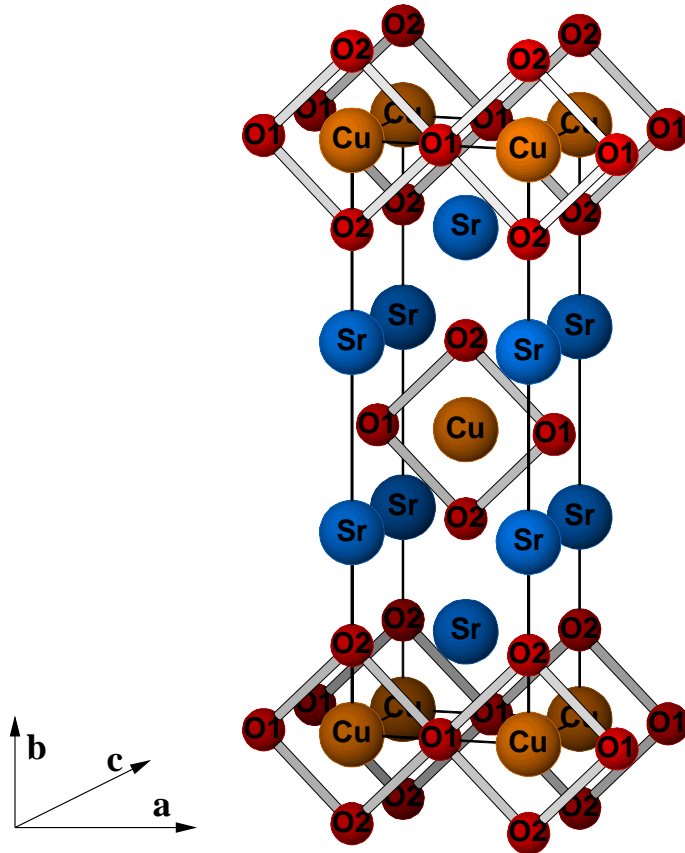
Figure 3.6: The body-centered orthorhombic unit cell of Sr_2CuO_3. The cuprate chains run along the **a** direction and lie in the drawing plane (corresponds to the **ab**-plane in the notation used).

The unit cell of Sr_2CuO_3 is shown in Fig. 3.6, the above mentioned Ca-compound is isostructural to the Sr-compound. Sr_2CuO_3 and Ca_2CuO_3 occur

in body-centered orthorhombic structure with lattice constants $a = 3.91$ Å, $b = 12.69$ Å, $c = 3.49$ Å and $a = 3.79$ Å, $b = 12.26$ Å, $c = 3.28$ Å, respectively [40, 41]. The CuO_3 chains run in a direction in the $a − b$ plane.

Experimentally, at high temperature, Sr_2CuO_3 and Ca_2CuO_3 are found to be the best known realizations of the one-dimensional (1D) spin-1/2 antiferromagnetic HEISENBERG model (AHM). Their NÉEL temperatures, $T_N \approx 5$ K for Sr_2CuO_3 and $T_N \approx 9$ K for Ca_2CuO_3, are very low compared to the intra-chain exchange integrals $J_\parallel \sim 0.2$ eV, and the ordered moments ($<0.1~\mu_B$) are extremely small [42, 43, 4]. The value $J_\parallel = 190$ meV for Sr_2CuO_3 [44, 45] appears to be the record value of an exchange integral among all known quasi-1D antiferromagnets. The correct description of the physics of a magnetic quasi-1D system with a weak magnetic inter-chain interaction has recently attracted much theoretical attention [46, 47, 48]. For all these reasons, Sr_2CuO_3 has been announced to become a 'superstar' in the field of low-dimensional magnetism in near future [2].

The self-consistent LDA-LCAO method has been applied to both compounds in the scalar relativistic version with a minimum basis treating the Cu-$(4s, 4p, 3d)$, O-$(2s, 2p)$, Sr-$(5s, 5p, 4d)$ and Ca-$(4s, 4p, 3d)$ orbitals as local valence basis states and the lower orbitals as core states. Due to the relatively open crystal structure two empty spheres per unit cell have been introduced with empty sphere s and p orbitals at each site. For the exchange and correlation potential the parameterization of VON BARTH and HEDIN was chosen[2].

The DOS and the bandstructure of Sr_2CuO_3 are shown in Fig. 3.7 and Fig. 3.8, respectively [49]. To check the accuracy of the LCAO band structure[3] by another method, also calculations using the linear muffin-tin orbital (LMTO) method were performed. No substantial differences were found, only the overall bandwidth of the whole pd band complex was slightly smaller in the LMTO results.

In agreement with the above mentioned general considerations of covalency, there is a single, well-separated, nearly one-dimensional, half-filled antibonding band crossing the FERMI level with large dispersion in **a**-direction (see Fig. 3.8). The width of this band is about 2.2 eV for both compounds. The characteristic quasi-1D VAN HOVE singularities near the band edges are clearly seen in the DOS (see Fig. 3.7). The dispersion in **c** direction corresponds to the inter-chain interaction via the shortest inter-chain distance and is about 100 meV (250 meV for Ca_2CuO_3). The smallest interaction is found in **b** direction with about 40 meV

---

[2]For historical reasons and due to comparability with the literature, we used different parameterizations (VON BARTH-HEDIN and PERDEW-ZUNGER) for the xc potential in different calculations of this work. The changes in the bandstructure due to this different parameterization were checked for one example and were found to be negligible.

[3]This check is useful because of the difficulties to optimize the minimum basis by determining the set of x_0 described in (2.2.2).

density of states of Sr₂CuO₃

Figure 3.7: Total and partial DOS of Sr₂CuO₃. The FERMI level is at zero energy. The contribution of Cu-4p states is less than 0.1 % in the region shown.

(60 meV for Ca₂CuO₃). It should be remarked again that the metallic behavior of the LDA-band structure is in sharp contrast to the experimental observation of large optical gaps $\sim$ 2 eV which are comparable to the bandwidth obtained above. This points to the necessity of dealing explicitly with the strong on-site COULOMB repulsion at the copper-site.

A tight-binding analysis of the orbitals involved shows that in first approximation the Cu $3d_{x^2-y^2}$ as well as the side oxygen $2p_y$ and the chain oxygen $2p_x$ orbitals are of direct relevance. Only a small admixture of Cu $4s$ states (the contribution of Sr or Ca states is much smaller) can be detected near both edges of this antibonding half-filled band. Its weight as determined by the ratio of the corresponding areas under the DOS curves is relatively small with 0.3 % for Sr₂CuO₃, but it increases to a weight of 2 % for the Ca compound. This enhanced

band structure of Sr$_2$CuO$_3$

Figure 3.8: LCAO energy-bands near the FERMI level for Sr$_2$CuO$_3$ along high-symmetry BRILLOUIN-zone directions. The notation of symmetry points is as follows: Γ=(000), X=(100), Y=(010), Z=(001), R=(101) in units of $(\pi/a, \pi/b, \pi/c)$. Strong dispersion can be seen along Γ–X (**a**-direction, parallel to the CuO$_3$-chains) whereas a small, but non-negligible dispersion in the perpendicular Γ–Z direction (**c**-direction, corresponds to the shortest inter-chain distance) can be seen. The smallest dispersion is found along **b.**

Cu $4s$ admixture is one reason for the larger inter-chain coupling in Ca$_2$CuO$_3$.

A parameterization of a one-band model, tight binding analyses for multi-band models and a detailed analysis of the deduced magnetic properties in terms of extended HUBBARD and anisotropic HEISENBERG models are given in sections (4.1) and (4.2).

3.3.2 Edge-shared cuprate chains

Planar edge-shared chains

Figure 3.5(c) shows two different anti-bonding states on an edge-sharing chain of cuprate-plaquettes. This chain is formed by anionic $[CuO_2]^{-2}$-complexes with a further reduced reduction state. With the phase rules as described above the upper pattern belongs to a zone-center state, and the lower pattern belongs to a zone-boundary state. Both are maximally anti-bonding, but are not quite σ-states. They are different in energy due to the crystal-field splitting between the two different oxygen $2p$-orbitals engaged. This type of chains is found, for instance, in Li_2CuO_2 [50, 51], in $CuGeO_3$ [52, 53] and in the recently discovered isostructural $CuSiO_3$ [54], which latter two are to be understood as $(GeO)CuO_2$ and $(SiO)CuO_2$, respectively, in our context. The main differences between the latter two compounds and Li_2CuO_2 are the positions and the valences of the cations and the canting of the CuO_2-chains against each other which strongly influences the inter-chain coupling.

The crystal structure of Li_2CuO_2 is shown in Fig. 3.9. Li_2CuO_2 exhibits a body-centered orthorhombic structure with lattice constants $a = 2.860$ Å, $b = 9.377$ Å and $c = 3.654$ Å [50, 51] where the edge-shared chain runs in a direction and lies parallel to the ab plane. The Cu-O-Cu bonding angle between nearest neighbor copper and oxygen atoms in the chain deviates with 94° only slightly from the 'ideal' 90° angle for an edge-shared chain of CuO_4-squares.

Experimentally, Li_2CuO_2 is an insulator. Neutron scattering indicates three-dimensional antiferromagnetic ordering at 9 K arising from an antialignment of ferromagnetic chains, and the magnetic moment of $0.9\mu_B$ was attributed to the Cu ion. This value is very close to the saturation moment of spin-only $Cu^{+2}(4s^0 3d^9)$.

We have performed LCAO band structure calculations [55] and, more recently, FPLO calculations in order to check the accuracy of the LCAO calculation. We found very good agreement between both treatments and also with other full potential calculations [56, 57]. A minimum basis was defined by treating the Cu $(4s, 4p, 3d)$, O $(2s, 2p)$, and the Li $(2s, 2p)$ orbitals as local valence basis states. In the LCAO calculations, two empty spheres per unit cell have been introduced. To improve the completeness of the basis set, we added O and Li $3d$ states in the FPLO calculation. The parameterization of VON BARTH and HEDIN and of PERDEW and ZUNGER, respectively, were chosen for the exchange and correlation potential.

The total and the partial DOS are shown in Fig. 3.10. The peak in the center of the antibonding band with nearly pure Cu $3d$ and O $2p$ character is in contrast to remnants of 1D VAN HOVE singularities near the band edges in the correspond-
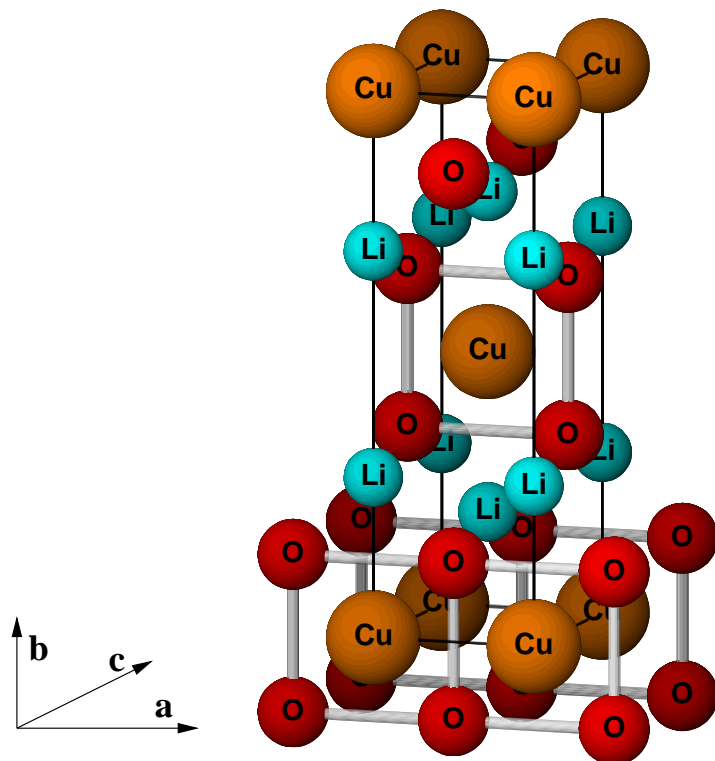
Figure 3.9: The body-centered orthorhombic unit cell of LiCuO$_2$. The edge-shared cuprate chains run along the **a** direction and lie in the drawing plane (corresponds to the **ab**-plane in the notation used).

ing antibonding bands of Sr(Ca)$_2$CuO$_3$ [49] (see Fig. 3.7) and CuGe(Si)O$_3$ [58] (see Fig. 3.13) and gives strong evidence for a non quasi-1D electronic structure. More detailed investigations show that the band at the FERMI level is composed mainly of Cu $3d_{xy}$ and O $2p_{x,y}$ states, with almost equal contributions from both O orbitals at variance with the above mentioned corner-sharing CuO$_3$ chain compounds. The last circumstance provides via HUND's rule coupling a natural explanation for the observed ferromagnetic ordering [50] in chain direction.

As expected from simple chemical considerations of the valence, there is a single, half-filled, well-separated antibonding band crossing the FERMI level (see Fig. 3.11). On the one hand, the width of this band is about 1 eV and similar to CuGeO$_3$, but on the other hand, its dispersion in chain direction ((0,0,0) $\rightarrow$ (1,0,0)) exceeds the dispersion in the other two directions by a factor of two only. A strong effect of next nearest neighbor interactions in chain direction has been derived from a strong second harmonic contribution to the calculated dispersion. The equivalence of the dispersion in the two transverse directions is important and points to a specific interchain interaction. The moderate anisotropy (compared
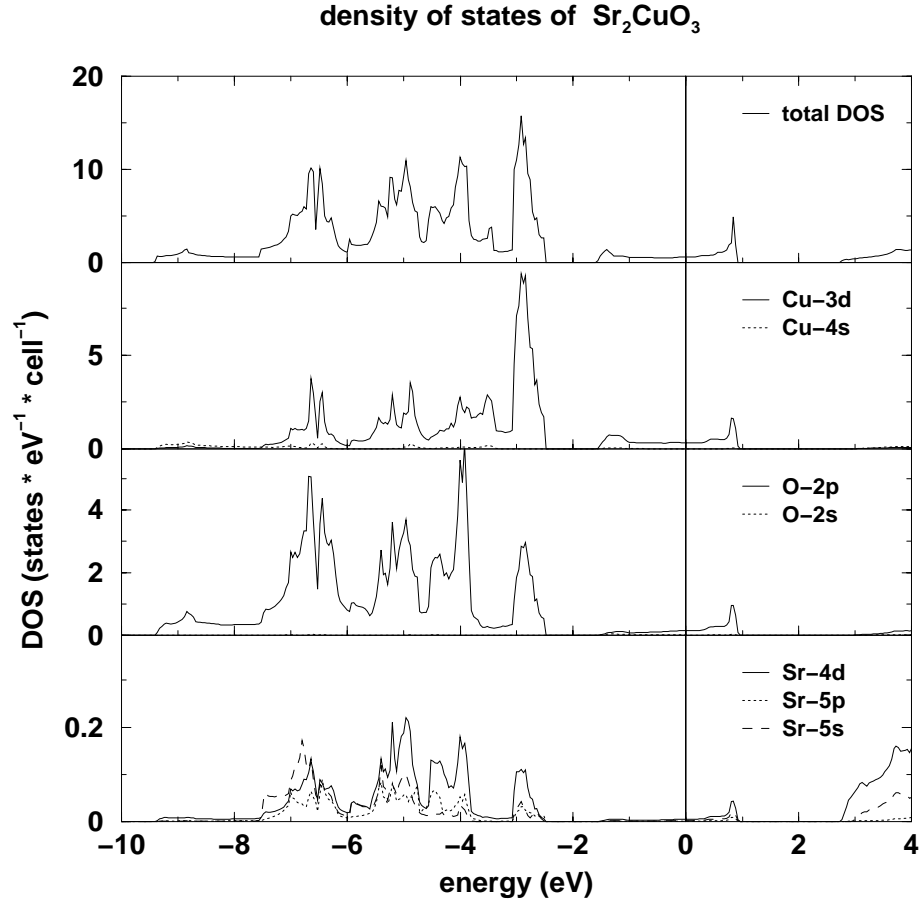
density of states of Li$_2$CuO$_2$

Figure 3.10: Total and partial DOS of Li$_2$CuO$_2$. The FERMI level is at zero energy. The contribution of Cu-4p states is less than 0.1 % in the region shown.

with the above mentioned cuprates) due to that interaction is in sharp contrast to the widely accepted intuitive view considering Li$_2$CuO$_2$ as the best realization of an 1D-edge-sharing CuO$_2$ chain [59]. A comparison of our LDA results and XAS measurements [60] will be presented in Section 5.4.

A second type of edge-shared chains is realized in CuGeO$_3$ and CuSiO$_3$, respectively. Instead of a single cation we have a cationic Ge(Si)O complex. The CuO$_2$ chains are canted against each other at variance with the planar arrangement in the above mentioned chain type. This canting mainly influences the inter-chain coupling. The crystal structure of CuGeO$_3$ (CuSiO$_3$ is isostructural) is shown in Fig. 3.12. CuGeO$_3$ and SiGeO$_3$ occur in the orthorhombic space group Pmmb with the lattice constants $a = 4.802$ Å $b = 8.475$ Å $c = 2.943$ Å [52, 53] and $a = 4.636$ Å $b = 8.774$ Å $c = 2.833$ Å [54], respectively. The Cu-O(2)-Cu

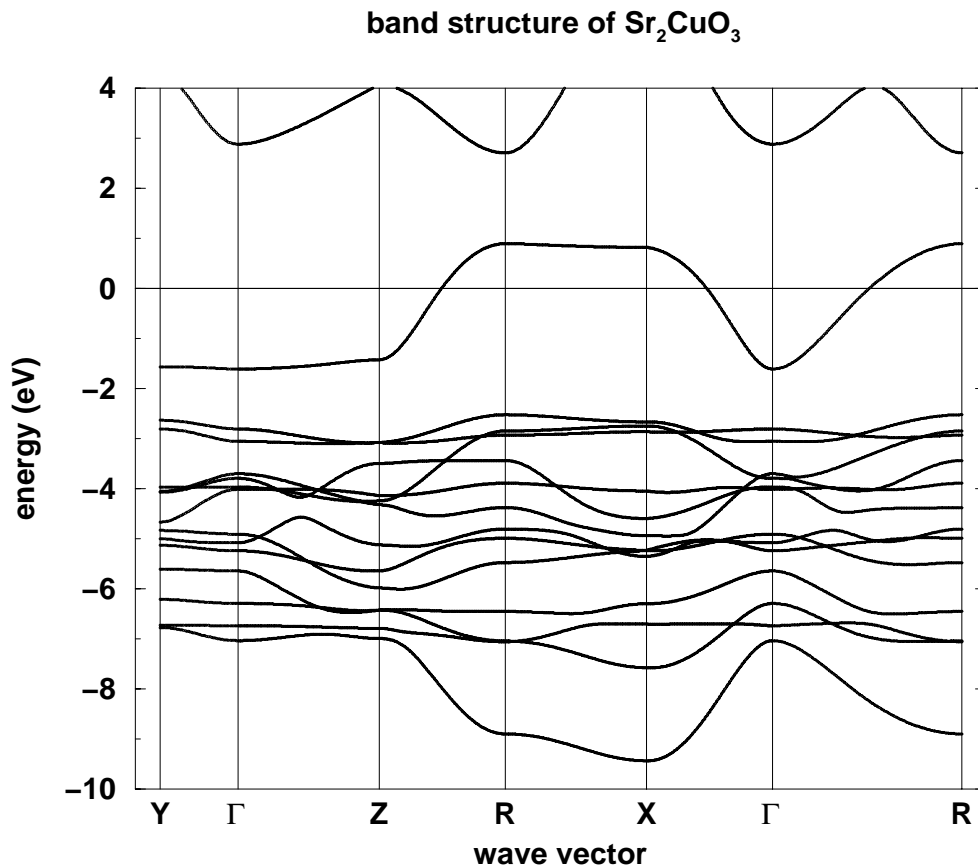**band structure of Li$_2$CuO$_2$**

Figure 3.11: LCAO energy-bands near the FERMI level for Li$_2$CuO$_2$ along high-symmetry BRILLOUIN-zone directions. The notation of symmetry points is as follows: Γ=(000), Y=(010), X=(100), R=(110) and A=(111) in units of (π/a, π/b, π/c).

bonding angles between nearest neighbor copper and oxygen atoms in the chain are about 98° in the Ge-compound and 94° in the Si-compound.

Some years ago, CuGeO$_3$ became famous because it was found as the first inorganic system which shows a spin-PEIERLS transition [5]. The transition temperature is $T_{\mathrm{SP}} = 14$ K. The antiferromagnetic exchange J_{AFM} was determined from the temperature dependence of the magnetic susceptibility $\chi(T)$ [5], from inelastic neutron- [61] and from RAMAN-scattering [62, 63, 64] between 8 and 22 meV. The spin-PEIERLS phase transition is found only in very pure samples. Impurities or doping, for example with a small amount of Zn (on the Cu site) [65] or Si (on the Ge site) [66] push the transition temperature down very fast. Already for some atom-percent of impurities, a phase transition to an antifer-
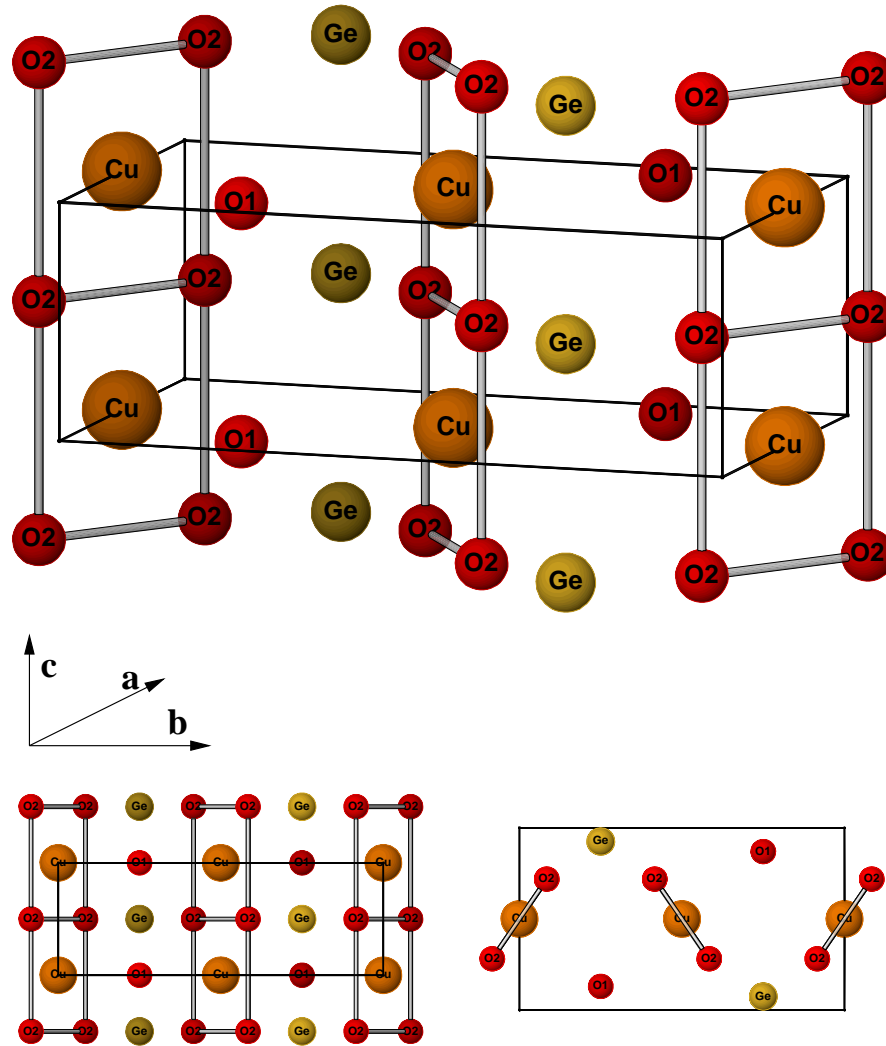
Figure 3.12: The orthorhombic unit cell of the $CuGeO_3$-crystal, perspective view (top), front view (down left) and top view (down right). The edge-shared cuprate-chains run along the **c** direction and are canted against each other.

romagnetic ordered state was observed with similar transition temperature T_N. This behavior can be explained with a chain-breaking due to the impurities and an ordering of the remaining unpaired spins. For certain concentrations of impurities, coexistence of AFM and the spin-PEIERLS phase was found [67, 68].

For the recently discovered $CuSiO_3$ compound, the experimental situation is less clear because the sample quality is not yet satisfactory. For the purest samples available, the temperature dependence of the magnetic susceptibility

$\chi(T)$ is rather similar to the CuGeO$_3$-data but shifted down in temperature. The $\chi(T)$ measurements show a broad maximum at about 13 K and an rapid decrease below $T_? = 8$ K to a constant value, but this decrease is less pronounced then for the Ge-compound. A sharp peak in the specific heat measurement at $T_?$ indicates clearly a phase transition [69]. The nature of this phase transition is still unclear (it may be AFM or spin-PEIERLS), but for a reliable determination the sample quality has to be improved because of the above mentioned role of impurities for the spin-ordering.

The band structure calculations for CuGeO$_3$ and CuSiO$_3$ were carried out using the FPLO code with Cu ($4s$, $4p$, $3d$), O ($2s$, $2p$, $3d$), Ge ($3d$, $4s$, $4p$, $4d$) and Si ($3s$, $3p$, $3d$) states, respectively, as minimum basis set. Our results are similar to the results of LAPW [58] and LMTO-ASA [70] bandstructure calculations, only the bandwidths are slightly smaller. The total as well as the partial DOS of CuGeO$_3$ are shown in Fig. 3.13. At variance with all above mentioned chain-compounds, the admixture of the cationic Ge-O(1) complex to the standard pd chain-bands is much stronger. This is important for the construction of tight binding models, where additional orbitals beyond the standard pd-model descriptions have to be taken into account. At variance with Li$_2$CuO$_2$, the remnants of 1D VAN HOVE singularities near the band edges of the antibonding band are clearly developed. This indicates a quasi 1D electronic structure in the vicinity of the FERMI-level.

The bandstructure of CuGeO$_3$, shown in Fig 3.14, confirms this indication. Corresponding to the two formula units per cell, we find two half-filled bands crossing the FERMI level. These bands show a dispersion of about 1 eV in chain direction, whereas the dispersion corresponding to the shortest inter-chain distance is about five times smaller. The dispersion in the direction orthogonal to the latter two is again smaller by a factor of five. With respect to the band dispersions in the main directions, the dimensionality of the electronic structure of this compound can be considered as in between the nearly ideal 1D compound Sr$_2$CuO$_3$ and the 3D compound LiCuO$_2$.

The DOS and the bandstructure of CuSiO$_3$ are very similar to that of the Ge-compound. The mostly changed features are the two antibonding bands crossing the FERMI level: They have the same shape in both compounds, but the bandwidth is reduced by about 40 % to 0.6 eV in CuSiO$_3$. This can be understood due to the change in the Cu-O(2)-Cu bonding angle which is closer to 90° for CuSiO$_3$, whereas the Cu-O distance in the chain is nearly the same for both compounds (1.941 Å for CuSiO$_3$ and 1.942 Å for CuGeO$_3$).

In both compounds, the next nearest neighbor coupling t_2 is important and about half as large as the nearest neighbor coupling t_1, which plays still the dominant role. For the above mentioned Li$_2$CuO$_2$ the situation is reversed, al-

density of states of CuGeO₃
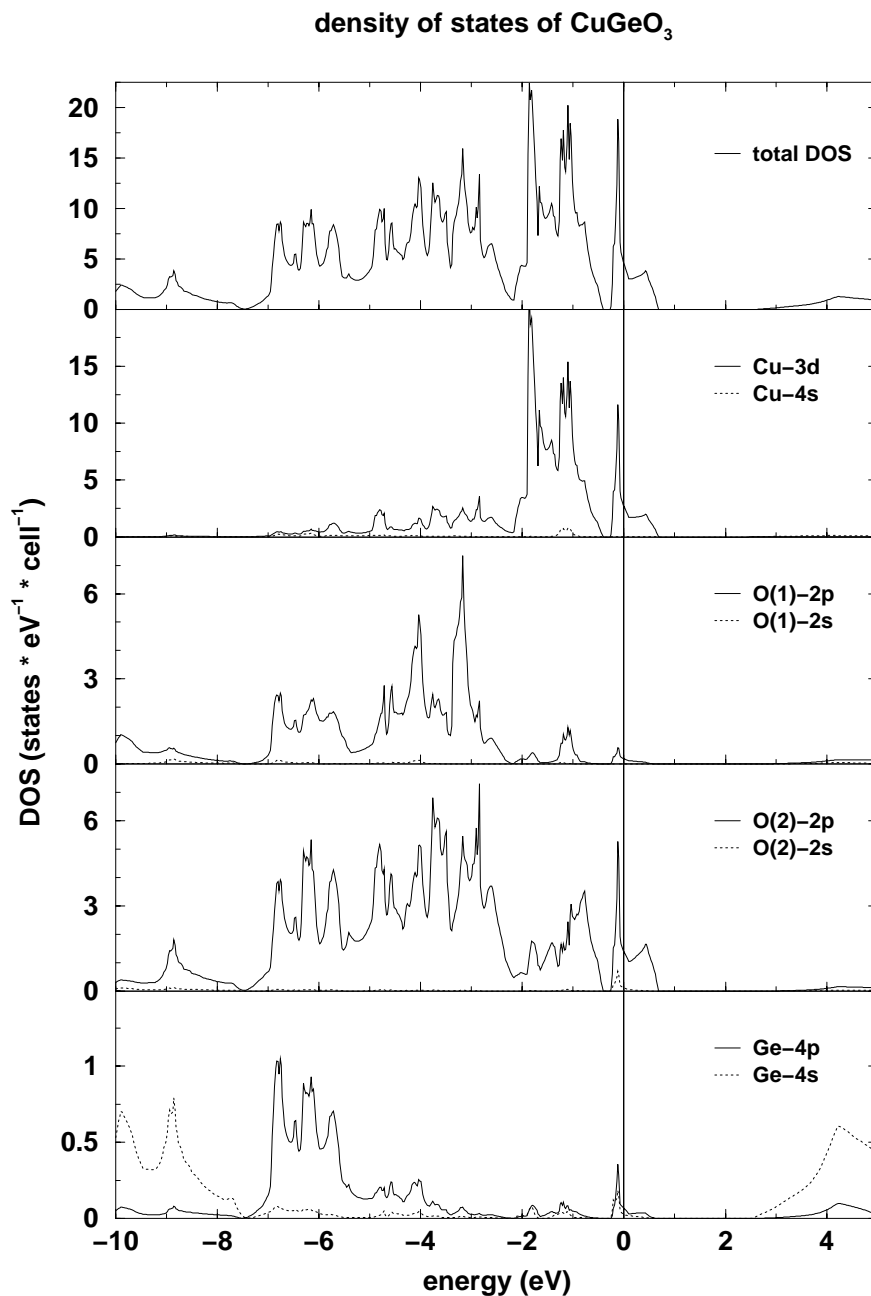
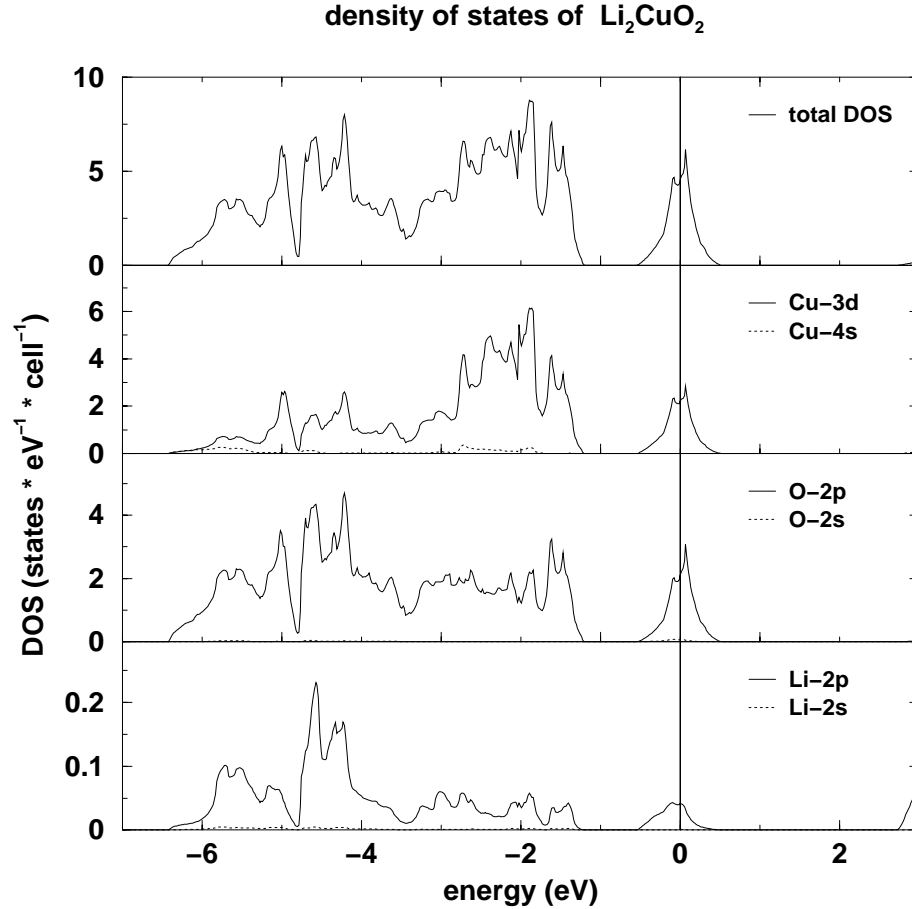Figure 3.13: Total and partial DOS of CuGeO₃. The FERMI level is at zero energy. The contribution of Cu-4*p* states is less than 0.2 % in the region shown.

though the Cu-O-Cu angle is the same for the Li- and the Si-compound. This fact underlines the importance of the cations for the electronic structure in these com-
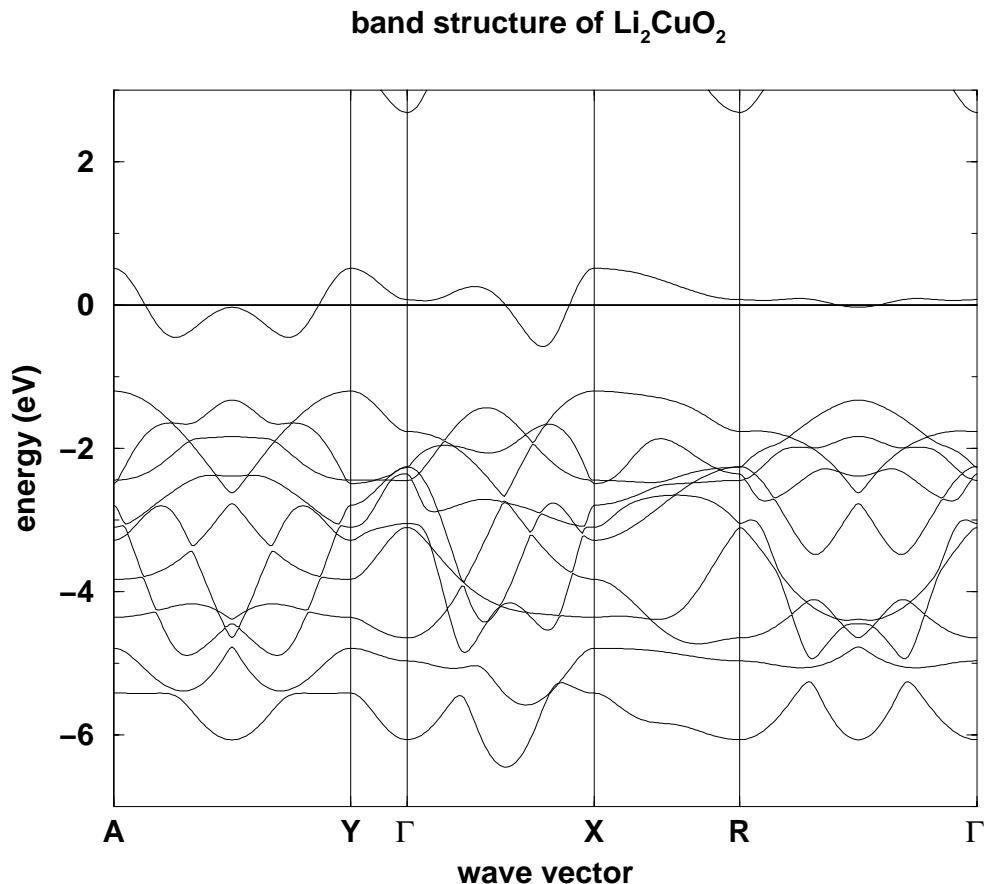
band structure of CuGeO$_3$
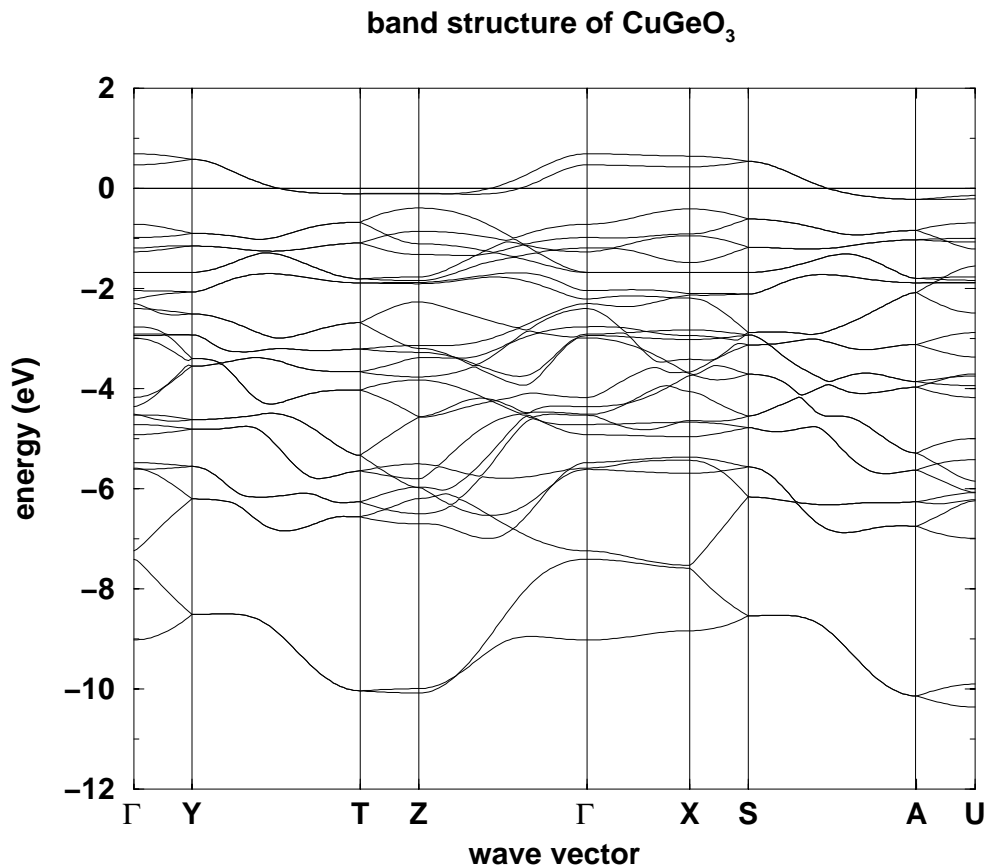
Figure 3.14: Band structure near the FERMI level for CuGeO$_3$ along high-symmetry BRILLOUIN-zone directions. The notation of symmetry points is as follows: X=(100), Y=(010), S=(110), Z=(001), T=(011), U=(101) and A=(111) in units of (π/a, π/b, π/c). Strong dispersion can be seen along Γ–Z (parallel to the CuO$_2$-chains) whereas a small, but non-negligible dispersion in the perpendicular Γ–Y direction (corresponding to the shortest inter-chain distance) can be seen. The smallest dispersion is found orthogonal to the latter two directions.

pounds. Moreover, the side groups can modify the 90° super-exchange and can cause a seeming violation of the GOODENOUGH-KANAMORI-ANDERSON (GKA) rules [71, 72, 73, 74]. An orbital analysis of the antibonding band shows that, besides the Cu-3d states, mainly the O(2)-2p_z orbitals contribute to this band. The other contributions are suppressed due to a shift in the on-site energies of the involved oxygen orbitals, caused by the side group. As a first approximation, the contribution of the perpendicular O-orbitals can be neglected. Therefore, the nearest neighbor exchange is antiferromagnetic for CuGeO$_3$ and CuSiO$_3$, whereas

for the Li-system the expected ferromagnetic interaction was found.

The splitting of the two antibonding bands, originating from the interchain coupling, has nearly the same value for $CuSiO_3$ and $CuGeO_3$. In this sense, with respect to the reduced in-chain coupling, the Si-compound is less 1D than the Ge-system. The less pronounced peak (remnant of the VAN HOVE singularity) in the DOS on the upper band edge for $CuSiO_3$ supports this argument.

Folded edge-shared chains

Folding the edge-shared CuO_4 plaquettes up and down, we get a still linear, but non-planar 'merlon' chain. The picture of the anti-bonding states is similar to Fig 3.5(c), but additionally the third oxygen orbital (in planar geometries not hybridizing with the shown orbitals due to symmetry) is involved in the binding. In the case of an ideal folding angle of 90°, each copper hybridizes with two of the oxygen orbitals, whereas one of the O orbitals parallel to the common plaquette edge hybridizes with both adjacent Cu atoms. Such a chain is realized in $Ba_3Cu_2O_4Cl_2$, which should be understood as $(Ba_3Cl_2)(CuO_2)_2$ in our notation. The crystal structure of this compound is shown in Fig. 3.15.

$Ba_3Cu_2O_4Cl_2$ occurs in the orthorhombic space group Pmma with the lattice constants $a = 6.553$ Å, $b = 6.000$ Å, $c = 10.563$ Å [75]. Due to the folding, the chain contains now two inequivalent copper positions, Cu_A and Cu_B. The Cu_B atom is slightly elongated from the the plaquette plane. The folding angle between the plaquettes is about 96°, whereas the plaquettes are ideally quadratic.

$Ba_3Cu_2O_4Cl_2$ shows insulating behavior and a phase transition to AFM below 20 K. In susceptibility measurements [76] on single crystals, a spin-flop transition was observed in a magnetic field of 2.6 T parallel to the chains (crystallographic a direction). This indicates a collinear antiferromagnetic structure with localized moments in this direction. The ordered magnetic moment was determined to be near the saturation value of 1 μ_B. Preliminary investigations by neutron scattering on powder[4] could not yet elucidate the magnetic ordered structure [77].

We performed FPLO band structure calculations with a minimum basis set consisting of Cu ($4s$, $4p$, $3d$), O ($2s$, $2p$, $3d$), Ba ($5s$, $5p$, $5d$, $6s$, $6p$), Cl ($3s$, $3p$, $3d$) states. Due to the large extension of the Ba ($5s$, $5p$) wave functions it was necessary to treat them as valence states (see 2.2.1). For the exchange and correlation potential the parameterization of PERDEW and ZUNGER was chosen.

The resulting total and partial DOS are shown in Fig. 3.16. Compared with all compounds mentioned above, $Ba_3Cu_2O_4Cl_2$ shows the smallest pd-band-complex

---

[4]The above mentioned single crystals are too small for neutron scattering.
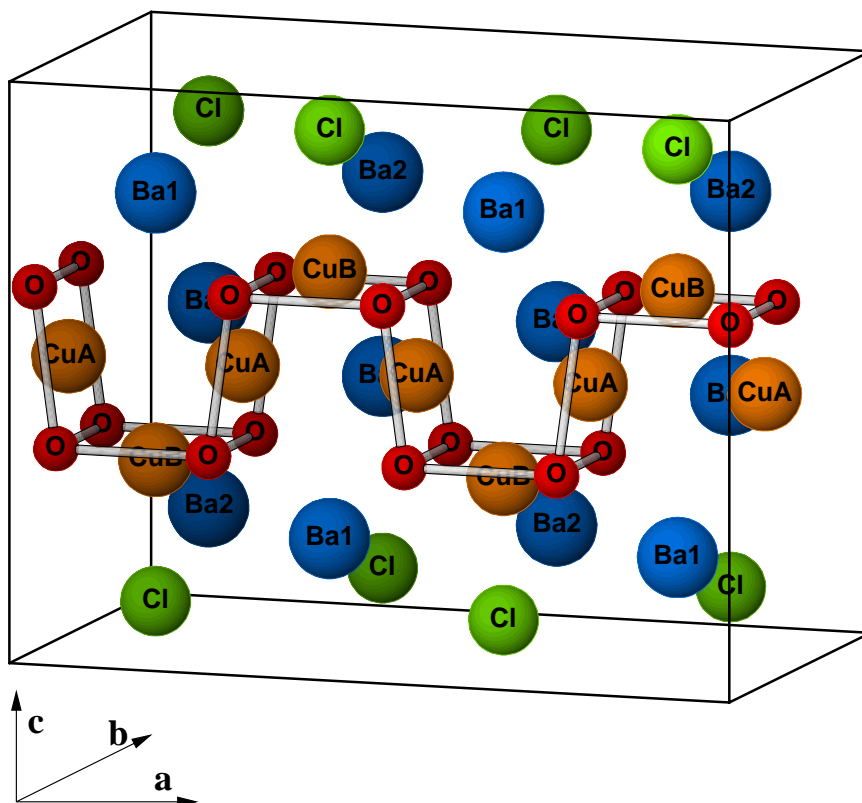
Figure 3.15: The orthorhombic unit cell of $Ba_3Cu_2O_4Cl_2$. The folded edge-shared cuprate-chains run along the **a** direction of the crystal. To demonstrate more clearly the typical structure of the 'merlon' chain, two unit cells are shown.

with a width of about 6 eV. The Cl $3p$ states are nearly filled and give a large contribution to the DOS about 4 eV below the FERMI-level. We find a small admixture of Ba $5d$ and $6s$ states to the pd-complex. The antibonding band complex at FERMI-level is the narrowest one for all considered cuprates with only 0.6 eV bandwidth and shows clear remnants of VAN HOVE-singularities. Cl-states do not contribute to the antibonding region.

Figure 3.17 shows the bandstructure of $Ba_3Cu_2O_4Cl_2$. The rather small dispersion of most bands in the pd-complex is peculiar. This finding can be explained by the nearly 90° folding of the chain and by the enlargement by 3% of the Cu-O distance compared with other edge-sharing compounds.

We see four half-filled bands crossing the FERMI-level corresponding to the four Cu atoms per unit cell. Astonishingly, the strongest dispersion of about 0.4 eV we find in Γ - Y direction, which is perpendicular to the merlon chain. The dispersion in chain direction is half as large, in the third direction almost no
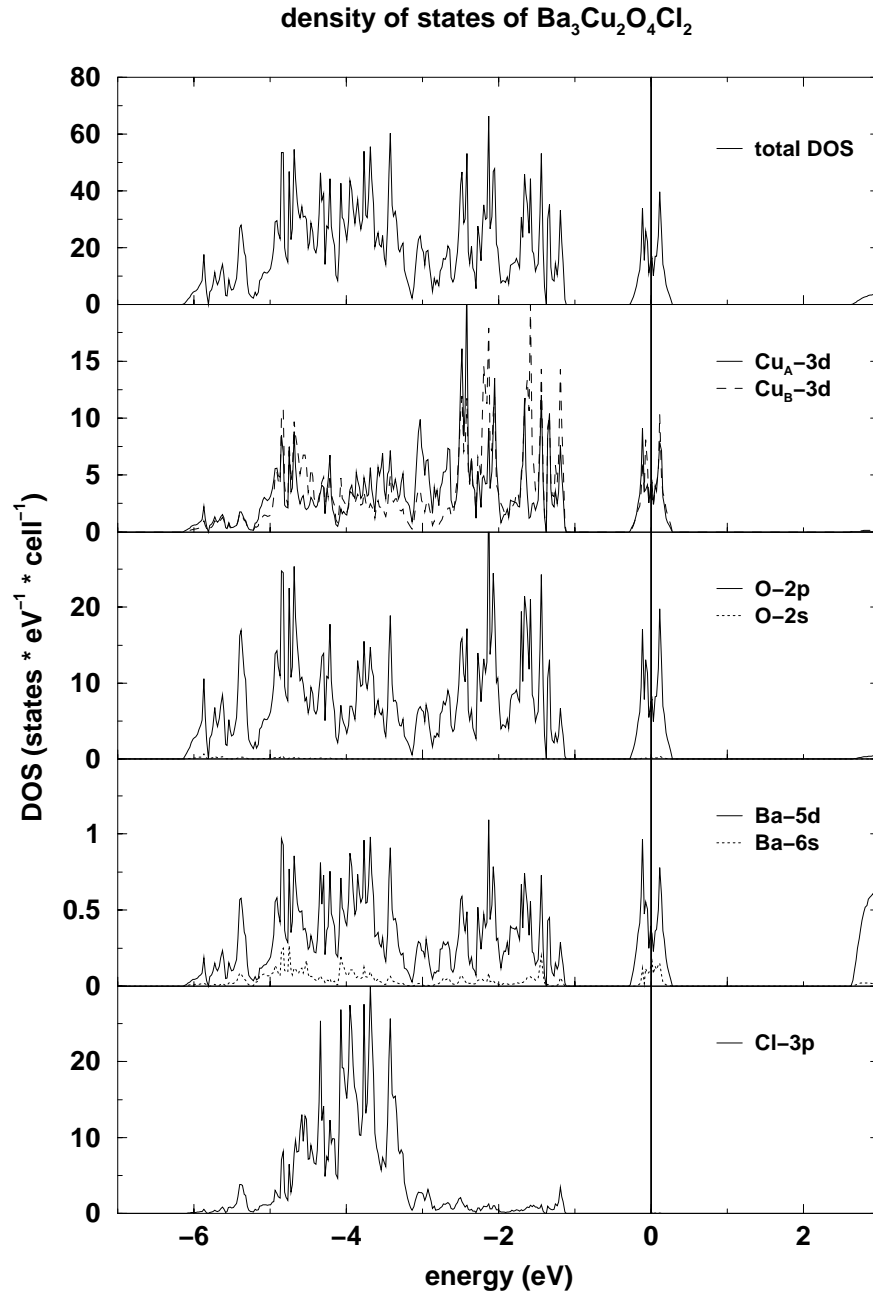
Figure 3.16: Total and partial DOS of $Ba_3Cu_2O_4Cl_2$. The FERMI level is at zero energy. The contribution of Cu-($4s$, $4p$), Ba-$6p$ and Cl-$3s$ states all together is less than 0.2 % in the region shown.

dispersion is found.

A more detailed consideration of interatomic distances and angles together

band structure of $Ba_3Cu_2O_4Cl_2$
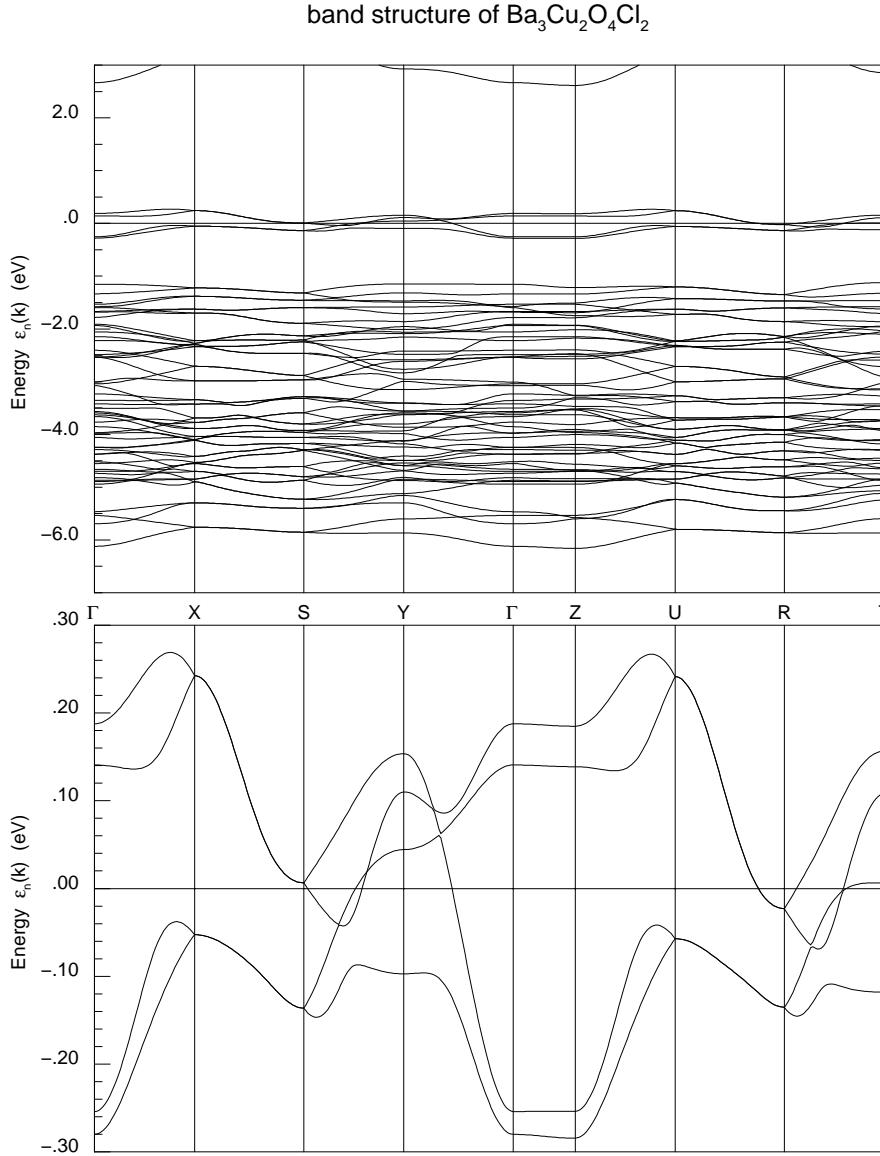
Figure 3.17: Band structure of $Ba_3Cu_2O_4Cl_2$. The FERMI level is at zero energy. In the upper panel the whole $p-d$ complex is shown, the band complex at the FERMI level is zoomed in the lower panel. The notation of symmetry points is as follows: Γ=(000), X=(100), Y=(010), S=(110), Z=(001), T=(011), U=(101) and R=(111) in units of $(\pi/a, \pi/b, \pi/c)$.

with an orbital analysis of the antibonding bands gives a first explanation for this unexpected behavior. Due to the folding angle of 96°, the inter-chain distance (6.000 Å) is shorter than the Cu_B-Cu_B distance in chain direction (6.553 Å). Calculating the orbital weight, we find that there are either strongly Cu_A dom-

inated or strongly Cu_B dominated bands in the chain direction. The band with
the strongest dispersion (in Γ - Y direction) contains only contributions of or-
bitals of the Cu_B-subsystem. Therefore, the main part of this dispersion results
from a direct interaction between plaquettes of the same Cu-type. Due to the
above mentioned shorter Cu-Cu distance perpendicular to the chain for the same
Cu type, the corresponding dispersion is stronger than in chain direction. In this
sense, the generally accepted picture of a folded edge-sharing chain is misleading
regarding to the electronic structure.

Within the orbital analysis, we find that for Cu_A mainly $3d_{yz}$ states contribute
to the antibonding bands with only a very small admixture of the $3d_{xy}$ orbital,
whereas for Cu_B the main contribution stems from the $3d_{xy}$ orbital with only very
small admixture of $3d_{yz}$ states. Therefore, for further investigation, a model with
only one orbital per Cu site should be applicable in first approximation. For the
Cu_A dominated bands, we see hybridization with O-$2p_y$ and O-$2p_z$ states, for the
Cu_B dominated bands with O-$2p_y$ and O-$2p_x$. Thus, Cu_A and Cu_B plaquettes
share only the O-$2p_y$ orbital. Considering the GKA rules, the superexchange via
only one oxygen orbital should lead to an antiferromagnetic exchange between
Cu_A and Cu_B similar to the situation in $CuGeO_3$. Whereas in the Ge compound
the suppression of the second O orbital in the antibonding bands is due to a shift
of the on-site energy, in $Ba_3Cu_2O_4Cl_2$ this suppression appears due to symmetry
because of the nearly 90° folding of the chain.

3.3.3 Double- or zigzag chain cuprates

The same reduction state $[CuO_2]^{-2}$ as in the above discussed edge-shared chains
is realized in the double-chain of Fig. 3.5(d), which is present in $SrCuO_2$ [78].
The crystal structure of this compound is shown in Fig. 3.18.

$SrCuO_2$ is centered orthorhombic (space group Cmcm) with lattice parameters
$a = 3.904$ Å, $b = 16.27$ Å, $c = 3.556$ Å [40]. The double-chains run along the
crystallographic a direction and lie in the ab plane. The Cu-O(1)-Cu bonding
angle between copper atoms in the different subchains of a double-chain and
oxygen is about 87°.

This material is magnetically even more complicated than Sr_2CuO_3, though
the in-chain exchange has a similar value of about 180 meV [79] (190 meV for
Sr_2CuO_3). A magnetically ordered structure appears below 5 K with a second
phase transition at about 2 K. The ordered magnetic moment was found to be
extremely small with an upper limit of 0.01 μ_B [80]. Recent experiments deter-
mined a value of about 0.03 μ_B [79] (0.06 μ_B for Sr_2CuO_3). Except of the chain
direction where the ordering is clearly AFM, the magnetic structure shows wave
vectors incommensurate to the crystal structure [79] at variance with the single
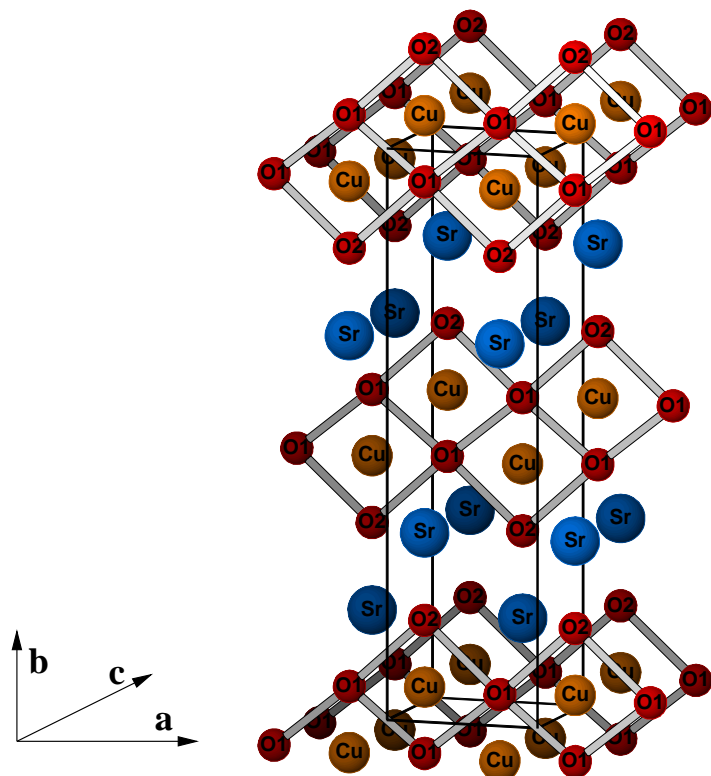
Figure 3.18: The orthorhombic unit cell of $SrCuO_2$. The cuprate-chains run along the **a** direction and lie in the drawing plane (corresponds to the **ab**-plane in the notation used).

chain compound Sr_2CuO_3.

Our bandstructure calculation was carried out using the LCAO code with a minimum basis consisting of Cu-$(4s, 4p, 3d)$, O-$(2s, 2p)$ and Sr-$(5s, 5p, 4d)$ valence states. To cope with the relatively open crystal structure, four empty spheres per unit cell have been introduced with empty sphere s and p orbitals at each site. For the exchange and correlation potential the parameterization of VON BARTH and HEDIN was chosen. Because the program used is not able to handle non-symmorphic space groups, we had to calculate a simple orthorhombic unit cell with four formula units inside. For that reason, we get twice the number of bands and twice the DOS per unit cell as in a centered case with two formula units in the primitive cell.

The total as well as the partial DOS and the band structure are drawn in Figs. 3.19 and 3.20. The DOS is very similar to that of Sr_2CuO_3 (cf. Fig. 3.7). The characteristic quasi-1D VAN HOVE singularities near the band edges are clearly seen and indicate a 1D electronic structure. The half-filled antibonding

density of states of SrCuO$_2$

Figure 3.19: Total and partial DOS of SrCuO$_2$. The FERMI level is at zero energy. The contribution of Cu-4p and O-2s states is less than 0.2 % in the region shown.

bands at FERMI level have nearly pure Cu 3$d_{x^2-y^2}$, oxygen 2p_y and 2p_x orbital character. Their large dispersion is parallel to the chain direction. The width of this band is about 2.4 eV. The dispersion in c direction corresponds to the inter-chain interaction via the shortest inter-double-chain distance and is about 100 meV. The smallest interaction is found in b direction with about 50 meV. The splitting of the bands at FERMI level is characteristic for the interaction between the two subchains of a double chain. This interaction is in the same order of magnitude like the above mentioned weak dispersions orthogonal to the chain direction. This nearly decoupled behavior can be related to the $\sim$ 90° Cu-O(1)-Cu bonding angle between the subchains.

band structure of SrCuO$_2$
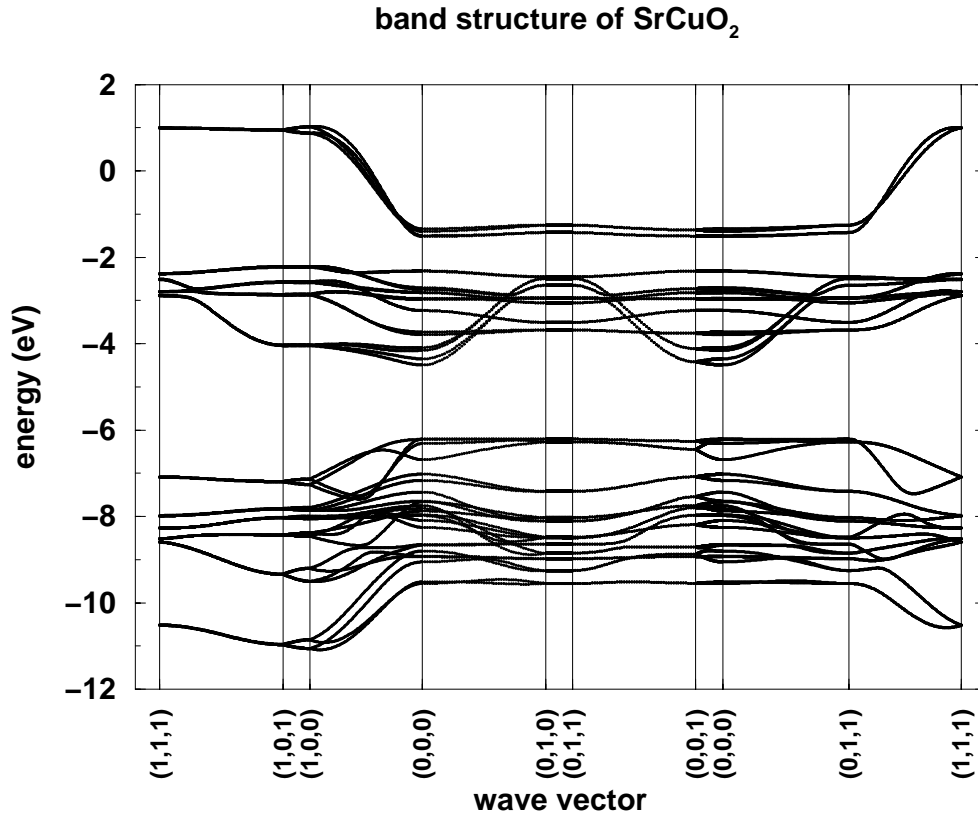
Figure 3.20: Band structure near the FERMI level for SrCuO$_2$ along high-symmetry BRILLOUIN-zone directions. The wave vector is given in units of $(\pi/a, \pi/b, \pi/c)$. Strong dispersion occurs along (000)–(100) (parallel to the Cu$_2$O$_4$ double-chains) whereas a small, but non-negligible dispersion in the perpendicular (000)–(010) direction (corresponds to the shortest inter-chain distance) can be seen. The smallest dispersion is found orthogonal to the latter two directions.

3.4 Plane cuprate structures

3.4.1 Planar cuprates with a CuO$_2$-plane

By joining together periodically repeated CuO$_3$-chains of Fig. 3.5(b) so that adjacent chains share the side oxygen ions of such chains, the checkerboard-like planar structure of Fig. 3.21(a) is obtained. This is an anionic $[\text{CuO}_2]^{-2}$-plane for nominal valence charges.

Doping with holes yields the famous $[\text{CuO}_2]^{-2+\delta}$-plane of the high-$T_c$ superconductors (see [81] for an overview). The undoped plane ($\delta = 0$) is insulating
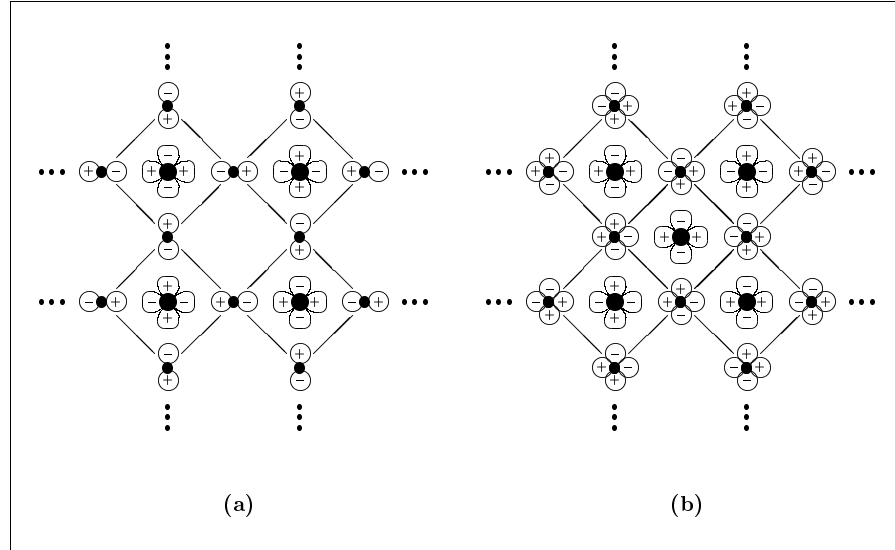
Figure 3.21: Cuprate-planes formed from plaquettes as the building blocks. The checkerboard pattern (a) may be obtained by joining together chains of Fig. 3.5(b). The pattern (b) is obtained by putting an additional copper ion on every second white field in horizontal rows of the checkerboard (a).

with an antiferromagnetic groundstate. Already at low doping rates it becomes a strange metal, and for $\delta \gtrsim 0.1$ (as well as for electron doping $\delta \lesssim -0.1$) it becomes superconducting. A schematic phase diagram is shown in Fig. 3.22.

The material for which high-T_c superconductivity was discovered first was barium-doped La_2CuO_4. The undoped compound is to be understood in our context as $(LaO)_2CuO_2$. Its structure is shown in Fig. 3.23(a). It consists of a stacking of two ionic $[LaO]^+$-planes followed by a covalent $[CuO_2]^{2-}$-plane, on top of each other. If La is partially replaced by an alkaline-earth atom (Ca, Sr or Ba), hole-doping results in the CuO_2-plane. For the understanding of that material it is crucial that the oxygen of the BaO-plane (the so-called apical-oxygen because it forms the apex of an oxygen pyramid whose basis is the CuO_4-plaquette) is at most very weakly covalently bound to the CuO_2-plane[5].

$LaCuO_4$ is generally considered as the parent compound for all materials with CuO_2 planes as structural element and therefore very useful as a reference system. At high temperatures, it occurs in the body-centered tetragonal space

---

[5]The difference of the apical-oxygen and the plane-oxygen is often discussed as originated by the JAHN-TELLER effect [82]. However, there is no true JAHN-TELLER distortion in most of the planar cuprates, they are layered structures far from cubic symmetry [81].
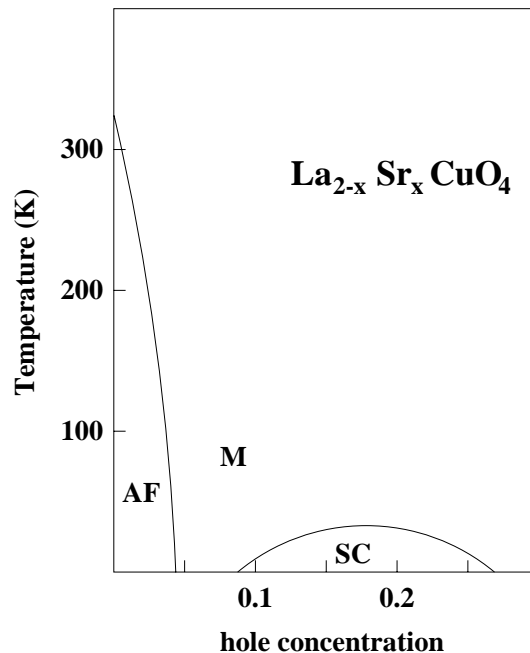
Figure 3.22: The simplified temperature - hole-concentration phase diagram for $La_{2-x}Sr_xCuO_4$ with antiferromagnetic (AF), metallic (M) and superconducting (SC) phase.

group I4/mmm (see Fig. 3.23(a)) with the lattice constants $a = 3.78$ Å and $c = 13.15$ Å. The Cu-O distance in the CuO_2 plane is 1.89 Å (corresponding to a covalent bondlenght), whereas the distance between Cu and the apical oxygen is 2.43 Å (corresponding to an ionic distance). The low temperature phase is orthorhombic due to lattice distortion.

For the tetragonal phase of $LaCuO_4$, we performed LCAO and FPLO band structure calculations with a minimum basis set consisting of Cu ($4s$, $4p$, $3d$), O ($2s$, $2p$, $3d$) as well as Ba and La ($5s$, $5p$, $5d$, $6s$, $6p$) states[6]. Due to the large extension of the Ba and La ($5s$, $5p$) wave functions it was necessary to treat them as valence states (see 2.2.1)[7]. In the LCAO calculation, two empty spheres per unit cell were introduced due to the relatively open structure of this compound. For the exchange and correlation potential the parameterization of VON BARTH and HEDIN for the LCAO and of PERDEW and ZUNGER for the

---

[6]The FPLO calculations were done recently to check *a posteriori* the accuracy and reliability of the LCAO calculations, which we used for most investigations of planar cuprates. This check should be representative for the planar structure type, because the already mentioned problems in the determination of the compression parameters x_0 are identical for all considered compounds of this family.

[7]In the LCAO calculation, these states were treated as core states for technical reasons.
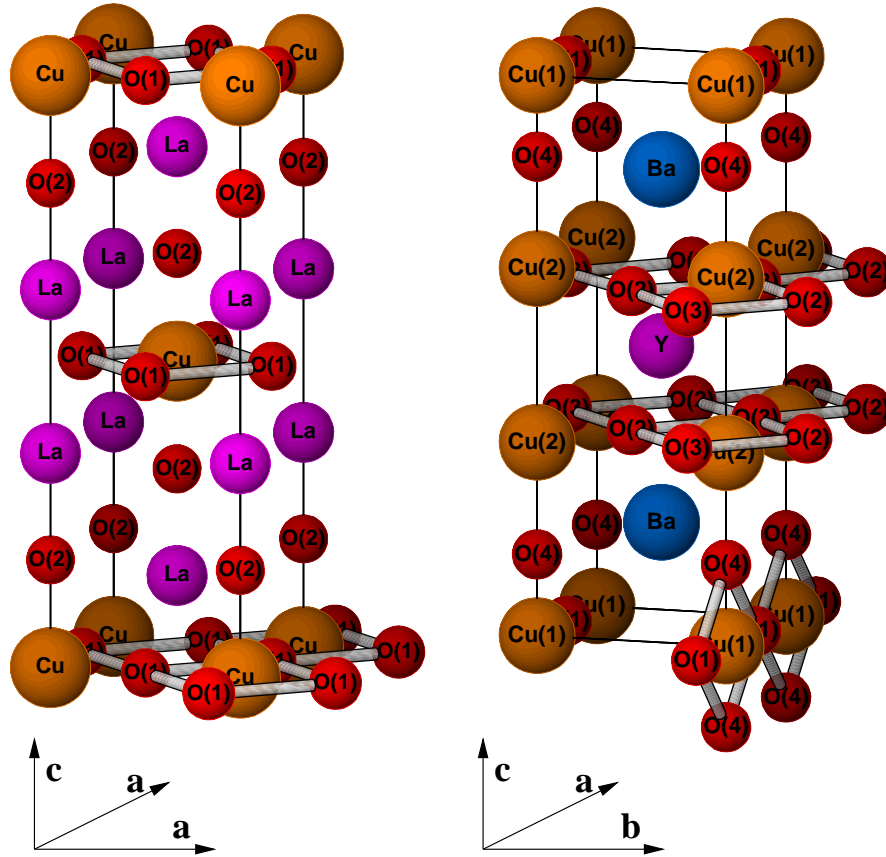
Figure 3.23: Unit cells (a) of the La_2CuO_4-crystal and (b) of the $YBa_2Cu_3O_7$-crystal.

FPLO calculation was chosen. Comparing the results of both calculations with each other and with results from the literature [81, 83], no substantial differences were found. The results of our FPLO calculation are nearly identical with those of Ref. [81]. There, the bandwidths are a few percent smaller than in our LCAO results, and a few percent larger than in Ref. [83]. The differences in band energies for the latter two calculations are of the same order as well.

The total and the partial densities of states are shown in Fig. 3.24. As in the previous cases, the LDA predicts metallic behavior in contradiction to the experimentally observed antiferromagnetic insulating behavior. The valence band is built mainly of Cu-3d and O-2p states with a small admixture of La-5d states. The oxygen contribution to the complex at the FERMI level stems predominantly from the plane-oxygen O(1).

Figure 3.25 shows the bandstructure of $LaCuO_4$. As expected from the chem-
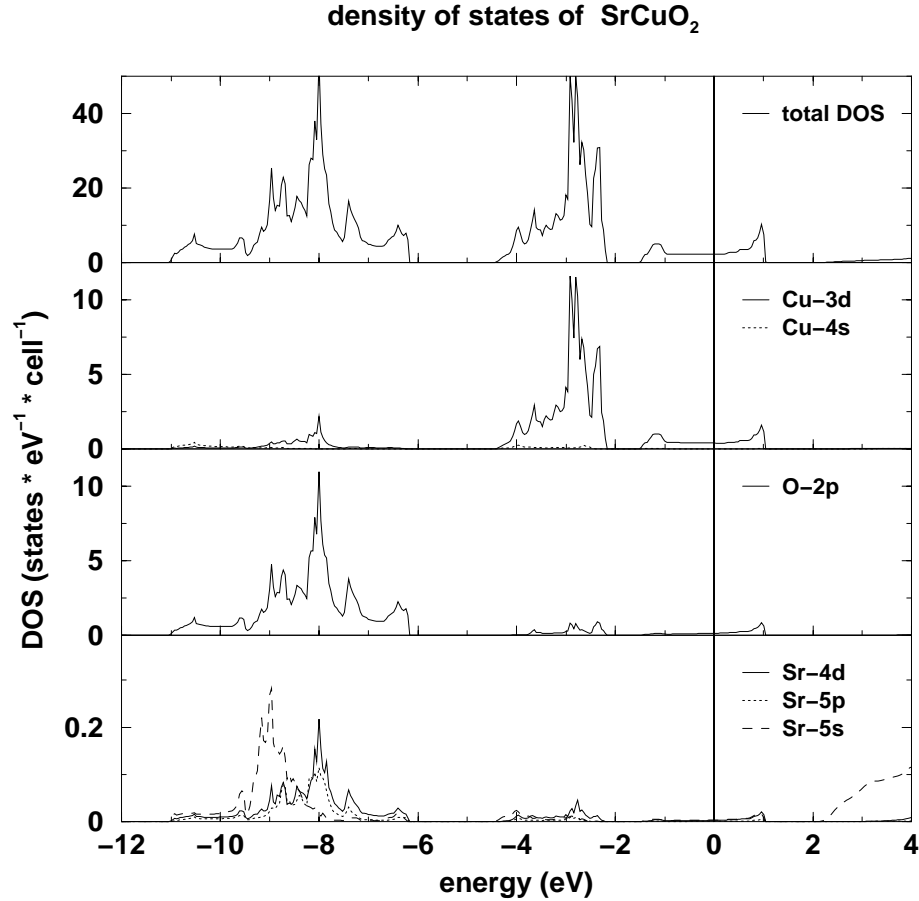
density of states of La$_2$CuO$_4$
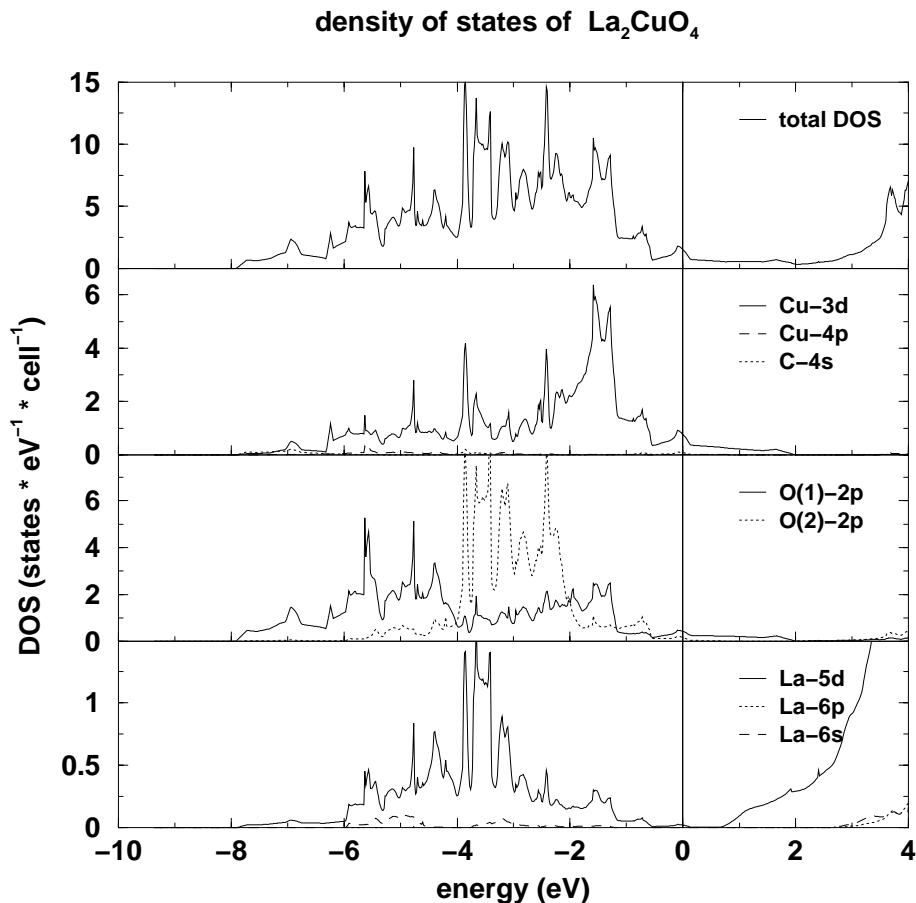
Figure 3.24: Total and partial DOS of La$_2$CuO$_4$. The Fermi level is at zero energy. The contribution of O-2s states is less than 0.1 % in the region shown.

ical considerations, we find one broad band crossing the Fermi level and 16 bands below inside the *pd*-complex (33 valence electrons). The bandwidth of the antibonding band is about 4 eV and approximately twice as large as in the corner-shared chain compound Sr$_2$CuO$_3$ (see Fig. 3.8). This is consistent with the doubled number of neighboring plaquettes in the CuO$_2$-plane compared with the CuO$_3$-chain. A considerable dispersion of the antibonding band is found only in the plane, whereas its dispersion along Γ - Z amounts only a few[8] meV . Other bands show non-negligible dispersion in the latter direction.

---

[8]At the first glance, it seems that the antibonding band has a considerable dispersion in Γ - Z direction. But it seems reasonable to define *antibonding* via the orbital character of the bands. Within this definition the antibonding band corresponds to the non-dispersing band just below -2 eV in Γ - Z direction.

bandstructure of La$_2$CuO$_4$
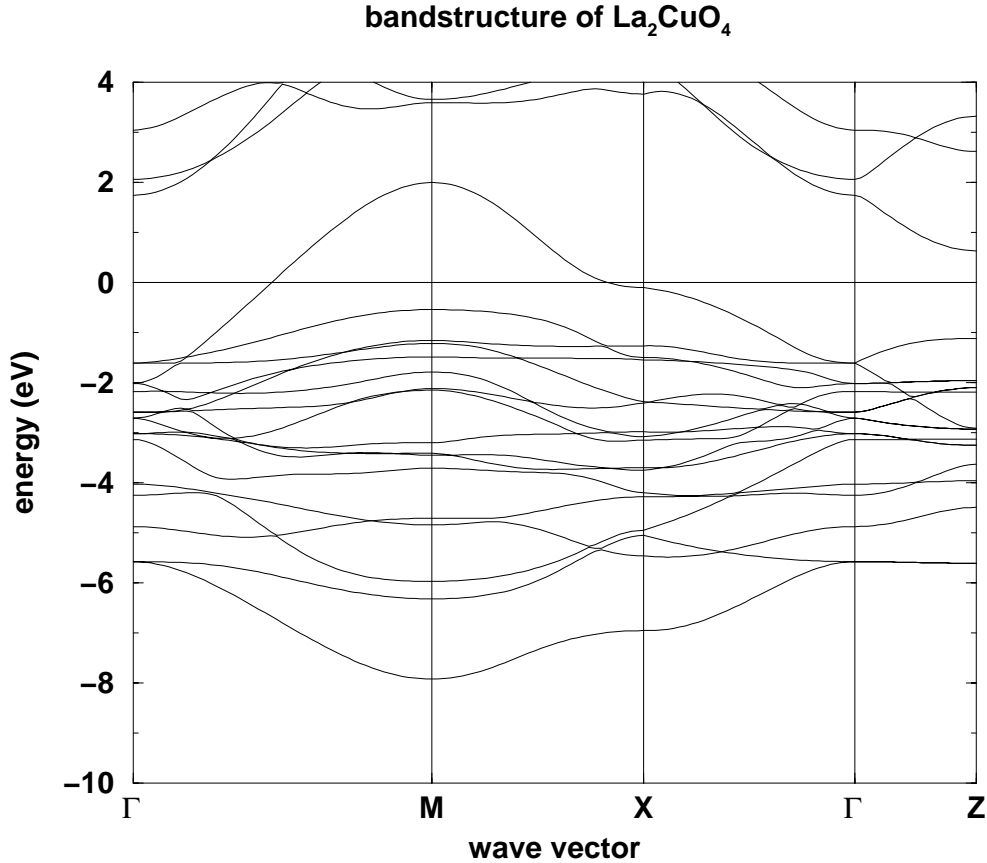
Figure 3.25: Band structure near the FERMI level for La$_2$CuO$_4$ along high-symmetry BRILLOUIN-zone directions. The notation of symmetry points is as follows: Γ=(000), X=(100), M=(110), Z=(001) in units of (π/a, π/a, π/c).

As an example for a doped cuprate compound, one of the HTSC shall be presented and discussed briefly. The high-T_c material investigated in most detail is YBa$_2$Cu$_3$O$_7$, which in our notation should be written YBa$_2$(CuO$_2$)$_2$(CuO$_3$). Its structure is shown in Fig. 3.23(b). It contains both CuO$_2$-planes and CuO$_3$-chains immersed in a lattice of barium and yttrium ions. By counting charges one finds that compared to nominal charges of those covalent cuprate structures one hole must be shared by two planes and one chain. Hence, the charge state of the planes and of the chains is [CuO$_2$]$^{-2+\delta}$ and [CuO$_3$]$^{-3-2\delta}$,respectively. This compound is, however, metallic[9], so the concept of formal valences itself is problematic[10].

---

[9]The antiferromagnetic insulator in the systematics of this chapter is YBa$_2$Cu$_3$O$_6$.

[10]Formal valences are integral quantities, their sum over the unit cell must vanish. They are not measurable quantities. In ionic compounds, formal valences are very useful for classification

density of states of YBa$_2$Cu$_3$O$_7$
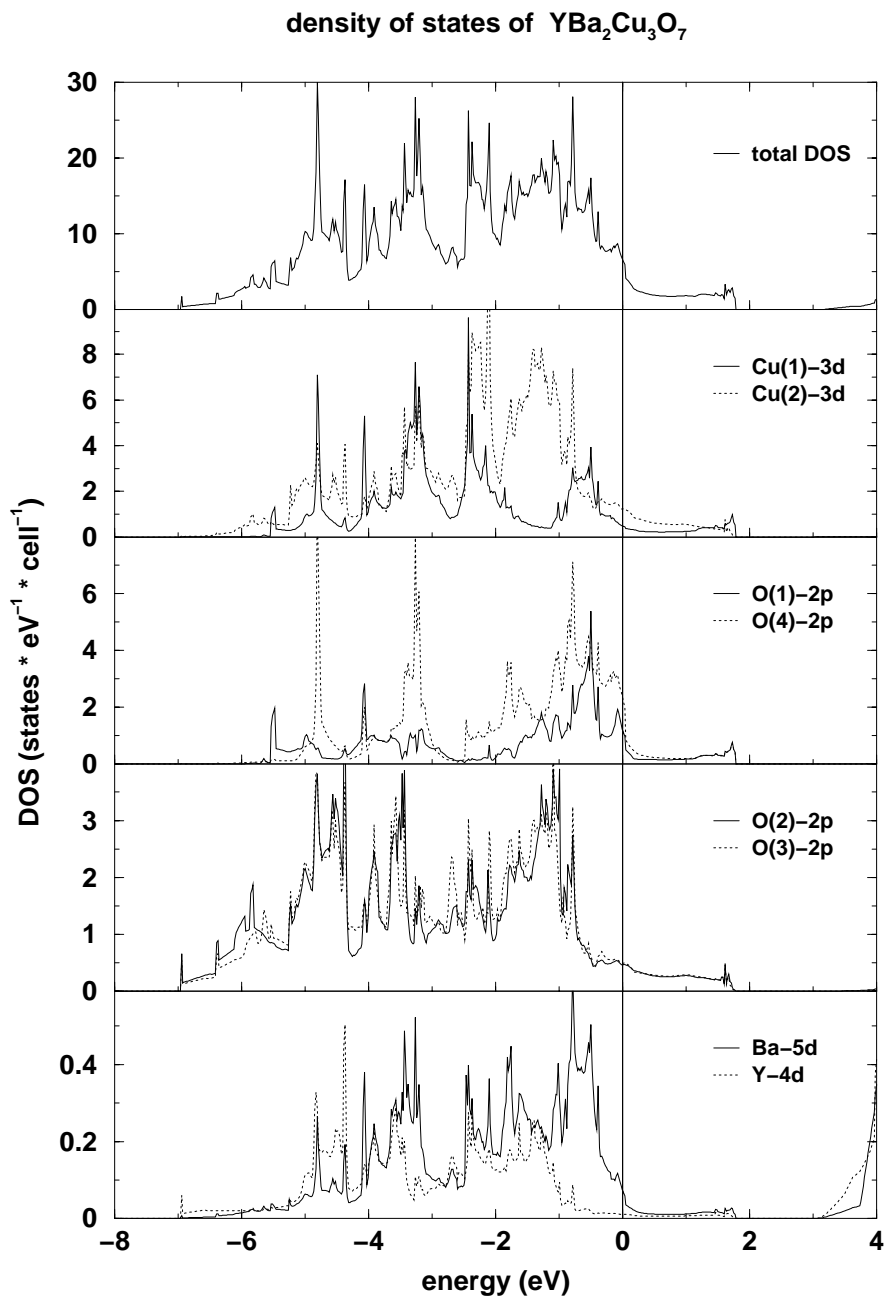
Figure 3.26: Total and partial DOS of YBa$_2$Cu$_3$O$_7$. The FERMI level is at zero energy. The contribution of Cu-4s states is less than 1% in the shown region.

and are widely used in chemical and physical models. In metallic materials, this concept looses rapidly its meaning because the assignment of charge to particular atoms becomes arbitrary.
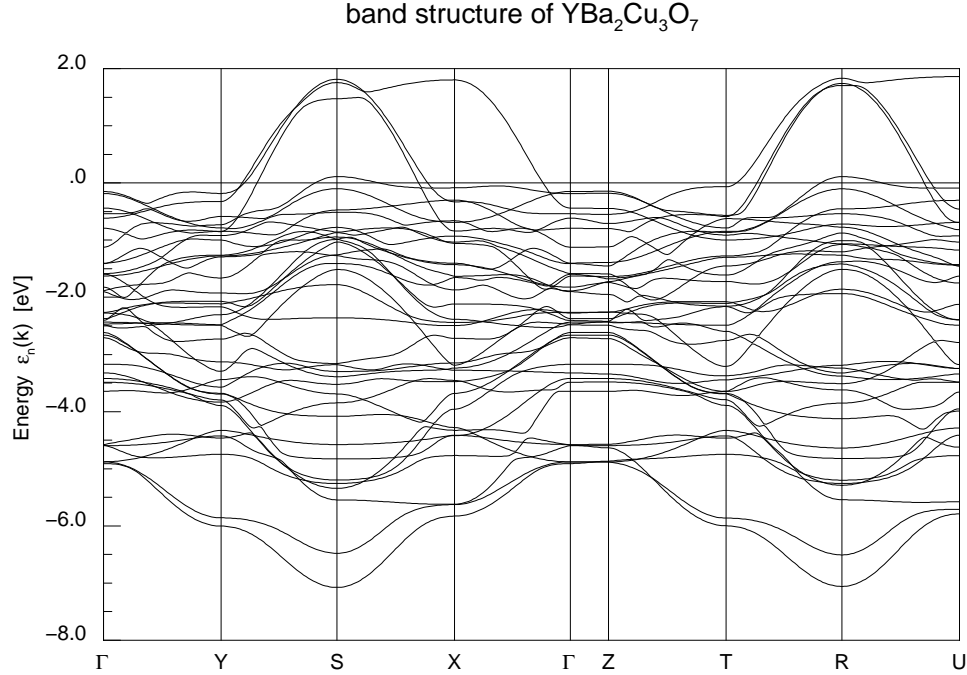
Figure 3.27: Band structure near the FERMI level for $YBa_2Cu_3O_7$ along high-symmetry BRILLOUIN-zone directions. The notation of symmetry points is as follows: $\Gamma=(000)$, X=(100), Y=(010), S=(110), Z=(001), T=(011), U=(101) and R=(111) in units of $(\pi/a,\ \pi/b,\ \pi/c)$.

$YBa_2Cu_3O_7$ has a transition temperature $T_c \approx 93$ K [84], however, it shows also short-range antiferromagnetic spin fluctuations [85]. It is generally accepted, that spin fluctuations can mediate attractive pairing-interactions and are involved in the superconducting state of high-T_c materials [86, 87]. This fact underlines that an advanced knowledge of the magnetic interactions in cuprate chains and planes is a prerequisite for the understanding of the pairing-mechanism in HTSC.

$YBa_2Cu_3O_7$ occurs in the simple orthorhombic space group Pmmm with the lattice constants $a = 3.9195$ Å, $b = 3.8591$ Å and $c = 13.15$ Å (see Fig. 3.23(b)) [88]. Corresponding to the presence of CuO_2-planes and CuO_3-chains, the crystal shows two inequivalent Cu-sites and four inequivalent O-sites. The CuO_2-planes, formed by Cu(2), O(2) and O(3), are slightly buckled due to lattice distortions. The chains consist of Cu(1), O(1) and O(4), the plaquettes are slightly racked in chain direction.

We performed FPLO band structure calculations with a minimum basis set consisting of Cu ($4s$, $4p$, $3d$), O ($2s$, $2p$, $3d$), Y ($4s$, $4p$, $5s$, $5p$, $5d$) and Ba ($5s$, $5p$, $5d$, $6s$, $6p$) states. Due to the large extension of the Y ($4s$, $4p$) and Ba ($5s$,

$5p$) wave functions it was necessary to treat them as valence states (see 2.2.1). For the exchange and correlation potential the parameterization of PERDEW and ZUNGER was chosen.

The results of our calculation agree well with those of other authors (for example see Refs. [89, 90, 91, 92]), but there are noticeable differences in a few details, especially for the shape of the FERMI-surface. Due to the lack of detailed information on the computations in most publications, the origin of the differences remains unclear. It is to mention, however, that the intrinsic charge transfer in this material may particularly call for a full potential treatment as FPLO.

The total DOS as well as the partial DOS of $YBa_2Cu_3O_7$ are shown in Fig. 3.26. The valence band is built of mainly Cu-$3d$ and O-$2p$ states with a small admixture of Y-$4d$ and Ba-$5d$ states. The O(2) and O(3) contributions to the valence band are nearly identical, showing that the influence of the orthorhombicity due to the CuO_3-chain on the electronic structure of the CuO_2-layer is rather small. The energies of the main features of chain-derived (Cu(1), O(1) and O(4)) and plane-derived (Cu(2), O(2) and O(3)) states are quite different. Thus, planes and chains in $YBa_2Cu_3O_7$ are relatively separated from each other in the HILBERT-space. The states forming a peak just below the FERMI level, and related to the above mentioned differences in the topology of the FERMI-surface, are clearly chain-derived.

Figure 3.27 shows the band structure of $YBa_2Cu_3O_7$. Besides the three broad bands crossing the FERMI-level that are expected in these positions according to all previous considerations, one additional band is found crossing the FERMI-level. Using the wavefunctions, it is possible to characterize the origin of the bands. The two broad bands with the maximum on the S-point consist of nearly pure CuO_2-plane states. The band with the large dispersion in Γ–X direction and the 'unexpected' band are built almost exclusively of chain states. The unexpected band causes the most important qualitative differences between different published calculations. We find it crossing the FERMI-level near the S and the R point. This leads to only a small hole pocket surface from this band in agreement with Refs. [90, 92], whereas other calculations [93, 89] find a more complicated FERMI-surface.

Because most high T_c cuprates have antiferromagnetic parent compounds that LDA does not describe well due to the strong correlations, its application to the metallic phase also has been considered with suspicion. Nevertheless, LDA band structure calculations yielded not only reasonable, but in fact very accurate results predicting a number of properties of metallic cuprates [94], such as lattice constants and atomic positions, phonon frequencies [95] and electric field gradients [96].

Angle-resolved photoemission spectroscopy (ARPES) [97, 98, 99] and DE HAAS-

VAN ALPHEN (dHvA) [100, 101] experiments were able to measure parts of the FERMI-surface of $YBa_2Cu_3O_7$. The results widely coincide with the predictions of bandstructure calculations [92, 94]. The existence of the hole pocket near the S and the R point is still under debate. Recent ARPES measurements [98, 99] could not confirm the existence of these hole pockets concluded from dHvA-data [100, 101]. This could be due to the influence of the surface.

Up to now, for the undoped standard planar cuprates, it was not possible to use ARPES for a measurement of the lowest lying excitations, because the surface quality after cleaving the crystals was not sufficient. If the apical oxygen is exchanged with an halogen atom in the La_2CuO_4 structure (for reasons of valence, the La-atom has to be replaced by a divalent atom like Sr or Ca simultaneously), the experimental situation is much more favorable. The samples can be cleaved with high-quality surfaces and the absence of the apical oxygen makes the analysis and the characterization of the measured spectra simpler.

The first undoped cuprate compound, where the dispersion of a single hole induced by photoemission was observed, is $Sr_2CuO_2Cl_2$ [102]. These lowest electron removal state can be interpreted in terms of ZHANG-RICE singlets [103]. $Sr_2CuO_2Cl_2$ is a quasi two-dimensional (2D) antiferromagnetic insulator with a NÉEL temperature [104] of 256 K, whose magnetic structure is well described by the 2D spin 1/2 HEISENBERG-model. Altogether, $Sr_2CuO_2Cl_2$ can be considered as an ideal model compound to answer many questions concerning the electronic structure of cuprate superconductors in the dialogue of experiment and theory.

The crystal structure of $Sr_2CuO_2Cl_2$ is shown in Fig. 3.28. $Sr_2CuO_2Cl_2$ is isostructural to La_2CuO_4 and exhibits a body-centered tetragonal structure (space group I4/mmm) with the lattice constants a= 3.975 Å and c= 15.618 Å [105, 106]. The Cu-O distance in the plane is with 1.99 Å somewhat larger than in La_2CuO_4. The Cu-Cl_{apex} distance in $Sr_2CuO_2Cl_2$ (2.96 Å) is significantly larger than the Cu-O_{apex} distance in La_2CuO_4 (2.42 Å). This is the structural reason for the model character of the system: the influence of the out-of-plane ions on the CuO_2-plane is considerably reduced.

LCAO band structure calculations were performed with a minimum basis set consisting of Cu ($4s$, $4p$, $3d$), O ($2s$, $2p$, $3d$), Sr ($5s$, $5p$,$4d$) and Cl ($3s$, $3p$) states. To cope with the relatively open crystal structure, two empty spheres per unit cell have been introduced with empty sphere s and p orbitals at each site. For the exchange and correlation potential the parameterization of VON BARTH and HEDIN was chosen.

The total DOS as well as the partial DOS and the band structure of $Sr_2CuO_2Cl_2$ are drawn in Figs. 3.29 and 3.30. As expected from our previous discussions, the LDA calculation for this undoped compound yields a metallic groundstate instead of the experimentally observed insulating behavior. The DOS is similar to that of
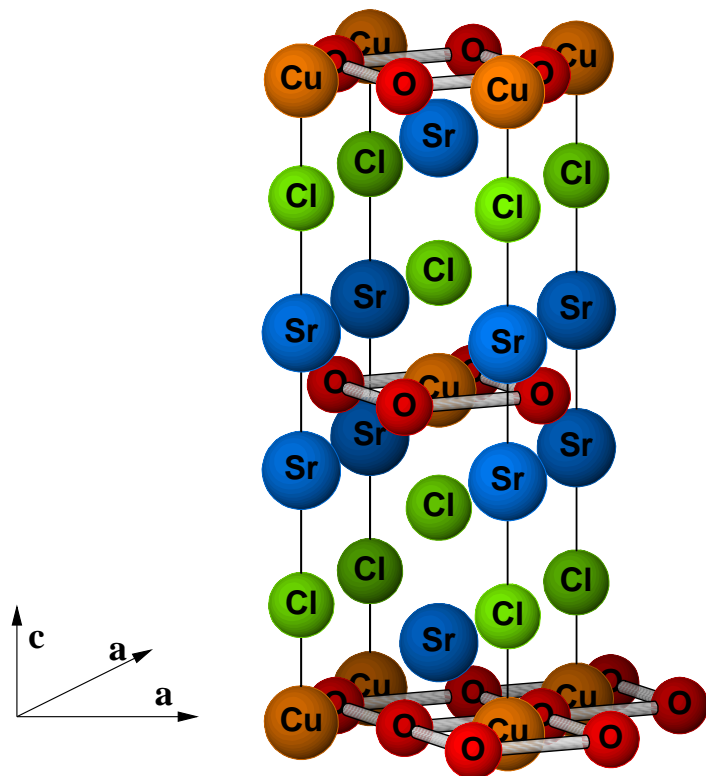
Figure 3.28: The body-centered tetragonal unit cell of $Sr_2CuO_2Cl_2$.

the parent compound La_2CuO_4 (cf. Fig. 3.24), especially the partial DOS of Cu and O (with O(1) in La_2CuO_4), whereas the width of the pd-complex is reduced by about half of an eV. The admixture of non-plane atoms to the antibonding band is considerably reduced, the chlorine states are shifted down in energy by about 2 eV compared with the apical oxygen in La_2CuO_4.

The close relation between La_2CuO_4 and $Sr_2CuO_2Cl_2$ is most visible in the very similar bandwidth and dispersion of the antibonding bands for both compounds (cf. Figs. 3.25 and 3.30). In $Sr_2CuO_2Cl_2$, this band is more separated from the rest of the pd complex due to the already discussed downwards shift in energy of the chlorine states.

A detailed study of the valence band of $Sr_2CuO_2Cl_2$ in combination with ARPES measurements is given in Section 5.3.

3.4.2   Planar cuprates with a Cu_3O_4-plane

A modification of the standard CuO_2-plane, which is shown in Fig. 3.21, is obtained by putting an additional copper atom in the center of every second plaquette. This leads to a Cu_3O_4-plane with two inequivalent copper sites. This
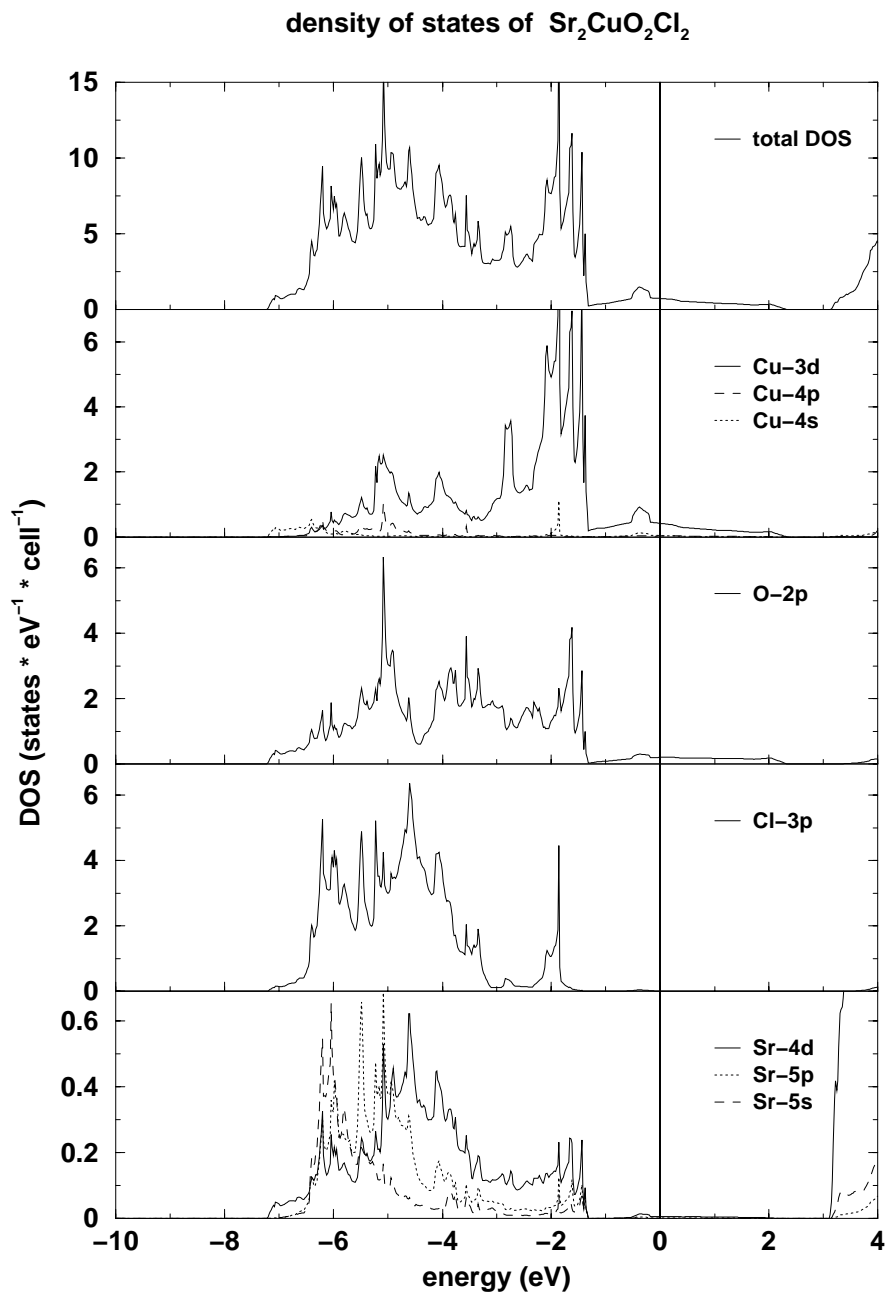
Figure 3.29: Total and partial DOS of $Sr_2CuO_2Cl_2$. The FERMI level is at zero energy. The contribution of O-2s and Cl-3s states is less than 0.1% in the region shown.

kind of plane is found in $Sr_2Cu_3O_4Cl_2$ [107] and the isostructural $Ba_2Cu_3O_4Cl_2$. $Ba_2Cu_3O_4Cl_2$ occurs in body-centered tetragonal structure in the space group

band structure of Sr$_2$CuO$_2$Cl$_2$
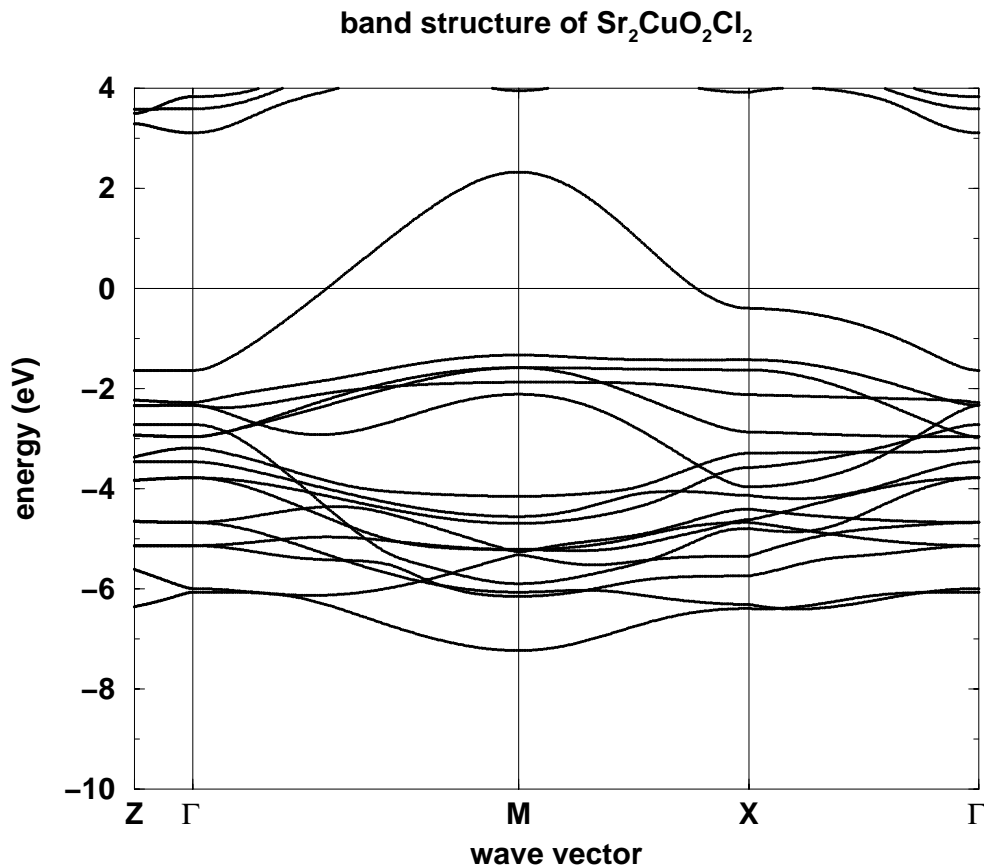
Figure 3.30: Band structure near the FERMI level for Sr$_2$CuO$_2$Cl$_2$ along high-symmetry BRILLOUIN-zone directions. The notation of symmetry points is as follows: Γ=(000), X=(100), M=(110), Z=(001) in units of (π/a, π/a, π/c).

I4/mmm with the lattice constants $a = 5.51$ Å and $c = 13.82$ Å [108, 109]. The Cu-O distance in the plane is 1.96 Å and slightly larger than in La$_2$CuO$_4$.

Experimentally, two NÉEL temperatures have been found, $T_N^A \sim 330$ K and $T_N^B \sim 31$ K [110, 111], connected with the two sublattices of A- and B-copper. The magnetic susceptibility and the small ferromagnetic moment have been explained phenomenologically [112] together with a determination of the exchange integrals. Like in undoped Sr$_2$CuO$_2$Cl$_2$ [102], the lowest electron removal states in Ba$_2$Cu$_3$O$_4$Cl$_2$ can be interpreted in terms of ZHANG-RICE singlets [103] with a new branch of singlet excitations connected with the B-sublattice [113] (see Section 5.2).

The self-consistent LDA-LCAO method has been applied to Ba$_2$Cu$_3$O$_4$Cl$_2$ in the scalar relativistic version with a minimum basis treating the Cu-($4s, 4p, 3d$),
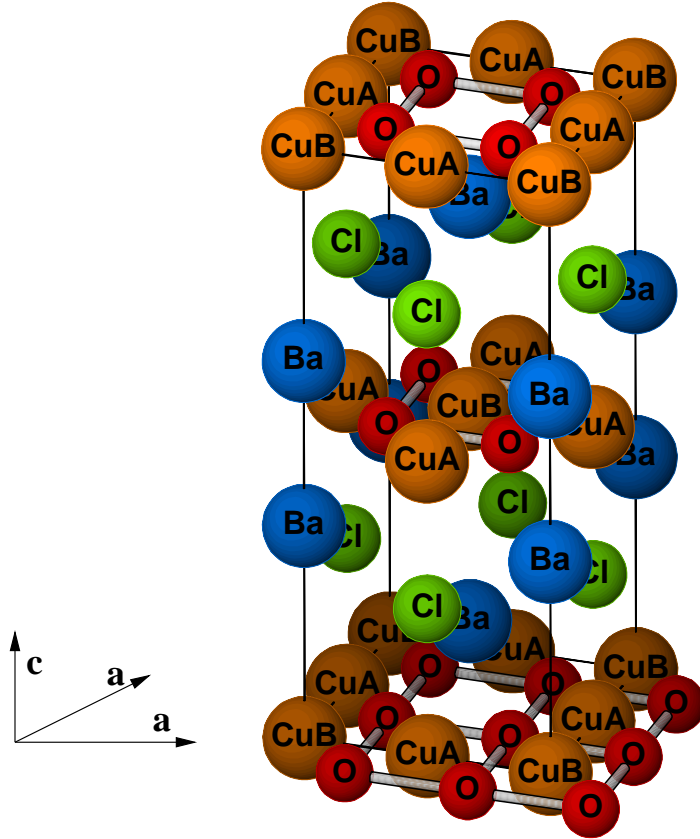
Figure 3.31: The body-centered tetragonal unit cell of $Ba_2Cu_3O_4Cl_2$.

O-$(2s, 2p)$, Sr-$(5s, 5p, 4d)$ and Cl-$(3s, 3p)$ orbitals as local valence basis states and the lower orbitals as core states. To treat this relatively open crystal structure, four empty spheres per unit cell have been introduced with empty sphere s and p orbitals at each site. For the exchange and correlation potential the parameterization of VON BARTH and HEDIN was chosen.

The calculation results in a paramagnetic and metallic behavior with two bands crossing the FERMI-level and a third band just below. The total and the partial DOS as well as the bandstructure of $Ba_2Cu_3O_4Cl_2$ are shown in Fig. 3.32 and Fig. 3.33, respectively.

The bands crossing the FERMI-level have no dispersion in z-direction . That means that the corresponding bonds lie in the x-y-plane. From the partial DOS it can be seen which states contribute to these bands (see Fig. 3.32). The two broad bands are essentially formed by a Cu_A3d-O2p-hybridization, whereas the small band is built by Cu_B3d-O2p-hybridization. Ba and Cl do not contribute to the states near the FERMI-level.

It might be expected that the additional Cu_B atoms give rise to consider-
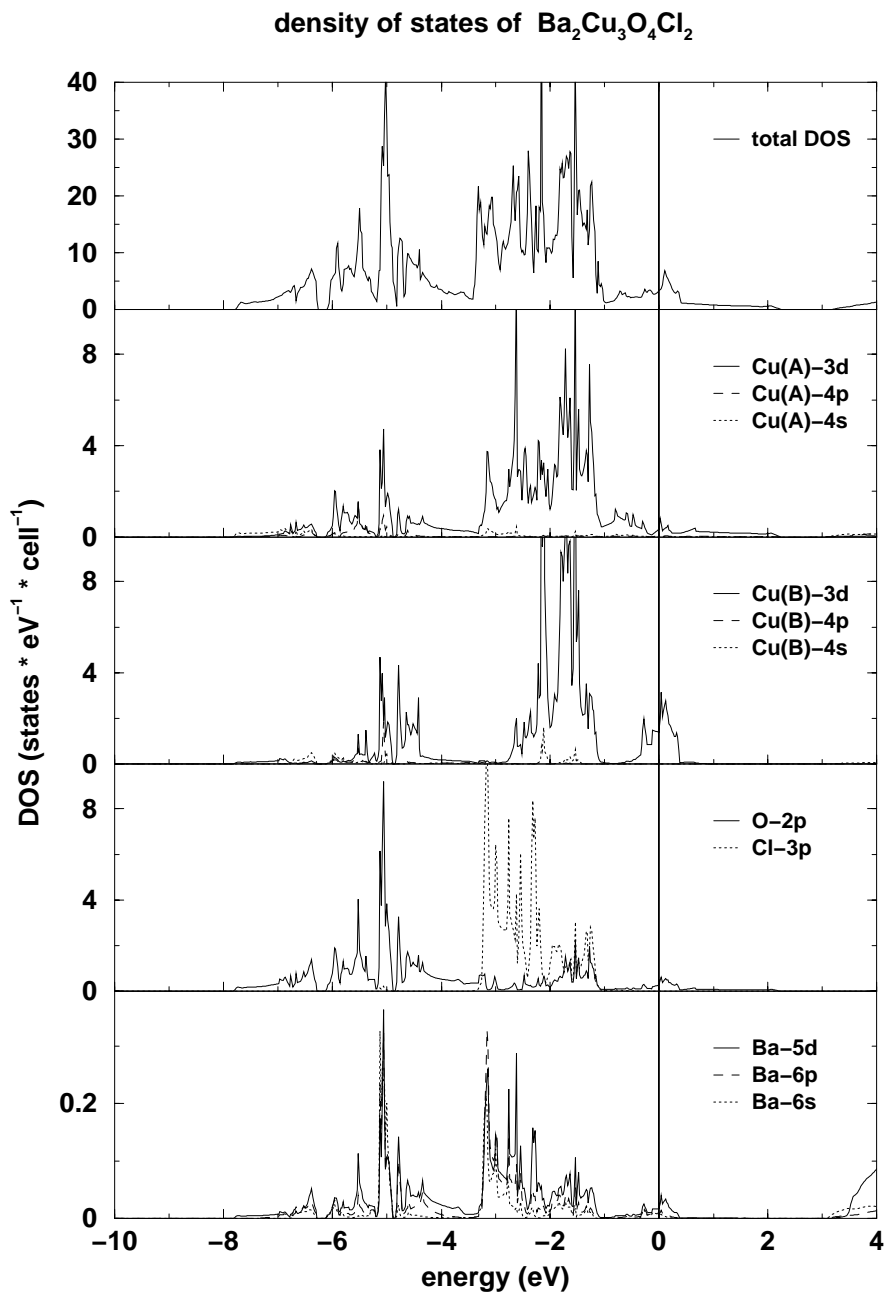
Figure 3.32: Total and partial DOS of $Ba_2Cu_3O_4Cl_2$. The Fermi level is at zero energy. The contribution of O-2s and Cl-3s states is less than 0.1% in the region shown.

able differences in the electronic structure in comparison with the usual CuO_2 plane. In particular, the amount of coupling between both subsystems seems to

band structure of Ba$_2$Cu$_3$O$_4$Cl$_2$
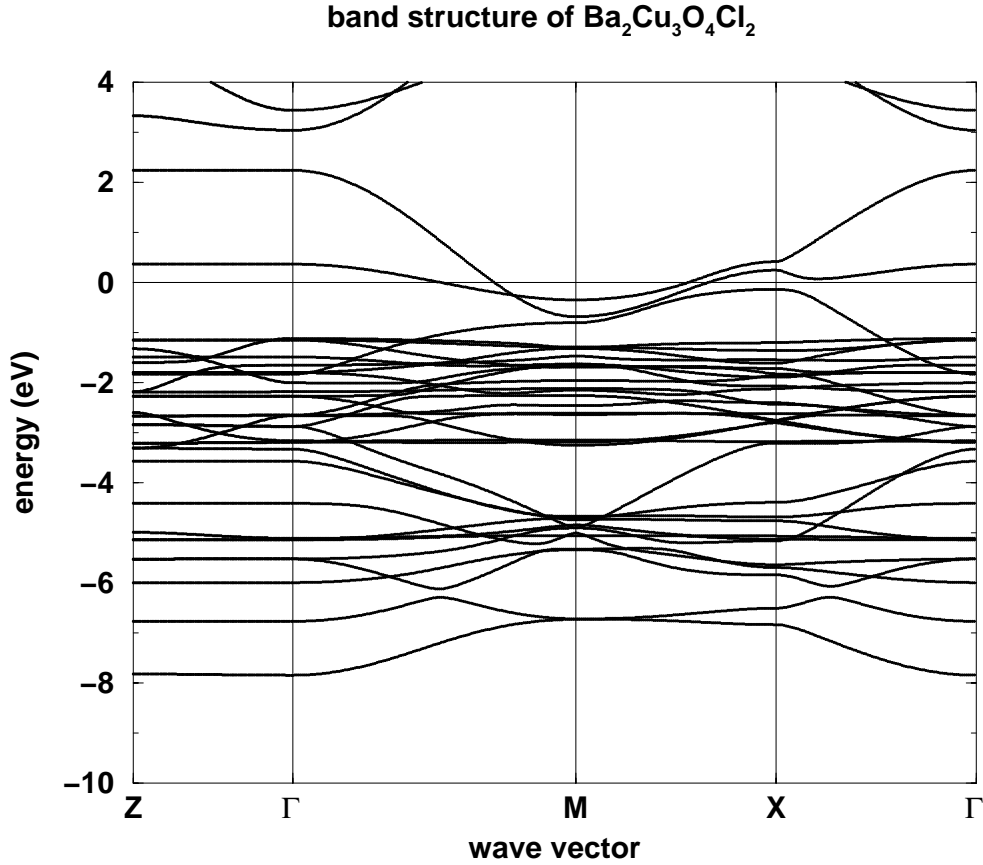
Figure 3.33: Band structure near the Fermi level for Ba$_2$Cu$_3$O$_4$Cl$_2$ along high-symmetry Brillouin-zone directions. The notation of symmetry points is as follows: Γ=(000), X=(100), M=(110), Z=(001) in units of $(\pi/a, \pi/a, \pi/c)$.

be crucial. Analyzing the orbital weight of the antibonding bands, we find two nearly decoupled subsystems, belonging to Cu$_A$ and Cu$_B$. The reason is that the two Cu atoms hybridize with linear combinations of O-2p_x and O-2p_y, which are orthogonal to each other. Due to the ideal 90° angle between Cu$_A$-O and Cu$_B$-O bonds, the coupling of the two subsystems takes place only via a small transfer-interaction between oxygen orbitals at different sites.

Keeping in mind the nearly decoupled behavior of both subsystems, it is easy to find that the two broad bands, stemming from the Cu$_A$-subsystem, are very similar to the bands which one gets by folding the bands of La$_2$CuO$_4$ or Sr$_2$CuO$_2$Cl$_2$ with respect to the half as large Brillouin-zone of Ba$_2$Cu$_3$O$_4$Cl$_2$. This shows that the physics of the Cu$_A$-subsystem is close to the standard CuO$_2$-plane. Considering the bandwidth of the Cu$_B$-derived antibonding band, we find

a strong reduction by a factor of about five compared with the CuO_2-plane. Thus, also the antiferromagnetic superexchange should be strongly reduced. These facts provide a first qualitative explanation of the two strongly different NÉEL temperatures of both subsystems.

A detailed analysis of the valence band of $Ba_2Cu_3O_4Cl_2$ in terms of an 11-band tight-binding model and the calculation of the exchange-integrals within an extended HUBBARD model is given in Section 4.3.1.

Chapter 4

Model description of cuprate compounds

4.1 Electronic structure and magnetic properties of the linear chain cuprates Sr_2CuO_3 and Ca_2CuO_3

Sr_2CuO_3 and Ca_2CuO_3 are considered to be the best appropriated model systems of strongly anisotropic, spin-1/2 Heisenberg antiferromagnets. In the following, on the basis of a band-structure analysis within the local density approximation (see Sec. 3.3.1) and on the basis of available experimental data a careful analysis of model parameters for extended Hubbard model (EHM) and for the Heisenberg models is given. Using the band-structure and experimental data we parameterize a one-band extended Hubbard model for both materials which can be further mapped onto an anisotropic Heisenberg model (AHM).

Comparing several approaches to anisotropic Heisenberg problems, namely the random-phase spin-wave approximation and modern versions of coupled quantum spin chains approaches, the advantage of the latter in the reproduction of reasonable values for the Néel temperature T_N and the magnetization m_0 at zero temperature is demonstrated. In a comparative study the compound $CuGeO_3$ will be included as well.

4.1.1 Tight-binding parameterization

The metallic behavior of the LDA band-structure, discussed in Section 3.3.1 (see Figs. 3.8, 4.1) is in sharp contrast to the experimental observation of large optical gaps ~ 2 eV. This points to the necessity of dealing explicitly with the strong on-site Coulomb repulsion at the copper-site. The experimental gap cannot be explained by a spin-density wave since it is large and persists also above the Néel temperature T_N. Instead it should be interpreted as a charge transfer gap between valence states of mostly oxygen character and a copper upper Hubbard band above the Fermi level.

antibonding band of Sr$_2$CuO$_3$
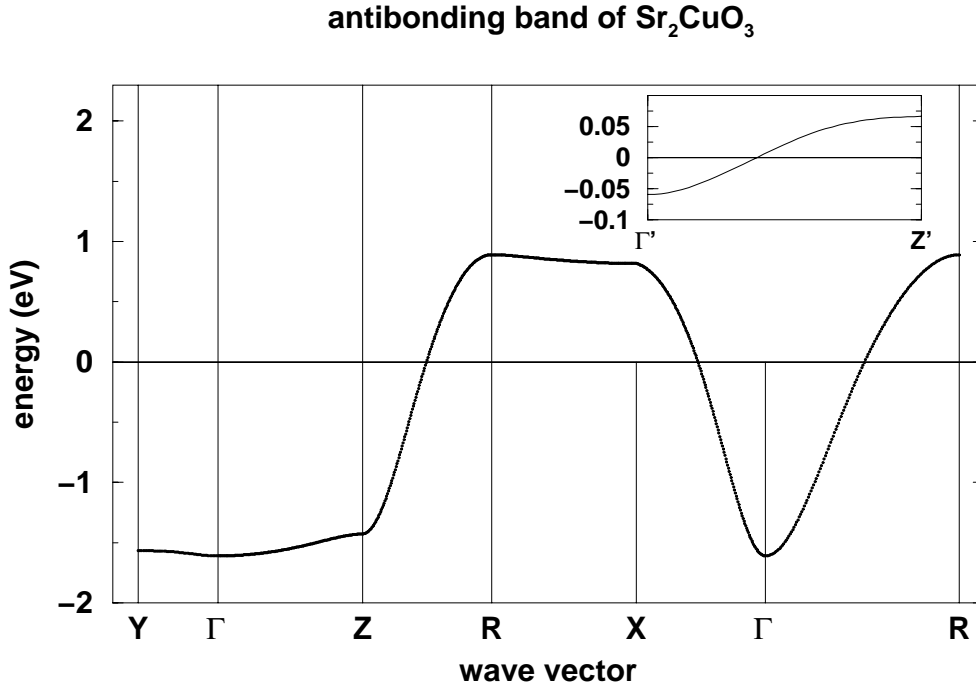
Figure 4.1: Dispersion of the nearly one-dimensional antibonding band of Sr$_2$CuO$_3$ along high-symmetry BRILLOUIN-zone directions. The notation of symmetry points is as follows: Γ=(000), X=(100), Y=(010), Z=(001), R=(101) in units of $(\pi/a, \pi/b, \pi/c)$. The inset is for fixed $k_z = k_{z\mathrm{Fermi}} = \pi/2c$.

Therefore, the construction of a multi-band, HUBBARD-like model Hamiltonian would be desirable. However, it is well known that such a Hamiltonian can be projected to an effective one-band picture which properly describes the low-energy physics [114, 115]. The existence of a well isolated, one-dimensional band in the present situation, shown in Fig. 4.1 in more detail, suggests such a possibility all the more. It is assumed that the parameters for the one band description in first approximation can be determined by fitting the band of Fig. 4.1 to a dispersion of the form

$$\varepsilon(\vec{k}) = -2t_{1,LDA}\cos(k_y a) - 2t_{2,LDA}\cos(2k_y a) - 2t_\perp \cos k_x c \qquad (4.1)$$

which yields the values listed in the Table 4.1[1].

---

[1]Strictly speaking, the fit of the dispersion along the **c**-direction requires more FOURIER-components. However, their individual weight is small with respect to the interchain exchange. It can be expected that within a proper treatment of the local electron correlation the influence of far-reaching hopping integrals should be reduced.

In Fig. 4.1 the dispersion in the **c**-direction is clearly visible as an energy increase with increasing k_z by nearly the same amount both at the bottom and the top of the band. This dispersion is present through the band and gives a value of $t_\perp = 30$ meV. To be more accurate, $t_\perp$ is determined from the dispersion at the FERMI level which is shown in the insert of Fig. 4.1. The corresponding dispersion for Ca$_2$CuO$_3$ is significantly larger by a factor of 2.5. The smaller lattice constant of Ca$_2$CuO$_3$ leads to an increase of the inter-chain overlap of the Cu-3d and O-2p orbitals, but this effect alone is too small to explain the strong enhancement.

The inspection of the SLATER-KOSTER integrals shows that the transfer in **c**-direction goes dominantly via the cation Sr and Ca, respectively. The two-center HAMILTON matrix elements between side oxygen O(2) and Ca are two times larger than the corresponding ones for Sr.

In the same manner (Eq. (4.1)) the energy bands for CuGeO$_3$ (see Fig. 3.14) were analyzed. The CuO$_2$-chains of edge-sharing CuO$_4$-plaquettes in CuGeO$_3$ result in a more complex highest antibonding band. There are two O-2p states per site involved, this results in two antibonding bands per chain. Because of the crystal-field they are different in energy (see Sec. 3.3.2) The sizable inter-chain interaction mediated by Ge and O(1) (see Fig. 3.12) and the presence of two chains per unit cell leads to two antibonding bands at FERMI level (see Fig. 3.14). For the qualitative comparison with the above considered CuO$_3$-chain, they were replaced by one half-filled band for the sake of simplicity. The tight-binding parameters of CuGeO$_3$ (see Tab. 4.1) contain a significantly smaller nearest neighbor transfer integral $t_{1,LDA} \approx 0.2$ eV and an anomalously large next nearest neighbor integral $t_{2,LDA} \approx t_{1,LDA}/2 = 0.1$ eV. The large difference of the transfer integrals $t_{1,LDA}$ between chains of corner-sharing plaquettes and CuGeO$_3$ should be related to the efficient 180° Cu-O-Cu hopping for the former (σ-pd bond) compared with the inefficient non-σ-pd hopping (about 140°)[2] for CuGeO$_3$; for further details see Ref. [74]. This special structure explains also the relative large next nearest neighbor transfer integrals t_2 in CuGeO$_3$ due to the involved effective σ p_z-p_z hopping along the chain. The inter-chain hopping $t_\perp$ can be deduced from the dispersion in the **b**-direction of the antibonding bands of CuGeO$_3$ (see Fig. 3.14) and is of the same order as in Sr$_2$CuO$_3$ and Ca$_2$CuO$_3$.

Based on both the available experimental data and the band structure information obtained here, a semi-microscopic strong correlation model will be constructed which then can be mapped approximately onto a spin-1/2 Hamiltonian to describe the magnetic properties. This is the objective of the next section.

---

[2]The angle is measured between the antibonding Ge-3d orbital lying in the plaquette-plane and the O-2p_z in chain direction.

4.1.2   Microscopic description in terms of the extended HUBBARD *and anisotropic*
       HEISENBERG *models*

General relations

We parameterize the well-known extended HUBBARD model (EHM) for one single
chain with hopping terms to first (t_1) and second neighbors (t_2):

$$
\begin{aligned}
H \;=\; & -\sum_{m;j=1,2;s} t_j \left(c^\dagger_{m,s} c_{m+j,s} + h.c. \right) + \frac{U}{2} \sum_{m;s} c^\dagger_{m,s} c_{m,s} c^\dagger_{m,-s} c_{m,-s} \\
& + \sum_{m;j=1,2} V_j n_m n_{m+j} - \mid K \mid \sum_i \vec{S}_i \vec{S}_{i+1} ,
\end{aligned}
\tag{4.2}
$$

where $n_m = \sum_s c^\dagger_{m,s} c_{m,s}$ is the density operator and s denotes the spin index. In
Eq. (4.2), a small, but non-negligible direct ferromagnetic exchange is included,
which naturally appears if we map a multi-band, HUBBARD-like Hamiltonian
including spin-flip terms to a one band model [114]. Its necessity and its main
effects will be discussed below.

   For the low-energy physics, at half-filling, the EHM (Eq. (4.2)) can be replaced
to leading order in t/U by a spin-1/2 HEISENBERG chain. It includes also a second
neighbor exchange J_2 [116] and reads

$$
\begin{aligned}
H &= J_1 \sum_i \vec{S}_i \vec{S}_{i+1} + J_2 \sum_i \vec{S}_i \vec{S}_{i+2} \;, \\
J_1^{AF} &= \frac{4t_1^2}{U - V_1} \;, \qquad J_2 = \frac{4t_2^2}{U - V_2} \;,
\end{aligned}
\tag{4.3}
$$

where the effective exchange integral J_1 of the spin-1/2 HEISENBERG Hamiltonian
of cuprates is reduced from the predominant antiferromagnetic superexchange
part by the ferromagnetic contribution (Eq. (4.2))

$$
J_1 \approx J_1^{AF} - |K| \,.
\tag{4.4}
$$

It is to notice that within this approach J_2 yields a competitional (frustrated)
character to the usually dominant short range antiferromagnetic correlations,
which are established by J_1. That term is especially important for $CuGeO_3$.

   The two main parameters U and t_1 of the effective extended HUBBARD model
are directly related to the optical gap E_g and the exchange integral between near-
est neighbors J_1, which are experimentally accessible. The following analysis is
considerably simplified within the strongly correlated limit $U > 4t$, and excitonic
effects at zero momentum transfer q are not very strong, i.e. $U \gg t_j > \quad V_j$

$(j = 1, 2)^3$. The parameter sets derived below support such a point of view. We take into account the effect of the intersite COULOMB interaction V_1 by renormalizing the on-site correlation in the form $U_{eff} = U - V_1$. Then we may use the optical gap E_g obtained from the BETHE-ansatz solution for the pure 1D HUBBARD model given by OVCHINNIKOV [118],

$$
\begin{aligned}
E_g &= \frac{16t_1^2}{U_{eff}} \int\limits_1^\infty \frac{\sqrt{x^2 - 1}\,dx}{\sinh(2\pi t_1 x/U_{eff})} \\
&\approx U_{eff} - 4t_1 + 2\ln2 J_1^{AF} \quad \text{for} \quad U_{eff} \gg t_1; \quad J_1^{AF} = 4t_1^2/U_{eff}.
\end{aligned}
\tag{4.5}
$$

In the strong-coupling case Eq. (4.5) can be transformed to the useful relation

$$
t_1 = 0.5 J_1^{AF} \left(1 + \sqrt{E_g/J_1^{AF} + 1 - 2\ln2} \right).
\tag{4.6}
$$

It has been assumed that the smaller parameters t_2 and $|K|$, i.e. the hopping to second neighbors and the ferromagnetic exchange in (4.2), have no substantial influence on the charge transfer gap (t_2 enhances the spin gap in the spin-PEIERLS state).

The presence of a weak second-neighbor exchange can be approximately described in some cases by an effective renormalized nearest neighbor exchange integral [119, 120]

$$
J = J_1 - rJ_2 \approx J_1 - J_2,
\tag{4.7}
$$

where $r = 1$ according to Ref. [119] and $r = 1.12$ according to Ref. [120]. Recently, STEPHAN and PENC [121] predicted a strong narrow excitonic peak in the density-density response function $N(q, \omega)$ of the EHM in the strong coupling limit at the zone boundary $q = \pi/b$:

$$
\omega_{ex}(\pi/b) = U - V_1,
\tag{4.8}
$$

provided $V_1 > 0$.

Parameter assignment

In principle, U_{eff} and t_1 can be determined from the experimentally measured E_g and J values using Eqs. (4.4–4.7) which are presented graphically in Fig. 4.2. In the case of Sr_2CuO_3, very recently also the narrow excitonic peak at the zone-boundary (Eq. (4.8)) and with it U_{eff} were determined experimentally [122]. However, to the best of our knowledge, the available experimental information

---

[3]From recent XAS measurements and related cluster calculations [117] we concluded, that V_j $(j = 1, 2)$ is somewhat larger as assumed here. Taking into account the enhanced value of V_j, some values calculated later in this section would change slightly, but the results do not change qualitatively.
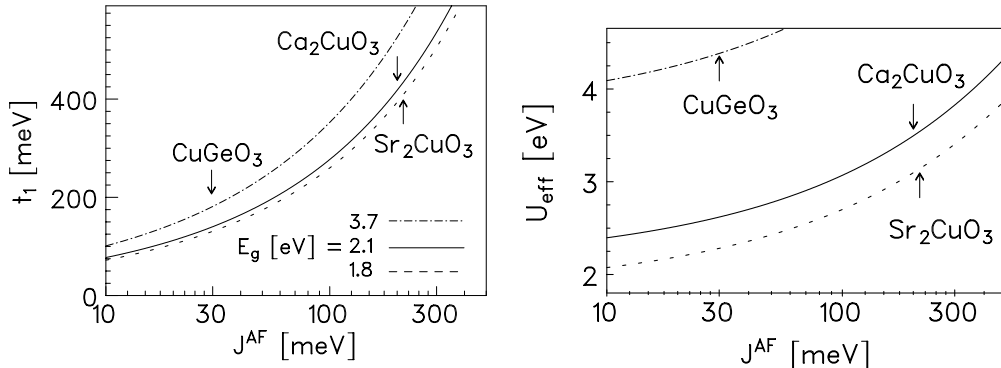
Figure 4.2: Dependence of the transfer integral t_1 (left panel) and the on-site COULOMB interaction U_{eff} (right panel) of the HUBBARD model according to its BETHE ansatz-solution *vs.* i-chain superexchange integral J_1^{AF} in the strong-coupling limit for typical values of the optical gap E_g. The experimental values for J_1^{AF} are depicted by arrows. They are determined from the total exchange integral J adopting ferromagnetic and second neighbor contributions discussed in the text.

on all three systems is incomplete or contradicting each other. For instance, for Ca_2CuO_3 the charge gap determined from the maximum of $\Im m(\varepsilon(\omega))$ is $E_g = 2.1$ eV [123], but a direct measurement of the J value from the magnetic susceptibility does not exist. Interpreting the midinfrared absorption as a phonon-assisted two-magnon process, a value of $J = 255$ meV was reported [124]. For Sr_2CuO_3 the experimental J values range from 140 to 260 meV [125, 44, 124]. In the following, 190 meV shall be used as a representative value. According to recent data for this system, the one-dimensional charge transfer gap $E_g(Sr) \approx 1.9 \pm 0.1$ [122] might be somewhat smaller as compared to the Ca-compound[4]. The elucidation of the observed broadening of the expected 1D VAN-HOVE singularity in terms of the inter-chain interaction, quantum fluctuations , disorder, or excitonic and other many-body effects is a difficult problem beyond the scope of the present discussion.

Taking this situation into account, the available experimental data and also our band-structure results are used to derive a consistent parameter set of Eq. (4.2) (t_1, t_2, U_{eff}, V_1 and $| K |$) for each of the three substances, separately. Vice versa, the demand of internal consistency weights the experimental information.

Sr_2CuO_3   Recent EELS data of NEUDERT *et al.* [122] allow to determine $U_{eff} = 3.15 \pm 0.1$ eV from the maximum of $\Im m(\varepsilon(\omega))$ at the zone boundary

---

[4]Strictly speaking, the optical absorption sets in already near 1.5 eV [126, 127, 122].

(Eq. 4.8). At the same time E_g was measured to be 1.9 ± 0.1 eV from the data at small momentum. Similarly $E_g = 1.92$ eV was found from the RAMAN resonance energy [128] observed for diagonal in-chain (yy) polarization only. The aim is to derive values for the magnetic coupling constants from Eqs. (4.4–4.7) using the experimental values of U_{eff} and E_g. Since it turned out that the derived J-values depend sensitively on U_{eff} and E_g, two sorts of extreme cases are to consider. From Eq. (4.5) we obtain $t_1 = 0.410$ eV with $U_{eff} = 3.15$ eV and $E_g = 1.8$ eV (lower bound). That corresponds to $J_1^{AF} = 213$ meV. According to Eqs. (4.4, 4.7), that value has to be reduced by the frustrated next nearest neighbor exchange J_2 of about 12 meV (corresponding to $t_2 = 100$ meV from our tight binding fit) and by the ferromagnetic contribution $|K|$ before it can be compared with the total experimental exchange integral $J = 190 \pm 17$ meV [44]. Thus we can estimate a direct ferromagnetic exchange of $|K| \approx 11 \pm 17$ meV. This K value is slightly smaller than the value of 35 meV for La_2CuO_4 obtained in Ref. [114], which might be attributed to the shorter Cu-O bond-length of 1.89 Å for the latter compound. The so-derived parameter set is listed in Table 4.1. A second parameter set is derived taking $E_g = 2$ eV and $U_{eff} = 3.25$ eV as the upper bounds of the experimental results. From Eq. (4.5), $t_1 = 0.394$ eV and correspondingly a considerable smaller value of $J_1^{AF} = 190$ meV are obtained. Such a parameterization is compatible with the total exchange integral 147^{+13}_{-9} meV [125] derived from the magnetic susceptibility data. It is to note, that both parameterizations are incompatible with the large J values of 246 meV [134] and 261 meV [124] derived from midinfrared optical absorption data[5]. Anyhow, the elucidation of the microscopic origin of the apparent discrepancy between the magnetic susceptibility and the midinfrared optical absorption data analyzed in terms of the simple nearest neighbor spin-1/2 HEISENBERG model remains a challenging problem.

Ca_2CuO_3 The slightly larger charge transfer gap of 2.1 eV suggests also an enhanced U_{eff}-value in comparison with the Sr-compound. That means that it is again difficult to find a reasonable parameterization which is compatible with the large J value of 254 meV from midinfrared absorption data. Due to the lack of experimental information on the magnetic susceptibility, in the following the theoretical estimate of 160 meV [115] for the J value of Ca_2CuO_3 will be used. Adding a ferromagnetic contribution of $|K| \approx 30$ meV (of the same order as

---

[5]We assume that there is no sizeable *ferromagnetic* second neighbor exchange overcompensating the ferromagnetic nearest neighbor contribution $|K|$ and the antiferromagnetic next nearest neighbor superexchange $J_2 = 4t_2^2/U_{eff}$. The small differences between both values arise mainly from the adopted phonon frequency of 70 and 80 meV, respectively, involved in the phonon-assisted absorption process.

for La_2CuO_4) and a frustrating $J_2 \approx 10$ meV, we may find $J_1^{AF} = 200$ meV as a rough estimate. Then, together with $E_g = 2.1$ eV, we calculate $t_1 = 418$ meV from Eq. (4.6). According to Eq. (4.5) that corresponds to $U_{eff} = 3.5$ eV, showing the expected enhancement. On the level of the *pd*-model the reason for the enhanced effective on-site interaction should be traced back to a larger $\Delta\varepsilon_{pd} \approx U_{eff}$. It seems to be related to a MADELUNG effect caused by the difference in the lattice parameters of the Sr- and the Ca-compound, respectively. This point of

group	quantity	Sr_2CuO_3	Ca_2CuO_3	$CuGeO_3$
I	$t_{1,LDA}$/meV	550	520	250
	$t_{2,LDA}$/meV	100	100	81
	$t_\perp$/meV	20 to 30	50 to 65	25 to 33
II	E_g/eV	$(1.8$ to $1.9)^{a,b}$	$(2.1)^c$	$(1.25)^d$, $(\underline{3.7})^e$
	$J_\parallel$/ meV	$(140)^f$, $(\underline{190})^g$, $(260)^h$	$(\underline{160})^i$ $(254)^h$	$(\underline{11} \pm 1)^j$, $(22)^k$
III	t_1/meV	410	419	187
	t_2/meV	100	100	90
	U_{eff}/eV	$(3.15)^b$	3.5	4.34 $(4.2)^e$
	V_1/eV	0.21	0.16	0.1
	$\mid K \mid$/meV	11	30	19
	$J_\perp$/meV	0.5 to 1.1	2.9 to 4.3	0.6 to 1, $(1.1)^l$
IV	T_N/K	$(5)^l$	$(8...10)^l$	$(4.5)^m$
	μ^{exp}/μ_B	$(0.06\pm0.01)^l$	$(0.09\pm0.01)^l$	$(0.23)^j$
V	μ^{CSC}/μ_B	0.08 to 0.11	0.19 to 0.24	0.35 to 0.45
	$J_\perp^{emp}$/meV	0.3 ± 0.1	0.6 ± 0.1	0.27

Table 4.1: Model parameters for Sr_2CuO_3, Ca_2CuO_3 and $CuGeO_3$. The LDA-LCAO-derived tight-binding parameters in the first group of rows are explained in Sec. 4.1.1. The second group contains experimental values (in the case of several data we prefer the underlined) which were used in addition to estimate the corresponding parameters of the EHM as well as the exchange integrals of the AHM (third group of rows) derived and discussed in Sec. 4.1.2. The experimental magnetic moment μ^{exp} and the NÉEL temperature T_N (group IV) may be compared with μ^{CSC} derived from Eq. (4.20) using the experimental data for $J_\parallel$ and our estimation of $J_\perp$. Vice versa, the experimental μ^{exp} determines via Eq. (4.20) the empirical inter-chain exchange integrals $J_\perp^{emp}$.
[a] RAMAN resonance [128], [b] EELS [122], [c] opt. absorption [123], [d] XPS [129], [e] XPS [130], [f] magn. suscept. [131, 125], [g] magn. suscept. [44], [h] midinfrared [124], [i] theory [115], [j] INS, RAMAN [61, 63, 64, 132, 120], [k] RAMAN [62], [l] μSR [4], [m] INS [133].

view is corroborated by the band-structure calculations discussed in Section 3.3.1 and in the previous section: for Ca_2CuO_3, the distance between the half-filled antibonding band and the filled bonding bands is larger by 0.7 eV compared to the corresponding distance for the Sr-compound.

Inter-site Coulomb repulsion and comparison with $CuGeO_3$ According to the microscopic calculations of GEERTSMA and KHOMSKI [74] the total nearest neighbor exchange integral of $CuGeO_3$ $J_1 = 11.6$ meV can be decomposed into an antiferromagnetic contribution of $J_1^{AF} = 30.4$ meV and into a relatively large ferromagnetic one of $|K| = 18.8$ meV. For $CuGeO_3$ charge transfer gaps of 3.66 eV [130] and 1.25 eV [129] have been reported[6]. Using the values $E_g = 3.7$ eV and $J_1^{AF} = 30.4$ meV in Eqs. (4.5) and (4.6), the main parameters of the extended HUBBARD model come out as $t_1 = 0.187$ eV and $U_{eff} = 4.34$ eV. Interestingly, the latter value nearly perfectly coincides with the charge transfer energy $\Delta = 4.2$ eV found out from the XPS data analyzed within the ANDERSON impurity model [130]. Within a *pd*-model the significantly enhanced corresponding $\Delta\varepsilon_{pd}$ value should be attributed to the Ge-cations located near the CuO_2-chain oxygens. This point of view is supported by the following observations: In compounds like $Sr_{14}Cu_{24}O_{41}$ where the considered CuO_2-chains are surrounded by earth alkaline cations, the corresponding charge gap is reduced to about 2.8 eV [135]. For that compound, $\Delta\varepsilon_{pd}$ as calculated within the ionic point charge model amounts to 3.7 eV [136].

Comparing the data collected in Table 4.1, we suggest that Ca_2CuO_3 should be somewhat stronger correlated than its Sr counterpart. Without doubt, the most strongly correlated compound among them all is $CuGeO_3$ having the smallest transfer integral $t_1(Ge) = 0.187$ eV and the largest $U_{eff}(Ge) = 4.34$ eV. The large ratios U_{eff}/t_1 obtained in all three cases (7.7(Sr), 8.4(Ca), and 23(Ge)) justify *a posteriori* the use of Eq. (4.5).

The difference between t_1 and $t_{1,LDA}$ may be explained by a renormalization of the transfer integral t_1 by the inter-site COULOMB interaction V_1. Within the HARTREE-FOCK approximation, the correction due to V_1 leads to a renormalized effective hopping integral $t_1 + pV_1$ with the bond order $p \sim 2/\pi$. This renormalized hopping integral can be compared with $t_{1,LDA}$, where the inter-site COULOMB interaction is already partially taken into account. From $t_{1,LDA} = t_1 + pV_1$ and the data of t_1 and $t_{1,LDA}$ given in Table 4.1 we may determine $V_1 = 0.21$ eV for Sr_2CuO_3, $V_1 = 0.16$ eV for Ca_2CuO_3, and $V_1 = 0.1$ eV for $CuGeO_3$ (here $t_1 = 0.187$ eV as estimated above has been adopted). Thus, the inter-site COULOMB

---

[6]The attribution of sharp peaks near 1.25 eV, 2.9 eV and 3.66 eV observed in $Im\varepsilon(\omega)$ to the *dp* charge transfer gap which is of interest here, to *dd*-transitions, and to Ge-states related interband transition is controverse.

interactions $V_1 \overset{<}{\sim} 0.2$ eV of all three compounds are quite close to each other and fulfill the relation $V_1 \ll U$. Notice that these numbers for V_1 roughly agree with the corresponding 2D-values 0.11 eV or 0.17 eV given in Refs. [114, 137], respectively, and the estimate based on the four-band model for CuO_3-chains [138]: $V_1 \approx n_d n_p V_{pd} + n_d^2 (V_{dd} - V_{2,dd}) \approx 0.23$ eV, where typical occupation numbers $n_d \approx 0.7, n_p \approx 0.13$ and typical values for $V_{pd} = 1.2$ eV, $V_{1,dd} = 0.5$ eV and $V_{2,dd} = 0.25$ eV have been taken. Herein, V_{pd} is the copper-oxygen inter-site COULOMB interaction, $V_{1,dd}$ and $V_{2,dd}$ eV are the nearest and next nearest neighbor copper-copper inter-site COULOMB interaction, respectively.

The value for t_2 in Table 4.1 was either taken from the fit to the band-structure data ($t_{2,LDA}$ for Sr_2CuO_3 and Ca_2CuO_3) or inferred from the experimentally known value for $J_2 = 4.3$ meV [139] for $CuGeO_3$ using Eq.(4.6).

Inter-chain exchange A first estimate of the magnetic couplings between chains shall be given. The inter-chain exchange interaction $J_\perp$ in the **c**-direction for Sr_2CuO_3 and Ca_2CuO_3 (corresponding to the **b**-direction in $CuGeO_3$) will be approximated by

$$J_\perp = \frac{4t_\perp^2}{U_{eff}}, \tag{4.9}$$

for simplicity, we assumed the same inter-site COULOMB interaction V_1 within the chain and perpendicular to it. The corresponding values are listed in Table 4.1. The discussion above about a possible direct ferromagnetic exchange which leads to a systematic reduction of exchange integrals suggests that these values should be considered as upper bounds. In the case of $CuGeO_3$ the so-determined $J_\perp = 1$ meV can be compared with experimental data from neutron scattering [133, 61] $J_\perp \approx 1.1$ meV showing a reasonable agreement. It is to notice that in the case of Sr_2CuO_3 our inter-chain interaction exceeds the dipolar interaction evaluated in Ref. [131] by two orders of magnitude.

The magnitude of the weakest interaction $J_{\perp,b}$ in the **b**-direction is difficult to estimate theoretically. It has been evaluated in Ref. [131] for Sr_2CuO_3, adopting the dipolar interaction for $J_{\perp,b} \approx 10^{-4}$ meV. Extracting the corresponding transfer integral $t_{\perp,b}$ from the bandstructure, we find $t_{\perp,b} = 1.8$ meV for Sr_2CuO_3 and $t_{\perp,b} = 2.6$ meV for Ca_2CuO_3. Because we neglected in our TB-model the higher FOURIER-components in the other two directions (Eq. 4.1), these small values are at the border of reliability. The corresponding value of $J_{\perp,b} \approx 10^{-3}$ (Eq. 4.9) should be considered only as an estimate of the order of magnitude. In any case it may be expected that $J_{\perp,b}$ is smaller than the other exchange integrals by several orders of magnitude.

4.1.3 Some aspects of the NÉEL state

The magnetic properties of undoped cuprates (i.e. one hole per Cu-site in the standard *pd*-model) are usually described by the anisotropic spin-1/2 antiferromagnetic HEISENBERG model

$$H = \sum_{<i,j>} J_{ij} \mathbf{S}_i \mathbf{S}_j \quad , \qquad (4.10)$$

with $J_{ij} = J_{\parallel}(= J_1)$ for (ij) beeing nearest neighbors in the chain direction (**a**-direction for Sr_2CuO_3 and Ca_2CuO_3) and $J_{\perp}$ for nearest neighbor copper-sites in **c**-direction (see Fig. 3.6). The weakest interaction will be denoted here by $J_{\perp,b}$. According to the results of the previous sections as well as to the experimental data, Sr_2CuO_3 and Ca_2CuO_3 are characterized by very anisotropic interaction strengths

$$J_{\parallel} \gg J_{\perp} \gg J_{\perp,b}. \qquad (4.11)$$

The anisotropy is about three orders of magnitude for each inequality. Instead of the spin-PEIERLS system $CuGeO_3$, the doped compound $GeCu_{1-x}Zn_xO_3$ (x=0.034) [132, 66], which shows antiferromagnetic order, will be considered in the following to allow a comparison. This is an example for an anisotropic HEISENBERG problem with weaker anisotropy than Sr_2CuO_3 and Ca_2CuO_3. For simplicity, we will use for $GeCu_{1-x}Zn_xO_3$ the same parameters which were derived in the previous section for $CuGeO_3$. We also neglect here the frustrated exchange J_2.

In the following we review several approaches for such strongly anisotropic systems where quantum and thermal fluctuations become important. We will mention the usual spin wave approach in self-consistent random phase approximation (RPA-SWA) where all directions are treated on an equal and simple footing, and the coupled quantum spin-chain approach (CQSCA) which involves first a sophisticated treatment of the intra-chain direction and then a mean-field treatment of the remaining inter-chain interactions.

RPA spin wave theory

The RPA-SWA yields simple analytical expressions for the NÉEL temperature T_N and for the staggered magnetization $< S_A^z >= m_0$ at zero temperature (see [131], [140] and references therein). Both quantities can be derived from the expression

$$2m(T) = \frac{1}{1+2\psi} \ , \quad \psi = \frac{1}{N} \sum_{\vec{q}} \left(\frac{\omega_0}{\Omega(q)} \coth\left(\frac{\Omega(q)}{2T} \right) - 1 \right), \qquad (4.12)$$

where

$$\Omega(q) = \sqrt{\omega_0^2 - \omega_1^2(q)} \ , \quad \omega_1 = 4m(T)J_{\parallel} \left(\cos q_x + R \cos q_z + R_b \cos q_y \right), \quad (4.13)$$

with $\omega_0 = 4m(T)\left(J_\parallel + J_\perp + J_{\perp,b}\right)$, $R = J_\perp/J_\parallel$ and $R_b = J_{\perp,b}/J_\parallel$. We put $k_B = 1$. The NÉEL temperature is defined by the condition of vanishing magnetization which yields

$$T_N = J_\parallel/2I(R, R_b), \tag{4.14}$$

where

$$I(R, R_b) = \frac{1}{\pi^3}\iiint_0^\pi \frac{dq_x dq_y dq_z}{R(1 - \cos q_z) + R_b(1 - \cos q_y) + (1 - \cos q_x)} . \tag{4.15}$$

Expanding $I(R, R_b)$ for $J_\parallel \gg J_\perp \gg J_{\perp,b}$ gives the approximate expression

$$I(R, R_b) = \frac{0.66}{\sqrt{R}}\left[1 + 0.24\ln(R/R_b)\right] , \tag{4.16}$$

which determines the NÉEL temperature together with (4.14). The zero temperature magnetization m_0 is in the same limit given by

$$m_0 = \frac{0.303}{1 - 0.386\ln(R)} , \tag{4.17}$$

where the small parameter R_b turned out to be irrelevant. Notice that the RPA-description adopted reveals a vanishing magnetic moment in the $R \to 0$ limit. Thus it differs from the ordinary spin-wave theory which yields a diverging expression $m_0 = |0.5 + (1/\pi)\ln R|$ in the weak inter-chain coupling limit.

Let us now check the above expressions using the estimates of the last section and compare them with the experimental data. These data for T_N and the magnetic moment $\mu^{exp} = g_L m_0$ are given in Table 4.1. In the following, a typical cuprate LANDÉ factor $g_L \approx 2.1$ for Cu^{+2} [131] will be adopted. Using the values $J_\parallel$ and $J_\perp$ from Table 4.1 and $J_{\perp,b} = 10^{-3}$ meV, we find $T_N^{Sr} = 38$ K, $T_N^{Ca} = 75$ K, $\mu^{Sr} = 0.20\ \mu_B$ and $\mu^{Ca} = 0.26\ \mu_B$ for the Sr- and the Ca-compound, respectively. The ratio of the two experimental NÉEL temperatures agrees approximately with the RPA-SWA prediction

$$T_N^{Ca}/T_N^{Sr} \approx \sqrt{J_\parallel^{Ca} J_\perp^{Ca}}/\sqrt{J_\parallel^{Sr} J_\perp^{Sr}} \approx 2 \tag{4.18}$$

where the logarithmic corrections in Eq. (4.14) can be neglected since they are not very important for the above ratio. However, the absolute values of μ and T_N within the RPA-SWA disagree with the experimental data. In the case of the more isotropic GeCu$_{1-x}$Zn$_x$O$_3$ we find $\mu^{Ge} = 0.32\ \mu_B$, in a better agreement to the experiment. But also here, the magnetic moment is overestimated by the RPA-SWA. In this case that may be ascribed to the effect of the frustrated second neighbor exchange.

For the Sr- and the Ca-compound, the opposite procedure could be tried using the given experimental data (including $J_\parallel$) to determine an "empirical" $J_\perp^{emp}$. The

resulting values for $J_\perp^{emp}$ are two (from T_N) or more than four (from m_0) orders of magnitude lower than those estimated in the previous section. This seems, therefore, to be unrealistic. Despite the fact that it gives the correct limits for m_0 both for $R \to 0$ and in the 2D isotropic case for $R \to 1$, the RPA-SWA seems to overestimate m_0 for large anisotropy ($R \ll 1$) quite considerably. That points to the necessity for an improved method. In the case of smaller anisotropy (e.g. $R \sim 0.1$ for $GeCu_{1-x}Zn_xO_3$), the RPA-SWA seems to give more reliable results.

Coupled quantum spin chain approach (CQSCA)

Adopting SCHULTZ's interchain RPA-expression (Eq. (7) of Ref. [46]), we replace $J_\perp \to 0.5(J_\perp + J_{\perp,b})$ as suggested by our strongly "orthorhombic" parameter regime $J_\parallel \gg J_\perp \gg J_{\perp,b}$. This leads to

$$m_0 = \gamma\sqrt{R}, \tag{4.19}$$

where the proportionality factor[7] γ is 0.72. The corresponding values for $\mu^{CSC} = g_L m_0$ are listed in Table 4.1.

Analogously, within these theories one expects $T_N \approx J_\perp$ [47], in particular, the slightly modified implicit expression for the transition temperature proposed by SCHULTZ [46] reads

$$T_N = \frac{2}{\pi} J_\perp \ln^{1/2}\left(\Lambda J_\parallel / T_N\right), \tag{4.20}$$

where $\Lambda \approx 5.8$.

From a principal point of view (MERMIN-WAGNER theorem), it is clear that Eq. (4.20) overestimates T_N because it does not depend on $J_{\perp,b}$. However, since its influence can be described by logarithmic terms like in Eq. (4.16) which then ensure a finite T_N, the relative changes might be quite small.

Like in the RPA-SWA, our estimated values for $J_\perp$ and the experimental $J_\parallel$ lead to too large values for T_N and m_0. But now, using the experimental m_0 and $J_\parallel$ we can determine from Eq. (4.16) an "empirical" $J_\perp^{emp}$ of the CuO_3-chain compounds which is of the same order of magnitude as our estimates. The value of $J_\perp^{emp}$ is smaller by a factor between 2 and 3 (Sr_2CuO_3, $GeCu_{1-x}Zn_xO_3$), or 6 (Ca_2CuO_3) compared to the theoretically estimated values (see Tab. 4.1). The NÉEL temperature can also be used to determine $J_\perp^{emp}$ which gives similar values showing the internal consistency of the CQSCA, but it should be kept in mind that Eq. (4.19) does not fulfill the MERMIN-WAGNER theorem [142]. In that respect, an alternative approach to the strongly anisotropic HEISENBERG model (CASTRO-NETO and HOHN [143]) is noted here, in which the NÉEL temperature

---

[7]A similar factor $2/\pi = 0.637$, was obtained by FUKUYAMA *et al.* [141].

was found to depend linearly on $J_{\perp,b}$. Naturally, the elucidation of the correct description, how this smallest interaction parameter does affect the finite temperature properties, remains a challenging problem. Without its generally accepted solution it makes no sense to discuss the absolute values of the NÉEL-temperature beyond an order of magnitude accuracy.

One possible explanation for the reduction of $J_{\perp}^{emp}$ in comparison with our estimated $J_{\perp}$ could be the proximity of a spin-PEIERLS state. Phase fluctuation effects beyond the mean-field inter-chain approach used in deriving Eq. (4.19) can then become quite important. Following the renormalization group approach of WANG [48] for a plane of weakly interacting chains at $T = 0$, one finds a strongly renormalized magnetization which can be traced back to a renormalized exchange integral. If that is true, Ca_2CuO_3 should be much closer to the spin-PEIERLS phase transition point than Sr_2CuO_3. Furthermore, for small exchange integrals compared with the phonon frequency ($\sim$ 10 to 20 meV), phonon exchange gives rise to a quasi-instantaneous interaction between localized spins, leading to a renormalization $J \to J_{eff} < J$ [144].

Another possible origin for the difference between $J_{\perp}$ and $J_{\perp}^{emp}$ might be our simple procedure to estimate $J_{\perp}$ based on the extended HUBBARD model. It was already mentioned that such a procedure has the tendency to overestimate the exchange integrals which becomes already apparent for $J_{\parallel}$. Last but not least, there is an uncertainty of the band-structure methods with respect to transfer integrals as small as in the considered case. The replacement of the full potential in the region in between the chains by empty spheres as explained in Sec. 3.3.1 might effect the transverse tails of the WANNIER-functions which determine the value of the transfer integral $t_{\perp}$. Anyhow, roughly the same accuracy for the Sr- and the Ca-compound should be expected. In this context the stronger deviation of the magnetic moment of the Ca-compound might be related to somewhat reduced accuracy of Eq. (4.17) in less anisotropic cases.

The isomorphic compounds Sr_2CuO_3 and Ca_2CuO_3 offer in principle the opportunity to study in detail the effect of the inter-chain interaction (despite of possible disorder effects) provided that it can be changed in a controlled way. Indeed, the study of the magnetic properties of the alloy system $Sr_{2-x}Ca_xCuO_3$ gives an interesting possibility to change continuously the magnitude of the inter-chain coupling. This is also interesting from the theoretical point of view since it gives a possibility to check in more detail sophisticated theories for weakly-coupled quantum spin-chains.

An analogous analysis of the inter-chain couplings and the antiferromagnetic interactions has been performed for the zigzag chain cuprate $SrCuO_2$ (see Fig. 3.18) [145]. Due to the similarity of some properties with the above mentioned single chains, the main results shall be shortly reported in the following

to complete this section (For the detailed analysis and discussion see Ref. [145]).

Within LDA calculations, the insulating compound $SrCuO_2$ shows two half-filled nearly one-dimensional antibonding bands (see Fig. 3.20) according to the presence of two spin-1/2 antiferromagnetic subchains with weakly frustrating intra- and inter-subchain interactions.

Recent EELS data provide for the first time clear experimental evidence for the subchain interaction in good agreement with the band structure calculation [145].

Using exact diagonalization studies to investigate the influence of different frustrating exchange interactions of the zigzag chain in the parameter region estimated by LDA, we find a rather small effect of the frustrating coupling terms between the two subchains on the magnetic susceptibility and on the specific heat.

The inter-chain HEISENBERG exchange in the direction of the weakest coupling is quite different for $SrCuO_2$ and Sr_2CuO_3 which might be responsible for the different magnetic ordering at low temperature. There is an indirect coupling in **b**-direction involving nearest neighbor zigzag chains in **b**-**c**-direction (see Fig. 3.18) ensuring this way a finite NÉEL temperature of about 5 K [79] similar to the NÉEL temperature of Sr_2CuO_3.

In addition, the quantum fluctuations within the **a**-**c** basal plane are enhanced in comparison with the single-chain case due to the reduced inter-chain interaction. The corresponding transfer integral in **c**-direction for $SrCuO_2$ is about half the value of Sr_2CuO_3. Applying quantum spin chain theories [146], that explains the further reduced magnetic moment of $0.033\mu_{Bohr}$[79].

Summarizing, it is to state, that the LDA band structure calculations yield useful insights into important material-dependent parameters as inter-chain electron transfer and tendencies of the crystal field (MADELUNG) potential, albeit that estimate of the on-site and inter-site COULOMB interaction requires more sophisticated methods such as LDA-calculations with local constraint.

4.2 The orbital-hole distribution in cuprate chains

In the previous section, we investigated the low-energy physics of single-chain cuprates in the framework of a one-band model. Here, multi-band models are presented, which are suited to describe processes where different orbitals are involved.

Combining the theoretical analysis and various spectroscopies, the main parameter values of extended HUBBARD models for the various chain-cuprates can be determined. In particular, it is the aim of the present discussion to find out

for the anisotropic Sr_2CuO_3 compound under consideration to which interactions the polarization-dependent x-ray absorption spectroscopy (XAS) is most sensitive and to determine the corresponding parameters (for a detailed discussion see Ref. [117]).

The experimentally measured O $1s$ spectra with the electric field vector parallel and perpendicular to the CuO_3-chains are shown in Fig. 4.3. XAS probes
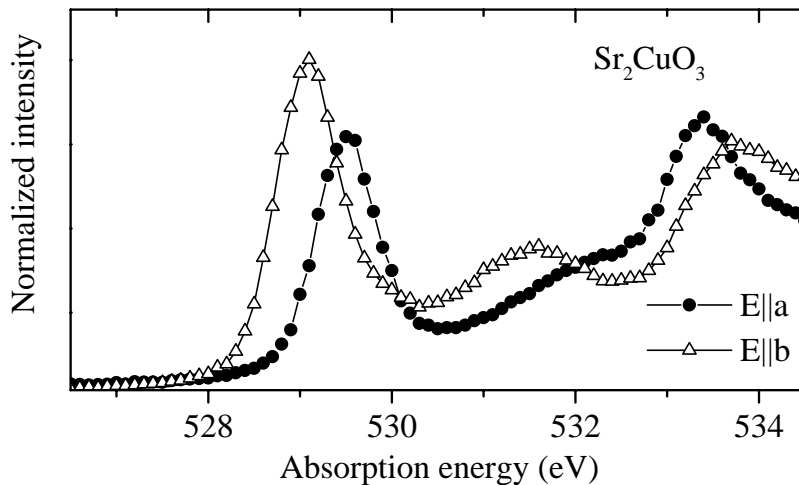
Figure 4.3: Polarization-dependent XAS spectra of Sr_2CuO_3 for the electric field vector **E** within the plane of the Cu-O$_4$-plaquettes. The **a**-axis corresponds to the chain direction. For experimental details see Ref. [117].

the unoccupied electronic structure. In particular, the first peaks above the absorption threshold measure the number of holes in the initial state of oxygen $2p$ orbitals contributing to the upper HUBBARD band. From the integrated spectral weight near the peak values an oxygen hole ratio $R = 2n_{O(2)}/n_{O(1)} \approx 1.22$ can be deduced. The chain oxygen O(1) and the side oxygen O(2) correspond to the notation in Fig. 3.6.

Starting from an LDA bandstructure calculation followed by the parameterization of appropriated TB models, we will adjust the on-site and inter-site COULOMB parameters of an extended HUBBARD model to this experimentally observed hole ratio.

4.2.1 Tight binding models

The LDA-LCAO bandstructure calculation for Sr_2CuO_3 yields a quasi 1D-band crossing the FERMI level (see Figs. 3.8 and 4.1). Three main orbitals contribute
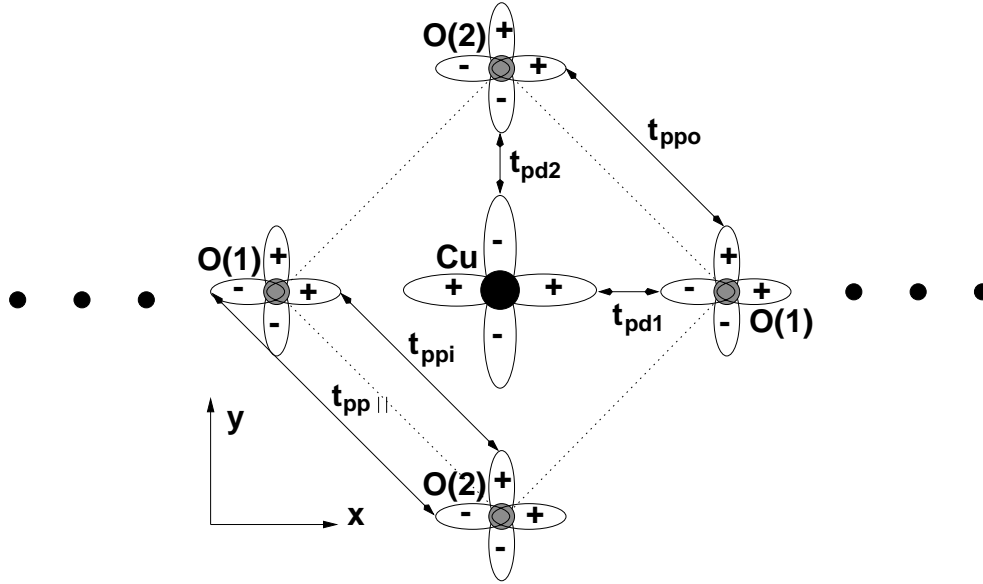
Figure 4.4: Sketch of a plaquette of the CuO_3-chain in Sr_2CuO_3. The orbitals and the corresponding transfer integrals of the 7-band TB model are depicted. For the 4-band TB-model, only the oxygen p-orbitals which form pd-σ bonds with the copper $3d$-orbital and the corresponding transfer integrals t_{ppi}, t_{pd1} and t_{pd2} are relevant.

more than 94 % to the net-DOS (see Appendix A) of the antibonding band, namely the O(1) $2p_x$ and O(2) $2p_y$ states as well as the Cu $3d_{x^2-y^2}$ orbitals. Hence, the usual dp-model with an extension to two non-equivalent oxygen sites per unit cell can be regarded as a quite good approximation for the description of the low-energy electronic structure at hand. This model contains three transfer integrals t_{pd1}, t_{pd2} and t_{ppi} (see Fig. 4.4) and three on-site energies $\varepsilon_{O(1)}$, $\varepsilon_{O(2)}$ and ε_d corresponding to the above mentioned orbitals.

At first glance, only the half-filled antibonding band at the FERMI level should be considered. However, the extended tight binding fit for this band is numerically not unique and therefore not suitable for the determination of three different transfer integrals required in the four-band pd-model (see Figs. 3.6, 4.4 and Eq. (4.21) for the notation of sites and parameters). Thus, additional lower-lying bands with bonding and nonbonding character have to be included. However, due to the non-negligible hybridization with further O $2p$ orbitals (having non-σ overlap), a discontinuity of the O(2) $2p_y$ orbital-character (see Appendix A) is observed in the region of the nonbonding oxygen-derived bands near -4 eV and -5 eV (see Fig. 4.5), if we restrict ourselves to the four-band model, only. Therefore, eventually, a fit was performed within the seven-band pd-model where
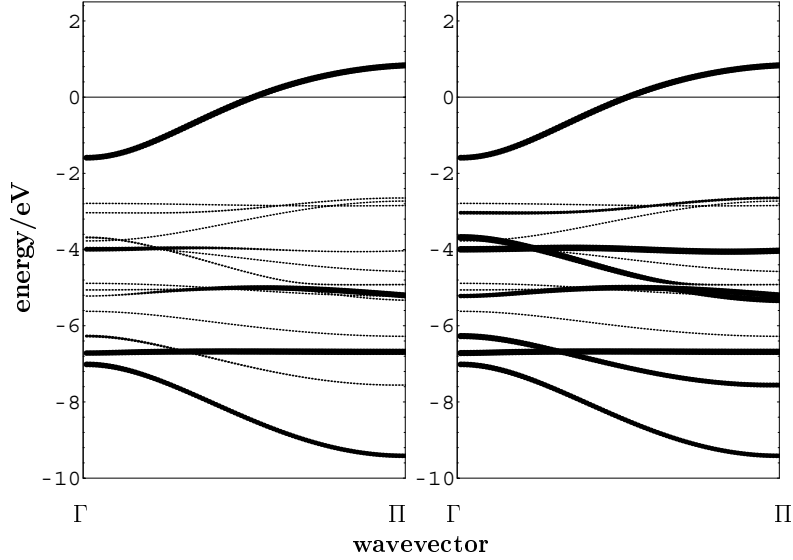
Figure 4.5: LDA-LCAO band structure of Sr_2CuO_3 along the chain direction. The symmetry points are denoted $\Gamma = 0$ and $\Pi = \pi/a$, the FERMI level is at zero energy. The thickness of the lines is scaled with the sum of all orbital projections of the 4-band TB model (left panel) and of the 7-band TB model (right panel).

the $O(1)$ $2p_y$ and two $O(2)$ $2p_x$-orbitals with corresponding on-site energies and transfer integrals t_{ppo} and $t_{pp\parallel}$ were taken into account additionally although they can be largely ignored in the physics described below. The fitting procedure of a multi-band TB model using the eigenvalues at high-symmetry points is described in detail in Section 4.3.1.

The transfer integrals for the TB-fit of the four- and the seven-band model are given in Table 4.2. Compared with the standard parameter $t_{pd} = 1.3$ eV for the CuO_2-plane, the transfer integrals t_{pd1} and t_{pd2} are enhanced. This is probably caused by a change of the corresponding WANNIER functions [147]. Similar values are reported for the transfer integrals of the CuO_3-chain in $YBa_2Cu_3O_{6+x}$ ($t_{pd1} = 1.5$ eV, $t_{pd2} = 1.95$ eV and $t_{ppi} = 0.6$ eV) [148].

However, the parameter $t_{ppi} = 1.15$ eV obtained from the four-band model seems to be unreasonably large. This is caused by the non-negligible influence of hopping processes corresponding to $t_{pp\parallel}$. The same is valid for the difference of oxygen on-site energies $\Delta_{pp} = \varepsilon_{O(2)}$ - $\varepsilon_{O(1)}$. We find $\Delta_{pp} = $ -1.5 eV and $\Delta_{pp} = 0.75$ eV for the four- and the seven-band model, respectively. The exact diagonalization studies presented in the following section show *a posteriori* the inconsistency of the values for t_{ppi} and Δ_{pp} found in the four-band model.

TB model	t_{pd1}	t_{pd2}	t_{ppi}	t_{ppo}	$t_{pp\|}$
4-band	1.45	1.8	1.15	-	-
7-band	1.56	1.8	0.62	0.41	0.35

Table 4.2: Transfer integrals for the four and seven-band TB fit for Sr_2CuO_3. All energies are given in eV.

Thus an extended fit with a subsequent selection of relevant orbitals is more favorable than a more restricted one with an uncontrolled renormalization due to neglect of other orbitals. In this context we mention that the small admixture of Cu $4s$ and O $2s$ states contributes also somewhat to the large band width of the antibonding band[8].

4.2.2 Exact diagonalization studies

In this section, a theoretical analysis of the hole distribution using the exact diagonalization method for a $(CuO_3)_N$-cluster ($N = 4,6$) with periodic boundary conditions is discussed. For the transfer integrals the above obtained values from the seven-band TB model are used as input.

According to the orbital analysis in the previous section, a four-band extended HUBBARD model [115] is suitable to describe the XAS measurement. Regarding the final state of the core level excitation, the corresponding Hamiltonian has to be supplemented with the core-pd-valence hole COULOMB interaction V_{ci}:

$$
\begin{aligned}
H &= \sum_i \varepsilon_i \hat{n}_i + \sum_{<i,j>,s} t_{ij}(c_{i,s}^\dagger c_{j,s} + h.c.) + \sum_i U_i \hat{n}_{i,\uparrow} \hat{n}_{i,\downarrow} \\
&+ \sum_{<i,j>} V_{ij} \hat{n}_i \hat{n}_j + \sum_i U_{ci} \hat{n}_c \hat{n}_i + \sum_i V_{ci} \hat{n}_c \hat{n}_i ,
\end{aligned}
\tag{4.21}
$$

where $c_{i,s}^\dagger$ creates a hole at the site i, $\hat{n}_{i,s} = c_{is}^\dagger c_{is}$ is the number operator, and $\hat{n}_i = \sum_s c_{is}^\dagger c_{is}$. In the following, we denote the difference of chain-oxygen O(1) $2p_x$ and Cu $3d_{x^2-y^2}$ on-site energies by Δ_{p1d}. For the on-site COULOMB repulsion at Cu and O sites we adopt $U_d = 8.8$ eV and $U_p = 4.4$ eV, respectively, as suggested in Ref. [149]. For the intersite COULOMB interactions we adopt for the sake of simplicity $V_{pd1} = V_{pd2} = V_{pd}$. Then, the latter value as well as the values of Δ_{pp} and Δ_{p1d} are taken as free parameters to reproduce the XAS data reported below. We have calculated the XAS spectral function as well as the hole

---

[8]Suppressing this admixture artificially in the final step of a self-consistent calculation, the bandwidth of the antibonding band is reduced by about 10 %.
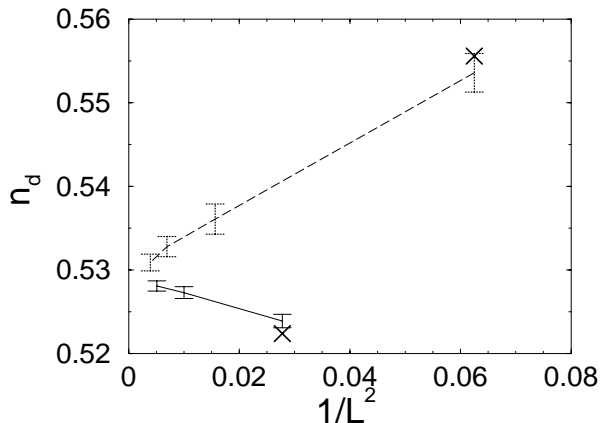
Figure 4.6: Size effect for the Cu hole-occupation number n_d in the CuO_3-chain of Sr_2CuO_3 depending on the cluster size L calculated within the Quantum Monte Carlo method . The crosses denote our exact diagonalization results for L = 4 and L = 6.

occupation numbers

$$n_i = \langle G|\hat{n}_i|G\rangle, \tag{4.22}$$

in the ground state $|G\rangle$ for Cu and for both non-equivalent oxygen sites O(1) and O(2), since the measured polarized O $1s$ XAS cross sections are proportional to the oxygen occupation numbers in the ground state.

In order to get some insight in the finite size effects caused by the small clusters which can be treated by exact diagonalization methods, the results are compared with those of Quantum Monte Carlo calculations [150], where up to 16 unit cells can be considered (see Fig. 4.6). The Quantum Monte Carlo calculations result in a $1/L^2$ asymptotic behavior on different curves for L = $4m$ and L = $4m+2$ ($m = 1, 2 \ldots$) clusters. Since the deviations at small m are very small (about 0.4 %), we regard the result for $L=16$ as an excellent estimate for the $L \to \infty$ limit. Therefore, the results for any quantity calculated at $m = 6$ and $m = 4$ cluster sizes can be regarded as lower and upper bounds for the infinite chain-limit.

The main results of the cluster calculations are the following: The hole ratio R is sensitively dependent on both the values of Δ_{pp} and V_{pd}. Compared to typical values for the layered cuprates, we find a significantly enhanced V_{pd} of 2.5 ± 0.5 eV (see right panel of Fig. 4.7). Thus, we confirmed the predictions based on an analysis of Cu $2p$ XPS spectra [126]. However, in contrast to this XPS analysis, which is less sensitive to the parameter Δ_{pp}, a sizable positive value of $\Delta_{pp} \sim 0.5 \ldots 1$ eV has to be taken into account in accord with the LDA result (see left panel of Fig. 4.7). Finally, EELS data of Ref. [151] yielding an effective
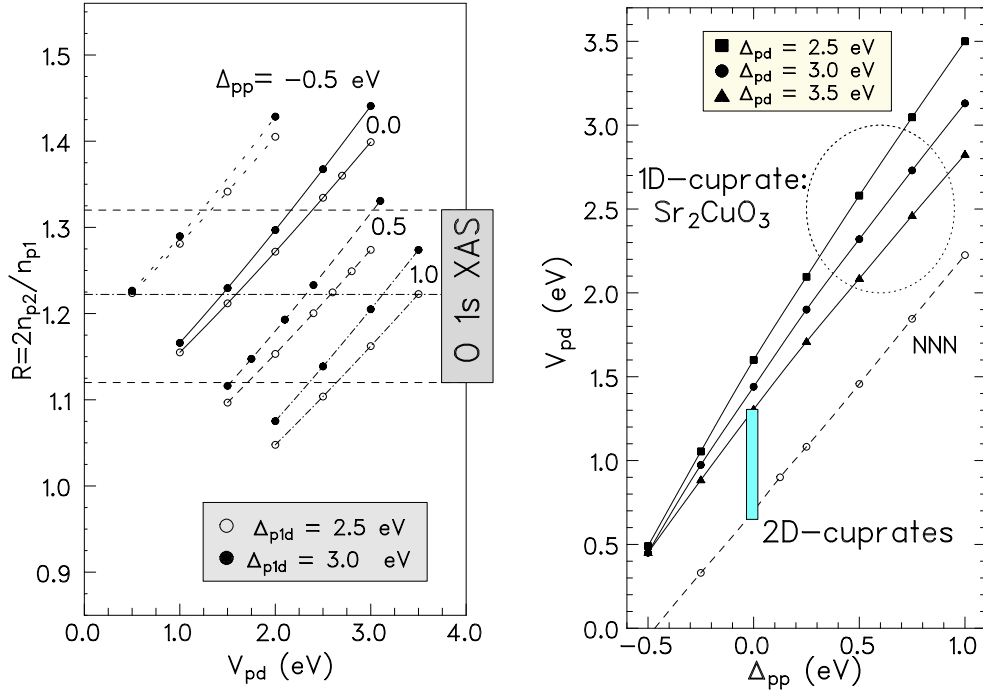
Figure 4.7: Left panel: Ratio of side- and chain-oxygen occupation numbers in Sr_2CuO_3 *vs.* intersite COULOMB interaction V_{pd} for the LDA-LCAO derived parameter set. The legend numbers denote the difference of oxygen on-site energies Δ_{pp} in eV. The stripe denotes the experimentally (XAS) derived oxygen hole ratio including error bars.

Right panel: Dependence of the inter-site COULOMB interaction V_{pd} on the oxygen on-site energy difference Δ_{pp} for different Δ_{pd}. The large circle denotes the expected region of V_{pd} and Δ_{pp}. NNN stands for Cu-Cu interaction $V_{dd} = 0.8$ eV included.

$U_{\mathrm{eff}} \sim 4.2$ eV analyzed within an extended one-band HUBBARD model. Adopting this value of U_{eff}, further COULOMB interaction V_{dd} should be included in the four-band model.

To summarize our results, based on bandstructure calculations for Sr_2CuO_3 a new parameter set at the level of the four-band extended HUBBARD pd model description has been proposed. Surprisingly, significant deviations from sets commonly accepted for layered cuprates have been found indicating that the t_{pd1}, t_{pd2} and t_{pp} do not scale with the Cu-O distance. These deviations can be considered as the origin of the unusual large values of the intrachain exchange integral (see Section 4.1.2). At variance to other spectroscopies the polarization-dependent XAS for the anisotropic single-chain Sr_2CuO_3 is found to be sensitive to the difference of on-site energies and of the inter-site COULOMB interaction.

4.3 Tight-binding parameter and exchange integrals of $Ba_2Cu_3O_4Cl_2$

In this section, the parameterization of a multi-band tight-binding model is demonstrated in more detail. The advantage of a the atomiclike character of the basis orbitals in our band structure scheme gives a natural possibility to extract the relevant orbitals for the construction of model Hamiltonians. This is exploited extensively in the following.

In Figs. 4.9(a) and 4.9(b) the weights of the Cu_A $3d_{x^2-y^2}$ and Cu_B $3d_{x^2-y^2}$ orbitals, respectively, are shown. We can observe that the broad band is built up of predominantly the Cu_A $3d_{x^2-y^2}$ orbital which hybridizes with one part of the planar oxygen $2p_{x,y}$ orbitals resulting in $dp\sigma$ bonds. The corresponding oxygen orbitals, directed to the Cu_A atoms, are denoted here as p_σ orbitals. Their weight is shown in Fig. 4.9(c). The p_σ orbitals are to distinguish from the oxygen p_π orbitals (Fig. 4.9(d)) which are perpendicular to them [152] (see Fig. 4.10). These oxygen p_π orbitals hybridize with Cu_B $3d_{x^2-y^2}$, building the narrow band at the FERMI-surface (see Fig. 4.9(b)). There is generally very small weight of the p_σ orbitals in this narrow band, indicating that there is only small coupling between the A and B subsystems. The only exception to this occurs around the wave vector $(\pi/a, 0)$. A further analysis shows that the band complex between -1 eV and -3 eV is predominantly built up of out-of-plane oxygen p_z together with the corresponding Cu $3d_{xz,yz}$ orbitals (not shown), as well as a large contribution of Cl-derived states [49]. The in-plane oxygen orbitals contribute mainly to the lower band complex between -4 eV and -8 eV (see Figs. 4.9(c) and 4.9(d)).

Thus, it is evident that the two bands crossing the FERMI-surface which we want to analyze have nearly pure $3d_{x^2-y^2}$ and $2p_{x,y}$ character[9]. Therefore, we have to consider all together 11 orbitals in the elementary cell of Cu_3O_4, namely 2 Cu_A $3d_{x^2-y^2}$, 1 Cu_B $3d_{x^2-y^2}$, 4 oxygen p_σ and 4 oxygen p_π orbitals. In Fig. 4.8(b) we pick out the corresponding bands from the LDA-bandstructure for which the sum of all 11 orbital weights (Eq. (A.7) in the Appendix) is large. It is to see that the sum of all orbital projections in Fig. 4.8(b) decreases with increasing binding energy. That can be explained by the reasons mentioned above. Further it is to observe that the lower 8 bands in Fig. 4.8(b) are not as pure as the upper three. For the upper bands only a very small weight of additional orbitals, in particular Cu $4s$ contributions, has been detected. These contributions are neglected in the following.

---

[9]The corresponding band complex with nearly pure $3d_{x^2-y^2}$ and $2p_{x,y}$ character includes also a third band just below the FERMI-surface. It has Cu_A $3d_{x^2-y^2}$ and O p_σ character similar to the broad band crossing the FERMI-surface. This is not surprising since there are two Cu_A in the elementary cell of Cu_3O_4.
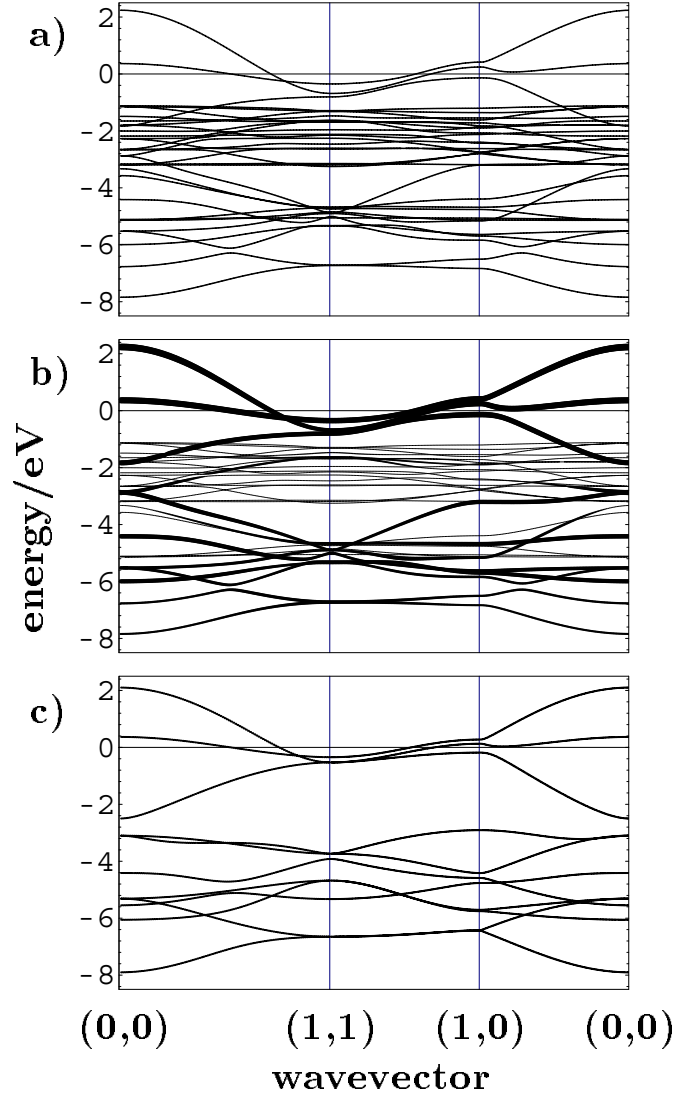
Figure 4.8: **a)** LCAO-LDA band structure of the Cu_3O_4-plane of $Ba_2Cu_3O_4Cl_2$, the FERMI level is at zero energy. **b)** The same as in (a), but the weight of the lines is scaled with the sum of all 11 orbital projections that are used in the TB model. **c)** The band structure of the TB model. The parameter set used is shown in Table 4.3. The wave vector is measured in units of $(\pi/a, \pi/a)$.

4.3.1 Tight-binding parameters

It is our main goal to find a TB description of the relevant bands crossing the FERMI-surface. This task is difficult due to the large number of bands between
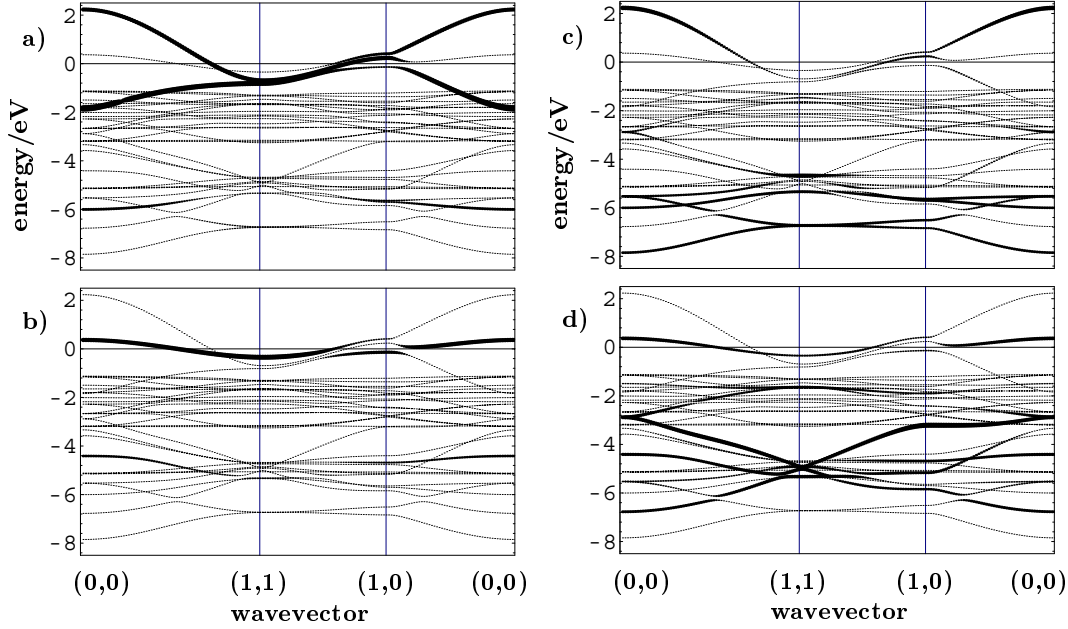
Figure 4.9:   Weight of **a)** Cu_A $3d_{x^2-y^2}$, **b)** Cu_B $3d_{x^2-y^2}$, **c)** O $2p_\sigma$ and **d)** O $2p_\pi$ orbitals in the LCAO-LDA band structure of $Ba_2Cu_3O_4Cl_2$. The wave vector is measured in units of $(\pi/a,\pi/a)$.

-1 eV and -8 eV of Fig. 4.8(a). There is no isolated band complex which would make a TB analysis easy. However, as it has been pointed out already, the relevant bands are a nearly pure combination of Cu $3d_{x^2-y^2}$ and O $2p_{x,y}$ orbitals. Thus, we will only concentrate on these orbitals, thereby accepting some deviations in the lower band complex between -3 eV and -8 eV. The relevant orbitals are depicted in Fig. 4.10. The tight-binding Hamiltonian H_{TB} can be written as a sum of three parts:

$$H_{TB} = H_A + H_B + H_{AB} \ . \tag{4.23}$$

There are two classes of orbitals corresponding to the two different subsystems. One consists of Cu_A $3d_{x^2-y^2}$ orbitals at the sites $\mathbf{R}$ with on-site energies ε_d^A and oxygen $2p_\sigma$ orbitals at the sites $\mathbf{r}$ with ε_p:

$$
\begin{aligned}
H_A &= \varepsilon_d^A \sum_{\mathbf{R}s} d^\dagger_{\mathbf{R}s} d_{\mathbf{R}s} + \varepsilon_p \sum_{\mathbf{r}s} p^\dagger_{\mathbf{r}s} p_{\mathbf{r}s} + t_{pd} \sum_{\substack{\mathbf{R}\mathbf{r}\\s}} (\alpha_{\mathbf{R}\mathbf{r}} d^\dagger_{\mathbf{R}s} p_{\mathbf{r}s} + \text{H.C.}) + \\
&+ t_{pp} \sum_{\substack{\mathbf{r}\mathbf{r}'\\s}} (\alpha_{\mathbf{r}\mathbf{r}'} p^\dagger_{\mathbf{r}s} p_{\mathbf{r}'s} + \text{H.C.})
\end{aligned} \tag{4.24}
$$
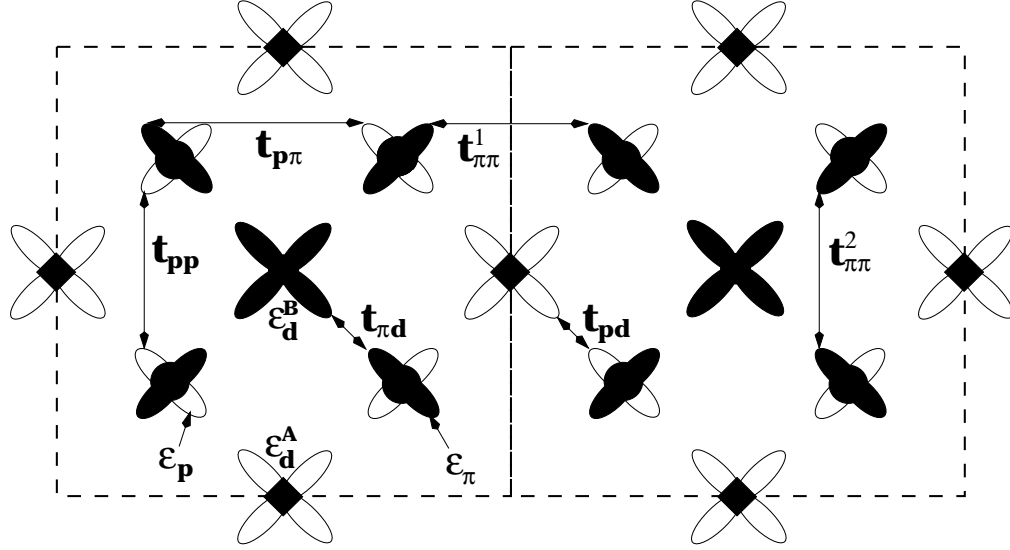
Figure 4.10: Two elementary cells of the Cu_3O_4-plane in $Ba_2Cu_3O_4Cl_2$ or $Sr_2Cu_3O_4Cl_2$ and the Cu $3d_{x^2-y^2}$ and O-$2p_{x,y}$ orbitals comprising the TB model. Also shown are the corresponding transfer integrals t_{pd}, $t_{\pi d}$, t_{pp}, $t^1_{\pi\pi}$, $t^2_{\pi\pi}$ and $t_{p\pi}$. The Cu_A orbitals with on-site energy ε_d^A are marked by black diamonds, the Cu_B orbitals with on-site energy ε_d^B by black squares and the two different kinds of O orbitals with on-site energies ε_p and ε_π, respectively, by black circles. The orbitals of the B-subsystem are shaded to distinguish them from the orbitals of the A-subsystem (white).

where $d^\dagger_{\mathbf{R}s}$ and $p^\dagger_{\mathbf{r}s}$ are the usual creation operators for Cu $3d_{x^2-y^2}$ and O $2p_\sigma$ orbitals, respectively, and $\alpha_{\mathbf{R}\mathbf{r}}$ is a phase factor corresponding to Fig. 4.10 which connects only neighboring sites. The other class incorporates Cu_B $3d_{x^2-y^2}$ orbitals at the sites $\mathbf{G}$ with on-site energies ε_d^B and oxygen p_π orbitals at the sites $\mathbf{r}$ with ε_π. The Hamiltonian H_B is obtained by replacing $\mathbf{R}$ with $\mathbf{G}$, and the on-site and transfer energies with the corresponding energies of the Cu_B-subsystem, respectively. The creation operators $p^\dagger_{\mathbf{r}s}$ should then be replaced with the operators $\pi^\dagger_{\mathbf{r}s}$ thus creating an O $2p_\pi$ orbital. The coupling between both classes of orbitals, which correspond to the Cu_A and Cu_B subsystems, respectively, is provided by the parameter $t_{p\pi}$:

$$H_{AB} = t_{p\pi} \sum_{\substack{\mathbf{r}\mathbf{r}' \\ s}} (\alpha_{\mathbf{r}\mathbf{r}'} p^\dagger_{\mathbf{r}s} \pi_{\mathbf{r}'s} + \mathrm{H.C.}) \,. \tag{4.25}$$

All together, there are 10 parameters to determine, 4 on-site energies (ε_d^A, ε_d^B, ε_p, ε_π), the nearest neighbor transfer integrals (t_{pd}, $t_{\pi d}$), and several kinds of oxygen transfers (t_{pp}, $t^1_{\pi\pi}$, $t^2_{\pi\pi}$, $t_{p\pi}$).

parameter	ε_d^A	ε_d^B	ε_p	ε_π	t_{pd}	$t_{\pi d}$	t_{pp}	$t_{\pi\pi}^1$	$t_{\pi\pi}^2$	$t_{p\pi}$
TB fit	-2.50	-2.12	-4.68	-3.73	1.43	1.19	0.81	0.41	0.50	0.25
EHM	2.50	2.12	6.68	5.73	-1.43	-1.19	-0.81	-0.41	-0.50	-0.25

parameter	U_d	U_p	U_{pd}	$U_{p\pi}$	K_{pd}	$K_{p\pi}$
EHM	10.5	4.0	1.2	3.2	-0.18	-0.4

Table 4.3: Parameters of the TB fit and the proposed extended HUBBARD model for the Cu_3O_4-plane in $Ba_2Cu_3O_4Cl_2$. The parameters are given in electron representation for the TB fit and in hole representation for the extended HUBBARD model. All energies are given in eV.

In our analysis we found that the Cu_A-Cu_B transfer t_{dd} can be neglected since its estimation[10] yields a value smaller than 0.08 eV. Each p_σ orbital is located between two Cu_A sites and we neglect the influence of different local environments on the t_{pp} transfer integral. In the case of the $t_{\pi\pi}$ transfer there exist two possible local arrangements, but the numerical difference between $t_{\pi\pi}^1$ and $t_{\pi\pi}^2$ is small (see Table 4.3). The necessity to distinguish between oxygen $2p_\sigma$- and $2p_\pi$-orbitals was first pointed out by MATTHEISS and HAMANN [152] for the case of the standard CuO_2-plane.

Since there is a considerable admixture of other orbitals, especially Cu $3d_{xy}$ and Cu $3d_{3z^2-r^2}$, in some of the lower bands of Fig. 4.8(b), it is impossible to determine the 10 TB parameters by a least square fit of the 11 TB bands to the heavily shaded LDA bands of Fig. 4.8(b). Instead, at the high symmetry points $\Gamma = (0,0)$ and $M = (\pi/a, \pi/a)$ we picked out those bands in Fig. 4.8(b) which have the most pure $3d_{x^2-y^2}$ and $2p_{x,y}$ character. Only those energies were compared with the TB bandstructure (Fig. 4.8(c)) derived by diagonalizing an 11×11 matrix. In this way it is possible to calculate the parameter set analytically because the TB matrix splits up into 3×3 and 4×4 matrices at the high symmetry points $\Gamma = (0,0)$ and $M = (\pi/a, \pi/a)$. The calculated eigenvalues are given in the Appendix A. That procedure results in the parameters given in Table 4.3. These values are similar to those which are known for the standard CuO_2-plane. The largest transfer integrals are $t_{pd} = 1.43$ eV and $t_{\pi d} = 1.19$ eV as expected. Nevertheless these values are somewhat smaller than in the previous TB fit [49]

---

[10]The parameter t_{dd} can be roughly estimated by the weight of the Cu_A in the Cu_B band crossing the FERMI-level at the $\Gamma = (0,0)$ point of the BRILLOUIN zone. At this point the coupling via $t_{p\pi}$ is not possible due to symmetry.

where all oxygen orbitals were treated as identical. The difference between t_{pp} and $t_{\pi\pi}$ is roughly a factor of 2 in coincidence with the situation in the standard CuO_2-plane [152], a fact which was not taken into account in [49]. We have found that only the smallest parameter, $t_{p\pi} = 0.25$ eV, is responsible for the coupling between the subsystems of Cu_A and Cu_B. Thus despite the fact that the two oxygen p_σ and p_π orbitals are located in real space at the same atom, they are quite far away from each other in the HILBERT space.

4.3.2   Exchange integrals

So far we have found that the TB parameters are rather similar to the standard CuO_2-case and that the coupling between Cu_A- and Cu_B-subsystem is quite small. This justifies the usage of standard parameters for the COULOMB interaction part of the Hamiltonian. Of course, it would be desirable to determine these values by a constrained density functional calculation for $Ba_2Cu_3O_4Cl_2$, but only small changes to the estimation of exchange integrals presented below are to expect.

The COULOMB interaction also changes the on-site copper and oxygen energies. Their difference, given in the first line of Table 4.3, is too small to explain the charge transfer gap of ~ 2 eV in $Ba_2Cu_3O_4Cl_2$ [153]. Adding 2 eV to the on-site oxygen energies, the difference $\Delta = \varepsilon_p - \varepsilon_d^A$ (in hole representation which is chosen from now on) becomes similar to the standard value derived by HYBERTSEN *et al.* [23] for La_2CuO_4. Our proposal of on-site energies for the multi-band HUB-BARD model $H = H_{TB} + H_{int}$ is given in the second line of Table 4.3. The values of Ref. [23] have been used also for the parameters of the COULOMB interaction part

$$H_{int} = \sum_i U_i n_{i\uparrow} n_{i\downarrow} + \frac{1}{2} \sum_{\substack{ij \\ ss'}} U_{ij} n_{is} n_{js'} + \sum_{ij} K_{ij} \mathbf{S}_i \mathbf{S}_j, \qquad (4.26)$$

where n_{is} is the occupation operator of the orbital i with the spin s and $\mathbf{S_i}$ the corresponding spin operator. From Ref. [23] the values for U_d, U_p, U_{pd} and K_{pd} are known. Since we now have two oxygen orbitals at one site we also have to take into account the corresponding HUND's rule coupling energy which is in the notation of (4.26) $K_{p\pi}$. That correlation energy is not given in [23] and we use here the simple rule $K_{p\pi} = -0.1U_p$ [154]. The COULOMB repulsion between two oxygen holes in p_σ- and p_π-orbitals is assumed to be $U_{p\pi} = U_p + 2K_{p\pi}$, which is a valid approximation given degenerate orbitals. The second part of Table 4.3 combines the TB parameters derived from the bandstructure of $Ba_2Cu_3O_4Cl_2$ (now in hole representation) with the standard COULOMB correlation terms. This parameter set defines an 11 band extended HUBBARD model for the Cu_3O_4-plane which is used for the following estimation.
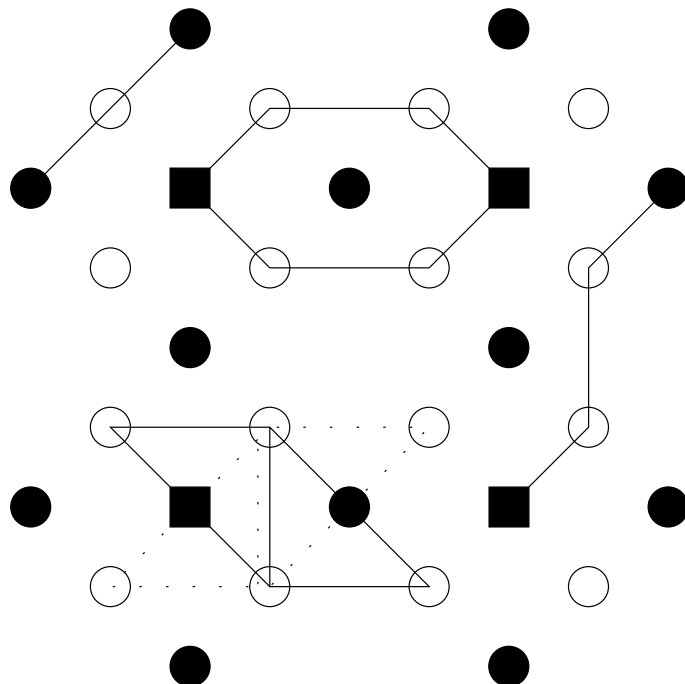
Figure 4.11: Clusters used for the calculation of the exchange integrals J_{AA} (upper left), J_{BB} (upper middle), $J_{AB}^{(1)}$ (lower left) and $J_{AB}^{(3)}$ (lower right). The Cu$_A$ sites are marked with filled circles, the Cu$_B$ sites with squares and the oxygen sites with open circles.

The exchange integrals have been calculated using the usual RAYLEIGH-SCHRÖDINGER perturbation theory on small clusters (Fig. 4.11). All transfer integrals (and $K_{p\pi}$) have been considered as a perturbation around the local limit. The exchange integrals have been calculated in the corresponding lowest order (see Appendix C). The exchange $J_{AA} \propto t_{pd}^4/\Delta^3$ between two Cu$_A$ spins is given in the 4th order for the simple Cu$_A$-O-Cu$_A$ cluster. It turns out that the influence of intersite COULOMB terms $U_{p(\pi)d}$ and of the exchange terms $K_{p(\pi)d}$ is rather large, decreasing J_{AA} from 246 meV to 99 meV (see Table 4.4). In spite of our rather approximate procedure, the latter value agrees quite reasonably with the phenomenological value (130 ± 40) meV [112] for Sr$_2$Cu$_3$O$_4$Cl$_2$. J_{AA} is thus also quite close to the standard value of the CuO$_2$-plane (~ 140 meV [23]).

The exchange J_{BB} is given only in 6th order for a larger cluster of two Cu$_B$, one Cu$_A$ and 4 oxygen orbitals. Correspondingly, it is roughly one order of magnitude smaller, $J_{BB} \sim 12$ meV (Table 4.4). For J_{AB} we need to distinguish between antiferromagnetic and ferromagnetic contributions. There are two AFM couplings between nearest neighbor copper atoms $J_{AB,af}^{(1)}$ and third nearest neighbor copper

exchange integral	without $U_{pd}, K_{pd}, K_{p\pi}$ (meV)	all parameters (meV)	experiment (meV)
J_{AA}	246	99	130 ± 40
J_{BB}	17	12	10 ± 1
$J_{AB,af}^{(1)}$	6.9	4.6	-
$J_{AB,f}^{(1)}$		-10.2	-
$J_{AB}^{(1)}$		-5.6	-12 ± 9
$J_{AB,af}^{(3)}$	1.4	0.8	-

Table 4.4: Different exchange integrals as explained in the text. Compared are estimations within the extended HUBBARD model with experimental values [112].

atoms $J_{AB,af}^{(3)}$, both being comparably small at 4.6 and 0.8 meV, respectively. The ferromagnetic contribution $J_{AB,f}$ = -10 meV between nearest neighbor copper spins arises in 5th order and is provided by HUND's rule coupling of two virtual oxygen holes sitting at the same oxygen. Since $K_{p\pi}$ is known with less accuracy than the other interaction parameters, this value has to be taken with care.

The derived exchange integrals J_{AA}, J_{BB} and J_{AB} are in reasonable agreement[11] with phenomenologically derived values from magnetic susceptibility data if we add to the TB parameters the standard local COULOMB correlation energies. It is to note, however, that we used a rather approximate perturbative procedure to estimate the exchange integrals. We expect that the RAYLEIGH-SCHRÖDINGER perturbation theory provides us with the right order of magnitude, but it may fail in the correct numbers[12]. In that sense the agreement of the theoretical exchange integrals with the experimental ones should not be overinterpreted. On the other hand, the TB parameters were obtained by fitting to a first principle band structure and they are accurate within the chosen orbital set.

---

[11]The anisotropic coupling $J \sim 20$ μeV which was found to be responsible for the small ferromagnetic moment in $Sr_2Cu_3O_4Cl_2$ [112] cannot be estimated within the model proposed here. It requires a more refined treatment incorporating spin-orbit coupling and more orbitals at the Cu site.

[12]In particulary, taking into account t_{pp}, which occurs in fifth order, J_{AA} would be enlarged [115, 155] and could easily reach the experimental value.

Chapter 5

Analysis of spectroscopy on cuprates

The aim of the this chapter is to demonstrate that especially the dialogue between experiment[1] and theory gives many insights into the electronic structure of cuprates. Starting with a short introduction in the experimental techniques, investigations of the occupied and the unoccupied electronic structure of representative model cuprates will be discussed.

5.1 Experimental methods

In this section, the experimental methods applied to gain information about the cuprate compounds will be presented shortly. The occupied and the unoccupied electronic structure have been investigated by means of angle-resolved photoelectron spectroscopy (ARPES) and x-ray absorption spectroscopy (XAS), respectively. The principles of these two methods are illustrated in the following.

5.1.1 Angle-resolved photoelectron spectroscopy

The principle of a photoemission experiment is drawn in Fig. 5.1. Incident photons with the energy $h\nu$ create photoelectrons which leave the sample. In an ARPES experiment the number of photoelectrons per time interval and solid angle (i.e. the intensity) in dependence on the momentum and the kinetic energy is measured. This yields the so-called energy distribution curve which contains valuable information about energy and momentum (if single crystals are used) of the occupied electronic states of the investigated compound. In the experiments presented in this work, a fixed photon energy was used (so-called energy distribution curve mode). The discrimination between different kinetic energies of the photoelectrons is done by means of an electrostatic analyzer. The direction of

---

[1]The experiments discussed in this chapter were performed at the *Institut für Festkörperforschung* of the *Institut für Festkörper- und Werkstofforschung Dresden*
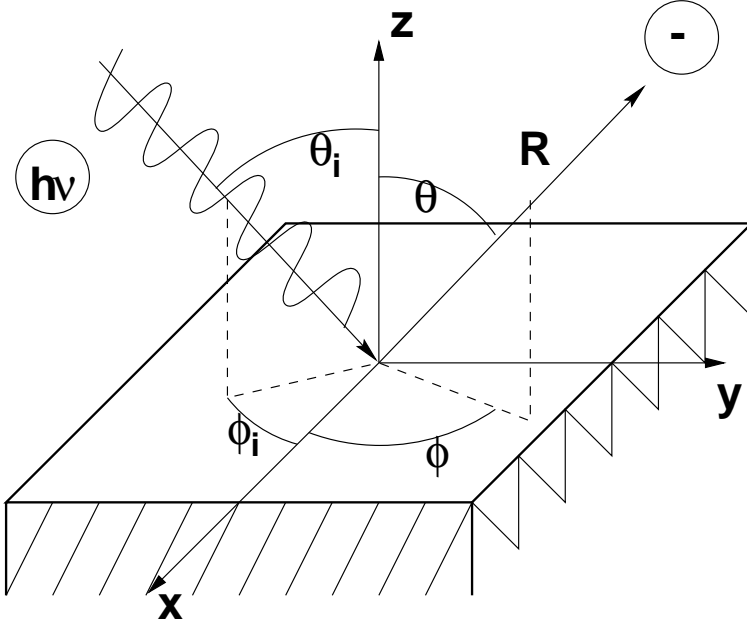
Figure 5.1: Schematic picture of an ARPES experiment

the photoelectron momentum vector is chosen by the azimutal and polar angles ϕ and θ of the energy analyzer with respect to the surface normal (see Fig. 5.1).

Under certain simplifying assumptions, the photocurrent can be written in the form [156]

$$I \propto \sum_{f,i} |\langle f|\mathbf{p}\mathbf{A}|i\rangle|^2 S(\mathbf{k}, E) f(E) \,, \tag{5.1}$$

where i and f denote the initial and the final state, respectively. The quantity $\mathbf{p}$ is the momentum vector of the photoelectron, $\mathbf{A}$ is the vector potential of the incident photon, $f(E)$ and S denote the FERMI- and the spectral function, respectively. In the case of photoelectron spectroscopy, the spectral function $S(\mathbf{k}, E)$ describes the probability to remove an electron with the energy E and the wave vector $\mathbf{k}$. It is related to the single-electron GREEN's function G via

$$S(\mathbf{k}, E) = -\frac{1}{\pi} \Im(G(\mathbf{k}, E)) \,. \tag{5.2}$$

The spectral function is composed of poles of Lorentzian shape, which represent quasiparticles of energy E_i, wave vector $\mathbf{k}$ and life time τ

$$\tau = |Z_{\mathbf{k}} \Im(\Sigma(\mathbf{k}, E))|^{-1} \,, \tag{5.3}$$

wherein $Z_{\mathbf{k}}$ is the spectral weight of the quasiparticle given by

$$Z_{\mathbf{k}} = | \, 1 - \frac{\delta}{\delta E} \Re(\Sigma(\mathbf{k}, E)) \, |_{E_i}^{-1} \,, \tag{5.4}$$

and $\Sigma(\mathbf{k}, E))$ is the self energy. All contributions to the spectral function which cannot be mapped onto a quasiparticle origin are incorporated in the so-called incoherent part of the spectrum.

Knowing the work function of the analyzer $\Phi_{analyzer}$, we can calculate the binding energy E_B of the quasiparticle via

$$E_B = h\nu - E_{kin} - \Phi_{sample} - (\Phi_{analyzer} - \Phi_{sample}) = h\nu - E_{kin} - \Phi_{analyzer}\,. \quad (5.5)$$

The term in brackets is due to the contact potential difference between the analyzer and the sample. The connection between the photoelectron momentum $\mathbf{p}$ and the quasiparticle momentum $\mathbf{k}$ is given by

$$\hbar\mathbf{k}_{\parallel} = \mathbf{p}_{\parallel} \quad (5.6)$$

for the components of the photoelectron and the quasiparticle momentum vectors parallel to the sample surface. There is no momentum conservation perpendicular to the surface. Therefore, it is not possible to determine the component of the quasiparticle momentum vector perpendicular to the sample surface in a direct way and quite sophisticated methods have to be applied to solve this problem [156]. In the case of measurements on $Sr_2CuO_2Cl_2$ and $Ba_2Cu_3O_4Cl_2$, due to the quasi 2D electronic structure, this problem does not arise. This means that there is practically no dependence of the quasiparticle binding energy on the wave vector component perpendicular to the Cu-O-plane and the knowledge of $\mathbf{p}_{\perp}$ is not needed. The component of the quasiparticle wave vector parallel to the sample surface can be easily evaluated from the polar and azimutal analyzer angles ϕ and θ (see Fig 5.1) and the kinetic energy at the quasiparticle peak:

$$\mathbf{k}_{\parallel} \propto \sqrt{E_{kin}}\sin\theta(\cos\phi\mathbf{x} + sin\phi\mathbf{y})\,, \quad (5.7)$$

wherein $\mathbf{x}$ and $\mathbf{y}$ are unit vectors which span the sample surface plane.

The energy-momentum relation of the quasiparticle is not the only information one can get from ARPES experiments. The photoionization matrix element depends on photon energy, the photoelectron momentum, the angle of incidence of the photons (θ_i and ϕ_i in Fig. 5.1) and the initial and final state wave functions.

The choice of photon energy can be used to select different kinds of orbitals because of the different cross sections (see Section 5.3.1). Moreover, it is possible to gain information about the parity of the states with respect to the emission plane. The emission plane is defined as the plane spanned by the photoelectron momentum vector and the sample surface normal. In Fig. 5.2, an example for an emission plane (grey) is shown with the analyzer in the (x-z) plane. Here, the sample meant to be a single crystal of $Sr_2CuO_2Cl_2$ with the CuO_2-planes parallel to the sample surface. The sample is oriented such that the emission plane is
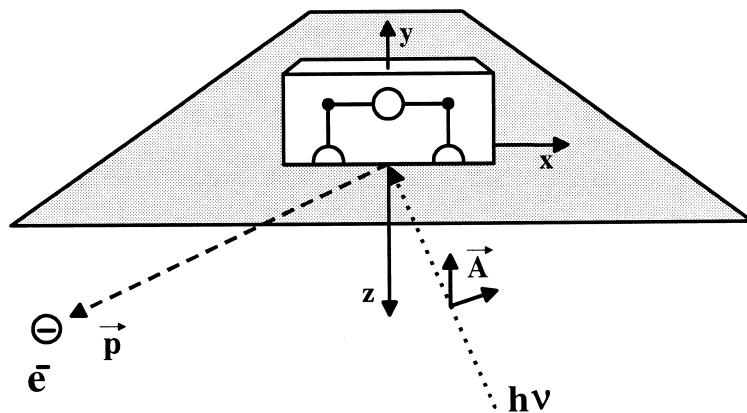
Figure 5.2: Example for an ARPES experiment using the polarization dependence of the photoionization matrix element (after HAFFNER [157]. For details see the text.)

a mirror plane of the geometric structure of the crystal and therefore also a mirror plane of the Hamiltonian describing the corresponding electronic system[2]. The eigenfunctions of the Hamiltonian are simultaneously eigenfunctions of the operator which creates the mirror operation with respect to the emission plane and have a definite parity with respect to this plane. The operator **pA** for the photoionization has definite parity to this plane for the case where **pA** is either completely in or out of the mirror plane. Thus, the operator **pA** has odd parity with respect to the emission plane when the vector potential **A** is perpendicular to this plane and even parity if **A** is parallel to it. In the later sections of this chapter, these situations will be called vertical and horizontal polarization. The photoionization matrix element can thus be brought to vanish in dependence on the parity of initial and final state with respect to the emission plane for vertical or horizontal polarization. Assuming that the states of other electrons do not change during the photoemission process, the photoionization matrix element reduces to

$$\langle i|\mathbf{pA}|f\rangle = \langle \phi_i|\mathbf{pA}|\phi_f\rangle,\tag{5.8}$$

were $\langle \phi_i|$ and $|\phi_f\rangle$ are the orbital of the initial state and the free-electron final state, respectively. The latter one has even parity with respect to the emission plane, otherwise the wavefunction would have a node in the emission plane and there would be no intensity in the detector. Therefore, for vertical polarization, only initial states with odd parity contribute to the photocurrent while only even initial states contribute for horizontal polarization. In this way, it is possible to

---

[2]We neglect here for sake of simplicity the antiferromagnetic order of $Sr_2CuO_2Cl_2$.

extract information about the parity of the initial wave function with respect to the emission plane. This possibility is extensively used in the analyses of Sections 5.2 and 5.3.

5.1.2 X-ray absorption spectroscopy

A method to investigate the unoccupied electronic structure of a solid is the x-ray absorption spectroscopy (XAS). The principle scheme of this experiment is
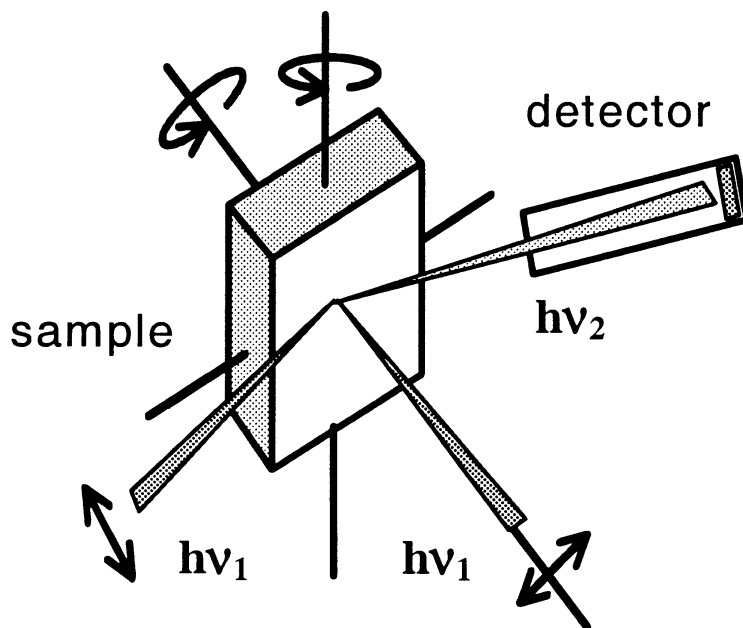
Figure 5.3: Schematic picture of an XAS experiment in fluorescence yield mode. Incoming linearly polarized photons (energy $h\nu_1$) at normal and grazing incidence and fluorescence radiation (energy $h\nu_2$) are shown (after HAFFNER[157].)

drawn in Fig. 5.3. Monochromated photons with the energy $h\nu_1$ are absorbed by the sample. If the photon energy is high enough, it is possible to excite core level electrons into the unoccupied valence states of the solid (see Fig. 5.4). The onset of core level excitations manifests itself as a step-like absorption edge at photon energies around the threshold energy, which is in first approximation the difference between the core level and the lowest lying unoccupied state that can be reached.

To extract information about the unoccupied electronic structure, a relation between the absorption coefficient and the electronic structure is needed. The
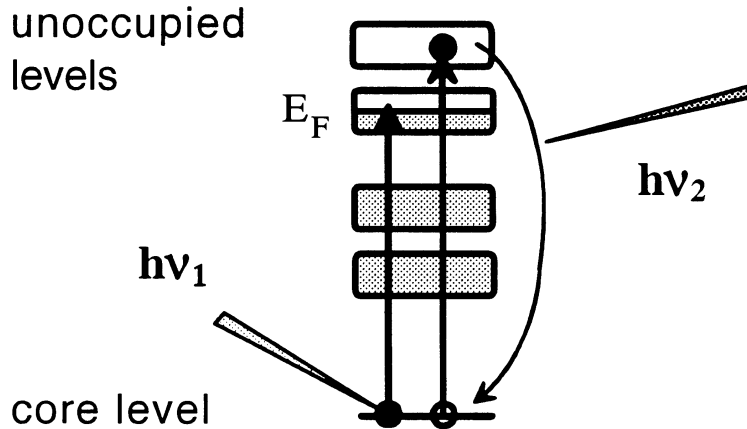
Figure 5.4: Schematic view of core-level excitations into unoccupied levels of the electronic structure by absorption of photons of the energy $h\nu_1$. As origin for the measured fluorescence radiation (energy $h\nu_2$), the decay of an electron-hole pair is drawn (after HAFFNER [157].)

absorption coefficient μ for a photon of the energy $h\nu_1$ in a sample is given by [158]

$$\mu(h\nu_1) = 4\pi^2 \sum_{f,i} |\langle i|H^{int}|f\rangle|^2 \delta(E_f - E_i - h\nu_1) \qquad (5.9)$$

with $\langle i|$ and $|f\rangle$ being the initial and the final state and E_i and E_f their corresponding energies, respectively. The electron photon interaction operator H_{int} is given by

$$H_{int} = -i\hbar\mathbf{A} \sum_j \exp(i\mathbf{k}\mathbf{r}_j)\mathbf{e}\nabla_j \qquad (5.10)$$

with $\mathbf{A}$, $\mathbf{k}$, $\mathbf{e}$ being the vector potential, the wave vector and the unit vector of polarization of the photon, respectively, $\mathbf{r}$ and ∇ are the position and the momentum operators of electrons. Regarding the typical extend of core level wave functions (< 0.5 Å) and the photon energies ($h\nu_1 < 1000$ eV) used in this work, the exponential function can be approximated by unity ($\mathbf{k}\mathbf{r} \ll 1$). With the assumption, that the wavefunctions of the electrons that are not involved in the excitation that and the unoccupied states are unaffected by the core level excitation (sudden approximation), Eq. (5.9) is reduced to a single-particle dipol matrix element. This leads to the following consequences: (I) XAS is a measure of the unoccupied DOS. Because the core level shows no dispersion in momentum space, the occupied DOS due to the core states are delta functions and hence Eq. (5.9) describes the unoccupied DOS only. (II) XAS is site-specific. The core level wave functions are well localized, therefore only transitions into wavefunctions with non-negligible amplitude at the core site are possible. (III) XAS fulfills

dipol selection rules. The angular momenta of the initial and the final state are connected via $l_f = l_i \pm 1$.

If single crystals and polarized radiation (synchrotron radiation) are used, it is possible to distinguish between orbitals of different symmetry. The transition matrix element can be decomposed into CLEBSCH-GORDON coefficients and reduced matrix elements, which only depend on the angular momentum and the main quantum number. Therefore, for a given symmetry, the possible excitations are easily to estimate via the CLEBSCH-GORDON coefficients.

In principle, an XAS experiment could be done in transmission geometry, but the x-ray absorption coefficient is rather high in the soft x-ray region. Thus, such an experiment would require extremely thin samples of 1μm or less which is hard to achieve. Therefore, usually decay products of the core level excitation (AUGER electrons and fluorescence photons ($h\nu$)) are detected (see Fig. 5.4).

5.2 Dispersion of a hole in the Cu_3O_4-plane: A tale of two singlets

Polarization-dependent ARPES measurements of $Ba_2Cu_3O_4Cl_2$ indicate the presence of two different ZHANG-RICE singlets in the two-dimensional Cu_3O_4-plane of this insulating copper oxychloride. With the aid of model calculations, we can show that one singlet is moving in the antiferromagnetically ordered cuprate-like Cu_AO_2 sub-system and the other on the paramagnetic sub-lattice formed by the extra Cu_B atoms.

The electronic structure of the CuO_2-planes is believed to hide the key to high temperature superconductivity in the cuprates. The lowest electron removal state in the CuO_2-plane cuprates is the so-called ZHANG-RICE singlet (ZRS) [103], in which the spin of an intrinsic copper hole, located in the Cu $3d_{x^2-y^2}$ orbital, is compensated by the spin of a hole distributed over the $2p_{x,y}$ orbitals of the surrounding four oxygen atoms. The ZRS forms as a result of p-type doping or of electron removal in photoemission spectroscopy. Recently, angle-resolved photoemission (ARPES) studies of the dispersion of a ZRS in the undoped CuO_2-plane of the oxychloride $Sr_2CuO_2Cl_2$ have gained considerable interest [102, 159], as these data were in approximate agreement with the earlier predictions of the t-J model [160].

In this section, a combined experimental and theoretical study of the dispersion of a single hole in the two-dimensional Cu_3O_4-plane of $Ba_2Cu_3O_4Cl_2$ is presented. As already discussed in Section 3.4.2, this plane can be regarded as a cuprate-like Cu_AO_2 sub-system with additional copper atoms, denoted here as Cu_B. Both Cu_A and Cu_B order antiferromagnetically: the former at 330 K and the latter only at 31 K [43]. We show that as a consequence of this, in a single

ARPES experiment carried out at T = 360 K, it is possible to study the disper-
sion of a ZRS in both an antiferromagnetic and paramagnetic spin background
simultaneously in the same Cu_3O_4-plane.

5.2.1   Experimental

ARPES measurements were recorded at the U2-FSGM beamline [161] at BESSY
with a photon energy of 35 eV using *in situ* cleaved single crystals. The experi-
mental resolution was set to 160 meV in energy and 2° in angle (corresponding
to a **k**-resolution of $0.16\pi/a$). During the measurements, the crystals were held
at a temperature of 360 K.
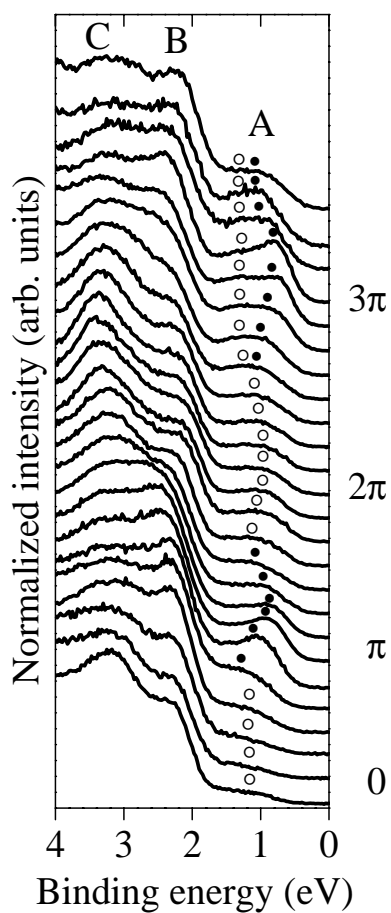
Figure 5.5: ARPES spectra of $Ba_2Cu_3O_4Cl_2$ measured along the $(k_x, 0)$
direction. The values of k_x are expressed in terms of $(1/a \ (\text{Å}^{-1}))$. For
the experimental details see the text and Ref. [162].

Figure 5.5 shows a series of ARPES spectra recorded along the $(k_x, 0)$ direction

in **k**-space, reaching beyond the edge of the second Brillouin zone (BZ). This direction is 45° to the Cu-O bonds in real space and is parallel to M_1 in Fig. 5.6. The electric field vector of the synchrotron radiation was perpendicular to M_1.
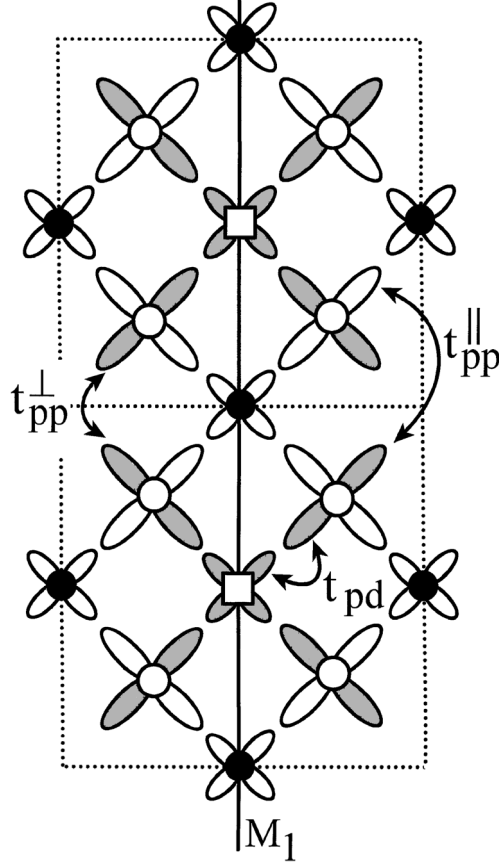
Figure 5.6: Two unit cells of the Cu_3O_4-plane of $Ba_2Cu_3O_4Cl_2$ showing: (•) cuprate-like Cu_A, (□) additional Cu_B and (○) oxygen. The Cu $3d_{x^2-y^2}$ and O $2p_{x,y}$ orbitals are also shown. The orbitals relevant for the motion of the ZRS on the Cu_B sub-lattice are shaded. Also shown schematically are the hopping matrix elements t_{pd}, $t_{pp}^{\parallel}$ and $t_{pp}^{\perp}$ as well as a mirror plane of the Cu_3O_4-surface, marked M_1.

There are three main features observed in the energy range shown in Fig. 5.5, labeled A, B and C. The deeper lying valence band features, B and C, are at least partially due to bands corresponding to the non-mixing oxygen states observed recently for $Sr_2CuO_2Cl_2$ [159]. A detailed discussion of features B and C, as well as other details of the ARPES spectra are given in [162]. It is the behavior of the feature at lowest binding energies (BE) that prompted the following discussion.

On moving away from the Γ point, a weak structure emerges from the main valence band and grows in intensity as its BE decreases, reaching a minimal BE of $\sim$0.8 eV at (π,0). At this $\mathbf{k}$ value, the peak has a width of some 700 meV and displays a considerable asymmetry to the high BE side. Spectra recorded at (π,0) under the same conditions except with a total energy resolution of 70 meV were identical.

At this stage it is instructive to compare these data with those observed for the CuO_2-plane of $Sr_2CuO_2Cl_2$. The analogous ARPES spectra showed a similar feature increasing in intensity and dispersing to lower BE's, reaching both maximal intensity and minimal BE at the ($\pi/2$, $\pi/2$) point of the $Sr_2CuO_2Cl_2$ BZ [102, 159], which is equivalent to the (π,0) point of the $Ba_2Cu_3O_4Cl_2$ BZ. On going beyond ($\pi/2$, $\pi/2$)$_{Sr}$, the ZRS peak in $Sr_2CuO_2Cl_2$ dispersed back to higher BE and its spectral weight fell away very rapidly, thus resulting in a strongly asymmetric intensity profile as a function of $\mathbf{k}$ around ($\pi/2$, $\pi/2$)$_{Sr}$. A detailed discussion of the ARPES data of $Sr_2CuO_2Cl_2$ is given Section 5.3.

As can be seen from Fig. 5.5, in $Ba_2Cu_3O_4Cl_2$, however, significant spectral weight remains at around 1 eV BE over a large region of $\mathbf{k}$-space between (π,0) and (3π,0). In addition, approaching (3π,0), the lineshape is strongly suggestive of the presence of two components (as marked in Fig. 5.5). Thus, while the dispersion of the lowest BE structure observed here around (π,0) and (3π,0) is similar to that in $Sr_2CuO_2Cl_2$, the existence of a clear structure remaining around $\sim$1 eV between (π,0) and (3π,0) and the double-peaked nature of the feature in $Ba_2Cu_3O_4Cl_2$ are significant and important differences with respect to the CuO_2-plane oxychloride. We suggest that these differences indicate that the data shown in Fig. 5.5 can be interpreted in terms of two singlets ZRS_A and ZRS_B, where the $3d_{x^2-y^2}$ orbitals of the Cu_A and Cu_B are hybridized with different sub-systems of the in-plane O $2p_{x,y}$ orbitals (see Fig. 5.6). The filled and open circles in Fig. 5.5 represent the energy positions of ZRS_A and ZRS_B, respectively.

In Fig. 5.7, we provide indirect experimental evidence that the lowest lying electron removal states in $Ba_2Cu_3O_4Cl_2$ are ZRS's. Here, we show ARPES spectra recorded at (π,0) with the polarization vector of the radiation aligned either parallel or perpendicular to the mirror plane M_1 (see Fig. 5.6). Due to the experimental geometry used, this results in photoemission from initial states of either pure even (parallel) or odd (perpendicular) symmetry in regard to reflection in M_1. As can be seen from Fig. 5.7, the ZRS peak (and part of feature B) disappears completely for the parallel case, thus attesting to the pure odd character of the initial state concerned. Further polarization-dependent measurements [162] show the same behavior for the lowest BE feature at $\mathbf{k}$-values between (π,0) and (3π,0). Upon consideration of the Cu_3O_4-plane geometry shown in Fig. 5.6, it is apparent that a purely antibonding combination of the Cu $3d_{x^2-y^2}$ and O $2p_{x,y}$
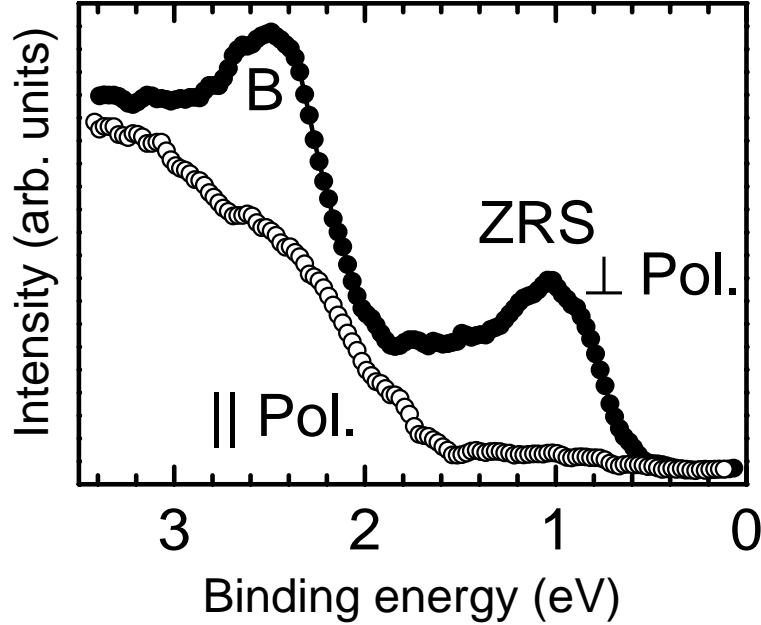
Figure 5.7: Polarization-dependent ARPES spectra of $Ba_2Cu_3O_4Cl_2$ at the $(\pi,0)$ point of the BRILLOUIN zone measured with the electric field vector perpendicular (●) and parallel (○) to the mirror plane M_1.

orbitals yields a feasible initial state with the correct symmetry, whereas a non-bonding configuration, for example, would not. This is fully consistent with the ZRS character of the first electron removal states in $Ba_2Cu_3O_4Cl_2$.

5.2.2 Model calculation

Up to now, we have discussed the qualitative differences between the dispersion relation of ZRS's in the Cu_3O_4-plane of $Ba_2Cu_3O_4Cl_2$ and the CuO_2 plane of $Sr_2CuO_2Cl_2$, and have suggested that the former indicates the presence of two different ZRS's. In order to explore this idea further, we have calculated the motion of these singlets using a model Hamiltonian containing the relevant orbitals and correlation at the copper sites only. The tight-binding parameters result from a fit [163] to the bandstructure for $Ba_2Cu_3O_4Cl_2$ (see Fig. 3.33). For sakes of simplicity, the parameter set is reduced to three transfer integrals (t_{pd}, $t_{pp}^{\perp}$, $t_{pp}^{\parallel}$, see Fig. 5.6) compared with the extended model presented in Section 4.3.1 The coupling between the two O $2p$ orbital sub-systems is provided by the small parameter $t_{pp}^{\parallel} = 0.2$ eV [163], which can be neglected in a first analysis (see also Sec. 4.3.1).

In analogy with $Sr_2CuO_2Cl_2$, the motion on the Cu_A sub-lattice can be described by a t-J model [160] including additional hopping parameters to second and third neighbors [164, 165]. The parameters of such an extended t-J model can be derived from the Cu_A part of our model Hamiltonian by means of the cell-perturbation method [137, 166, 167]. An analogous reduction procedure was also performed for the Cu_B sub-lattice. Each Cu_B $3d_{x^2-y^2}$ hybridizes with a combination of O $2p$ orbitals with b_1 symmetry (shown shaded in Fig. 5.6), denoted here by $\pi_{i\sigma} = (p_{1\sigma} - p_{2\sigma} - p_{3\sigma} + p_{4\sigma})_i/2$. The Hamiltonian (in hole representation) reads:

$$
\begin{aligned}
H \;=\; & \varepsilon_d^B \sum_{i\sigma} d_{i\sigma}^\dagger d_{i\sigma} + U_d \sum_i n_{i\uparrow}^d n_{i\downarrow}^d + \varepsilon_p \sum_{i\sigma} \pi_{i\sigma}^\dagger \pi_{i\sigma} \\
& -\frac{t_{pp}^\perp}{2} \sum_{<ij>} \pi_{i\sigma}^\dagger \pi_{j\sigma} + 2t_{pd} \sum_i (d_{i\sigma}^\dagger \pi_{i\sigma} + h.c.) \,,
\end{aligned}
\tag{5.11}
$$

where the summations run over the Cu_B sub-lattice only and the parameters[3] are: $t_{pp}^\perp = 0.45$ eV, $t_{pd} = 1.7$ eV, $\varepsilon_p - \varepsilon_d^B = 3.6$ eV and $U_d = 10.5$ eV [163, 23]. In the cell perturbation method Eq. (5.11) is diagonalized within a single cell consisting of one Cu_B and four oxygen atoms and considers the coupling to neighboring cells as a perturbation. Adding a hole to the lowest one-hole state within one cell $|\bar{d}\sigma> = \cos\beta|d\sigma> - \sin\beta|\pi\sigma>$ creates predominantly the ZRS_B state $|\Psi>$ which is given by a linear combination of the three possible one-cell singlet states. The higher lying states are projected out and the overlap between neighboring ZRS_B's is provided by $t_{pp}^\perp$. The hopping of ZRS_B's can be derived from the corresponding hopping term in Eq. (5.11):

$$
-\frac{t_{pp}^\perp}{2} \pi_{i\sigma}^\dagger \pi_{j\sigma} \longrightarrow t_B X_i^{\Psi,\bar{d}\sigma} X_j^{\bar{d}\sigma,\Psi}
\tag{5.12}
$$

with $t_B = -\eta^2 t_{pp}^\perp/2$ and written in terms of HUBBARD operators $X_i^{\Psi,\bar{d}\sigma} = |\Psi i><\bar{d}\sigma i|$. The value of $\eta = 0.75$ is calculated by diagonalizing the $3*3$ matrix of the two-hole singlet states within one cell which results in $t_B = -0.13$ eV.

To calculate the dispersion of one hole in the two independent t-J models, the corresponding magnetic background has to be taken into account. As pointed out above, this reveals an important difference between Cu_A and Cu_B. The experiment was performed at T = 360 K which is much larger than T_N^B but of the order of T_N^A. Therefore, we may assume that while the magnetic correlation length on the Cu_A sub-lattice is much larger than the size of the magnetic polaron, its value on the Cu_B sub-lattice can be expected to be of the order of the Cu_B sub-lattice spacing. Correspondingly, the ZRS_B moves in a paramagnetic background

---

[3]Due to the different number of transfer integrals, the parameters of the reduced model are slightly different from the corresponding values given in Sec. 4.3.1.

where its dispersion is determined by the nearest neighbor hopping

$$E_k^{(B)} = E_0^{(B)} + t_B(\cos k_x a + \cos k_y a) \tag{5.13}$$

with a reduction of the bandwidth by only a factor of two [168] in comparison with free fermions, and where a strong broadening from thermal fluctuations can be expected. On the contrary, the ZRS_A moves in an antiferromagnetic background where nearest neighbor hopping (with respect to Cu_A) is suppressed and where the dispersion is well known [160]:

$$\begin{aligned} E_k^{(A)} &= E_0^{(A)} + 0.55 J_A(\cos k_S + \cos k_D)^2 \\ &\quad + \lambda(\cos k_S - \cos k_D)^2 \;, \end{aligned} \tag{5.14}$$

where $k_{S/D} = a(k_x \pm k_y)/2$ is the transformation to the BZ of $Ba_2Cu_3O_4Cl_2$. The bandwidth of (5.14) is $2.2 J_A$ [160], with the parameter $\lambda=0.1$ eV describing the influence of the additional hopping parameters [164, 165]. The energy difference $E_0^{(B)} - E_0^{(A)}$ is determined by the local orbital energies and the binding energies of both the ZRS's and the magnetic polaron on the Cu_A sub-lattice. Its value was estimated to be roughly 0.5 eV.

In Fig. 5.8, we plot the experimental $E(\mathbf{k})$ dispersion relation of the ZRS's in the Cu_3O_4-plane. The width of the symbols represents the experimental $\mathbf{k}$-resolution, and the height of the error bars represents the uncertainty in pinpointing the energy position of the feature concerned (showing, for example, that around the Γ point the exact energy position of the ZRS's is difficult to define). The dispersion relations of the ZRS_A and ZRS_B from (5.13) and (5.14) are shown as the dotted and solid lines in Fig. 5.8. It is clear that the experimentally observed dispersion can be well described without exceeding the limits of the parameters' theoretical estimation. In particular, the dispersion of ZRS_B between $(\pi,0)$ and $(3\pi,0)$ is reproduced, as is the presence of the ZRS_B as an "extra" feature at higher BE's, seen experimentally near $(3\pi,0)$. The overall ZRS bandwidth is hard to determine exactly, thus using Eq. (5.14) only a rough estimate of $J_A=(230 \pm 60)$ meV can be made, which is somewhat larger than both the value derived in Section 4.3.2 and in Ref. [112] and also larger than the usual values for CuO_2-cuprate planes.

In summary, ARPES spectra of $Ba_2Cu_3O_4Cl_2$ indicate the presence of two ZHANG-RICE singlets in the Cu_3O_4-plane. The first belongs to the Cu_AO_2 sub-system whose antiferromagnetic ordering results in a dispersion proportional to the exchange integral, J_A, in analogy with observations of the paradigm CuO_2 plane antiferromagnet $Sr_2CuO_2Cl_2$. The second stems from the Cu_B sub-system, and our model calculations show that its dispersion is consistent with that of a hole moving in a *paramagnetic* background - the bandwidth being proportional to
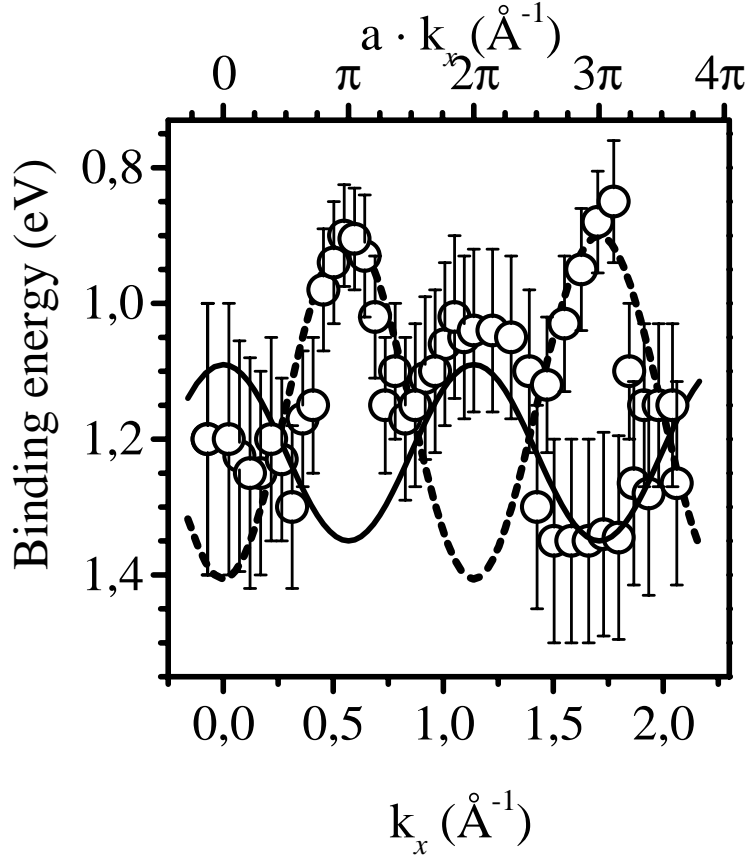
Figure 5.8: Experimental dispersion relation of the ZHANG-RICE singlets in $Ba_2Cu_3O_4Cl_2$ along $(k_x, 0)$ (symbols), compared with a superposition of the calculated dispersions $(5.13)(ZRS_B$, solid line) and $(5.14)(ZRS_A$, dotted line). For the parameters used in the calculation, see the text.

the hopping integral between Cu_B sites, t_B. Thus, as regards the dispersion of a hole in a magnetic spin background, the Cu_3O_4 plane of $Ba_2Cu_3O_4Cl_2$ represents simultaneously both the low and very high doping limits in cuprate materials.

In the present discussion, we concentrated our interest on the interpretation of the lowest electron removal state. The following section will show for the example[4] of $Sr_2CuO_2Cl_2$ that ARPES is a powerful tool to analyze the valence band as well.

---

[4]We made also a similar analysis of the VB photoemission spectrum for $Ba_2Cu_3O_4Cl_2$ [162].

5.3   Analysis of the valence-band photoemission spectrum of $Sr_2CuO_2Cl_2$ along the high symmetry directions

$Sr_2CuO_2Cl_2$ was the first undoped cuprate for which the angle resolved photoemission measurement of its lowest excitations was successful [102, 169, 170]. These excitations are well described by one hole in a 2D quantum antiferromagnet [171, 172, 173]. Deviations from the one-hole dispersion of the pure *t-J* model can be reduced by taking into account hopping terms to second and third neighbors [164, 167]. In the same substance the low binding energy edge of the main valence band has been interpreted in terms of non-bonding oxygen orbitals which are completely decoupled from the copper system [159]. These features were known before as "1 eV-peak" [174]. The non-bonding states are especially pronounced at (π, π) where they have minimal binding energy. But the detailed structure of the complete valence band has never been analyzed up to now and that is the aim of the present work. Furthermore, we will show that additional information on the low binding-energy features can be obtained by analyzing their dependence on the polarization of the photon.

Polarization-dependent photoemission measurements are an effective tool to analyze the electronic structure of the valence band in detail. By measuring along high-symmetry directions all bands can be classified according to their symmetry properties. This allows a very precise comparison between experiment and different theoretical predictions. As already discussed, in all the cuprates electron correlations have a strong influence on the electronic bands near the FERMI level which is especially pronounced in undoped substances [172]. However, the influence of correlations on those parts of the valence band with larger binding energies is less clear. We will show that the combination of polarization-dependent ARPES measurements with theoretical investigations taking into account the electron correlation to a differing extent (LDA, LDA+U) provides a unique possibility to answer this question.

The model cuprate $Sr_2CuO_2Cl_2$ is very well suited for such an investigation. It has a tetragonal structure with ideal planar CuO_2-layers [106] and cleaves readily parallel to the CuO_2-planes. Furthermore, the presence of Cl instead of apex oxygen allows a restriction of the states which contribute to the ARPES spectra to those of the pure CuO_2-plane alone. This can be achieved by choosing a photon energy close to the COOPER minimum for Cl $3p$ photoemission, i.e. Cl $3p$ states will then have a small photon cross section. In this manner we intend to study an ideal situation whose main characteristics should be generic to all the cuprates.

It is known that simple LDA fails to predict the insulating ground state of undoped cuprates [81]. There are several improvements of LDA such as the self-interaction correction (SIC) method [21] or LDA+U [175] which has al-

ready been applied to the case of lanthanum cuprate La_2CuO_4 [176]. Here,
we apply LDA+U plus a symmetry analysis at special k-points to interpret
the polarization-dependent photoemission data for $Sr_2CuO_2Cl_2$, where the ac-
tual value of U is chosen to describe the experimental situation.

5.3.1 Experimental

The ARPES measurements were performed[5] using linearly polarized 35 eV pho-
tons from the crossed undulator beamline U2 of the BESSY I facility and BESSY's
HIRES photoelectron spectrometer [161]. The angular resolution was set to $\pm$
1° which gives a momentum resolution of $\pm$ 0.05 Å^{-1} for states of 1 eV binding
energy, this corresponds to 12 % of the distance between Γ and $(\pi,0)$. A total
energy resolution (resulting from both the monochromator and electron analyzer
resolutions) of 150 meV was applied. The ARPES spectra have been recorded in
the electron distribution curve (EDC) mode from both Γ to (π,π) and Γ to $(\pi,0)$.
In the latter case, the sample was oriented in such a way that the Cu - O bonds
of the CuO_2-plane were aligned parallel to the fixed, horizontal emission plane,
while in the former case, the Cu - O bonds were aligned at an angle of 45° with
respect to the emission plane. All spectra were recorded at 300 K.

The electronic structure of the valence band (VB) is derived from O $2p$, Cu $3d$
and Cl $3p$ orbitals, but for 35 eV photon energy, the photoionization cross section
of the Cl $3p$ orbitals is much smaller than that of the O $2p$ and Cu $3d$ orbitals[6],
which therefore dominate the ARPES VB spectra. The measurements had been
performed at room temperature which is slightly above the Neél temperature of
$Sr_2CuO_2Cl_2$ (256 K). Although we are aware that AFM fluctuations are impor-
tant, we nevertheless analyzed the spectra in terms of the first BRILLOUIN zone
(BZ) of the paramagnetic CuO_2 plane of $Sr_2CuO_2Cl_2$. We will see that this is
especially justified for the bands with dominant oxygen character, whereas one
observes some deviations for those bands which couple strongly with the copper
spins. The geometrical structure of a CuO_2 plane has two mirror planes[7] (de-
noted M_1 and M_2 in Fig. 5.9). All the bands with a wave vector between Γ and
(π, π), parallel to the mirror plane M_1, can be classified to be either symmetric
or antisymmetric with respect to M_1, and analogously also for wave vectors along
$\Gamma - (\pi, 0)$ with respect to reflections at M_2. Experimental information about the
parity of the valence band states with respect to a mirror plane can be obtained by

---

[5]For further experimental details see Ref. [177].

[6]For 35 eV photons the corresponding cross sections are 9.4 Mb for Cu $3d$, 8.0 Mb for O $2p$
and 0.69 Mb for Cl $3p$ [178].

[7]In fact, there is a second mirror plane parallel to M_2 but going only through oxygen position.
From the point of view of group theory it is identical to M_2 in the paramagnetic case.
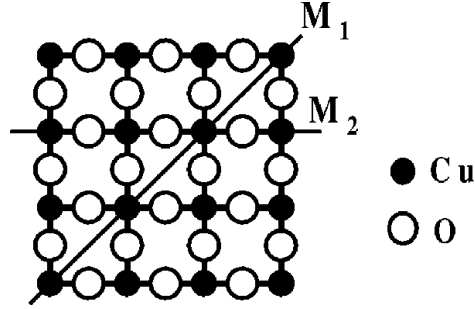
Figure 5.9: The mirror planes of the CuO_2-plane in $Sr_2CuO_2Cl_2$. Filled (open) circles correspond to copper (oxygen) atoms.

recording the ARPES spectra with either perpendicular or parallel polarization of the electric field vector of the incoming radiation with respect to an emission plane which is parallel to a mirror plane of the system. It can be shown [179], that for parallel polarization only initial valence band states which are even with respect to the emission/mirror plane contribute to an ARPES spectrum while for perpendicular polarization, only states which are odd with respect to the emission/mirror plane are seen in a spectrum (see Section 5.1). The polarization of the electric field vector was chosen by using either the vertical or horizontal undulator, which corresponds to perpendicular or parallel polarization with respect to the emission plane. The emission plane is parallel to the mirror plane M_1, if the ARPES spectra are recorded along the (π,π) direction, while it is parallel to the mirror plane M_2 for spectra along the $(\pi,0)$ direction. For perpendicular polarization, the electric field vector is always parallel to the CuO_2-planes, i.e. only in-plane orbitals as O $2p_{x,y}$ or Cu $3d_{x^2-y^2}$ contribute to the spectra. For parallel polarization, the electric field vector is completely in-plane only at normal-incidence. At any other incidence angle of the photon beam, the electric field vector has an out-of-plane component and there are also contributions from out-of-plane orbitals such as O $2p_z$ to the ARPES spectra.

5.3.2 Band structure calculations

As already discussed in Section 3.4.1, the LDA band structure of $Sr_2CuO_2Cl_2$ (Fig. 3.30) shows an antibonding band built up of Cu $3d_{x^2-y^2}$ and O $2p_{x,y}$ orbitals crossing the FERMI level. This contradicts the experimentally observed non-metallic behavior which already indicates that one has to treat the electron correlations in a more explicit way. One could conjecture that the only effect of correlations is to split the half-filled antibonding band leaving the structure of

the other valence bands roughly unchanged. That is not the case, however, as will become clear from our following analysis. One can also observe in Fig. 3.30 that there is nearly no dispersion of the relevant band in the z direction and all discussions in the present paper will be restricted to the CuO_2-plane only.

To obtain more information about the structure of the valence band in our LCAO-LDA we have calculated the orbital weight (see Appendix A) of each band at the high symmetry points. Due to the low cross section of the Cl $3p$ orbitals for 35 eV photon energy we concentrate on the Cu $3d$ and O $2p$ orbitals (i.e. on 11 bands). The eigenfunctions with a dominant contribution from Cu $3d$ and O $2p$ orbitals are collected in Table 6.1 in Appendix D. The in-plane oxygen orbitals are divided into p_σ orbitals which are directed to the Cu-site and p_π orbitals perpendicular to them [152]. There are two combinations for each: p_σ and $\tilde{p}_\sigma$, (p_π and $\tilde{p}_\pi$), which are antisymmetric and symmetric with respect to reflection in M_1, respectively. The precise definition of these orbitals will be given in the next section.

Thus, we are able to predict the symmetry of each band at the high symmetry points in the BRILLOUIN zone (BZ). However, as will be seen later, the order of energy levels of the LDA calculation is incompatible with the experimental spectra. Moreover, as it was mentioned already, LDA calculations are unable to describe the MOTT insulating ground states of the undoped cuprates and do not produce the Cu local moments that are present in these systems. The splitting of the spectral density due to the $3d_{x^2-y^2}$ states away from the FERMI energy E_F due to COULOMB correlations and the resulting reduction in Cu-O hybridization is expected to be largely missing in such calculations. However, what, if any, changes there are from the LDA bands away from E_F is unclear, particularly well above T_N, where the magnetic scattering due to antiferromagnetic spin fluctuations should be more or less incoherent. Addressing this question is one of the main goals of the present discussion. In the following we develop a more sophisticated LDA+U calculation taking into account explicitly the effects of strong correlations. As a preliminary step we formulate an effective tight-binding model which will be fitted both to the LDA+U band structure calculations and the ARPES VB spectra.

5.3.3 Symmetry analysis and tight-binding model

The polarization-dependent ARPES measurements of VB states along the two high-symmetry directions $\Gamma - (\pi, \pi)$ and $\Gamma - (\pi, 0)$ discriminate the parity of these states with respect to reflections in the corresponding mirror planes M_1 and M_2. To make the analysis of the experimental data more straightforward it is helpful to incorporate the symmetry properties of the VB states in our approach

from the beginning. This becomes especially clear by constructing an effective tight-binding (TB) model taking into account the point-group symmetry of the VB states. The TB model will be restricted to the 11 bands of Cu $3d$ and O $2p$. Of course, as can be seen in Table 6.1 (Appendix D), there occurs in some cases a quite strong mixing with the Cl subsystem, but in the following we will assume that this mixing is taken into account by the particular values of the TB parameters.

We start with the description of in-plane oxygen orbitals whose analysis is more involved than that for the copper orbitals or for the out-of-plane orbitals. We introduce the annihilation operator of an electron in the two oxygen π-orbitals belonging to an elementary cell at position $\vec{i}$ ($\vec{i}$ is a site of the square lattice) as $p_{i+\beta/2}^{(\alpha)}$, where $(\vec{\alpha}, \vec{\beta}) = (\vec{x}, \vec{y})$ or $(\vec{y}, \vec{x})$ with $\vec{x}$ and $\vec{y}$ to be the two orthogonal unit vectors of the lattice. The d_{xy} orbitals hybridize with a particular combination of oxygen orbitals arranged over the plaquette at site $\vec{i}$: $p_{\pi i} = \frac{1}{2}(p_{i+x/2}^{(y)} - p_{i-x/2}^{(y)} + p_{i+y/2}^{(x)} - p_{i-y/2}^{(x)})$. This plaquette's π-orbitals are not orthogonal to each other. The orthogonalization can be made by introducing first the FOURIER transformation for the original p_π-orbitals

$$p_\pi^{(\alpha)}(q) = \frac{1}{\sqrt{N}} \sum_i p_{i+\beta/2}^{(\alpha)} e^{-i\vec{q}(\vec{i}+\vec{\beta}/2)} . \qquad (5.15)$$

At the second step we define two kinds of canonical FERMI-operators

$$\begin{aligned} p_\pi(q) &= \lambda_q^{-1} i(s_{q,y} p_\pi^{(y)}(q) - s_{q,x} p_\pi^{(x)}(q)) \\ \tilde{p}_\pi(q) &= \lambda_q^{-1} i(s_{q,x} p_\pi^{(y)}(q) + s_{q,y} p_\pi^{(x)}(q)) \end{aligned} \qquad (5.16)$$

where $s_{q,\alpha} = \sin(q_\alpha/2)$ ($\alpha = x, y$) and $\lambda_q = \sqrt{s_{q,x}^2 + s_{q,y}^2}$. It is easy to see that p_π and $\tilde{p}_\pi$ are orthogonal with respect to each other. The definition (5.16) provides an equivalent representation for π-orbitals in terms of $p_\pi(q)$ and $\tilde{p}_\pi(q)$, instead of the original $p_\pi^{(x)}(q)$ and $p_\pi^{(y)}(q)$ operators and takes into account the point group symmetry of the CuO_2-plane. In particular, for q along $\Gamma - (\pi, \pi)$, the p_π-orbital is antisymmetric with respect to reflections in the mirror plane M_1, while the $\tilde{p}_\pi$-orbital is symmetric (see Fig. 5.10). Along $\Gamma - (\pi, 0)$, we find p_π to be symmetric and $\tilde{p}_\pi$ to be antisymmetric with respect to reflection in M_2.

Turning now to the oxygen σ-orbitals we carry out the same procedure as above with the corresponding $p_{i+\alpha/2,\sigma}^{(\alpha)}$ operators ($\vec{\alpha} = \vec{x}, \vec{y}$). In this case, introducing the plaquette representation instead of defining the original $p_\sigma^{(\alpha)}$ operators in momentum space, we define a new pair of canonical FERMI-operators p_σ and $\tilde{p}_\sigma$:

$$\begin{aligned} p_\sigma(q) &= \lambda_q^{-1} i(s_{q,x} p_{q\sigma}^{(x)} - s_{q,y} p_{q\sigma}^{(y)}) \\ \tilde{p}_\sigma(q) &= \lambda_q^{-1} i(s_{q,y} p_{q\sigma}^{(x)} + s_{q,x} p_{q\sigma}^{(y)}) . \end{aligned} \qquad (5.17)$$
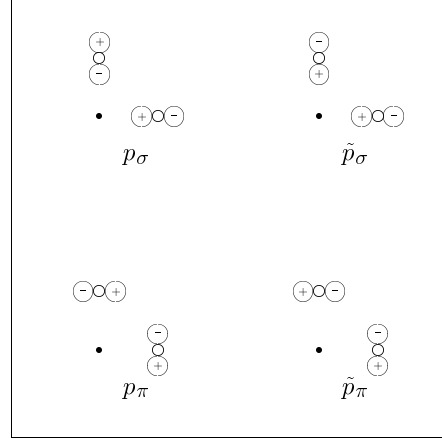
Figure 5.10: Sketch of the different oxygen orbitals within one unit cell of $Sr_2CuO_2Cl_2$ (filled circles - copper, open circles - oxygen) for momenta $q \to 0$ along $\Gamma - (\pi, \pi)$.

The notation is chosen in such a way that the $p_\sigma(q)$ $(\tilde{p}_\sigma(q))$-orbitals have the same symmetry properties with respect to reflections at M_1 and M_2 as the $p_\pi(q)$ or $\tilde{p}_\pi(q)$-orbitals, respectively.

As the definition of the corresponding copper annihilation operators is quite standard, we may write down the TB Hamiltonian

$$H_t = \sum_{q\mu\nu s} c^\dagger_{\mu s}(q) H_{\mu\nu}(q) c_{\nu s}(q) \ . \tag{5.18}$$

Here, $c_{\mu s}$ is an annihilation operator of either an oxygen p orbital or a copper d orbital, where the indices μ and ν denote the 11 different orbitals and s denotes the spin. All orbitals can be classified as to whether they hybridize in-plane or out-of-plane and there is no coupling between the two subsystems. The orbitals involved in the hybridization in-plane are p_σ, p_π, $\tilde{p}_\sigma$, $\tilde{p}_\pi$, $d_{x^2-y^2}$, d_{xy}, $d_{3z^2-r^2}$. The explicit form of the TB-Hamiltonian for in-plane orbitals is given in Ref. [177]. The in-plane part of the TB-model has 11 parameters: the on-site energies ε_d (for $d_{x^2-y^2}$), ε_D (for d_{xy}) and $\varepsilon_{\tilde{d}}$ (for $d_{3z^2-r^2}$) as well as ε_p (corresponding to p_σ) and ε_π; the hopping matrix elements t_{pd}, t_{pD}, $t_{p\tilde{d}}$, t_{pp}, $t_{\pi\pi}$ and $t_{p\pi}$. Besides the orbitals hybridizing in-plane we have to consider those involved in hybridization out-of-plane: O $2p_z$, Cu $3d_{xz}$ and Cu $3d_{yz}$. Restricting ourselves to nearest neighbor hopping leads to two 2×2 matrices with on-site energies ε_{pz} and ε_{dz} and the hopping matrix element t_{pdz}.

In order to analyze the experiment it is important to know the parity of the orbitals with respect to reflections at the corresponding mirror planes M_1 and

M$_2$. This can also be expressed in terms of group theory since for k vectors along the line $\Gamma - (\pi, \pi)$ all wave functions can be classified in terms of irreducible representations of the small group C_{2v} [180, 181, 182]. The bands built up from the in-plane orbitals d_{xy}, $d_{3z^2-r^2}$, $\tilde{p}_\sigma$ and $\tilde{p}_\pi$ belong to the representation A_1 and are symmetric with respect to reflections at M$_1$, whereas $d_{x^2-y^2}$, p_σ and p_π belong to A_2 and are antisymmetric. The same small group C_{2v} also acts along $\Gamma - (\pi, 0)$ and the subdivision of the in-plane orbitals is as follows: A_1 (symmetric): $d_{x^2-y^2}$, $d_{3z^2-r^2}$, p_σ, p_π and A_2 (antisymmetric): d_{xy}, $\tilde{p}_\sigma$, $\tilde{p}_\pi$. The corresponding small groups at the high-symmetry points Γ, (π, π) and $(\pi, 0)$ are D_{4h} and D_{2h} and the assignment of the different orbitals to the corresponding irreducible representations is given in Table 6.3 in Appendix D. Of course, the group theoretical analysis is not only valid for the TB model but also for the LDA bands (Table 6.1 in Appendix D).

The TB-Hamiltonian (5.18) should be completed by an interaction term

$$H = H_t + H_U \qquad (5.19)$$

which will not be written out explicitly. This is just a direct extension of the three-band EMERY model to the case of the complete set of 11 bands for the CuO$_2$-plane. The interaction term H_U involves intrasite HUBBARD repulsion for different kinds of copper- and oxygen-orbitals and appropriate intersite copper-oxygen repulsions. In order to establish the one-electron parameters entering into Eq. (5.19) one has to keep in mind that these parameters are "bare" ones while the results of the band structure calculations should be interpreted in terms of a mean-field solution of Eq. (5.19) [183]. To arrive at the bare parameters, one would have to take into account the ground-state properties of the CuO$_2$-plane and approximate the COULOMB interaction terms.

In an undoped cuprate compound as Sr$_2$CuO$_2$Cl$_2$, the ground state of a particular CuO$_2$-plane contains one hole per cell which is shared between $d_{x^2-y^2}$ and p_σ orbitals. Thus a convenient description of the ground state is to introduce the deviations $\langle n_s^d \rangle_h = 1 - \langle n_s^d \rangle$ and $\langle n_s^p \rangle_h = 1 - \langle n_s^p \rangle$ from the full band (Cu $3d^{10}$ O $2p^6$) electron occupancy. A rough estimate is $\langle n_s^d \rangle_h \approx 0.7$ and $\langle n_s^p \rangle_h \approx 0.3$. Here $\langle n_s^p \rangle$ means the electron number in the p_σ orbital with spin s (one should note that the occupation of a local oxygen orbital is only half that number). Now the mean-field ("screened") one-electron energies $\bar{\varepsilon}_{\mu s}$ read as follows:

$$\bar{\varepsilon}_{ds} = \varepsilon_d + U_d - U_d \langle n_{\bar{s}}^{(d)} \rangle_h - 2U_{pd} \langle \sum_{s'} n_{s'}^{(p)} \rangle_h$$

$$\bar{\varepsilon}_{ps} = \varepsilon_p + U_p - 2U_{pd} \langle \sum_{s'} n_{s'}^{(d)} \rangle_h - \frac{1}{2} U_p \langle n_{\bar{s}}^{(p)} \rangle_h$$

$$\bar{\varepsilon}_D = \varepsilon_D + U_d - U_{dD} \langle \sum_{s'} n_{s'}^{(d)} \rangle_h - 2U_{Dp} \langle \sum_{s'} n_{s'}^{(p)} \rangle_h$$

$$\bar{\varepsilon}_\pi \;\; = \;\; \varepsilon_p + U_\pi - \frac{1}{2}U_{p\pi}\langle\sum_{s'} n_{s'}^{(p)}\rangle_h - 2U_{d\pi}\langle\sum_{s'} n_{s'}^{(d)}\rangle_h \; , \qquad (5.20)$$

where $\bar{s} = -s$. There are also similar expressions for $\bar{\varepsilon}_{\tilde{d}}$, $\bar{\varepsilon}_{dz}$, $\bar{\varepsilon}_{pz}$ which we do not specify here.

In the paramagnetic LDA band structure where the correlation effects are treated only in an averaged manner, the screening effect is nearly the same for all d-levels. So, in the LDA approach the effects of strong correlations due to U_d are missed. An obvious way to adopt these effects is to treat the ferromagnetic solution by putting, for instance, $\langle n_\downarrow^d\rangle_h = 0$, and $\langle n_\uparrow^d\rangle_h = n^d$. Then $\bar{\varepsilon}_{d\uparrow} = \varepsilon_d + U_d - 2U_{pd}\, n^p$ ($n^p = \sum_s \langle n_s^p\rangle_h$), is shifted upwards while $\bar{\varepsilon}_{d\downarrow} = \varepsilon_d + U_d(1-n^d) - 2U_{pd}n^p$ is shifted equally downwards with respect to the paramagnetic solution. Regarding the other d-levels, let us assume for the moment the rough estimate for the intra-site COULOMB parameters $U_{dD} \simeq U_d$. Then we can see that

$$\bar{\varepsilon}_D = \varepsilon_D + U_d(1 - n^d) - 2U_{pd}\, n^p \; , \qquad (5.21)$$

and the d_{xy} level as well as all the other remaining Cu d-levels are shifted as was the lower $\bar{\varepsilon}_{d\downarrow}$. The spin dependence of $\bar{\varepsilon}_{ps}$ in Eq. (5.20) is much less pronounced than for $\bar{\varepsilon}_{ds}$ and is neglected in the following.

Thus, although being somewhat awkward, the ferromagnetic solution provides a better description of the strong electron correlations, giving a more reasonable energy position and occupancy of the different orbitals. Just this approach is taken by us to carry out the LDA+U calculation. The details of the procedure and some results of these calculation are presented in the next section.

5.3.4   LDA+U calculation

The main effect of a mean-field treatment of the multi-band HUBBARD model is a shift of the on-site copper energies against the oxygen ones. Furthermore, the on-site energy of the Cu $3d_{x^2-y^2}$ orbital is split into one for single occupation and one for double occupation. If the site is singly occupied with a spin down electron, this corresponds to a split of the levels into one for spin up $\bar{\varepsilon}_{d\uparrow}$ (minority spin) and one for spin down $\bar{\varepsilon}_{d\downarrow}$ (majority spin). This can also be achieved by an LDA+U calculation [175] including all valence orbitals.

We performed LDA+U calculations for $Sr_2CuO_2Cl_2$ using a ferromagnetic splitting in order to study changes in hybridization compared to the LDA results. The on-site energy of the unoccupied, spin up Cu $3d_{x^2-y^2}^{\uparrow}$ orbital (minority spin) is shifted by 2 eV upwards and the occupied, spin down Cu $3d_{x^2-y^2}^{\downarrow}$ orbital (majority spin), as well as both spin directions for all the remaining Cu d-orbitals are shifted by 2 eV downwards. The energy shifts were added at each step of the

self-consistency cycle until the charge-distribution was stable. We did not try to connect the chosen energy shifts with the model parameters such as, for instance, U_d, U_{pd}, U_p. According to Eq. (5.20), the actual shift depends also on the occupation numbers $\langle n_s^{(d)} \rangle_h$ and $\langle n_s^{(p)} \rangle_h$. Since we did not shift the oxygen levels, our choice corresponds in fact to the difference between U_d and U_p weighted with the corresponding occupation numbers.
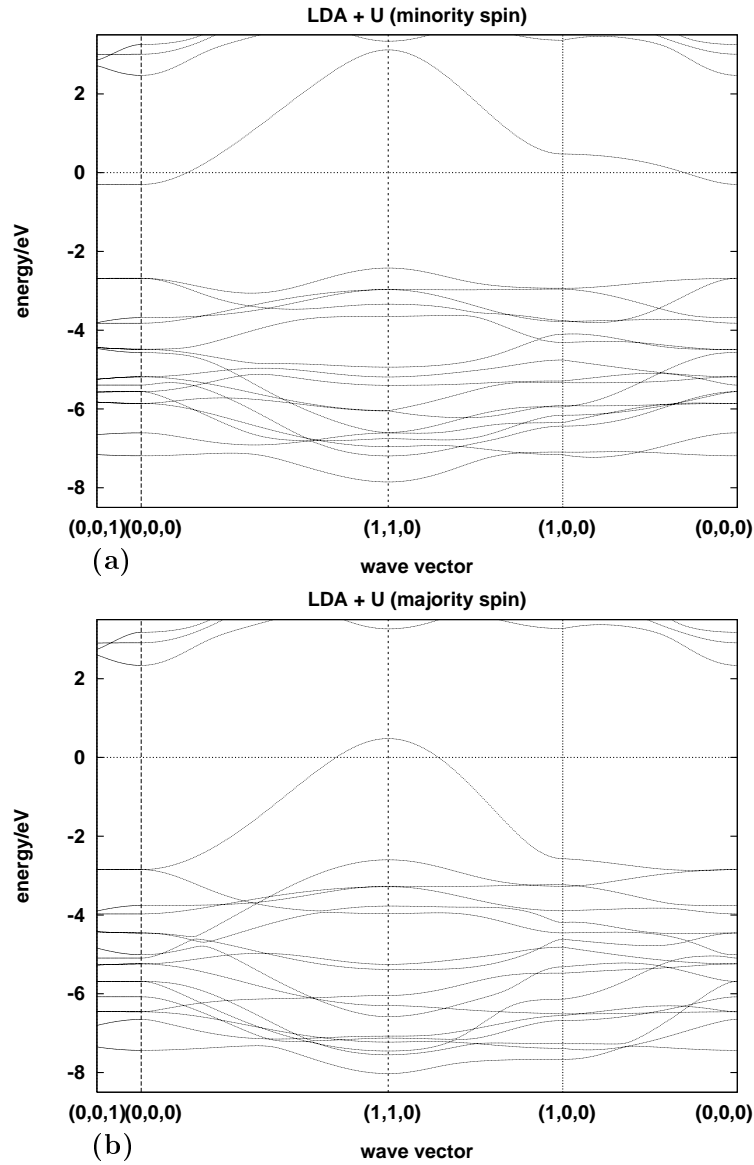
Figure 5.11: LDA+U band structure of $Sr_2CuO_2Cl_2$: (a) minority spin ($\uparrow$), (b) majority spin ($\downarrow$).

The results of the LDA+U calculation are presented in Fig. 5.11 and Table 6.2 in Appendix D. The mainly unoccupied, minority band of $d_{x^2-y^2}$ and p_σ character can be roughly interpreted as the upper HUBBARD band. The corresponding band for majority spin lies just below the FERMI level and has dominantly oxygen character. Since its spin is opposite to the spin of the copper hole, there is some justification to interpret that band as the mean field representation of the ZHANG-RICE singlet. But due to our ferromagnetic spin structure it has a completely wrong dispersion relation[8]. The bandwidth of both bands is expected to be strongly reduced by correlation effects in comparison with Fig. 5.11 such that a gap opens.

Next in binding energy we find bands with dominantly oxygen character. The nonbonding oxygen band with lowest binding energy at (π, π) is identified to be of pure p_π character. The oxygen bands occur at nearly the same energy for both spin directions. In fact, only the bands with a considerable weight of the Cu $3d_{x^2-y^2}$ orbital show a strong splitting between spin up and spin down. Therefore we present in Table 6.2 (Appendix D) only the position of minority spin bands and both spin directions for bands with a contribution from the $3d_{x^2-y^2}$ orbital[9]. The actual value of the energy shifts of the copper bands in our LDA+U calculation has little influence on the upper oxygen bands, only their copper character is changed. We have chosen such a shift that the copper bands are at the lower edge of the valence band, but are not yet split off the valence band. This is important in order to achieve good agreement with the experimental results.

Let us now compare the LDA and LDA+U results starting at (π, π). In both cases (Figs. 3.30 and 5.11), we find a group of 5 bands at around 3 eV binding energy, but the order of energy levels is completely different in the two cases. For example, the antisymmetric p_π band has lowest binding energy of ≈ 2.5 eV in the LDA+U calculation. In Fig. 3.30 (LCAO-LDA), however, all the other 4 bands of that group have lower BE than the p_π level. A similar rearrangement of energy levels can be observed at the Γ point. Due to symmetry reasons there is no hybridization between copper and oxygen bands there. The energy position of the oxygen bands is nearly the same for LDA and LDA+U, but the copper bands

---

[8]The energy position and dispersion of the ZHANG-RICE singlet are very sensitive to local AFM correlations which are well pronounced in the sample measured. To provide a correct description of the ZHANG-RICE singlet (and its triplet partner) one has to subtract two orbitals, p_σ and $d_{x^2-y^2}$, from the 11-band manifold. Supplementary calculations for this two-band HUBBARD model, done within the cell-perturbation method, led to a good account of the ZHANG-RICE singlet dispersion measured [167].

[9]It should be noted that even the pure oxygen bands have a small energy difference of 0.17 eV between both spin directions which is the same for all bands. The reason for that difference is the overlap between spin up and spin down at the FERMI energy. The position of spin down bands in Table 6.2 in Appendix D is corrected by this 0.17 eV.

are shifted. The in-plane oxygen bands are twofold degenerated and occur twice in the LDA+U result with binding energies of 2.69 and 5.57 eV, respectively.

5.3.5 Comparison with the experiment

High-symmetry points

The experimental ARPES spectra at the high symmetry points for both polarization directions are presented in Fig. 5.12. At the Γ point, there are two possible orientations of the sample. Therefor, the symmetry of states may be probed with respect to reflections in either M_1 (sample directed such that the photoelectron momentum is along $\Gamma - (\pi, \pi)$, Fig. 5.12(a)), or M_2 (sample directed such that the photoelectron momentum is along $\Gamma - (\pi, 0)$, Fig. 5.12(b)). The first peak at 2.9 eV binding energy in the experimental spectra at the Γ point with the sample oriented such that the k-vector is along $\Gamma - (\pi, \pi)$ (Fig. 5.12(a)) is equally strong for both polarization directions. This leads us to interpret it as the two pure oxygen bands $(p_\pi p_\sigma)$ and $(\tilde{p}_\pi \tilde{p}_\sigma)$ which are antisymmetric and symmetric with respect to reflections at M_1, respectively[10]. These bands occur in the LDA+U calculation as the two-fold degenerated in-plane oxygen bands at 2.69 eV binding energy. According to this interpretation we would expect an identical peak for both spin directions also at the Γ point with the sample oriented such that the k-vector is along $\Gamma - (\pi, 0)$ (Fig. 5.12(b)). As one can see, Fig. 5.12(b) deviates only slightly from that expectation. In the LDA result, however, there are three copper levels between 2.3 and 3 eV binding energy. Since every copper-level has different symmetry properties with respect to M_1 and M_2 that would lead to strong differences between both polarization directions which is not observed. Therefore, we assign each experimental peak with the help of the LDA+U results. Each pure band is denoted by one orbital only. For the mixed bands we choose a notation using two orbitals, where the first one is the dominant one. The experimental peak positions are compared with the LDA+U positions in Table 5.1.

Let us continue our interpretation of the spectra at the Γ point with the peak at 3.9 eV. It is seen with horizontal polarization in Figs. 5.12(a) and 5.12(b). Therefore, we interpret it as the out-of-plane oxygen $2p_z$ orbital. We observe also a small contribution of this peak with the "wrong" polarization in Fig. 5.12(a) which is even larger in Fig. 5.12(b). However, there is no band with the corre-

---

[10]In fact, the oxygen in-plane wave functions have to be defined by the limit $k_x = k_y = k \to 0$ to have a defined parity with respect to M_1. In the limit $k_x = k \to 0$, $k_y = 0$ they have a defined parity with respect to M_2. That arbitrariness can be explained since they build the two-dimensional representation E_u at the Γ point.
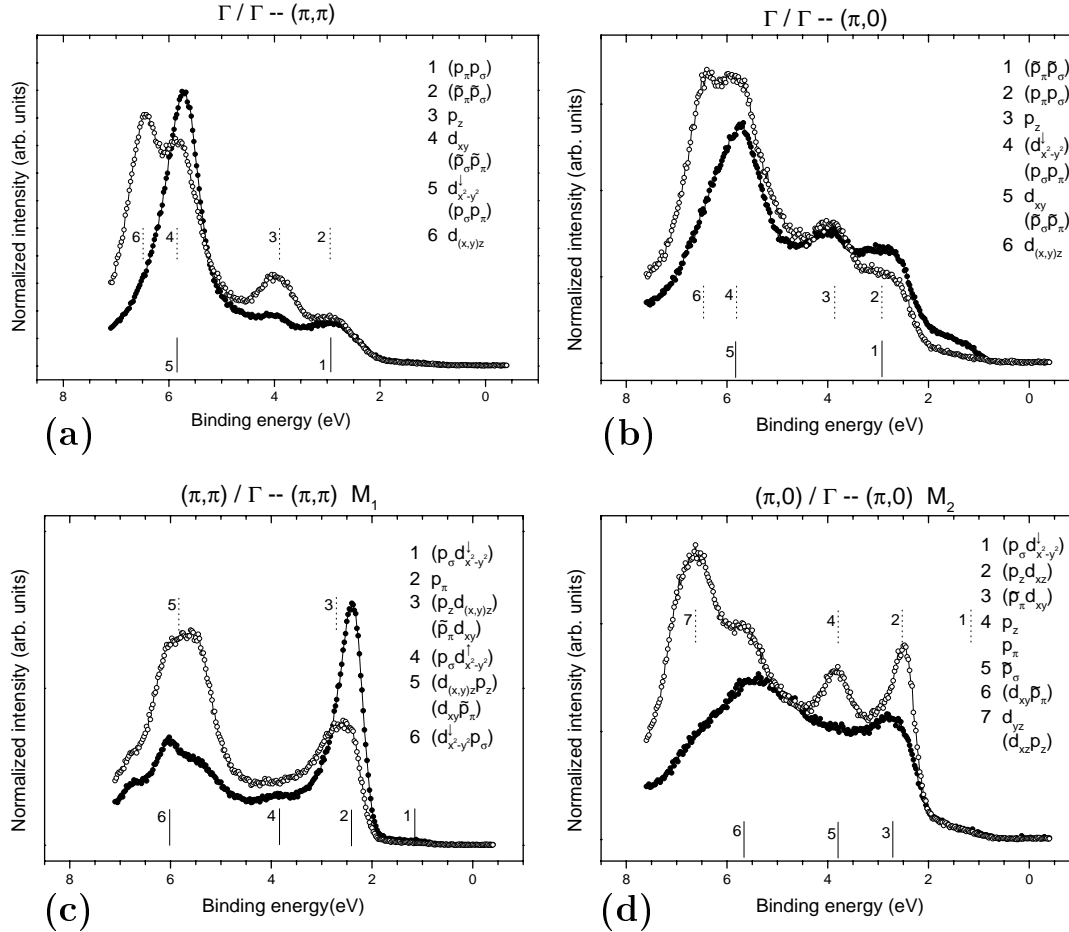
Figure 5.12: Experimental photoemission data of $Sr_2CuO_2Cl_2$ at high-symmetry points, with the relevant mirror plane given in brackets: (a) at the Γ point (M_1), (b) at the Γ point (M_2), (c) at (π, π) (M_1) and (d) $(\pi, 0)$ (M_2). The assignment of peaks is according to the LDA+U results. The filled circles and full lines correspond to vertical polarization, whereas the open circles and broken lines give the results for horizontal polarization.

sponding symmetry in that energy region in our LDA+U calculation. The large peaks at around 6 eV binding energy in Figs. 5.12(a) and 5.12(b) with big differences between both polarization directions indicate that there are additional contributions besides the oxygen orbitals there. Due to the low cross section of Cl $3p$ orbitals, we are only left with the pure copper d orbitals. To simplify the analysis we did not try to assign the Cu $3d_{3z^2-r^2}$ orbital which mixes strongly with the Cl orbitals and should have reduced intensity. The remaining in-plane copper orbitals change their polarization dependence between Figs. 5.12(a) and 5.12(b). The $d_{x^2-y^2}^{\downarrow}$ is antisymmetric with respect to M_1 and the d_{xy} is symmet-

Γ

Orbital	LDA+U	Exp.
$(p_\pi p_\sigma)$ $(\tilde{p}_\pi \tilde{p}_\sigma)$	-2.69	-2.9
p_z	-3.83	-3.9
$d^{\downarrow}_{x^2-y^2}$	-4.92	-5.8
d_{xy}	-5.40	
$(p_\sigma p_\pi)$ $(\tilde{p}_\sigma \tilde{p}_\pi)$	-5.57	
$d_{(x,y)z}$	-5.87	-6.5

(π, π)

Orbital	LDA+U	Exp.
$(p_\sigma d^{\downarrow}_{x^2-y^2})$ (ZRS)	0.65	-1.2
p_π	-2.43	-2.4
$(p_z d_{(x,y)z})$	-2.98	-2.7
$(\tilde{p}_\pi d_{xy})$	-3.35	
$(p_\sigma d^{\uparrow}_{x^2-y^2})$ (ZRT)	-4.94	-3.8
$(d_{(x,y)z} p_z)$	-6.62	-5.8
$(d_{xy} \tilde{p}_\pi)$	-7.20	
$(d^{\downarrow}_{x^2-y^2} p_\sigma)$	-7.28	-6.0

$(\pi, 0)$

Orbital	LDA+U	Exp.
$(p_\sigma d^{\downarrow}_{x^2-y^2})$ (ZRS)	-2.40	-1.1
$(p_z d_{xz})$	-2.96	-2.5
$(\tilde{p}_\pi d_{xy})$	-2.94	-2.7
p_z	-3.79	-3.8
p_π	-4.32	
$\tilde{p}_\sigma$	-4.11	-3.8
$(d_{xy} \tilde{p}_\pi)$	-6.17	-5.6
d_{yz}	-5.93	-6.6
$(d_{xz} p_z)$	-6.37	

Table 5.1: Comparison of experimental peak positions (in eV) with the LDA+U results of $Sr_2CuO_2Cl_2$ at the high-symmetry points (ZRS and ZRT mean the ZHANG-RICE singlet or triplet, respectively).

ric. However, this situation is reversed when the sample is oriented such that the k-vector is along $\Gamma - (\pi, 0)$. The intensity ratio between horizontal and vertical polarization of the peak at 5.8 eV is indeed exchanged if we compare Fig. 5.12(a) and 5.12(b). The last peak at 6.5 eV occurs for both sample orientations only with horizontal polarization and is interpreted as the out-of-plane d_{xz}- or d_{yz}-orbital.

Turning now to the spectra at (π, π), we can only probe the parity with respect to M_1 (Fig. 5.12(c)). The small prepeak at 1.2 eV in the curve with vertical polarization is usually interpreted as the ZHANG-RICE singlet [102]. The dominant peak at 2.4 eV binding energy in the spectra with perpendicular polarization can be identified as the pure p_π orbital which has already been discussed in Ref. [159]. The p_π band is the only one among the group of 5 bands at around 3 eV binding energy in both calculations (LDA or LDA+U, Figs. 3.30 and 5.11) which has odd symmetry with respect to M_1. It has lowest BE in the experiment and in the LDA+U calculation. That indicates that the LDA+U calculation is better in predicting the correct order of energy levels at high symmetry points than the pure LDA calculation. At slightly higher binding energy at 2.7 eV we observe a smaller, broader peak with horizontal polarization. According to our calculation it should be comprised of three bands, the out-of-plane ($p_z d_{(x,y)z}$) bands and the in-plane ($\tilde{p}_\pi d_{xy}$) band. The small structure at 3.8 eV binding energy (vertical polarization) can be related to the oxygen p_σ-orbital hybridizing with $d_{x^2-y^2}$ but having the opposite spin ($\uparrow$) than that of the copper hole. The corresponding band occurs in the LDA+U at 4.94 eV binding energy and can be interpreted as the ZHANG-RICE triplet. A similar structure was also observed in our previous analysis of the polarization-dependent photoemission spectra of another undoped model cuprate $Ba_2Cu_3O_4Cl_2$ [162].

The peaks at around 6 eV binding energy should be assigned to bands with a dominant copper character. However, we note in Table 5.1 systematic deviation between experimental and theoretical peak positions at (π, π): the theoretical binding energies are too large. That is plausible since it is expected that the copper-bands feel the antiferromagnetic correlations much more than the oxygen-bands which are decoupled from the copper-spins. As a result the copper bands are expected to follow more the AFM BZ where Γ and (π, π) are identical. However, such AFM correlations were not considered in our calculation.

At $(\pi, 0)$ (Fig. 5.12(d)) a prepeak with low intensity is to observe, which may be prescribed to the ZHANG-RICE singlet state comprised in our calculation by the hybridization between the p_σ orbital and $d^\downarrow_{x^2-y^2}$. The strong peak with horizontal polarization at 2.5 eV is assigned to the out-of-plane ($p_z d_{xz}$) orbital. The peak at 3.8 eV consists of two orbitals, p_z and p_π, which are separated by only 0.5 eV in the LDA+U calculation. Therefore, it is difficult to use that peak to extract the parameter $t_{\pi\pi}$ from the experimental spectra as it was done in Ref. [159]. Furthermore, it should distinguished between different oxygen hopping matrix elements (t_{pp}, $t_{p\pi}$ and $t_{\pi\pi}$)[152] which was also not done there [159].
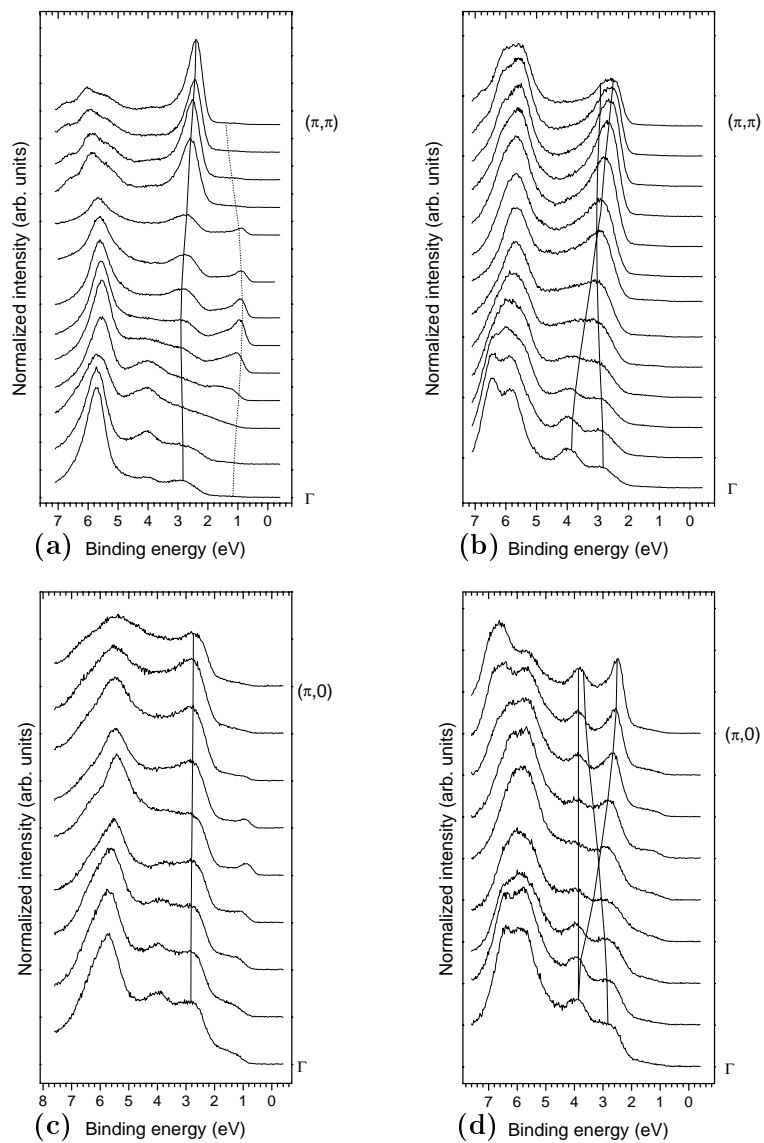
Figure 5.13: Angle-resolved photoemission curves calculated bands (solid lines) along: (**a**) Γ – (π,π) for vertical polarization together with the antisymmetric TB band with dominant oxygen (p_π) contribution and the dispersion of the ZRS according to Ref. [167] (dotted line). (**b**) Γ – (π,π) for horizontal polarization together with the oxygen out-of-plane TB bands and the in-plane bands having even symmetry. (**c**) Γ – $(\pi,0)$ for vertical polarization together with the antisymmetric oxygen TB band. (**d**) Γ – $(\pi,0)$ for horizontal polarization together with the oxygen out-of-plane TB bands and the in-plane bands having even symmetry.

Dispersion relations

The experimental spectra along both high symmetry directions show clear differences between both polarization directions (Fig. 5.13). The first electron removal

peak along $\Gamma - (\pi, \pi)$ has minimal BE at $(\pi/2, \pi/2)$ and occurs exclusively with vertical polarization (Fig. 5.13(a)). That is in complete agreement with the usual interpretation of that peak as the ZHANG-RICE singlet. In our mean-field treatment it is built up of the $d^{\downarrow}_{x^2-y^2}$ and p_σ orbitals having odd symmetry with respect to M_1. The dispersion is well described within the extended t-J model [167] and the corresponding theoretical curve is included in Fig. 5.13(a) for completeness. Along $\Gamma - (\pi, 0)$ (Figs. 5.13(c) and 5.13(d)) the ZHANG-RICE singlet feature is less pronounced. According to our symmetry analysis based on a simple mean-field treatment, we would expect it only with horizontal polarization. However, it is more clearly seen in Fig. 5.13(c) (vertical polarization) than in Fig. 5.13(d) (horizontal polarization). Recent experiments [184] on several new single crystals lifted this discrepancy, the ZHANG-RICE singlet feature appeared as expected only with horizontal polarization. The origin of the discrepancy in the present experiment is still unclear [184].

The peak next in binding energy in Fig. 5.13(a) was already analyzed as the p_π-orbital and it has a clear dispersion going from Γ to (π, π). The valence band edge at around 2.5 eV BE is different for both polarizations: it has no dispersion for vertical polarization (Fig. 5.13(c)) and is built up of only one ($\tilde{p}_\pi$) orbital. In contrast to that, we see for horizontal polarization (Fig. 5.13(d)) one dispersionless out-of-plane band at 3.9 eV and two crossing bands from the out-of-plane orbitals and the in-plane p_π band.

To analyze this dispersion quantitatively it is more convenient to use the TB model than the LDA+U calculation due to the restricted number of bands in the former. The parameters of the TB model were found as follows. The LDA+U results at high symmetry points (see Table 6.2 in Appendix D) were used to obtain a first parameter set. For the fit have been chosen only such energy levels which have no or very small contribution from other orbitals (Cu $4s$, O $2s$, Cl). In such a way our effective TB parameters also contain the influence of hybridization to Cl or s orbitals. Fitting to the pure LDA results (see Table 6.1 in Appendix D) gave nearly the same hopping integrals but different on-site energies. The parameters are very similar to those known for La_2CuO_4 [23]. After fitting to the LDA+U results there remained small differences to the experimental dispersions even for the peaks with lowest binding energy. These small discrepancies to the experimental peak positions were corrected by small changes of the on-site and off-site energies (here, especially t_{pdz} was increased). The resulting parameter set is shown in Table 5.2.

In Fig. 5.14 we have collected all the peak positions from Fig. 5.13 together with the dispersion of the TB bands. We have distinguished between the results for vertical polarization (Fig. 5.14(a)) and horizontal polarization (Fig. 5.14(b)). According to our previous analysis, the peaks in Fig. 5.14(a) between $(\pi, 0)$ and Γ

$\overline{\varepsilon}_d^{\uparrow}$	$\overline{\varepsilon}_d^{\downarrow}$	$\overline{\varepsilon}_{\tilde{d}}$	$\overline{\varepsilon}_D$	$\overline{\varepsilon}_{d_z}$	$\overline{\varepsilon}_\pi$	$\overline{\varepsilon}_{p_z}$	$\overline{\varepsilon}_p$
2.00	-4.90	-4.78	-5.22	-6.40	-3.88	-3.86	-4.59

t_{pd}	$t_{p\tilde{d}}$	t_{pp}	$t_{p\pi}$	$t_{\pi\pi}$	$t_{\pi D}$	t_{pdz}	
1.33	0.77	0.71	0.34	0.37	0.84	1.15	
				(0.32)	(0.77)	(0.77)	

Table 5.2: TB-parameters of $Sr_2CuO_2Cl_2$ obtained by fitting the LDA+U band structure and the VB photoemission spectra. The off-site energies in parentheses are the values from a fit only to the theoretical band structure in the cases where experimental corrections were appropriate.

should only be compared with the 3 TB bands stemming from the $\tilde{p}_\sigma$, $\tilde{p}_\pi$ and d_{xy} orbitals. Analogously, between Γ and (π,π) (Fig. 5.14(a)), only the antisymmetric bands from the p_σ, p_π, $d_{x^2-y^2}^{\downarrow}$ and $d_{x^2-y^2}^{\uparrow}$ orbitals are presented. In Fig. 5.14, we have collected the bands arising from both the $d_{x^2-y^2}^{\downarrow}$ or $d_{x^2-y^2}^{\uparrow}$ orbitals, and have neglected the band corresponding to the ZHANG-RICE singlet since we cannot expect to obtain its correct dispersion in our simple mean-field treatment. The number of bands which contribute to the spectra for horizontal polarization (Fig. 5.14(b)) is considerably larger: these include all of the out-of-plane orbitals and additionally the corresponding symmetric bands (representation A_1 of C_{2v}) of the in-plane orbitals. In Fig. 5.14 we have distinguished between bands with dominant oxygen character for all k values (solid lines) and those bands which have a considerable coupling to the copper spins (dashed lines). A considerable agreement is found between experimental and theoretical dispersions for the oxygen bands with small BE. Furthermore, there is some similarity at the Γ point besides the peak with vertical polarization at 3.9 eV BE for which we have no explanation. On the other hand, the copper-bands at around 6 eV disperse strongly in the TB calculation whereas they are nearly dispersionless in the experiment. Probably this failure of the theoretical description arises due to the neglect of antiferromagnetic correlations. To avoid misunderstanding it should be stressed, that also the oxygen bands of our mean-field calculation have a copper contribution (except some cases at the high-symmetry points), but that the copper contribution is not dominant. The calculated dispersion relations of the oxygen bands are shown in Fig. 5.13 as solid lines in order to guide the eye.

(a)

(b)
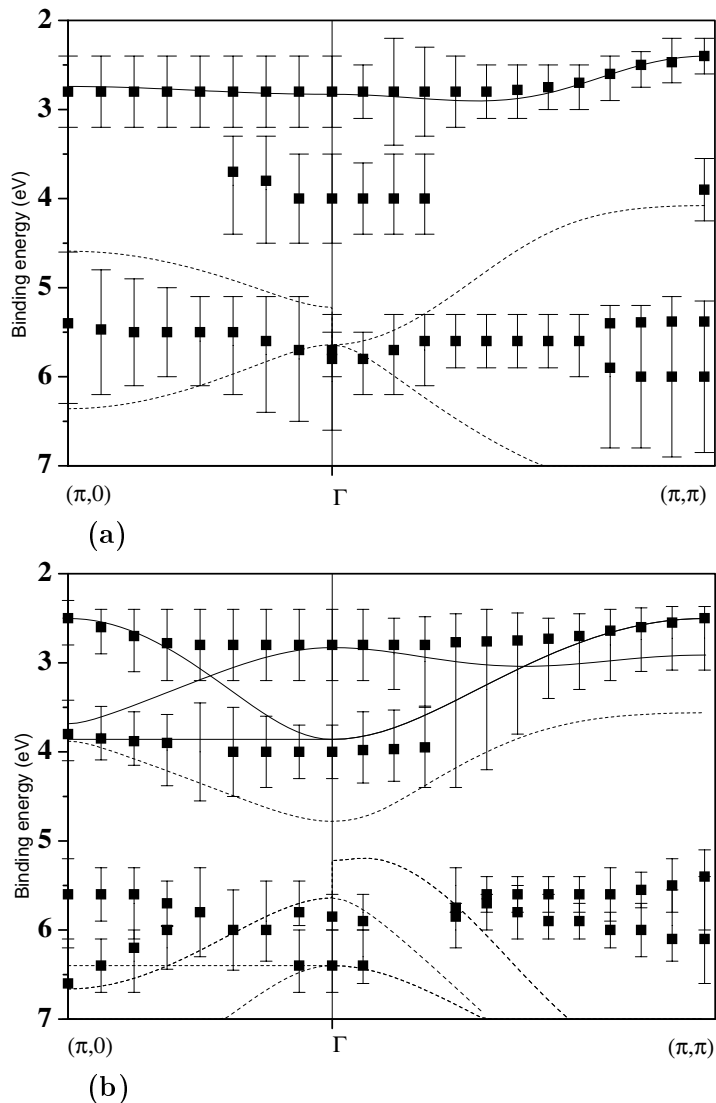
Figure 5.14: Position of the main experimental peaks for $Sr_2CuO_2Cl_2$ together with the TB-bands of the corresponding symmetry along $(\pi, 0) - (0, 0) - (\pi, \pi)$: (a) antisymmetric bands and experimental data for vertical polarization, (b) out-of-plane and symmetric bands together with experimental data for horizontal polarization. Full lines denote the TB bands with dominantly oxygen character, whereas the dashed lines correspond to bands with a considerable mixing to the copper system.

5.3.6   Conclusions

It can be summarized that polarization-dependent ARPES at Γ, (π, π) and $(\pi, 0)$ and along the two high-symmetry directions gives detailed information about the

bands with different parity with respect to reflections at the mirror planes M_1 and M_2. The assignment of the peaks can be performed by means of a symmetry analysis of band structure results. Here we pick out the three major results.

(I) Rearrangement of energy levels: Comparing LDA with LDA+U results at high-symmetry points we found that the strong electron correlation leads to a changed order of energy levels, whereby the experimental peak positions could be more accurately assigned with the help of the LDA+U calculation. In comparison with an LDA calculation we found the copper bands shifted to higher BE. So, we conclude that the correlation influences not only the band near the FERMI level but leads to a rearrangement of energy levels throughout the whole VB.

(II) Check of the non-bonding p_π band: Polarization-dependent ARPES measurements provide a sensitive test of the symmetries of the excitations with low BE which were already analyzed before. The p_π orbital is seen at (π, π) with vertical polarization as a single peak. At $(\pi, 0)$ it is visible with horizontal polarization but it overlaps with out-of-plane orbitals which makes a parameter assignment difficult. This means that in polarization independent measurement, such as those in Ref. [159], the spectral weight assigned to the p_π peak at (π, π) will have additional contributions besides the pure p_π orbital (of roughly one third of the total intensity as seen in Fig. 5.12(c)). As a consequence, the experimental estimate of the spectral weight of the ZHANG-RICE singlet part, which was performed there using the intensity of the p_π feature as a calibration, should be increased by 50 %.

(III) Dispersion relations: Analyzing the dispersion relations we observe a difference between the copper bands which couple strongly to the antiferromagnetic spin structure and thus feel the antiferromagnetic BZ and the nonbonding oxygen bands which are decoupled from the spin system and follow the paramagnetic (or ferromagnetic) BZ. To take that effect into account for Sr₂CuO₂Cl₂ we should extend our theory incorporating the antiferromagnetic order. Then all the bands are defined within the AFM BZ. To obtain in such a scheme the observed difference between Γ and (π, π) deserves the calculation of matrix elements.

Despite the fact that the experimental order of energy levels can be explained by an LDA+U calculation one should be aware that the agreement between photoemission and LDA+U cannot be perfect. First of all, the LDA+U calculation cannot reproduce the satellite structure present in the spectra at about 14 eV binding energy. And second, the LDA+U has the tendency to push the copper levels towards too large binding energy. That was visible in our analysis especially at (π, π). The k-integrated copper density of states can also be measured by x-ray photoemission with large photon energy such that the copper cross section dominates that of oxygen [185]. It was found that the x-ray photoemission spectrum of the valence band of Sr₂CuO₂Cl₂ showed the existence of Cu $3d$ electron

removal states over an energy range of some 5-6 eV. To compare our LDA+U calculation with earlier ones for La_2CuO_4 [176], it should be kept in mind that we had to choose a rather small shift of the copper levels to find agreement with the experimental situation, and we did not choose correlation parameters from a constrained density functional calculation as in Ref. [176]. It can be expected that the consideration of self-energy corrections as was done recently by calculating the three-body scattering contributions [186, 187] improves the situation and allows to work with real correlation parameters instead of fitted ones. Our main goal here was the assignment of peaks and not the determination of parameters. To extract parameters from polarization-dependent ARPES measurements there are several improvements necessary both from the experimental and the theoretical side of view.

5.4   The unoccupied electronic structure of Li_2CuO_2

Among the large family of chain and ladder networks [39], the simple straight chains are essential as they appear as building blocks in all of these materials. They can be classified structurally into two types, namely chains formed by CuO_4 plaquettes connected via shared corners ('corner-sharing chain') or shared edges ('edge-sharing chain'). The former is realized in Sr_2CuO_3, the unoccupied electronic structure of which has been studied recently [188]. The edge-sharing chain occurs in other insulating cuprates such as Li_2CuO_2, the spin-PEIERLS compound $GeCuO_3$ and the ladder-type material $La_6Ca_8Cu_{24}O_{41}$. The latter system represents the undoped parent compound of $Sr_{0.4}Ca_{13.6}Cu_{24}O_{41.84}$, which exhibits superconductivity under high pressure [189]. Within the class of materials with edge-sharing chains, at first glance Li_2CuO_2 seems to be an ideal model substance since in this case the CuO_2-chain is the only building block in the crystal structure apart from the Li counter ions, and thus a direct access to properties connected with the chain geometry alone is possible.

In contrast to the corner-sharing case, where a 180° Cu-O-Cu exchange path implies an antiferromagnetic (AFM) nearest-neighbor Cu spin interaction ($J_1 > 0$), the ideal edge-sharing geometry results in a 90° Cu-O-Cu interaction, which favors a ferromagnetic (FM) spin interaction ($J_1 < 0$) between the Cu-sites [71, 190, 73]. At the same time, the exchange path Cu-O-O-Cu plays a more important role, leading to an AFM next-nearest-neighbor interaction, J_2, and thus to frustration. For Li_2CuO_2, with an Cu-O-Cu angle of $\theta = 94°$, exchange constants of $J_1 = -100\,K$ and $J_2 = 62\,K$ have been obtained from magnetic susceptibility data and an analysis within a standard pd-model [136]. Besides the magnetic order along the chain direction (crystallographic **a**-direction), Li_2CuO_2

shows a three-dimensional magnetic structure. Different chains in the (**a**,**c**)-plane are FM ordered, whereas in **b**-direction an AFM coupling of the different layers of chains is found [50]. A detailed knowledge of the electronic structure of Li_2CuO_2 is necessary to understand the fundamentals of these magnetic properties.

In this section we study the unoccupied electronic structure of Li_2CuO_2 by means of polarization-dependent x-ray absorption spectroscopy and discuss the results in the light of the predictions of band structure calculations.

To obtain some insight into the electronic structure from the theoretical point of view we have performed LDA calculations using the linear combination of atomic-like orbitals which were already discussed in Section 3.3.2 (see Figs. 3.10 and 3.11). For the comparison with the XAS data, we calculated the orbital-projected net densities of states (described in detail in Appendix A). [191]. The calculation shows a paramagnetic and metallic behavior, with one isolated band crossing the FERMI level. Due to strong on-site electron correlations ignored in LDA, this antibonding band will split in an upper and a lower HUBBARD band in accordance with the experimentally observed insulating behavior.

Depending on the coordinate system adopted in the (**a**,**b**)-plane, the orbitals relevant for the discussion below are denoted by O $2p_{x'}$, O $2p_{y'}$, Cu $3d_{x'^2-y'^2}$ in the case of (x',y')-axes along the Cu-O bonds as sketched in Fig. 5.15(a), and O $2p_x$, O $2p_y$, Cu $3d_{xy}$ for axes parallel to the crystallographic directions ((x,y)-axes, Fig. 5.15(b)).

5.4.1 The intrinsic hole distribution in Li_2CuO_2

The XAS experiments were carried out using *in-situ* cleaved single crystals at the SX700/II beamline [192] operated by the *Freie Universität Berlin* at BESSY with an energy resolution of the monochromator of 280 and 660 meV at the O $1s$ and Cu $2p$ absorption thresholds, respectively. For the O $1s$ and Cu $2p$ absorption spectra the fluorescence yield (FY) and total electron yield (TEY) detection mode, respectively, were chosen. The spectra for different crystal orientations[11] are normalized ~ 80 eV above the absorption threshold, where the final states are nearly free-electron-like and therefore essentially isotropic.

XAS provides information on the character and symmetry of the unoccupied electronic states of solids and has played an important role in the investigation of cuprate-based materials [158]. Dipole selection rules and the localized initial core states enable a site-specific study of the hole distribution. In addition, by using linearly polarized synchrotron radiation and single crystalline samples, orbitals with different symmetry can be probed by appropriately aligning the sample with

---

[11]The spectra for **E**∥**c** were obtained by extrapolation from measurements at grazing incidence (70° off the sample surface normal).
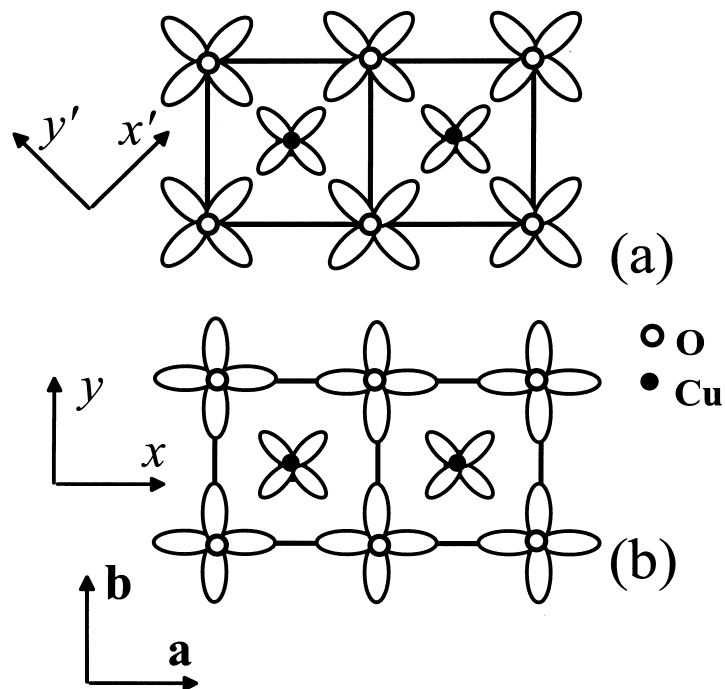
Figure 5.15:   A sketch of the edge-sharing chain in Li_2CuO_2. The directions **a** and **b** refer to the crystallographic axes. Cu and O orbitals are shown for two different coordinate systems: (a) axes of coordinates along the Cu-O bonds (x', y'-axes) with O $2p_{x'}$, O $2p_{y'}$, and Cu $3d_{x'^2-y'^2}$ orbitals. (b) axes of coordinates rotated by 45° (x, y-axes) with O $2p_x$, O $2p_y$, Cu $3d_{xy}$ orbitals.

respect to the electric field vector **E** of the incoming radiation. For example, in the geometry **E**∥**a** only O $1s \rightarrow$ O $2p_x$ transitions are selected (Fig. 5.15(b)).

Figure 5.16(a) shows the polarization-dependent Cu$2p_{3/2}$ x-ray absorption spectra of Li_2CuO_2. A narrow peak at ~ 931.8 eV (the so-called 'white line') is observed, which can be ascribed to the Cu $3d$ contributions to the upper HUB-BARD band (UHB)[12]. As expected from the isotropic neighborhood of the Cu ion within the (**a**, **b**) - plane (Fig. 5.15), almost identical spectra for **E**∥**a** and **E**∥**b** are observed. A completely different variation in intensity is found for light polarization perpendicular to the CuO$_4$-units (**E**∥**c**). The strong anisotropy of the white line between the in-plane (**E**∥(**a**,**b**)) and out-of-plane (**E**∥**c**) geometry implies that the low lying Cu $3d$ derived unoccupied states have predominantly Cu $3d_{xy}$ character, with only less than 7% of the intrinsic hole density located in

---

[12]Transitions into unoccupied Cu $4s$ orbitals are also allowed, but show a reduced transition probability by a factor of 20 compared to Cu $3d$ final states [193, 158]
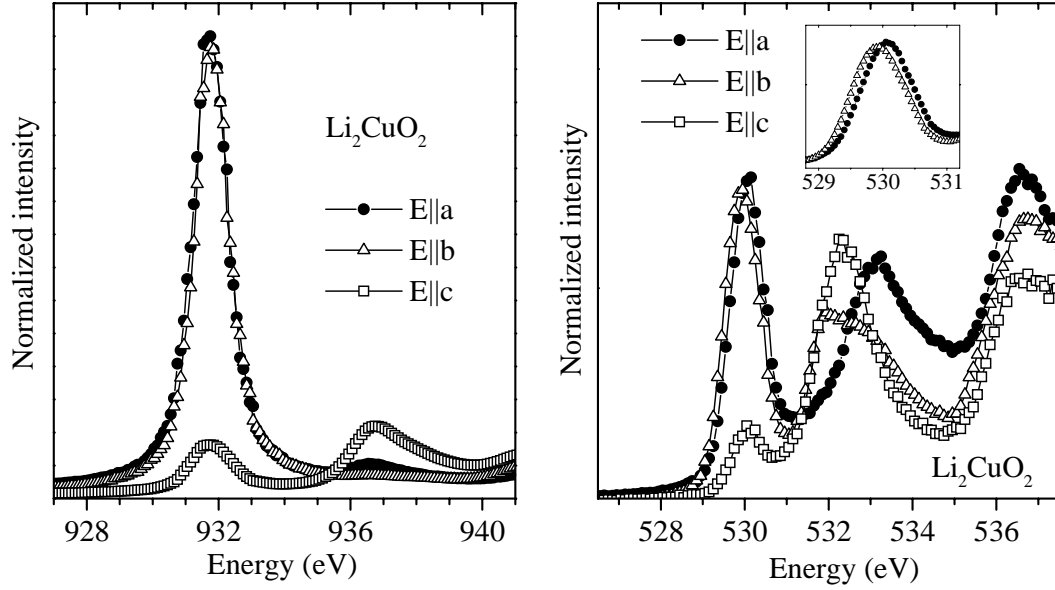
Figure 5.16: left panel: Cu $2p_{3/2}$ absorption edges of Li_2CuO_2 for the electric-field vector $\mathbf{E}$ parallel to the three crystallographic axes.

right panel: O $1s$ absorption edges of Li_2CuO_2 for the electric-field vector $\mathbf{E}$ parallel to the three crystallographic axes. The inset concentrates on the upper HUBBARD band derived features for the two in-plane light polarizations measured with smaller step size.

out-of-plane orbitals (Cu $3d_{3z^2-r^2}$)[13].

Besides the white line, a strongly polarization-dependent absorption feature is found at 936.8 eV. Features in this energy range in the out-of-plane geometry have been seen in many other cuprates [158] and can be attributed to transitions into Cu $3d_{3z^2-r^2}$ orbitals which become partly unoccupied via hybridization with empty Cu $4s$ states [194].

Turning to oxygen, Fig. 5.16(b) the O $1s$ absorption edges for Li_2CuO_2 is shown. These measurements probe O $2p_x$ ($\mathbf{E}\|\mathbf{a}$), O $2p_y$ ($\mathbf{E}\|\mathbf{b}$) and O $2p_z$ ($\mathbf{E}\|\mathbf{c}$) unoccupied states. The unoccupied states in the 'high' energy range above 530.5 eV result from the hybridization of Li $2s/2p$ states with previously occupied O bands. We will mainly concentrate on the peak directly above the absorption onset at ~ 530 eV which is related to transitions into O $2p$ orbitals hybridized with Cu $3d$ states forming the UHB [158]. The polarization dependence is expected to be similar to that found for the white line in the Cu $2p$ absorption spectra. Indeed, in the out-of-plane geometry ($\mathbf{E}\|\mathbf{c}$) the spectral weight of the

---

[13]In the evaluation of the spectral weight, different matrix elements for transitions into Cu $3d_{xy}$ and Cu $3d_{3z^2-r^2}$ states were taken into account.

UHB is strongly suppressed, with less than ~ 11 % of the holes with O $2p$ character located in orbitals perpendicular to the (**a**,**b**)-plane. From the observed anisotropy in the Cu $2p$ and O $1s$ absorption edges one can conclude that the UHB is predominantly built up from the in-plane orbitals Cu $3d_{xy}$, O $2p_x$, and O $2p_y$. A similar result is found within our LDA approach, in which states other than these three contribute jointly less than one percent to the band at the FERMI level. Compared to the LDA result, the larger out-of-plane contributions observed in experiment are most likely a result of the finite degree of linear polarization ($> 90\%$) of the monochromatized synchrotron radiation. An alternative explanation could be related to phonons or zero-point motion. They cause a breaking of the local symmetry and therefore hybridization between in- and out-of-plane states is no longer suppressed by symmetry. Although the relevant orbitals for the formation of the UHB have almost exclusively in-plane character, the LDA band structure shows a dispersion of the corresponding antibonding band in the z-direction which is equivalent to the dispersion in y-direction and comparable to that in chain direction x [55]. From this we can conclude that there is a relatively large inter-chain coupling via oxygen orbitals, and that Li_2CuO_2 is not an ideal 1D model system as the crystal structure might suggest at the first glance. From the dispersion of the antibonding band of an effective one-band model in chain direction,

$$
\begin{aligned}
E(\vec{k}) &= -2t_1 \cos(k_x a) - 2t_2 \cos(k_x a) - \\
&\quad 8t_1' \cos(k_x \frac{a}{2}) \cos(k_y \frac{b}{2}) \cos(k_z \frac{c}{2}) - \\
&\quad 8t_2' \cos(k_x \frac{3}{2}a) \cos(k_y \frac{3}{2}b) \cos(k_z \frac{3}{2}c),
\end{aligned} \tag{5.22}
$$

where $t_{1,2}$ denote the intra-chain transfer integrals and $t_{1,2}'$ the corresponding interchain integrals, we estimate for the transfer integrals values of $t_1 = $ -52 meV (-63 meV), $t_2 = $ -80 meV (-94 meV), $t_1' = $ -12 meV (-16 meV), $t_2' = $ -44 meV (-44 meV). The numbers in parentheses are the results obtained by WEHT and PICKETT [56]. The nearest-neighbor intra-chain transfer integral is significantly smaller than the corresponding value of the corner-sharing chain in Sr_2CuO_3 ($t_1 = 0.55$ eV [49]), reflecting the hindered hopping along the chain direction due to the $\sim 90°$ Cu-O-Cu geometry in Li_2CuO_2.

5.4.2 Character and width of the upper HUBBARD band

We will now focus on the O $1s$ absorption edges for $\mathbf{E}\|\mathbf{a}$ and $\mathbf{E}\|\mathbf{b}$ near 530 eV, where the chain geometry would suggest identical spectra. As illustrated in Fig. 5.15(a), the alignment of the light polarization parallel to the **a** axis is identical to the situation of $\mathbf{E}\|\mathbf{b}$ as far as the projection of the unoccupied O $2p_{x'}/2p_{y'}$

states along these two directions is concerned. Surprisingly, in our XAS measurements the UHB derived feature for $\mathbf{E}\|\mathbf{a}$ and $\mathbf{E}\|\mathbf{b}$ turn out not to be identical. The hole density in the orbitals O $2p_x$ and O $2p_y$ is almost the same[14], but we observe a distinct shift in energy of $150\,\mathrm{meV}$ between the two polarization directions. Although an absolute energy calibration can hardly be performed to an accuracy of $0.1\,\mathrm{eV}$, we can very sensitively and significantly determine a relative shift between the $\mathbf{E}\|\mathbf{a}$ and $\mathbf{E}\|\mathbf{b}$ spectra[15].

To discuss a possible anisotropy between the $\mathbf{a}$ and $\mathbf{b}$-direction we make use of the orbital representation shown in Fig. 5.15(b), which corresponds to the experimental geometry probing O $2p_x$ and O $2p_y$ states. The Cu ions still have an isotropic neighborhood consistent with the observations in the Cu $2p$ XAS, but now the O $2p_x$ and O $2p_y$ orbitals are not *a priori* symmetrically equivalent. For example, the presence of counterions strongly hybridized with the O $2p_y$ orbitals would lead to a sizable anisotropy. The crystal structure of $CuGeO_3$ is a good illustration for this situation, as the Ge ions are located directly opposite the oxygen atoms of the edge-sharing chain. In Li_2CuO_2, however, the Li ions do not reside opposite to the oxygen atoms, but are situated in between them with a O-Li-O bonding angle of approximately $90°$. Thus, in the present case the counterions do not give a basis for a possible anisotropy.

In contrast to the corner-sharing chain in Sr_2CuO_3, where one can naturally ascribe two different peak positions to two symmetrically inequivalent oxygen sites [188], the crystal symmetry in Li_2CuO_2 contains only one oxygen site. As the excitation into the two oxygen orbitals starts from the *same* core level, one would consequently expect to observe *one* UHB at a certain energy, provided that possible excitonic effects between the excited electron and the core hole do not depend on the final state (O $2p_x$, O $2p_y$).

In a first step we look for an explanation of the observed energy shift in the framework of the LDA calculation where the partial, orbital-resolved unoccupied DOS near the FERMI energy is expected to be reflected in our XAS data directly above the absorption threshold. The character of the orbitals building a dispersive band may change across the BRILLOUIN zone, e.g. from predominantly O $2p_x$ to

---

[14]This is consistent with our LDA calculation (see Fig. 5.17) but contradicting to the FLAPW calculations of TANAKA *et. al.* [57]. They found mainly contributions of the O $2p_x$ orbitals to the antibonding band, this can be related to the orbital projection in the FLAPW scheme. The orbital contribution of O $2p_x$ and O $2p_y$ is crucial for the magnetic coupling in Li_2CuO_2.

[15]For the measurement, we use the following scheme: the corresponding directions have been measured immediately one after another in a cycle $\mathbf{E}\|\mathbf{a}$, $\mathbf{E}\|\mathbf{b}$, $\mathbf{E}\|\mathbf{a}$. After a new fill of the storage ring, the measurements were repeated but now starting the cycle with $\mathbf{E}\|\mathbf{b}$. Thus a jump in the monochromator energy due to the mechanical drive of the grating and/or instabilities of the electron beam in the storage ring can be excluded as an explanation of the shift. Moreover, measurements were performed on several samples with identical results.

O $2p_y$. Since the XAS experiment yields k-space-integral information, one would then observe a different energy position when probing O $2p_x$ and O $2p_y$ orbitals, each dominating a different part of the band. Indeed, some effect is visible in the O $2p$ net density of states derived from our LDA bandstructure calculations shown in Fig. 5.17. In the lower part of the figure, the calculated DOS has been
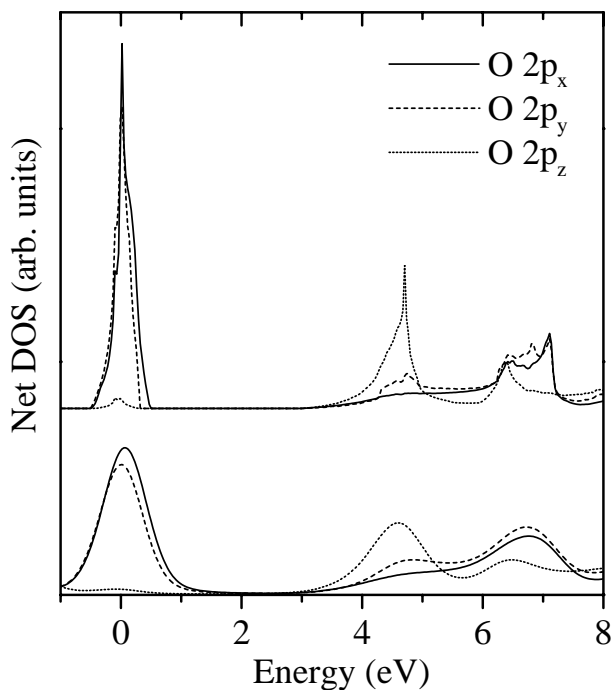
Figure 5.17: O $2p$ net density of states of the LDA-LCAO band structure for Li_2CuO_2 near the FERMI energy (E_F=0). Upper curves: calculated DOS. Lower curves: calculated DOS broadened to account for lifetime effects, phonons and experimental resolution. For the parameters used, see the text.

broadened to account for lifetime effects of the core hole[16] (0.2 eV Lorentzian) and energy resolution (0.28 eV Gaussian) [196]. The use of these values leads to a total linewidth of 0.6 eV in discrepancy to the experimentally observed linewidth of about 1 eV. The same discrepancy occurs in Ref. [196] for the case of La_2CuO_4 and is ascribed therein to an reduced lifetime of the core hole in a solid compared with a free atom. This seems unrealistic because it requires a three times larger life time broadening in the solid. The intersite AUGER processes, proposed to be responsible for this broadening in Ref. [196], would cause an anisotropy for the

---

[16]The value of 0.2 eV corresponds to the lifetime of the core hole in a free oxygen atom [195].

linewidths for **E**∥**a** and **E**∥**b** which is not observed. Therefore, we suppose an only slightly enhanced broadening (compared with the free atom) of 0.3 eV as more realistic.

We have to look for an additional mechanism of broadening to reproduce the experimental linewidth. Usually, it was characterized as partially originating from the dispersion of the UHB and partially stemming from phononic contributions. Mostly, they are difficult to separate from each other and are discussed together as *solid-state broadening* [197]. Because of the extremely small bandwidth, Li$_2$CuO$_2$ is the most suitable model compound for a separate investigation of both contributions.

The experimentally observed linewidths of the UHB in Li$_2$CuO$_2$, Sr$_2$CuO$_3$, and Sr$_2$CuO$_2$Cl$_2$ are nearly identical with about 1 eV, whereas the LDA bandwidths are strongly different: 1 eV for Li$_2$CuO$_2$, 2.2 eV for Sr$_2$CuO$_3$, and about 4 eV for Sr$_2$CuO$_2$Cl$_2$. Since the correlations are poorly described in LDA, the actual bandwidths should be essentially smaller. The exchange integrals J in these compounds are substantially distinct from each other, hence the magnetic coupling seems to play a minor role for the broadening. The comparison of these three compounds of different dimensionality points to the dominance of an 'universal' broadening mechanism originating from phonons which should be similar in all three compounds due to the common CuO$_4$ building block.

The vibrational broadening in the XAS is usually discussed on the basis of the FRANCK-CONDON principle [197]. Since a general quantitative description is complicated, we consider a simplified model where the initial and the final states are given by two harmonic oscillators (force constant K, phonon frequency ω_{ph}) with a difference of ΔR in the configuration coordinate [198, 199]. For this case, the FRANCK-CONDON factor is reduced to a POISSON distribution:

$$F_n = e^{-\beta}\frac{\beta^n}{n!}\,, \tag{5.23}$$

where

$$n = \frac{E}{\hbar\omega_{ph}} \qquad \beta = \frac{K(\Delta R)^2}{2\hbar\omega_{ph}}\,. \tag{5.24}$$

In the limit of $\beta \gg 1$ this can be approximated by a symmetric Gaussian:

$$F_n = \frac{1}{\sqrt{2\pi\beta}}\exp(-\frac{(\beta - n)^2}{2\beta})\,. \tag{5.25}$$

This corresponds to the experimentally observed nearly symmetric line shape[17] (see Fig. 5.16).

---

[17]A more accurate analysis of the remaining asymmetry is difficult due to the overlap of the UHB with the higher lying absorption features. Furthermore, the symmetric broadening mechanisms (life time, resolution) will cover the asymmetry.

In the symmetric limet, the phononic contribution to the linewidth is given by [200]

$$\Gamma_{ph} = 2.35 \sqrt{\beta} \hbar \omega_{ph} . \tag{5.26}$$

The relevant bond stretching phonon modes have a typical energy of about 100 meV [201]. Thus, Eq. (5.26) leads to $\beta = 6.5$ for a phononic contribution of 0.6 eV to the linewidth derived from the XAS data. This relatively high number of involved phonons implies the importance of electron-phonon coupling, i.e. polaronic effects. Within a theory of small polarons [202], Eq. (5.24) can be transformed in

$$\Delta E_{lat} + \Delta E_{el} = 0 , \tag{5.27}$$

using the HUBBARD-HOLSTEIN model. Here, ΔE_{lat} corresponds to the change of the lattice energy due to the emitted phonons, and $\Delta E_{el} = -\beta \hbar \omega_{ph}$ describes the polaronic shift due to electron-lattice interaction. This results in an enlarged effective mass m^* of the quasiparticle (polaron) and therefore in a reduced bandwidth. A quantitative theoretical description is complicated because the phononic energy $\hbar \omega$ is similar to the electronic transfer integral t and we find a medium electron-phonon coupling constant $\lambda_{el-ph} \approx \beta \hbar \omega_{ph}/W \approx 0.6 \ldots 0.7$. Herein, W is the bandwidth of the LDA calculation which can be regarded as an upper estimate.

These values for the parameters require a big numerical effort for solving the related equations [203]. Qualitatively, the similar linewidth of the UHB in the XAS data of all insulating cuprate compounds (independent of the dispersion in the LDA bandstructure) can be understood as a combination of polaronic narrowing and phononic broadening. Similar explanations within this simple polaronic picture were given for the broadening in photoemission spectra [204, 205].

Let us direct our attention now to the anisotropy of the UHB. One recognizes a small energy shift between the calculated O $2p_x$ and O $2p_y$ densities of states at the FERMI energy, in the same direction as experimentally observed. However, the theoretically estimated shift of 50 meV turns out to be not sufficient to fully explain the experimental value of 150 meV. Therefore, there must be some additional mechanism involved.

As the phonon contributions have significant influence on the actual linewidth, the chain structure of Li_2CuO_2 could lead one to expect some anisotropy of the phonon properties, thus accounting for the experimentally observed energy shift. For example, O $1s$ core-level excitations into the O $2p_x$ and O $2p_y$ orbitals could result in coupling either to different numbers of phonons or to phonons of different energies. However, considering the role of phonons in the excitation process in terms of a simple EINSTEIN model, one finds that the first moment (center of

gravity) of the spectral function is independent of the coupling strength [206, 207]. For an asymmetric lineshape, an energy shift between the two polarization directions could result from the different energy positions of the peak maximum with respect to the center of gravity in each case. However, as the peak maximum and the center of gravity coincide in the strong coupling limit (symmetric lineshape), it would appear unlikely that, within this simple framework, the observed energy shift is caused by phonon contributions.

As a final point we mention the possible role played by electronic correlation effects in the XAS final state. Since there are only 0.1 holes per O $2p_{x,y}$ orbital, the excited electron must be distributed over several surrounding ions. This charge redistribution in the XAS final state depends sensitively on the transfer integrals between the orbitals involved. These are in turn influenced by geometric effects (the Cu-O-Cu bond angle is 94°) and in the case of the oxygen-oxygen transfer integrals additionally by the proximity of cations in the immediate vicinity. Both of these effects could lead to a situation in which the final state charge distribution is different for the two polarization conditions. Taking this fact, in combination with the various intersite COULOMB interactions (both core-valence and valence-valence), it is conceivable that the final state energies for $\mathbf{E}\|\mathbf{a}$ and $\mathbf{E}\|\mathbf{b}$ result in a shift of both the same magnitude and direction as observed in experiment. Consequently, the direction and magnitude of the experimentally observed energy shift provides a useful constraint for the parameters involved in future model calculations of edge sharing CuO$_2$-chains.

To summarize our results, direct experimental information on the character and symmetry of the intrinsic holes in the edge-sharing chain of Li$_2$CuO$_2$ has been obtained by polarization-dependent x-ray-absorption spectroscopy. Although for light polarization within the plane of the CuO$_4$-plaquettes the chain geometry suggests isotropic oxygen contributions to the UHB, we observe a shift in energy in dependence of the direction of the light polarization. This shift has been discussed within the framework of bandstructure effects, the role of phonons in the excitation process as well as the impact of electronic correlations in the XAS final state.

Chapter 6

Summary and outlook

The physics of cuprates is strongly influenced by the dimension of the copper-oxygen network in the considered crystals. Due to the rich manifoldness of different network geometries realized by nature, cuprates are ideal model systems for experimental and theoretical studies of low-dimensional, strongly correlated systems. The dimensionality of the considered model compounds varies between zero and three with a focus on one- and two-dimensional compounds.

Starting from LDA band structure calculations, the relevant orbitals for the low-energy physics have been characterized together with a discussion of the chemical bonding in the investigated compounds. It was shown, that qualitative results can already be estimated by considering structural elements like local and crystal symmetry, interatomic distances, and bond-lengths. By means of this systematic approach, the influence of particular structural components on the electronic structure could be concluded.

For all undoped cuprate compounds, paramagnetic LDA band structure calculations yield a metallic groundstate instead of the experimentally observed insulating behavior, and the strong correlations have to be taken into account in a more explicit way. Model calculations using HUBBARD- or HEISENBERG-like models are suitable to investigate most of the magnetic couplings in cuprates. The necessary parameters were obtained from tight-binding parameterizations of LDA band structures, except the correlation part which was obtained from experiments or from constrained LDA calculations reported in the literature. In a comparative study of the chain compounds Sr_2CuO_3, Ca_2CuO_3, and $CuGeO_3$, the in-chain and inter-chain interactions were investigated, which are responsible for the phase transition either to an AFM or to a spin PEIERLS state at low temperatures. Even if the absolute values calculated for exchange integrals, magnetic moments, and ordering temperature are too large, the ratio for different compounds was found in agreement with experiment. This emphasizes the necessity to improve the models available for such anisotropic compounds.

Each theoretical result has to be verified by experiment, and the interpretation of experiments usually needs a theoretical background. In the dialogue between experiment and theory, valuable insights into the occupied and unoccupied valence band structure of cuprates were obtained. ARPES measurements on $Ba_2Cu_3O_4Cl_2$ were interpreted in terms of two ZHANG-RICE singlets moving in different magnetic spin backgrounds and representing in this way simultaneously the low and very high doping limit. A valence band analysis of $Sr_2CuO_2Cl_2$ compared with polarization-dependent ARPES experiments showed, that an LSDA+U scheme is more appropriate to interpret the spectra than simple LDA, which gives not only the wrong groundstate, but also the wrong energy order of the orbitals. A comparison of XAS spectra with the calculated density of states for Li_2CuO_2 highlighted the importance of phononic and polaronic effects for the interpretation of high energy spectroscopy.

The present work shows, that the combination of experiment, LDA, and model calculations is a powerful tool for the investigation of the electronic structure of strongly correlated systems. Using the presented paramagnetic and the not discussed spin-polarized band structure results, further work could follow these lines: Starting with a TB parameterization, the magnetic coupling in the "zero-dimensional" Bi_2CuO_4 and in the merlon chain compound $Ba_3Cu_2O_4Cl_2$ can be analyzed. For the edge-sharing chain compound Li_2CuO_2 a multi-band model can be constructed to calculate the exchange integrals. First estimates are in contradiction to experimental values from neutron scattering by at least one order of magnitude. Furthermore, a comparative study between the spin PEIERLS compound $CuGeO_3$ and the recently discovered isostructural $CuSiO_3$ including experimental results is already in preparation. A more general aspect for further investigations concerns the influence of orbitals beyond the standard pd models. Preliminary results show their importance for physical properties connected with long range interactions in strongly anisotropic compounds, like ordering temperature or magnetic moments.

Appendix

A Definition of the net-DOS and of the orbital weight

In our LCAO calculations, the BLOCH wave function $|\mathbf{k}\nu\rangle$ is composed of over-lapping atomic-like orbitals $|Lij\rangle$ centered at the atomic site j in the elementary cell i with coordinates $\mathbf{R}_i + \mathbf{S}_j$,

$$|\mathbf{k}\nu\rangle = \sum_{Lij} C_{Lij}^{\mathbf{k}\nu} e^{i\mathbf{k}(\mathbf{R}_i+\mathbf{S}_j)} |Lij\rangle \tag{A.1}$$

with the normalization condition $\langle \mathbf{k}\nu|\mathbf{k}\nu\rangle = 1$. Here, $L = \{nlm\}$ where n, l, and m denote the main quantum number, the angular momentum and the magnetic quantum numbers, respectively (see Section 2.2.1). Note that for each l only one main quantum number n is considered. With the usual definition for the density of states

$$\rho(\omega) = \frac{1}{N_{\mathbf{k}}} \sum_{\mathbf{k}\nu} \int d^3r \, \langle \mathbf{k}\nu|\mathbf{r}\rangle\langle\mathbf{r}|\mathbf{k}\nu\rangle \delta(\omega - E_{\mathbf{k}\nu}) \tag{A.2}$$

where $N_{\mathbf{k}}$ is the number of elementary cells equivalent to the number of $\mathbf{k}$-values, ρ can be written as

$$
\begin{aligned}
\rho(\omega) &= \frac{1}{N_{\mathbf{k}}} \sum_{\mathbf{k}\nu} \int d^3r \sum_{Lij} \sum_{L'i'j'} C_{Lij}^{\mathbf{k}\nu} C_{L'i'j'}^{\mathbf{k}\nu*} \langle Lij|\mathbf{r}\rangle\langle\mathbf{r}|L'i'j'\rangle \\
&\quad \times e^{i\mathbf{k}(\mathbf{R}_i+\mathbf{S}_j-\mathbf{R}_{i'}-\mathbf{S}_{j'})} \delta(\omega - E_{\mathbf{k}\nu})
\end{aligned}
\tag{A.3}
$$

or

$$\rho(\omega) = \frac{1}{N_{\mathbf{k}}} \sum_{\mathbf{k}\nu} \sum_{Lij} \sum_{L'i'j'} C_{Lij}^{\mathbf{k}\nu} C_{L'i'j'}^{*\mathbf{k}\nu} S_{Lij,L'i'j'} e^{i\mathbf{k}(\mathbf{R}_i+\mathbf{S}_j-\mathbf{R}_{i'}-\mathbf{S}_{j'})} \delta(\omega - E_{\mathbf{k}\nu}) \tag{A.4}$$

where $S_{Lij,L'i'j'}$ is the overlap matrix. Now we can decompose ρ into an on-site part ($i = i'$ and $j = j'$) and an overlap part ($i \neq i'$ or $j \neq j'$). For the on-site

part we find $S_{Lij,L'ij} = \delta_{LL'}$ due to the orthogonality of atomic-like orbitals at the same site. So we can define a net density of states (net-DOS)

$$\rho_{net}(\omega) = \frac{1}{N_{\mathbf{k}}} \sum_{\mathbf{k}\nu} \sum_{Lij} |C_{Lij}^{\mathbf{k}\nu}|^2 \delta(\omega - E_{\mathbf{k}\nu}) \; . \tag{A.5}$$

The difference between the DOS and the net-DOS consists in the overlap density and is relatively small near the nonbonding states (see Fig. 2 of Ref.[191]).

To define the orbital character of a k-point of a band ν, we write the net-DOS (A.5) as

$$\rho_{net}(\omega) = \frac{1}{N_{\mathbf{k}}} \sum_{\mathbf{k}\nu} \sum_{Lj} W_{Lj}^{\mathbf{k}\nu} \delta(\omega - E_{\mathbf{k}\nu}) \; , \tag{A.6}$$

where we define the weight of the orbital $|Lj\rangle$ in the state $|\mathbf{k}\nu\rangle$ in the form:

$$W_{Lj}^{\mathbf{k}\nu} = \sum_i |C_{Lij}^{\mathbf{k}\nu}|^2 \; . \tag{A.7}$$

The sum of all weights is approximately unity, $\sum_{Lj} W_{Lj}^{\mathbf{k}\nu} \approx 1$, with small deviations due to the neglect of the overlap density.

B   Analytical expressions for the eigenvalues of the 11-band tb-model of the $\mathbf{Cu_3O_4}$-plane

As written in Section 4.3.1, the tight-binding matrix is block-diagonal at the high symmetry points $\Gamma = (0,0)$ and $M = (\pi/a, \pi/a)$, so it is possible to calculate the eigenvalues analytically. In the following these eigenvalues are listed corresponding to the different parts of the tight-binding Hamiltonian.

Eigenvalues at $\mathbf{k} = (0,0)$:

Cu$_A$-subsystem:

$$\varepsilon_d^A$$
$$\varepsilon_p - 4t_{pp} \tag{B.1}$$
$$\frac{1}{2} \left[\varepsilon_d^A + \varepsilon_p + 4t_{pp} \pm \sqrt{(\Delta_A + 4t_{pp})^2 + 32t_{pd}^2} \right]$$

Cu$_B$-subsystem:

$$\varepsilon_\pi - 2t_{\pi\pi}^+$$
$$\frac{1}{2} \left[\varepsilon_d^B + \varepsilon_\pi + 2t_{\pi\pi}^+ \pm \sqrt{(\Delta_B + 2t_{\pi\pi}^+)^2 + 16t_{\pi d}^2} \right] \tag{B.2}$$

coupling between the subsystems:

$$1/2(\varepsilon_p + \varepsilon_\pi \pm \sqrt{\Delta_{p\pi}^2 + 64t_{p\pi}^2})$$ (B.3)

The eigenvalues in (B.3) are twofold degenerated.

Eigenvalues at $\mathbf{k} = (\pi, \pi)$:

Cu_A-subsystem:

$$\frac{1}{2}\left[\varepsilon_d^A + \varepsilon_p \pm \sqrt{\Delta_A^2 + 16t_{pd}^2}\right]$$ (B.4)

Cu_B-subsystem:

$$\frac{1}{2}\left[\varepsilon_d^B + \varepsilon_\pi - 2t_{\pi\pi}^- \pm \overset{\textstyle \varepsilon_\pi + 2t_{\pi\pi}^-}{\sqrt{(\Delta_B - 2t_{\pi\pi}^-)^2 + 16t_{\pi d}^2}}\right]$$ (B.5)

coupling between the subsystems:

$$\begin{matrix} \varepsilon_p \\ \varepsilon_\pi \end{matrix}$$ (B.6)

where $\Delta_A = \varepsilon_p - \varepsilon_d^A$, $\Delta_B = \varepsilon_\pi - \varepsilon_d^B$, $\Delta_{p\pi} = \varepsilon_p - \varepsilon_\pi$, $t_{\pi\pi}^\pm = t_{\pi\pi}^1 \pm t_{\pi\pi}^2$. The eigenvalues in (B.4) and (B.6) are twofold degenerated.

C   Exchange integrals in pertubation theory for the Cu_3O_4-plane

$$\Delta_A = \varepsilon_p - \varepsilon_d^A, \quad \Delta_B = \varepsilon_\pi - \varepsilon_d^B, \quad \Delta_{AB} = \varepsilon_p - \varepsilon_d^B, \quad \Delta_{BA} = \varepsilon_\pi - \varepsilon_d^A$$ (C.1)

$$t_{pdA} = t_{pd}, \quad t_{pdB} = t_{\pi d}$$ (C.2)

$$J_{AA}^{[4]} = \frac{4t_{pdA}^2}{(\Delta_A + U_{pd})^2}\left\{K_{pd} + \frac{2t_{pdA}^2}{2\Delta_A + U_p} + \frac{t_{pdA}^2}{U_d} + \frac{K_{pd}^2}{\Delta_A + U_{pd}}\right\}$$ (C.3)

$$J_{BB}^{[6]} = \frac{8t_{pdB}^2(t_{\pi\pi}^1)^2}{\Delta_B^2}\left\{\frac{1}{(\Delta_B + U_{pd})^2}\left(K_{pd} + \frac{2t_{pdB}^2}{U_d}\right) + \frac{K_{pd}^2}{(\Delta_B + U_{pd})^3}\right.$$
$$\left. + t_{pdB}^2\left(\frac{1}{2\Delta_B + U_p} + \frac{1}{2\Delta_B}\right)\left(\frac{1}{\Delta_B + U_{pd}} + \frac{2}{2\Delta_B}\right)^2\right\}$$ (C.4)

$$
J_{AB}^{(3)[6]} \;=\; \sum_{A\leftrightarrow B} \frac{2t_{p\pi}^2 t_{pdB}^2 K_{pd}}{\Delta_B^2 (\Delta_{AB} + U_{pd})^2}\left(1 + \frac{K_{pd}}{\Delta_{AB} + U_{pd}}\right)
$$
$$
+ \sum_{A\leftrightarrow B} \frac{2t_{p\pi}^2 t_{pdA}^2 t_{pdB}^2}{\Delta_B^2 (\Delta_{AB} + \Delta_A + U_p)}\left(\frac{1}{\Delta_A} + \frac{1}{\Delta_{AB} + U_{pd}}\right)^2
$$
$$
+ \sum_{A\leftrightarrow B} \frac{2t_{p\pi}^2 t_{pdA}^2 t_{pdB}^2}{\Delta_B^2 (\Delta_{AB} + U_{pd})^2 (\varepsilon_d^A - \varepsilon_d^B + U_d)} \tag{C.5}
$$

$$
J_{AB,af}^{(1)[6]} \;=\; \sum_{A\leftrightarrow B} \frac{4t_{p\pi}^2 t_{pdB}^2 K_{pd}}{\Delta_B^2 (\Delta_{AB} + U_{pd})^2}\left(1 + \frac{K_{pd}}{\Delta_{AB} + U_{pd}}\right)
$$
$$
+ \sum_{A\leftrightarrow B} \frac{4t_{p\pi}^2 t_{pdA}^2 t_{pdB}^2}{\Delta_B^2 (\Delta_A + \Delta_{AB})}\left(\frac{1}{\Delta_A} + \frac{1}{\Delta_{AB} + U_{pd}}\right)^2
$$
$$
+ \sum_{A\leftrightarrow B} \frac{4t_{p\pi}^2 t_{pdA}^2 t_{pdB}^2}{\Delta_B^2 (\Delta_{AB} + \Delta_A + U_p)}\left(\frac{1}{\Delta_A} + \frac{1}{\Delta_{AB} + U_{pd}}\right)^2
$$
$$
+ \sum_{A\leftrightarrow B} \frac{8t_{p\pi}^2 t_{pdA}^2 t_{pdB}^2}{\Delta_B^2 (\Delta_{AB} + U_{pd})^2 (\varepsilon_d^A - \varepsilon_d^B + U_d)} \tag{C.6}
$$

$$
J_{AB,f}^{(1)[5]} \;=\; \frac{22t_{pdA}^2 t_{pdB}^2 2K_{p\pi}}{(\Delta_A + \Delta_B + U_{p\pi})^2}\left(\frac{1}{\Delta_A} + \frac{1}{\Delta_B}\right)^2 \tag{C.7}
$$

D   Orbital weight of valence bands in Sr$_2$CuO$_2$Cl$_2$

Γ

Nr.	E/eV	p_z	p_σ	p_π	$d_{3z^2-r^2}$	$d_{(x,y)z}$	d_{xy}	$d_{x^2-y^2}$	O_s	Cu_s	$\sum$Cl	not.	M$_1$	M$_2$
1	-1.64	0	0	0	0	0	0	.903	.097	0	0	$d_{x^2-y^2}$	A	S
2	-2.28	0	0	0	.817	0	0	0	.015	.005	.163	$d_{3z^2-r^2}$	S	S
3,4	-2.34	0	.456	.530	0	0	0	0	0	0	.014	$(p_\pi p_\sigma)$	A	S
												$(\tilde{p}_\pi \tilde{p}_\sigma)$	S	A
5	-2.72	0	0	0	0	0	1.00	0	0	0	0	d_{xy}	S	A
6,7	-2.96	0	0	0	0	.984	0	0	0	0	.016	$d_{(x,y)z}$	o	o
8,9	-3.46	1.00	0	0	0	0	0	0	0	0	0	p_z	o	o
	(-3.19)	(.526)									(.474)			
10,11	-5.14	0	.495	.495	0	0	0	0	0	0	.010	$(p_\sigma p_\pi)$	A	S
												$(\tilde{p}_\sigma \tilde{p}_\pi)$	S	A

(π,π)

Nr.	E/eV	p_z	p_σ	p_π	$d_{3z^2-r^2}$	$d_{(x,y)z}$	d_{xy}	$d_{x^2-y^2}$	Cu_s	O_s	$\sum$Cl	not.	M$_1$
1	2.32	0	.554	0	0	0	0	.446	0	0	0	$(d_{x^2-y^2} p_\sigma)$	A
2	-1.33	0	0	.196	.006	0	.792	0	0	0	.006	$(d_{xy} \tilde{p}_\pi)$	S
3,4	-1.58	.563	0	0	0	.437	0	0	0	0	0	$(d_{(x,y)z} p_z)$	o
5	-1.87	0	.038	0	.637	0	.009	0	.055	0	.261	$(d_{3z^2-r^2} \tilde{p}_\sigma)$	S
6	-2.12	0	0	1.00	0	0	0	0	0	0	0	p_π	A
7,8	-4.56	.641	0	0	0	.268	0	0	0	0	.091	$(p_z d_{(x,y)z})$	o
9	-5.21	0	.424	0	0	0	0	.576	0	0	0	$(p_\sigma d_{x^2-y^2})$	A
10	-6.15	0	.003	.702	.001	0	.291	0	0	0	.003	$(\tilde{p}_\pi d_{xy})$	S
11	-7.23	0	.495	0	.018	0	0	0	.294	0	.193	$(\tilde{p}_\sigma d_{3z^2-r^2})$	S

$(\pi,0)$

Nr.	E/eV	p_z	p_σ	p_π	$d_{3z^2-r^2}$	d_{yz}	d_{xz}	d_{xy}	$d_{x^2-y^2}$	Cu_s	O_s	$\sum$Cl	not.	M$_2$
1	-.40	0	.128	0	.015	0	0	0	.599	.105	.105	.049	$(d_{x^2-y^2} p_\sigma)$	S
2	-1.42	0	0	.335	0	0	0	.665	0	0	0	0	$(d_{xy} \tilde{p}_\pi)$	A
3	-1.63	.395	0	0	0	0	.601	0	0	0	0	.004	$(d_{xz} p_z)$	o
4	-2.12	0	.002	.001	.655	0	0	0	.096	.007	.019	.220	$(d_{3z^2-r^2} d_{x^2-y^2})$	S
5	-2.87	0	0	0	0	.880	0	0	0	0	0	.120	d_{yz}	o
6	-3.29	.594	0	0	0	0	.019	0	0	0	0	.387	p_z	o
7	3.58	0	.532	0	0	0	0	0	0	0	0	.468	$\tilde{p}_\sigma$	A
8	-3.96	0	0	.935	0	0	0	0	0	0	.046	.019	p_π	S
9	-4.13	.403	0	0	0	0	.270	0	0	0	0	.327	$(p_z d_{xz})$	o
10	-4.62	0	.057	.475	0	0	0	.348	0	0	0	.120	$(\tilde{p}_\pi d_{xy})$	A
11	-5.74	0	.268	.004	.079	0	0	0	.149	.032	.009	.459	$(p_\sigma d_{x^2-y^2})$	S

Table 6.1: LDA data of Sr$_2$CuO$_2$Cl$_2$ at high-symmetry points showing the weights of the different orbital groups contributing to each band. Also given are the different reflection symmetries with respect to M$_1$ and M$_2$ (see Fig. 5.9, respectively (antisymmetric (A), symmetric (S) and out-of-plane bands (o)).

$$\Gamma$$

Nr.	E/eV	p_z	p_σ	p_π	$d_{3z^2-r^2}$	d_{yz}	d_{xz}	d_{xy}	$d_{x^2-y^2}$	O_s	Cu_s	$\sum Cl$	not.	M_1	M_2
1	-.30	0	0	0	0	0	0	0	.909	.091	0	0	$d^\uparrow_{x^2-y^2}$	A	S
2,3	-2.69	0	.439	.543	0	0	0	0	0	0	0	.018	$(\tilde{p}_\pi \tilde{p}_\sigma)$	S	A
													$(p_\pi p_\sigma)$	A	S
4,5	-3.83	1.00	0	0	0	0	0	0	0	0	0	0	p_z	o	o
	(-3.69)	(.567)										(.433)			
6	-4.58	0	0	0	.640	0	0	0	0	.031	0	.329	$d_{3z^2-r^2}$	S	S
7*	-4.92	0	0	0	0	0	0	0	.893	.107	0	0	$d^\downarrow_{x^2-y^2}$	A	S
7	-5.40	0	0	0	0	0	0	1.00	0	0	0	0	d_{xy}	S	A
8,9	-5.57	0	.499	.463	0	0	0	0	0	0	0	.038	$(\tilde{p}_\sigma \tilde{p}_\pi)$	S	A
													$(p_\pi p_\sigma)$	A	S
10,11	-5.88	0	0	0	0	.803	(.803)	0	0	0	0	.197	$d_{y(x)z}$	o	o

$$(\pi, \pi)$$

Nr.	E/eV	p_z	p_σ	p_π	$d_{3z^2-r^2}$	d_{yz}	d_{xz}	d_{xy}	$d_{x^2-y^2}$	O_s	Cu_s	$\sum Cl$	not.	M_1
1	3.12	0	.467	0	0	0	0	0	.533	0	0	0	$(d^\uparrow_{x^2-y^2} p_\sigma)$	A
1*	.65	0	.704	0	0	0	0	0	.296	0	0	0	$(p_\sigma d^\downarrow_{x^2-y^2})$	A
2	-2.43	0	0	1.00	0	0	0	0	0	0	0	0	p_π	A
3,4	-2.98	.711	0	0	0	.143	.143	0	0	0	0	.002	$(p_z d_{x(y)z})$	o
	(-2.97)											(.006)		
5	-3.35	0	.009	.345	.030	0	0	.564	0	0	.004	.048	$(\tilde{p}_\pi d_{xy})$	S
6	-3.66	0	.096	.020	.356	0	0	.053	0	0	.051	.424	$(d_{3z^2-r^2} \tilde{p}_\sigma)$	S
7	-4.94	0	.561	0	0	0	0	0	.439	0	0	0	$(p_\sigma d^\uparrow_{x^2-y^2})$	A
8,9	-6.62	.155	0	0	0	.341	.341	0	0	0	0	.123	$(d_{x(y)z} p_z)$	o
	(-6.06)	(.093)				(.275)	(.275)					(.357)		
10	-7.20	0	.003	.392	.010	0	0	.591	0	0	0	.004	$(d_{xy} \tilde{p}_\pi)$	S
10*	-7.28	0	.207	0	0	0	0	0	.793	0	0	0	$d^\downarrow_{x^2-y^2} p_\sigma$	A
11	-7.86	0	.478	.001	.073	0	0	0	0	0	.280	.168	$(\tilde{p}_\sigma d_{3z^2-r^2})$	S

$$(\pi, 0)$$

Nr.	E/eV	p_z	p_σ	p_π	$d_{3z^2-r^2}$	d_{xz}	d_{yz}	d_{xy}	$d_{x^2-y^2}$	O_s	Cu_s	$\sum Cl$	not.	M_2
1	.47	0	.053	0	0	0	0	0	.696	.124	.106	.021	$(d^\uparrow_{x^2-y^2} p_\sigma)$	S
1*	-2.40	0	.273	0	.039	0	0	0	.323	.083	.119	.163	$(p_\sigma d^\downarrow_{x^2-y^2})$	S
2	-2.94	0	0	.659	0	0	0	.341	0	0	0	0	$(\tilde{p}_\pi d_{xy})$	A
3	-2.96	.704	0	0	0	.245	0	0	0	0	0	.051	$(p_z d_{xz})$	o
4	-3.76	0	.086	.003	.344	0	0	0	.057	.006	.017	.487	$(d_{3z^2-r^2} p_\sigma)$	S
5	-3.79	.705	0	0	0	.013	0	0	0	0	0	.282	p_z	o
6	-4.11	0	.635	0	0	0	0	0	0	0	0	.365	$\tilde{p}_\sigma$	A
7	-4.32	0	0	.933	.001	0	0	0	.049	0	0	.017	p_π	S
8	-5.93	0	0	0	0	0	.859	0	0	0	0	.141	d_{yz}	o
9	-6.17	0	0	.199	0	0	0	.801	0	0	0	0	$(d_{xy} \tilde{p}_\pi)$	A
10	-6.37	.128	0	0	0	.384	0	0	0	0	0	.488	$(d_{xz} p_z)$	o
11	-6.44	0	.390	0	.409	0	0	0	.104	.035	.062	0	$(p_\sigma d_{3z^2-r^2})$	S
11*	-7.49	0	.298	0	.060	0	0	0	.520	.004	.076	.042	$(d^\downarrow_{x^2-y^2} p_\sigma)$	S

Table 6.2: The LDA+U data of $Sr_2CuO_2Cl_2$ at the high-symmetry points. The bands noted by a star correspond to majority spin ($\downarrow$), whereas all the other data are given for minority spin ($\uparrow$). The column "not." gives the notation used in Section 5.3.3 to describe the bands.

(a) Γ

orbitals	repr.		M_1	M_2
p_σ, $\tilde{p}_\sigma$	$E_u^{(1)}$	(5^-)	0	0
p_π, $\tilde{p}_\pi$	$E_u^{(2)}$	(5^-)	0	0
$(p_z^{(1)} + p_z^{(2)})/\sqrt{2}$	A_{2u}	(2^-)	+	+
$(p_z^{(1)} - p_z^{(2)})/\sqrt{2}$	B_{2u}	(4^-)	−	+
$d_{x^2-y^2}$	B_{1g}	(3^+)	−	+
d_{xy}	B_{2g}	(4^+)	+	−
$d_{(x,y)z}$	E_g	(5^+)	0	0
$d_{3z^2-r^2}$	A_{1g}	(1^+)	+	+

(b) (π,π)

orbitals	repr.		M_1
$d_{3z^2-r^2}$, $\tilde{p}_\sigma$	A_{1g}	(1^+)	+
p_π	A_{2g}	(2^+)	−
$d_{x^2-y^2}$, p_σ	B_{1g}	(3^+)	−
d_{xy}, $\tilde{p}_\pi$	B_{2g}	(4^+)	+
$d_{(x,y)z}$, $p_z^{(1,2)}$	E_g	(5^+)	0

(c) $(\pi,0)$

orbitals	repr.		M_2
$d_{x^2-y^2}$, $d_{3z^2-r^2}$, p_σ	A_g	(1^+)	+
d_{xy}, $\tilde{p}_\pi$	B_{1g}	(2^+)	−
$\tilde{p}_\sigma$	B_{2u}	(3^-)	−
p_π	B_{3u}	(4^-)	+
d_{xz}, $p_z^{(1)}$	B_{2g}	(3^+)	+
$p_z^{(2)}$	B_{1u}	(2^-)	+
d_{yz}	B_{3g}	(4^+)	+

Table 6.3: Assignment of the orbitals to irreducible representations of the corresponding small groups at high-symmetry points: a) Γ (group D_{4h}), b) (π,π) (D_{4h}) and c) $(\pi,0)$ (D_{2h}). The notations in parentheses are according to LUEHRMANN [181] (see also Ref. [152]). Also given are the characters with respect to reflections at M_1 or M_2, respectively, whereby + and - correspond to the S and A given in Table 6.1. The orbital $p_z^{(1)}$ means p_z orbitals at positions $i \pm x/2$, and $p_z^{(2)}$ at positions $i \pm y/2$.

Bibliography

[1] J. G. Bednorz and K. A. Müller, "Possible high T_c Superconductivity in the La-Ba-Cu-O System," *Z. Phys. B*, vol. 64, p. 189, 1986.

[2] A. Tsvelik, *Quantum Field Theorie in Condensed Matter*. Cambridge: Cambridge University Press, 1995.

[3] C. Kim, A. Y. Matsuura, Z.-X. Shen, N. Motoyama, H. Eisaki, S. Uchida, and T. T. S. Maekawa, "Observation of spin-charge separation in one-dimensional $SrCuO_2$," *Phys. Rev. Lett.*, vol. 77, no. 19, pp. 4054–4057, 1996.

[4] K. M. Kojima, Y. Fudamoto, M. Larkin, G. M. Luke, J. Merrin, B. Nachumi, Y. J. Uemura, N. Motoyama, H. Eisaki, S. Uchida, K. Yamada, Y. Endoh, S. Hosoya, B. J. Sternlieb, and G. Shirane, "Reduction of ordered moment and Néel temperature of quasi-one-dimensional antiferromagnets Sr_2CuO_3 and Ca_2CuO_3," *Phys. Rev. Lett.*, vol. 78, no. 9, pp. 1787–1790, 1997.

[5] M. Hase, I. Terasaki, and K. Uchinokura, "Observation of the spin-Peierls transition in linear Cu^{2+} (spin 1/2) chains in an inorganic compound $CuGeO_3$," *Phys. Rev. Lett.*, vol. 70, no. 23, pp. 3651–3654, 1993.

[6] Y. M. W. Kohn and D. E. Makarov, "van der Waals energies in Density Functional Theory," *Phys. Rev. Lett.*, vol. 80, no. 19, pp. 4153–4156, 1998.

[7] P. Hohenberg and W. Kohn, "Inhomogeneous electron gas," *Phys. Rev.*, vol. 136, pp. B864–B871, 1964.

[8] M. Born and R. Oppenheimer *Ann. Phys. (N.Y.)*, vol. 84, p. 457, 1927.

[9] M. Levy, "Electron densities in search of Hamiltonians," *Phys. Rev. A*, vol. 26, pp. 1200–1208, 1982.

[10] E. H. Lieb, "Density functionals for coulomb systems," *Int. J. Quant. Chem.*, vol. XXIV, pp. 243–277, 1983.

[11] P. Ziesche and G. Lehmann, *Ergebnisse in der Elektronentheorie der Metalle*. Berlin: Springer-Verlag, 1983.

[12] D. M. Ceperly and B. J. Alder, "Ground state of the electron gas by a stochastic method," *Phys. Rev. Lett.*, vol. 45, pp. 566–569, 1980.

[13] S. Kenny, G. Rajagopal, R. Needs, W.-K. Leung, M. Godfrey, A. Williamson, and W. Foulkes, "Quantum monte carlo calculations of the energy of the relativistic homogeneous electron gas," *Phys. Rev. Lett.*, vol. 77, pp. 1099–1102, 1996.

[14] W. Kohn and L. J. Sham, "Self-consistent equations including exchange and correlation effects," *Phys. Rev.*, vol. 140, pp. A1133–A1138, 1965.

[15] O. Gunnarsson, M. Jonson, and B. I. Lundqvist, "Description of exchange and correlation effects in inhomogeneous electron systems," *Phys. Rev. B*, vol. 20, pp. 3136–3164, 1979.

[16] P. Fulde, *Electron correlations in molecules and solids.* Berlin: Springer, 1995.

[17] U. von Barth and L. Hedin, "A local exchange-correlation potential for the spin polarized case: I," *J. Phys. C*, vol. 5, pp. 1629–1642, 1972.

[18] L. Hedin and S. Lundqvist *Solid State Physics*, vol. 23, p. 1, 1969.

[19] L. Sham and W. Kohn *Phys. Rev.*, vol. 145, p. 561, 1966.

[20] L. Hedin and B. I. Lundqvist, "Explicit local exchange-correlation potentials," *J. Phys. C: Solid State Phys.*, vol. 4, pp. 2064–2083, 1971.

[21] J. P. Perdew and A. Zunger, "Self-interaction correction to density-functional approximations for many-electron systems," *Phys. Rev. B*, vol. 23, pp. 5048–5079, 1981.

[22] M. Richter, *Electronic Structure and Magnetism of Lanthanide-, Actinide-, and Transition Metal Systems.* Habilitationsschrift, TU Dresden, 1997.

[23] M. S. Hybertsen, E. Stechel, M. Schlüter, and D. R. Jennison, "Renormalization from density-functional theory to strong-coupling models for electronic states in Cu-O materials," *Phys. Rev. B*, vol. 41, no. 16, p. 11068, 1990.

[24] H. Eschrig, *Optimized LCAO Method and the Electronic Structure of Extended Systems.* Berlin: Springer-Verlag, 1989.

[25] M. Richter. Dissertation am Zentralinstitut für Festkörperphysik und Werkstoffwissenschaften Dresden, 1988.

[26] P. P. Ewald *Ann. Phys. (Leipzig)*, vol. 64, p. 253, 1921.

[27] K. Koepernik and H. Eschrig, "Full-potential nonorthogonal local-orbital minimum-basis band-structure scheme," *Phys. Rev. B*, vol. 59, no. 3, pp. 1743–1757, 1999.

[28] H. Eschrig and I. Bergert *phys.stat.sol (b)*, vol. 90, p. 621, 1978.

[29] H. Eschrig, "LCAO und Wannier-Funktionen," in *Ergebnisse in der Elektronentheorie der Metalle* [11], pp. 210–236.

[30] D. J. Singh, *Planewaves, Pseudopotentials and the LAPW Method*. Boston: Kluwer, 1994.

[31] B. Blaha, K. Schwarz, and J. Luitz, "WIEN97, Vienna University of Technology, 1997. Improved and updated version of the original copyrighted WIEN code, which was published by B. Blaha, K. Schwarz, P Soratin, and S. B. Trickey," *Comput. Phys. Commun.*, vol. 59, p. 399, 1990.

[32] J. Hubbard, "Electron correlations in narrow energy bands," *Proc. Roy. Soc. A*, vol. 276, p. 238, 1963.

[33] V. J. Emery, "Theory of High-T_c Superconductivity in Oxides," *Phys. Rev. Lett.*, vol. 58, p. 2794, 1987.

[34] A. B. Harris and R. V. Lange *Phys. Rev. B*, vol. 157, p. 295, 1967.

[35] H. Müller-Buschbaum, "Oxometallate mit ebener Koordination," *Angew. Chem.*, vol. 89, pp. 704–717, 1977.

[36] J. L. García-Muñoz, J. Rodríguez-Carvajal, F. Sapiña, M. J. Sanchis, R. Ibáñez, and D. Beltrán-Porter, "Crystal and magnetic structure of Bi_2CuO_4," *J. Phys.: Condens. Matter*, vol. 2, p. 2205, 1990.

[37] E. W. Ong, G. H. Kwei, R. A. Robinson, B. L. Ramakrishna, and R. B. von Dreele, "Long-range antiferromagnetic ordering in Bi_2CuO_4," *Phys. Rev. B*, vol. 42, no. 7, p. 4255, 1990.

[38] T. Böske, K. Maiti, O. Knauff, K. Ruck, M. S. Golden, G. Krabbes, J. Fink, T. Osafune, N. Motoyama, H. Eisaki, and S. Uchida, "Cu-O network-dependent core-hole screening in low-dimensional cuprate systems: A high-resolution x-ray photoemission study," *Phys. Rev. B*, vol. 57, no. 1, pp. 138–141, 1998.

[39] E. Dagotto and T. M. Rice, "Surprises on the way from one- to two-dimensional quantum magnets: The ladder materials," *Science*, vol. 271, p. 618, 1996.

[40] C. L. Teske and H. Müller-Buschbaum, "Zur Kenntnis von Sr_2CuO_3," *Z. Anorg. Allg. Chem.*, vol. 371, pp. 325–332, 1969.

[41] C. L. Teske and H. Müller-Buschbaum, "Zur Kenntnis von Ca_2CuO_3," *Z. Anorg. Allg. Chem.*, vol. 371, pp. 234–241, 1970.

[42] K. Kojima, M. Larkin, B. Namuchi, Y. Uemura, H. Eisaki, M. Motoyama, S. Uchida, B. Sternlieb, and G. Shirane *Czech. J. Phys.*, vol. 46 Suppl. S4, p. 1945, 1996.

[43] K. Yamada, N. Suzuki, and J. Akimitsu, "Magnetic-properties of $(Sr,Ba)_2Cu_3O_4Cl_2$ - 2-dimensional antiferromagnetic cuprates containing 2 types of cu-site," *Physica B*, vol. 213 & 214, p. 191, 1995.

[44] N. Motoyama, H. Eisaki, and S. Uchida, "Magnetic susceptibility of ideal spin 1/2 Heisenberg antiferromagnetic chain systems, Sr_2CuO_3 and $SrCuO_2$," *Phys. Rev. Lett.*, vol. 76, pp. 3212–3215, 1996.

[45] M. Takigawa, N. Motoyama, H. Eisaki, and S. Uchida, "Dynamics in the S = 1/2 one-dimensional antiferromagnet Sr_2CuO_3 via ^{63}Cu NMR," *Phys. Rev. Lett.*, vol. 76, pp. 4612–4615, 1996.

[46] H. J. Schulz, "Dynamics of coupled quantum spin chains," *Phys. Rev. Lett.*, vol. 77, pp. 2790–2793, 1996.

[47] I. Affleck, M. Gelfand, and R. Singh, "A plane of weakly coupled Heisenberg chains: theoretical arguments and numerical calculations.," *J. Phys. A*, vol. 27, pp. 7313–7325, 1994.

[48] Z. Wang, "Weakly coupled antiferromagnetic quantum spin chains," *Phys. Rev. Lett.*, vol. 78, pp. 126–129, 1997.

[49] H. Rosner, H. Eschrig, R. Hayn, S.-L. Drechsler, and J. Malek, "Electronic structure and magnetic properties of the linear chain cuprates Sr_2CuO_3 and Ca_2CuO_3," *Phys. Rev. B*, vol. 56, no. 6, pp. 3402–3412, 1997.

[50] F. Sapiña, J. Rodríguez-Carvajal, M. J. Sanchis, R. Ibáñez, D. Beltrán, and A. Beltràn, "Crystal and magnetic structure of Li_2CuO_2," *Solid State Comm.*, vol. 74, no. 8, pp. 779–784, 1990.

[51] R. Hoppe and H. Rieck, "Die Kristallstruktur von Li_2CuO_2," *Z. Anorg. Allg. Chem*, vol. 379, pp. 157–164, 1970.

[52] H. Völlenkle, A. Wittmann, and H. Nowotny, "Zur Kristallstruktur von $CuGeO_3$," *Monatsh. Chem.*, vol. 98, pp. 1352–1357, 1967.

[53] M. Hidaka, M. Hatae, I. Yamada, M. Nishi, and J. Akimitsu, "Re-examination of the room temperature crystal structure of $CuGeO_3$ by x-ray diffraction experiments: observation of new superlattice reflections," *J. Phys.: Condens. Matter*, vol. 9, pp. 809–824, 1997.

[54] H. H. Otto and M. Meibohm, "Crystal structure of copper polysilicate, $CuSiO_3$," *Z. Kristallogr., to be published*, 1999.

[55] H. Rosner, R. Hayn, and S.-L. Drechsler, "The electronic structure of Li_2CuO_2," *Physica B*, vol. 259–261, pp. 1001–1002, 1999.

[56] R. Weht and W. E. Pickett, "Extended moment formation and second neighbor coupling in Li_2CuO_2," *Phys. Rev. Lett.*, vol. 81, pp. 2502–2505, 1998.

[57] N. Tanaka, M. Suzuki, and K. Motizuki, "Electronic structure and magnetic properties of Li_2CuO_2," *J. Phys. Soc. Jpn.*, vol. 68, no. 5, pp. 1684–1692, 1999.

[58] L. F. Mattheiss, "Band picture of the spin-Peierls transition in the spin-1/2 linear chain cuprate $CuGeO_3$," *Phys. Rev. B*, vol. 49, no. 19, pp. 14050–14053, 1994.

[59] Y. Mizuno, T. Tohyama, S. Maekawa, T. Osafune, N. Motoyama, H. Eisaki, and S. Uchida, "Electronic states and magnetic properties of edge-sharing Cu-O chains," *Phys. Rev. B*, vol. 57, pp. 5326–5335, 1998.

[60] R. Neudert, H. Rosner, S.-L. Drechsler, M. Kielwein, M. Sing, M. Knupfer, M. Golden, J. Fink, N. Nücker, S. Schuppler, N. Motoyama, H. Eisaki, S. Uchida, Z. Hu, M. Domke, and G. Kaindl, "The unoccupied electronic structure of Li_2CuO_2," *Phys. Rev. B*, in press.

[61] L. P. Regnault, M. Aïn, B. Hennion, G. Dhalenne, and A. Revcolevschi, "Inelastic-neutron-scattering investigation of the spin-Peierls system $CuGeO_3$," *Phys. Rev. B*, vol. 53, no. 9, pp. 5579–5597, 1996.

[62] H. Kuroe, J. Sasaki, T. Sekine, N. Koide, Y. Sasago, K. Uchinokura, and M. Hase, "Spin fluctuations in $CuGeO_3$ probed by light scattering," *Phys. Rev. B*, vol. 55, no. 1, pp. 409–415, 1997.

[63] V. N. Muthukumar, C. Gros, W. Wenzel, R. Valent, P. Lemmens, B. Eisener, G. G. M. Weiden, C. Geibel, and F. Steglich, "Frustration-induced Raman scattering in $CuGeO_3$," *Phys. Rev. B*, vol. 54, pp. R9635–R9638, 1996.

[64] V. N. Muthukumar, C. Gros, R. Valent, M. Weiden, C. Geibel, F. Steglich, P. Lemmens, M. Fischer, and G. Güntherodt, "J_1-J_2 model revisited: Phenomenology of CuGeO$_3$," *Phys. Rev. B*, vol. 55, no. 9, pp. 5944–5952, 1997.

[65] M. Hase, I. Terasaki, Y. Sasago, K. Uchinokura, and H. Obara, "Effects of substitution of Zn for Cu in the spin-Peierls cuprate CuGeO$_3$: The suppression of the spin-Peierls transition and the occurence of a new spin-glass state," *Phys. Rev. Lett.*, vol. 71, no. 24, pp. 4059–4062, 1993.

[66] M. Poirier, R. Beaudry, M. Castonguay, M. L. Plumer, G. Quirion, F. S. Razavi, A. Revcolevschni, and G. Dhalenne, "Doping effects on the magnetic phase diagram of the spin-Peierls system CuGe$_{1-x}$Si$_x$O$_3$," *Phys. Rev. B*, vol. 52, no. 10, pp. 6971–6974, 1995.

[67] K. M. Kojima, Y. Fudamoto, M. Larkin, G. M. Luke, J. Merrin, B. Nachumi, Y. J.Uemura, M. Hase, Y. Sasago, K. Uchinokura, Y. Ajiro, A. Revcolevschi, and J.-P. Renard, "Antiferromagnetic order with spatially inhomogeneous ordered moment size of Zn- and Si-doped CuGeO$_3$," *Phys. Rev. Lett.*, vol. 79, no. 3, pp. 503–506, 97.

[68] P. Fronzes, M. Poirier, A. Revcolevschi, and G. Dhalenne, "Coexistence of spin-Peierls and antiferromagnetic Néel states in doped CuGeO$_3$: A magnetic-phase-diagram approach," *Phys. Rev. B*, vol. 55, no. 13, pp. 8324–8329, 1997.

[69] M. Baenitz *private communication.*

[70] Z. S. Popović, F. R. Vukajlović, and Ž. V. Šljivančanin, "Band structure of spin-Peierls cuprate CuGeO$_3$," *J. Phys.: Condens. Matter*, vol. 7, pp. 4549–4559, 1995.

[71] J. Kanamori *Progr. Theor. Phys. (Kyoto)*, vol. 17, pp. 177, 190, 1957.

[72] P. W. Anderson, "New approach to the theory of superexchange interaction," *Phys. Rev.*, vol. 115, no. 1, pp. 2–12, 1959.

[73] J. Goodenough, *Magnetism and the chemical bond.* New York: John Wiley and Sons, 1963.

[74] W. Geertsma and D. Khomskii, "Influence of side groups on 90° superexchange: a modification of the Goodenough-Kanamori-Anderson rules," *Phys. Rev. B*, vol. 54, no. 5, pp. 3011–3014, 1996.

[75] R. Kipka and H. Müller-Buschbaum, "Zur Kenntnis von Ba$_3$Cu$_2$O$_4$Cl$_2$," *Z. anorg. allg. Chem.*, vol. 422, pp. 231–236, 1976.

[76] M. Wolf, K. Ruck, D. Eckert, G. Krabbes, and K.-H. Müller, "Spin-flop transition in the low-dimensional compound $Ba_3Cu_2O_4Cl_2$," *J. Magn. Magn. Mat.*, vol. 196-197, pp. 579–580, 1999.

[77] A. Kreissig *private communication.*

[78] Y. Matsushita, Y. Oyama, M. Hasegawa, and H. Takei, "Growth and structural refinement of orthorhombic $SrCuO_2$ crystals," *J. Solid State Chem.*, vol. 114, pp. 289–293, 1994.

[79] I. A. Zalisnyak, C. Broholm, M. Kibune, M. Nohara, and H. Takagi, "Anisotropic spin freesing in the S=1/2 zigzag ladder compound $SrCuO_2$," to be published.

[80] M. Matsuda, K. Katsumata, K. M. Kojima, M. Larkin, G. M. Luke, J. Merrin, B. Nachumi, Y. J. Uemura, H. Eisaki, N. Motoyama, S. Uchida, and G. Shirane, "Magnetic phase transition in the S = (1/2) zigzag-chain compound $SrCuO_2$," *Phys. Rev. B*, vol. 55, no. 18, pp. 11953–11956, 1997.

[81] W. E. Pickett, "Electronic structure of the high-temperature oxide superconductors," *Rev. Mod. Phys.*, vol. 61, p. 433, 1989.

[82] H. A. Jahn and E. Teller *Proc. R. Soc. London, Ser. A*, vol. 161, p. 220, 1937.

[83] L. F. Mattheiss, "Electronic band properties and superconductivity in $La_{2-y}X_yCuO_4$," *Phys. Rev. Lett.*, vol. 58, no. 10, p. 1028, 1987.

[84] M. K. Wu, J. R. Ashburn, C. J. Torng, P. H. Hor, R. L. Meng, L. Gao, Z. J. Huang, Y. Q. Wang, and C. W. Chu, "Superconductivity at 93 K in a new mixed phase Y-Ba-Cu-O compound system at ambient pressure," *Phys. Rev. Lett.*, vol. 60, p. 941, 1987.

[85] J. Rossat-Mignod et al., "Neutron scattering study of the $YBa_2Cu_32O_{6+x}$ system," *Physica C*, vol. 185-189, p. 86, 1991.

[86] N. E. Bickers, D. J. Scalapino, and S. R. White, "Conserving approximations for strongly correlated electron systems: Bethe-Salpeter equation and dynamics for the two-dimensional Hubbard model," *Phys. Rev. Lett.*, vol. 62, no. 8, p. 961, 1989.

[87] N. Bulut and D. J. Scalapino, "Analysis of NMR data in the superconducting state of $YBa_2Cu_3O_7$," *Phys. Rev. Lett.*, vol. 68, no. 5, p. 706, 1992.

[88] J. D. Jorgensen, M. A. Beno, D. G. Hinks, L. Soderholm, K. J. Volin, R. L. Hitterman, J. D. Grace, I. K. Schuller, C. U. Segre, K. Zhang, and M. S. Kleefisch, "Oxygen ordering and the orthorhombic-to-tetragonal phase transition in $YBa_2Cu_3O_{7-x}$," *Phys. Rev. B*, vol. 36, no. 7, pp. 3608–3616, 1987.

[89] H. Krakauer, W. E. Pickett, and R. E. Cohen *J. Supercond.*, vol. 1, p. 111, 1988.

[90] K. T. Park, K. Terakura, T. Oguchi, A. Yanase, and M. Ikeda, "Implications of band-structure calculations for high-T_c related oxides," *J. Phys. Soc. Jpn.*, vol. 57, pp. 3445–3456, 1988.

[91] L. F. Mattheiss and D. R. Hamann, "Electronic-structure of the high-t_c superconductor $Ba_2YCu_3O_{6.9}$," *Solid State Comm.*, vol. 63, pp. 395–399, 1988.

[92] W. E. Pickett, R. E. Cohen, and H. Krakauer, "Precise band structure and Fermi-surface calculation for $YBa_2Cu_3O_7$: Importance of three-dimensional dispersion," *Phys. Rev. B*, vol. 42, no. 13, pp. 8764–8767, 1990.

[93] S. Massidda, J. Yu, A. J. Freeman, and D. D. Koelling, "Electronic structure and properties of $YBa_2Cu_3O_{7-\delta}$, a low dimensional, low density of states superconductor," *Phys. Lett. A*, vol. 122, pp. 198–202, 1987.

[94] W. E. Pickett, H. Krakauer, R. E. Cohen, and D. J. Singh, "Fermi surfaces, Fermi liquids, and high-temperature superconductors," *Science*, vol. 255, pp. 46–54, 1992.

[95] R. E. Cohen, W. E. Pickett, and H. Krakauer, "Theoretical determination of strong electron-phonon coupling in $YBa_2Cu_3O_7$," *Phys. Rev. Lett.*, vol. 64, no. 21, pp. 2575–2578, 1990.

[96] K. Schwarz, C. Ambrosch-Draxl, and P. Blaha, "Charge distribution and electric-field gradients in $YBa_2Cu_3O_{7-x}$," *Phys. Rev. B*, vol. 42, no. 4, pp. 2051–2061, 1990.

[97] J. C. Campuzano, G. Jennings, M. Faiz, L. Beaulaigue, B. W. Veal, J. Z. Liu, A. P. Paulikas, K. Vandervoort, H. Claus, R. S. List, A. J. Arko, and R. J. Bartlett, "Fermi surfaces of $YBa_2Cu_3O_{6.9}$ as seen by angle-resolved photoemission," *Phys. Rev. Lett.*, vol. 64, no. 19, pp. 2308–2311, 1990.

[98] M. C. Schabel, C.-H. Park, A. Matsuura, Z.-X. Shen, D. A. Bonn, R. Liang, and W. N. Hardy, "Angle-resolved photoemission on untwinned

$YBa_2Cu_3O_{6.95}$. I. Electronic structure and dispersion relations of surface and bulk bands," *Phys. Rev. B*, vol. 57, no. 10, pp. 6090–6106, 1998.

[99] M. C. Schabel, C.-H. Park, A. Matsuura, Z.-X. Shen, D. A. Bonn, R. Liang, and W. N. Hardy, "Angle-resolved photoemission on untwinned $YBa_2Cu_3O_{6.95}$. II. Determination of Fermi surfaces," *Phys. Rev. B*, vol. 57, no. 10, pp. 6107–6115, 1998.

[100] C. M. Fowler, B. L. Freeman, W. L. Hults, J. C. King, F. M. Mueller, and J. L. Smith, "de Haas-van Alphen effect and Fermi surface of $YBa_2Cu_3O_{6.97}$," *Phys. Rev. Lett.*, vol. 68, no. 4, pp. 534–537, 1992.

[101] I. I. Mazin, O. Jepsen, O. K. Andersen, A. I. Liechtenstein, S. N. Rashkeev, and Y. A. Uspenskii, "Fermi-surface and low-energy excitation spectrum of $YBa_2Cu_3O_7$: Role of the Ba-O plane," *Phys. Rev. B*, vol. 45, no. 9, pp. 5103–5106, 1992.

[102] B. O. Wells, Z. X. Shen, A. Matsuura, D. M. King, M. Greven, and R. J. Birgenau, "E versus k relations and many body effects in the model insulating copper oxide $Sr_2CuO_2Cl_2$," *Phys. Rev. Lett.*, vol. 74, p. 964, 1995.

[103] F. C. Zhang and T. M. Rice, "Effective Hamiltonian for the superconducting Cu oxides," *Phys. Rev. B*, vol. 37, no. 7, p. 3759, 1988.

[104] M. Greven, R. J. Birgeneau, Y. Endoh, M. A. Kastner, B. Keimer, M. Matsuda, G. Shirane, and T. R. Thurston, "Spin correlations in the 2D Heisenberg antiferromagnet $Sr_2CuO_2Cl_2$: Neutron scattering, Monte Carlo simulation, and theory," *Phys. Rev. Lett.*, vol. 72, no. 7, pp. 1096–1099, 1994.

[105] B. Grande and H. Müller-Buschbaum, "Zur Kenntnis von $Sr_2CuO_2Cl_2$," *Z. anorg. allg. Chem.*, vol. 417, pp. 68–74, 1975.

[106] L. L. Miller, X. L. Wang, S. X. Wang, C. Stassis, D. C. Johnston, J. Faber, and C.-K. Loong, "Synthesis, structure, and properties of $Sr_2CuO_2Cl_2$," *Phys. Rev. B*, vol. 41, no. 4, pp. 1921–1915, 1990.

[107] B. Grande and H. Müller-Buschbaum *Z. Naturforsch.*, vol. 31B, p. 405, 1976.

[108] R. Kipka and H. Müller-Buschbaum, "Zur Kenntnis von $Ba_2Cu_3O_4Cl_2$," *Z. anorg. allg. Chem.*, vol. 419, pp. 58–62, 1976.

[109] W. Pitschke, G. Krabbes, and N. Mattern, "Powder diffraction and Rietveld refinement of the compound $Ba_2Cu_3O_4Cl_2$," *Powder Diffraction*, vol. 10, p. 2, 1995.

[110] S. Noro, T. Kouchi, H. Harada, T. Yamada, M. Tadokoro, and H. Suzuki, "Magnetic properties of $ba_2cu_3o_4cl_2$ single crystals," *Materials Science and Engineering*, vol. 25, p. 167, 1994.

[111] T. Ito, H. Yamaguchi, and K. Oka, "Anisotropic magnetization characteristic of Cu_3O_4 planes in $Ba_2Cu_3O_4Cl_2$," *Phys. Rev. B*, vol. 55, no. 3, p. R684, 1997.

[112] F. C. Chou, A. Aharony, R. J. Birgeneau, O. Entin-Wohlman, M. Greven, A. B. Harris, M. A. Kastner, Y. J. Kim, D. S. Kleinberg, Y. S. Lee, and Q. Zhu, "Ferromagnetic moment and spin rotation transitions in tetragonal antiferromagnetic $Sr_2Cu_3O_4Cl_2$," *Phys. Rev. Lett.*, vol. 78, no. 3, p. 535, 1997.

[113] M. S. Golden, H. C. Schmelz, M. Knupfer, S. Haffner, G. Krabbes, J. Fink, V. Y. Yushankhai, H. Rosner, R. Hayn, A. Müller, and G. Reichhard, "The dispersion of a hole in a two-dimensional Cu_3O_4 plane: a tale of two singlets," *Phys. Rev. Lett.*, vol. 78, pp. 4107–4110, 1997.

[114] H.-B. Schüttler and A. J. Fedro, "Copper-oxygen charge excitations and the effective-single-band theory of cuprate superconducto," *Phys. Rev. B*, vol. 45, no. 13, pp. 7588–7591, 1992.

[115] S.-L. Drechsler, J. Málek, S. Zalis, and K. Rosciszewski, "Exchange integral and the charge gap of the linear-chain cuprate Sr_2CuO_3," *Phys. Rev. B*, vol. 53, no. 17, pp. 11328–11331, 1996.

[116] K. Schulten, I. Ohmine, and M. Karplus *J. Chem. Phys.*, vol. 64, p. 4442, 1976.

[117] R. Neudert, S.-L. Drechsler, J.Málek, H. Rosner, M. Kielwein, Z. Hu, M. Knupfer, M. Golden, J. Fink, N. Nücker, M. Merz, S. Schuppler, N. Motoyama, H. Eisaki, S. Uchida, M. Domke, and G. Kaindl, "Hole distribution and strong intersite Coulomb interaction in the one-dimensional cuprate Sr_2CuO_3," to be published.

[118] A. Ovchinnikov *Sov. Phys. JETP*, vol. 30, p. 1160, 1969.

[119] D. Gottlieb, M. Lagos, K. Hallberg, and C. Balseiro, "Antiferromagnetic Heisenberg model with anisotropic coupling between nearest and next-nearest neighbors," *Phys. Rev. B*, vol. 43, no. 16, pp. 13668–13671, 1991.

[120] A. Fledderjohann and C. Gros, "Spin dynamics of dimerized Heisenberg chains," *Europhys. Lett.*, vol. 37, no. 3, pp. 189–194, 1997.

[121] W. Stephan and K. Penc, "Dynamical density-density correlations in one-dimensional Mott insulators," *Phys. Rev. B*, vol. 54, no. 24, pp. 17269–17272, 1996.

[122] R. Neudert *private communication.*

[123] Y. Tokura, S. Koshihara, T. Arima, H. Takagi, S. Ishibashi, T. Ido, and S. Uchida, "Cu-O network dependence of optical charge-transfer gaps and spin-pair excitations in single-CuO_2-layer compounds," *Phys. Rev. B*, vol. 41, no. 16, pp. 11657–11660, 1990.

[124] H. Suzuura, H. Yasuhara, A. Furusaki, N. Nagaosa, and Y. Tokura, "Singularities in optical spectra of quantum spin chains," *Phys. Rev. Lett.*, vol. 76, no. 14, pp. 2579–2582, 1996.

[125] S. Eggert, "Accurate determination of the exchange constant in Sr_2CuO_3 from recent theoretical results," *Phys. Rev. B*, vol. 53, no. 9, pp. 5116–5118, 1996.

[126] K. Okada, A. Kotani, K. Maiti, and D. D. Sarma, "Cu 2p core-level photoemission spectrum of Sr_2CuO_3," *J. Phys. Soc. Jpn.*, vol. 65, no. 6, pp. 1844–1848, 1996.

[127] K. Maiti, D. D. Sarma, T. Mizokawa, and A. Fujimori, "Electronic structure of one-dimensional cuprate, Sr_2CuO_3," *Europhys. Lett.*, vol. 37, no. 5, pp. 359–364, 1997.

[128] O. V. Misochko, S. Tajima, C. Urano, H. Eisaki, and S. Uchida, "Raman-scattering evidence for free spinons in the one-dimensional spin-1/2 chains of Sr_2CuO_3 and $SrCuO_2$," *Phys. Rev. B*, vol. 53, no. 22, pp. 14733–14736, 1996.

[129] I. Terasaki, R. Itti, N. Koshizuka, M. Hase, I. Tsukada, and K. Uchinokura, "Spectroscopic study of the electronic states of single-crystal $CuGeO_3$," *Phys. Rev. B*, vol. 52, no. 1, pp. 295–298, 1995.

[130] F. Parmigiani, L. Sangaletti, A. Goldoni, U. del Pennino, C. Kim, Z.-X. Shen, A. Revcolevschi, and G. Dhalènne, "Electron-spectroscopy study of correlation mechanisms in $CuGeO_3$ single crystals," *Phys. Rev. B*, vol. 55, no. 3, pp. 1459–1468, 1996.

[131] T. Ami, M. K. Crawford, R. L. Harlow, Z. R. Wang, D. C. Johnston, Q. Huang, and R. W. Erwin, "Magnetic susceptibility and low-temperature structure of the linear chain cuprate Sr_2CuO_3," *Phys. Rev. B*, vol. 51, no. 9, pp. 5994–6001, 1995.

[132] M. Hase, Y. Sasago, I. Terasaki, K. Uchinokura, G. Kido, and T. Hamamoto, "Effect of impurity on magnetic phase of spin-Peierls system; magnetization of $Cu_{1-x}Zn_xGeO_3$," *J. Phys. Soc. Jpn.*, vol. 65, no. 1, pp. 273–279, 1996.

[133] M. Nishi, O. Fujita, J. Akimitsu, K. Kakurai, and Y. Fujii *Physica B*, vol. 213 & 214, p. 275, 1995.

[134] J. Lorenzana and R. Eder, "Dynamics of the one-dimensional heisenberg model and optical absorption of spinons in cuprate antiferromagnetic chains," *Phys. Rev. B*, vol. 55, no. 6, pp. 3358–3361, 1997.

[135] T. Osafune, N. Motoyama, H. Eisaki, and S. Uchida, "Optical study of the $Sr_{14-x}Ca_xCu_{24}O_{41}$ system: Evidence for hole-doped Cu_2O_3 ladders," *Phys. Rev. Lett.*, vol. 78, no. 10, pp. 1980–1983, 1997.

[136] Y. Mizuno, T. Tohyama, and S. Maekawa, "Electronic states of doped spin ladders $(Sr,Ca)_14Cu_{24}O_{41}$," *J. Phys. Soc. Jpn.*, vol. 66, no. 4, pp. 937–940, 1996.

[137] L. F. Feiner, J. H. Jefferson, and R. Raimondi, "Effective single-band models for the high-T_c cuprates. I. Coulomb interactions," *Phys. Rev. B*, vol. 53, no. 13, pp. 8751–8773, 1996.

[138] S.-L. Drechsler, J. Málek, and H. Eschrig, "Exact diagonalization study of the hole distribution in CuO_3 chains within the four-band dp model," *Phys. Rev. B*, vol. 55, no. 1, pp. 606–620, 1997.

[139] J. Riera and A. Dobry, "Magnetic susceptibility in the spin-Peierls system $CuGeO_3$," *Phys. Rev. B*, vol. 51, no. 22, pp. 16098–16102, 1995.

[140] N. Majlis, S. Selzer, and G. C. Strinati, "Dimensional crossover in the magnetic properties of highly anisotropic antiferromagnets," *Phys. Rev. B*, vol. 45, no. 14, pp. 7872–7881, 1992.

[141] H. Fukuyama, T. Tanimoto, and M. Saito, "Antiferromagnetic long range order in disordered spin-Peierls systems," *J. Phys. Soc. Jpn.*, vol. 65, no. 5, pp. 1182–1185, 1996.

[142] N. Mermin and H. Wagner *Phys. Rev. Lett.*, vol. 17, p. 1133, 1966.

[143] A. H. Castro Neto and D. Hone, "Doped planar quantum antiferromagnets with striped phases," *Phys. Rev. Lett.*, vol. 76, no. 12, pp. 2165–2168, 1996.

[144] H. J. Schulz, "Low dimensional conductors and superconductors," vol. 155 of *NATO Advanced Study Institute*, (New York), Plenum Press, 1987.

[145] H. Rosner, S.-L. Drechsler, S. Atzkern, R. Neudert, M. Knupfer, M. Golden, J. Fink, H. Eschrig, R. Hayn, and J. Richter, "Electronic structure, interchain coupling, and antiferromagnetic interactions in the zigzag chain cuprate $SrCuO_2$," to be published.

[146] A. W. Sandvik, "Multi-chain mean-field theory of quasi one-dimensional quantum spin systems," *cond-mat/9904218*, 1999.

[147] M. E. Simón and A. A. Aligia, "Phase separation and valence instabilities in cuprate superconductors: Effective one-band-approach," *Phys. Rev. B*, vol. 53, no. 22, pp. 15327–15334, 1996.

[148] A. A. Aligia, E. R. Gagliano, and P. Vairus, "Electronic structure of the CuO_3 chains in $RBa_2Cu_3O_{6+x}$ (R=Y or a rare earth)," *Phys. Rev. B*, vol. 52, no. 18, pp. 13601–13604, 1995.

[149] K. Okada and A. Kotani, "Intersite coulomb interactions in quasi-one-dimensional copper oxides," *J. Phys. Soc. Jpn.*, vol. 66, no. 2, pp. 341–344, 1997.

[150] R. Hetzel *private communication*.

[151] R. Neudert, M. Knupfer, M. S. Golden, J. Fink, W. Stephan, K. Penc, N. Motoyama, H. Eisaki, and S. Uchida, "Manifestation of spin-charge separation in the dynamic dielectric response of one-dimensional Sr_2CuO_3," *Phys. Rev. Lett.*, vol. 81, no. 3, pp. 657–660, 1998.

[152] L. F. Mattheiss and D. R. Hamann, "Oxygen hole symmetry and bonding in cuprate superconductors," *Phys. Rev. B*, vol. 40, p. 2217, 1989.

[153] O. Knauff, T. Böske, M. Knupfer, M. S. Golden, G. Krabbes, and J. Fink, "EELS and XPS investigations of $Ba_2Cu_3O_4Cl_2$," *J. Low Temp. Phys.*, vol. 105, no. 3–4, pp. 353–358, 1996.

[154] A. M. Olés, "Antiferromagnetism and correlation of electrons in transition-metals," *Phys. Rev. B*, vol. 28, no. 1, pp. 327–339, 1983.

[155] H. Eskes and J. H. Jefferson, "Superexchange in the cuprates," *Phys. Rev. B*, vol. 48, no. 13, pp. 9788–9798, 1993.

[156] S. Hüfner, *Photoelectron Spectroscopy*. Berlin: Springer, 1995.

[157] S. Haffner, *A study of the electronic structure of Cu-O planes at half filling using high energy spectroscopies.* Dissertation an der Technischen Universität Dresden, 1999.

[158] J. Fink, N. Nücker, E. Pellegrin, H. R. M, Alexander, and M. Knupfer, "Electron-energy-loss and x-ray-absorption spectroscopy of cuprate superconductors and related-compounds," *J. Electron Spec. Rel. Phenom.*, vol. 66, no. 3-4, p. 395, 1994.

[159] J. J. M. Pothuizen, R. Eder, N. T. Hien, M. Matoba, A. A. Menovsky, and G. A. Sawatzky, "Single hole dynamics in the CuO_2 plane at half filling," *Phys. Rev. Lett.*, vol. 78, no. 4, pp. 717–720, 1997.

[160] E. Dagotto, "Correlated electrons in high-temperature superconductors," *Rev. Mod. Phys.*, vol. 66, no. 3, pp. 763–840, 1994.

[161] W. B. Peatman, J. Bahrdt, F. Eggenstein, G. Reichardt, and F. Senf *Rev. Sci. Instrum.*, vol. 66, p. 2801, 1995.

[162] H. C. Schmelz, M. S. Golden, S. Haffner, M. Knupfer, G. Krabbes, J. Fink, H. Rosner, R. Hayn, H. Eschrig, A. Mller, C. Jung, and G. Reichardt, "Electronic structure of the Cu_3O_4 plane of $Ba_2Cu_3O_4Cl_2$: Experiment and theory," *Phys. Rev. B*, vol. 57, no. 17, pp. 10936–10945, 1998.

[163] H. Rosner and R. Hayn, "The elctronic structure of $Ba_2Cu_3O_4Cl_2$," *Physica B*, vol. 230–232, pp. 889–891, 1997.

[164] A. Nazarenko, K. J. E. Vos, S. Haas, E. Dagotto, and R. J. Gooding, "Photoemission spectra of $Sr_2CuO_2Cl_2$: A theoretical analysis," *Phys. Rev. B*, vol. 51, no. 13, pp. 8676–8679, 1995.

[165] J. Bala, A. M. Oles, and J. Zaanen, "Spin polarons in the $t - t' - J$ model," *Phys. Rev. B*, vol. 52, no. 6, pp. 4597–4606, 1995.

[166] V. I. Belinicher, A. L. Chernyshev, and V. A. Shubin, "Generalized $t - t' - J$ model: Parameters and single-particle spectrum for electrons and holes in copper oxides," *Phys. Rev. B*, vol. 53, no. 1, pp. 335–342, 1996.

[167] V. Y. Yushankhai, V. S. Oudovenko, and R. Hayn, "Proper reduction scheme to an extended t-j model and the hole dispersion in $Sr_2CuO_2Cl_2$," *Phys. Rev. B*, vol. 55, no. 23, pp. 15562–15575, 1997.

[168] R. Hayn, V. Yushankhai, and S. Lovtsov, "Analysis of the singlet-triplet model for the copper oxide plane within the paramagnetic state," *Phys. Rev. B*, vol. 47, no. 9, pp. 5253–5262, 1993.

[169] S. LaRosa, I. Vobornik, F. Zwick, H. Berger, M. Grioni, G. Margaritondo, R. J. Kelley, M. Onellion, and A. Chubukov, "Electronic structure of CuO_2 planes: From insulator to superconductor," *Phys. Rev. B*, vol. 56, no. 2, pp. 525–528, 1997.

[170] C. Kim, P. J. White, Z.-X. Shen, T. Tohyama, Y. Shibata, S. Maekawa, B. O. Wells, Y. J. Kim, R. J. Birgeneau, and M. A. Kastner, "Systematics of the photoemission spectral function of cuprates: Insulators and hole- and electron-doped superconductors," *Phys. Rev. Lett.*, vol. 80, no. 19, pp. 4245–4248, 1998.

[171] K. J. von Szczepanski, P. Horsch, W. Stephan, and M. Ziegler, "Single-particle excitations in a quantum antiferromagnet," *Phys. Rev. B*, vol. 41, no. 4, pp. 2017–2029, 1990.

[172] E. Dagotto, R. Joynt, A. Moreo, S. Bacci, and E. Gagliano, "Strongly correlated electronic systems with one hole: Dynamical properties," *Phys. Rev. B*, vol. 41, no. 13, pp. 9049–9073, 1990.

[173] R. Eder and K. W. Becker, "Coherent motion of a hole in a 2-dimensional quantum antiferromagnet," *Z. Phys. B*, vol. 78, no. 2, pp. 219–227, 1990.

[174] J. G. Tobin, C. G. Olson, C. Gu, J. Z. Liu, F. R. Solal, M. J. Fluss, R. H. Howell, J. C. O'Brien, H. B. Radousky, and P. A. Sterne, "Valence bands and Fermi-surface topology of untwinned single-crystal $YBa_2Cu_3O_{6.9}$," *Phys. Rev. B*, vol. 45, no. 10, pp. 5563–5576, 1992.

[175] V. I. Anisimov, J. Zaanen, and O. K. Andersen, "Band theory and Mott insulators: Hubbard U instead of Stoner I," *Phys. Rev. B*, vol. 44, no. 3, pp. 943–954, 1991.

[176] M. T. Czyzyk and G. A. Sawatzky, "Local-density functional and on-site correlations: The electronic structure of La_2CuO_4 and $LaCuO_3$," *Phys. Rev. B*, vol. 49, no. 20, pp. 14211–14228, 1994.

[177] R. Hayn, H. Rosner, H. Eschrig, V. Y. Yushankhai, S. Haffner, C. Duerr, M. Knupfer, G. Krabbes, M. S. Golden, J. Fink, D. J. Singh, N. T. Hien, A. A. Menovsky, C. Jung, and G. Reichardt, "Analysis of the valence band spectrum of $Sr_2CuO_2Cl_2$ along the high-symmetry directions," *Phys. Rev. B*, vol. 60, no. 1, pp. 645–658, 1999.

[178] J. J. Yeh and I. Lindau *At. Data Nucl. Data Tables*, vol. 32, p. 1, 1985.

[179] A. Zangwill, *Physics at Surfaces*. Cambridge, England: Cambridge University Press , 1988.

[180] L. P. Bouckaert, R. Smoluchowski, and E. P. Wigner *Phys. Rev.*, vol. 50, p. 58, 1936.

[181] A. W. Luehrmann *Adv. Phys.*, vol. 17, p. 1, 1968.

[182] S. F. A. Kettle, *Symmetry and Structure*. New York: Wiley, 1995.

[183] M. S. Hybertsen, M. Schlüter, and N. E. Christensen, "Calculation of coulomb-interaction parameters for La_2CuO_4 using a constrained-density-functional approach," *Phys. Rev. B*, vol. 39, no. 13, pp. 9028–9041, 1989.

[184] C. Dürr, S. Legner, Z. Hu, M. Knupfer, M. S. Golden, S. H. J. Fink, H. Eisaki, S. Uchida, G. Reichardt, C. Janowitz, R. Müller, and R. L. Johnson, "The polarization dependence of the first electron removal state in $Sr_2CuO_2Cl_2$," to be published.

[185] T. Böske, O. Knauff, R. Neudert, M. Kielwein, M. Knupfer, M. S. Golden, J. Fink, H. Eisaki, S. Uchida, K. Okada, and A. Kotani, "High-resolution x-ray-photoemission study of single crystalline $Sr_2CuO_2Cl_2$," *Phys. Rev. B*, vol. 56, no. 6, pp. 3438–3446, 1997.

[186] J. Igarashi, P. Unger, K. Hirai, and P. Fulde, "Local approach to electron correlations in ferromagnetic nickel," *Phys. Rev. B*, vol. 49, no. 23, pp. 16181–16190, 1994.

[187] M. Takahashi and J. Igarashi (unpublished).

[188] R. Neudert, S.-L. Drechsler, J. Málek, H. Rosner, M. Kielwein, Z. Hu, M. Knupfer, M. Golden, J. Fink, N. Nücker, M. Merz, S. Schuppler, N. Motoyama, H. Eisaki, S. Uchida, M. Domke, and G. Kaindl, "Hole distribution and strong intersite Coulomb interaction in the one-dimensional cuprate Sr_2CuO_3," to be published.

[189] M. Uehara, T. Nagata, J. Akimitsu, H. Takahashi, N. Mori, and K. Kinoshita, "Superconductivity in the ladder material $Sr_{0.4}Ca_{13.6}Cu_{24}O_{41.84}$," *J. Phys. Soc. Jpn.*, vol. 65, no. 9, pp. 2764–2767, 1996.

[190] J. Kanamori, "Electron correlation on ferromagnetism of transition metals," *Prog. Theor. Phys.*, vol. 30, no. 1, p. 275, 1963.

[191] H. Rosner, R. Hayn, and J. Schulenburg, "Tight-binding parameters and exchange integrals of $Ba_2Cu_3O_4Cl_2$," *Phys. Rev. B*, vol. 57, no. 21, pp. 13660–13666, 1998.

[192] M. Domke, T. Mandel, A. Puschmann, C. Xue, D. A. Shirley, G. Kaindl, H. Petersen, and P. Kuske, "Performance of the high-resolution SX700/II monochromator," *Rev. Sci. Inst.*, vol. 63, no. 1, pp. 80–89, 1992.

[193] B. K. Teo and P. A. Lee *J. Am . Chem. Soc.*, vol. 101, p. 2815, 1979.

[194] S. Haffner, R. Neudert, M. Kielwein, M. Knupfer, M. S. Golden, K. Ruck, G. Krabbes, J. Fink, H. Rosner, R. Hayn, H. Eisaki, S. Uchida, Z. Hu, M. Domke, and G. Kaindl, "Unoccupied electronic structure of $Sr_2CuO_2Cl_2$ and $Ba_2Cu_3O_4Cl_2$: Experiment and theory," *Phys. Rev. B*, vol. 57, no. 6, pp. 3672–3678, 1998.

[195] J. Stöhr, *NEXAFS Spectroscopy.* Berlin: Springer, 1992.

[196] C. T. Chen, F. Sette, Y. Ma, M. S. Hybertsen, E. B. Stechel, W. M. C. Foulkes, M. Schulter, S.-W. Cheong, A. S. Cooper, L. W. Rupp, J. B. Batlogg, Y. L. Soo, Z. H. Ming, A. Krol, and Y. H. Kao, "Electronic states in $La_{2-x}Sr_xCuO_{4+\delta}$¡ probed by soft-x-ray absorption," *Phys. Rev. Lett.*, vol. 66, no. 1, pp. 104–107, 1991.

[197] F. M. F. de Groot, J. C. Fuggle, B. T. Thole, and G. A. Sawatzky, "$L_{2,3}$ x-ray-absorption edges of d^0 compounds: K^+, Ca^{2+}, Sc^{3+}, and Ti^{4+} in O_h (octahedral) symmetry," *Phys. Rev. B*, vol. 41, no. 2, pp. 928–937, 1990.

[198] J. B. Birks, *Photophysics of Aromatic Molecules.* New York: Wiley, 1970.

[199] J. W. Gadzuk *Phys. Rev. B*, vol. 14, p. 5458, 1976.

[200] S. L. Drechsler *private communication.*

[201] A. Damascelli, D. van der Marel, F. Parmigiani, G. Dhalenne, and A. Revcolevschi, "Infrared signatures of the spin-Peierls transition in $CuGeO_3$," *Phys. Rev. B*, vol. 56, no. 18, pp. 11373–11376, 1997.

[202] A. S. Alexandrov and N. Mott, *Polarons & Bipolarons.* Singapore: World Scientific, 1995.

[203] G. Wellein, H. Röder, and H. Fehske, "Polarons and bipolarons in strongly interacting electron-phonon systems," *Phys. Rev. B*, vol. 53, no. 15, pp. 9666–9675, 1996.

[204] A. Alexandrov and J. Ranninger *Physica C*, vol. 198, p. 360, 1992.

[205] J. Ranninger, "Spectral properties of small-polaron systems," *Phys. Rev. B*, vol. 48, no. 17, pp. 13166–13169, 1993.

[206] G. D. Mahan, *Many particle physics*. New York: Plenum Press, 1993.

[207] Z.-X. Shen and J. R. Schrieffer, "Momentum, temperature, and doping dependence of photoemission lineshape and implications for the nature of the pairing potential in high-T_c superconducting materials," *Phys. Rev. Lett.*, vol. 78, no. 9, pp. 1771–1774, 1997.

List of Publications

H. Rosner and R. Hayn, "The electronic structure of $Ba_2Cu_3O_4Cl_2$," *Physica B*, vol. 230–232, pp. 889–891, 1997.

H. Rosner, H. Eschrig, R. Hayn, S.-L. Drechsler, and J. Malek, "Electronic structure and magnetic properties of the linear chain cuprates Sr_2CuO_3 and Ca_2CuO_3," *Phys. Rev. B*, vol. 56, no. 6, pp. 3402–3412, 1997.

M. S. Golden, H. C. Schmelz, M. Knupfer, S. Haffner, G. Krabbes, J. Fink, V. Yu. Yushankhai, H. Rosner, R. Hayn, A. Müller, and G. Reichhard, "The dispersion of a hole in a two-dimensional Cu_3O_4 plane: a tale of two singlets," *Phys. Rev. Lett.*, vol. 78, pp. 4107–4110, 1997.

S.-L. Drechsler, H. Eschrig, J. Malek, R. Hayn and H. Rosner, "Electronic structure and BOW-CDW states of CuO_3 chains," *J. of Supercond.*, vol. 10, no. 4 pp. 393-396, 1997.

S. Haffner, R. Neudert, M. Kielwein, M. Knupfer, M. S. Golden, K. Ruck, G. Krabbes, J. Fink, H. Rosner, R. Hayn, H. Eisaki, S. Uchida, Z. Hu, M. Domke, and G. Kaindl, "Unoccupied electronic structure of $Sr_2CuO_2Cl_2$ and $Ba_2Cu_3O_4Cl_2$: Experiment and theory," *Phys. Rev. B*, vol. 57, no. 6, pp. 3672–3678, 1998.

H. Rosner, R. Hayn, and J. Schulenburg, "Tight-binding parameters and exchange integrals of $Ba_2Cu_3O_4Cl_2$," *Phys. Rev. B*, vol. 57, no. 21, pp. 13660–13666, 1998.

H. C. Schmelz, M. S. Golden, S. Haffner, M. Knupfer, G. Krabbes, J. Fink, H. Rosner, R. Hayn, H. Eschrig, A. Müller, C. Jung, and G. Reichardt, "Electronic structure of the Cu_3O_4 plane of $Ba_2Cu_3O_4Cl_2$: Experiment and theory," *Phys. Rev. B*, vol. 57, no. 17, pp. 10936–10945, 1998.

H. Rosner, R. Hayn, and S.-L. Drechsler, "The electronic structure of Li_2CuO_2," *Physica B*, vol. 259–261, pp. 1001–1002, 1999.

V. Yu. Yushankhai, R. Hayn and H. Rosner "Multi-band effective tight-binding model for the CuO_2 plane and hole dispersion in $Sr_2CuO_2Cl_2$," *Physica B*, vol. 259-261, pp. 762–763, 1999

H. Eschrig and H. Rosner "Crystal structures from building blocks: The metallates," *Nova Acta Leopoldina NF*, vol. 79, no. 310, pp. 59–71, 1999.

R. Neudert, M. S. Golden, M. Knupfer, S. Haffner, J. Fink, S.-L. Drechsler, J. Malek, H. Rosner, R. Hayn, K. Ruck, G. Krabbes, W. Stephan, K. Penc,

V. Yu. Yushankhai, C. Waidacher, J. Richter, K. W. Becker, T. Osufane, N. Motoyama, H. Eisaki, and S. Uchida "The electronic structure of one and two-dimensional cuprates from high energy spectroscopy," *Physica C*, vol. 317-318, pp. 312–319, 1999.

S.-L. Drechsler, S. V. Shulga, K.-H. Müller, G. Fuchs, J. Freudenberger, H. Eschrig, L. Schultz, M. S. Golden, H.v. Lips, J. Fink, H. Rosner, P. Zahn, A. Gladun, D. Lipp, A. Kreyssig, M. Loewenhaupt, K. Winzer, and K. Krug, "Superconducting rare earth transition metal borocarbides," *Physica C*, vol. 317-318, pp. 117–126, 1999.

R. Hayn, H. Rosner, H. Eschrig, V. Yu. Yushankhai, S. Haffner, C. Duerr, M. Knupfer, G. Krabbes, M. S. Golden, J. Fink, D. J. Singh, N. T. Hien, A. A. Menovsky, C. Jung and G. Reichardt, "Analysis of the valence band spectrum of $Sr_2CuO_2Cl_2$ along the high-symmetry directions", *Phys. Rev. B*, vol. 60, no. 1, pp. 645–658, 1999.

R. Neudert, H. Rosner, S.-L. Drechsler, M. Kielwein, M. Sing, M. Knupfer, M. S. Golden, J. Fink, N. Nücker, S. Schuppler, N. Motoyama, H. Eisaki, S. Uchida, Z. Hu, M. Domke and G. Kaindl, "The unoccupied electronic structure of Li_2CuO_2", *Phys. Rev.B*, in press

H.v. Lips, Z. Hu, C. Grazioli, S.-L. Drechsler, G. Behr, M. Knupfer, M. S. Golden, J. Fink, H. Rosner, M. Domke and G. Kaindl, "Polarization dependent X-ray absorption spectroscopy on single crystal YNi_2B_2C superconductors," *Phys. Rev. B*, in press

J. Freudenberger, G. Fuchs, K.-H. Müller, K. Nenkow, S.-L. Drechsler, A. Kreissig, H. Rosner, K. Koepernik, D. Lipp and L. Schulz, "Diluted and concentrated isoelectronic substitutional effects in superconducting $R_xY_{1-x}Ni_2B_2C$ compounds," *J. Low. Temp. Phys.*, in press

S.-L. Drechsler, H. Rosner, S. V. Shulga, H.v. Lips, J. Freudenberger, G. Fuchs, K.-H. Mïler, M. S. Golden, J. Fink, and H. Eschrig, "Electronic structure and superconductivity of nonmagnetic transition metal borocarbides," *J. Low. Temp. Phys.*, in press

R. Neudert, S.-L. Drechsler, J. Málek, H. Rosner, M. Kielwein, Z. Hu, M. Knupfer, M. S. Golden, J. Fink, N. Nücker, M. Merz, S. Schuppler, N. Motoyama, H. Eisaki, S. Uchida, M. Domke, and G. Kaindl, "Hole distribution and strong intersite Coulomb interaction in the one-dimensional cuprate Sr_2CuO_3," submitted to *Phys. Rev. B*.

H. Rosner, S.-L. Drechsler, S. Atzkern, R. Neudert, M. Knupfer, M. S. Golden, J. Fink, H. Eschrig, R. Hayn, and J. Richter, "Electronic structure, interchain

coupling, and antiferromagnetic interactions in the zigzag chain cuprate $SrCuO_2$," submitted to *Phys. Rev. B.*

S.-L. Drechsler, J. Malek, H. Rosner, R. Neudert, M. Knupfer, M. S. Golden, J. Fink, H. Eschrig, C. Waidacher and R. Hetzel, "The hole distribution in cuprate chains," submitted to *J. Low. Temp. Phys.*

J. Freudenberger, A. Kreyssig, H. Rosner, K. Koepernik, S.-L. Drechsler, G. Fuchs, K. Nenkov, K. H. Müller, M. Loewenhaupt, H. Eschrig, L. Schultz "Quantifization of the superconducting transition temperature in nonmagnetic $R_x R'_{1-x} Ni_2 B_2 C$ series (R = Sc, Y, Lu)", to be published

Acknowledgment

This work would not have been possible without mental, practical and moral support of many persons. Certainly, none of these backings is unimportant. If somebody is not mentioned here, this is, consequently, only a sign of my unreliable memory.

Firstly, I would like to thank Prof. Helmut Eschrig for supervision of this interesting and challenging work. He taught me do distinguish important from unimportant, to say what you have to say and to do this without frills.

I am much obliged to Drs. Roland Hayn and Stephan-Ludwig Drechsler. Roland, without your deep insight, this thesis would not have been possible. You counterbalanced my sometimes rash conclusions and convinced me about the necessity to do certain things really carefully. Stephan, discussions with you gave me back the feeling that physics is a passion.

All members of our working group as well as many of our guests contributed to the completion of this work. Thank you for your collaboration and for many discussions, Mrs. Ulrike Nitzsche, Drs. Manuel Richter, Klaus Koepernik, Viktor Yushankhai, Jörg Forstreuter, Thomas Kraft, Clemens Kress, Lutz Steinbeck, Martin Diviš, Arthur Ernst, Samed Halilov, Alexander Yaresko, Peter Oppeneer, Manfred Taut, Mr. Vito Servedio, Mr. Igor Tschaplygine and Mr. Ingo Opahle. Especially I am indebted to you, Ulrike, Manuel, Klaus, Vito and Viktor for inspiring discussions, collaboration and help concerning tricky computer problems. Vito, your *espresso* was a real elexier of life during the work!

Mrs. Helga Kotte is acknowledged for excellent secretary work and for a smooth running of the administration. Helga, you were the soul of our group always creating a pleasant atmosphere.

This work was carried out within the framework of the *Graduiertenkolleg* "Struktur- und Korrelationseffekte in Festkörpern" of the *Technische Universität Dresden*. I would like to thank all the members of the *Graduiertenkolleg* for fruitful discussions and collaborations. I would like to thank Prof. C. Holste and B. Wilczek for the professional organization of the *Graduiertenkolleg*.

Especially, the collaboration with the *Institut für Festkörperforschung* of the *Institut für Festkörper- und Werkstofforschung Dresden* is gratefully acknowledged. Thank you Drs. Stefan Haffner, Mark Golden, Heike Schmelz, Martin Knupfer and Mr. Ralph Neudert for the patience in discussions, where the same terms had a different meaning for experimentalists and theoreticians at the beginning.

I really wish to thank for the pleasant collaboration and discussions with you, Mr. Christoph Waidacher, Drs. Ingrid Mertig , Peter Zahn and Mr. Jörg Binder from the *Institut für Theoretische Physik* of the *Technische Universität Dresden*.

I would like to thank my dear family and my parents for the help and understanding through all the time. Andrea, you prepared the breakfast when I was tired in the morning; Maria you were a sweet and *silent* baby and you let me sleep when I really needed it.

Finally, I wish to thank all friends outside the scientific work who have turned these years into such pleasant time. THANKS to Uwe, Micha, Holger, Steffi, Christiana, Thomas, Paule, Ute, Kathrin, Katharina, and many others...

Versicherung

Hiermit versichere ich, daß ich die vorliegende Arbeit ohne unzulässige Hilfe Dritter und ohne Benutzung anderer als der angegebenen Hilfsmittel angefertigt habe. Die aus fremden Quellen direkt oder indirekt übernommenen Gedanken sind als solche kenntlich gemacht. Die Arbeit wurde bisher weder im Inland noch im Ausland in gleicher oder ähnlicher Form einer anderen Prüfungsbehörde vorgelegt.

Diese Dissertation wurde unter der Betreuung von Prof. Dr. H. Eschrig in der Arbeitsgruppe "Theorie komplexer und korrelierter Elektronensysteme" der Max-Planck-Gesellschaft im Rahmen des Graduiertenkollegs "Stuktur- und Korrelationseffekte in Festkörpern" an der Technische Universität Dresden angefertigt.

Dresden, den 10. August 1999   Helge Rosner

HSSS AdminTools (c) 2001, last visited: Thu May 31 14:12:46 GMT+02:00 2001